THÈSE

En vue de l'obtention du

DOCTORAT DE L'UNIVERSITÉ DE TOULOUSE

Délivré par : *l'Université Toulouse 3 Paul Sabatier (UT3 Paul Sabatier)*

Présentée et soutenue le *22 Septembre 2017* **par :**

FILIPA CATARINA MARTINS VARINO

Typologie des tempêtes du XXe siècle.

JURY

FRANCK ROUX	Université Toulouse 3	Président du jury
PASCAL YIOU	LSCE,Paris	Examinateur
GREGOR C. LECKEBUSCH	Birmingham University	Rapporteur
FRANCIS CODRON	LMD,Paris	Rapporteur
LEN SHAFFREY	Reading University	Rapporteur
MARIE-LAURE FANDEUR	SCOR	Examinateur

École doctorale et spécialité :
SDU2E : Océan, Atmosphère, Climat

Unité de Recherche :
Météo-France
Centre National de Recherches Météorologiques (CNRM, UMR 3589)

Directeur(s) de Thèse :
Philippe Arbogast, *Gwendal Rivière* et *Bruno Joly*

Rapporteurs :
Gregor C. Leckebusch, *Len Shaffrey* et *Francis Codron*

Acknowledgements

I could not start the acknowledgements from someone else than my supervisors. Philippe Arbogast , Gwendal Riviere and Bruno Joly to whom I am very grateful.Thank you for having the patience to explaining me everything in the windstorms world, for the good talks and for the all the time. I would never be able to to half of what I did without you. I must also thanks Marie-Laure Fandeur and Henry Bovy for the support and for helping me understanding windstorms from a re-insurance point of view and, of course, to SCOR for co-financing this thesis. I am also grateful for the time and feedbacks form the member of the jury Franck Roux, Gregor C. Leckebusch, Francis Codron, Len Shaffrey and Pascal Yiou.

There are also so many to whom I am entirely grateful. To my dear Marie Drouard that has proven to be not only a very good friend, but also a very good french teacher, merci Marie. To the recyf Team (Carole, Pierrick, Alan, Anne-Lise, Laurent Dominique, Pascal, Benoit, Marie, Laure, and Matteo) that helped me integrate so easily. Thank you for all the PhDs student that welcomed me warmly at the lunch table every day for 3 years.

Je ne pouvais pas non plus passer sans remercier mon MI pour toute ta patience et le soutien et le positivisme constant. Un gros merci à Zinda et Michel, ma famille française que j'ai connue à Toulouse, que m'ont très bien accueillie et sans laquelle je n'aurais jamais compris la bureaucratie française.

Por fim, eu tenho de agradecer a todos aqueles que a mais de 1500 quilómetros de distancia conseguiram estar sempre presentes. Aos meninos e meninas da fcul (Sílvia Catarina Joana, a Ana a Sofia o Tomas o Pedro o Alex entre tantos outros) por se lembrarem me mim. Às meninas do IPMA (Inês e Marta) pelas mensagens quase-semanais de preocupação e apoio.
Finalmente, tenho de agradecer aos que foram essenciais para que pudesse estar aqui. Nunca teria sido a primeira da família a ter acabado o liceu e chegar a fazer um doutoramento se não fossem os meus pais e todo o que eles fizeram durante

a vida para me ajudarem a la chegar. Serei eternamente grata. Obrigada à minha irmã por estar la sempre para a pipa, aos meus avós por serem uns fofos, aos meus tios e primos que fazem tão parte da minha vida.

Abstract

Extratropical cyclones (ETCs) variability is not only a subject that raises interest among the scientific community, but also extremely important in terms of social-economical impacts. Nevertheless, the study of both the extratropical cyclones variability and windstorms impacts is still scarce, particularly at time-scales that cover the twentieth century.

This thesis aims to study, both storms track variability and associated losses from the beginning of the 20th century until 2010. In order to do so, the work was separated in two main parts, one witch focus on ETCs climatology during the last century using reanalysis data and another focused on loss indexes calculations and risk assessment of windstorms.

The first part of this PhD concerns the study of ETCs variability after applying a tracking algorithm on the long-term ECMWF reanalysis ERA-20C. The number of ETCs per year shows three distinct periods for the moderate and deep cyclones. Two periods, one at the beginning and another at end of the century (1900-1935 and 1980-2010) for which no significative trends are observed and a middle-century period between 1935-1980 which presents a significative positive trend. This last trend, however, a deeper analysis on this period should be done due to time-inhomogeneity of long-term reanalysis datasets. For this reason, a set of physical parameters are analysed and a physical interpretation made for each one of the periods. During the middle period, a general cooling of the atmosphere is observed, particularly at high-latitudes, which increases the meridional gradients of temperature and consequently baroclinicity and baroclinic conversion. Besides that, this increase is also observed more specifically in the Pacific (Atlantic) in the first (second) half of this period and linked with a Pacific Decadal Oscillation (Atlantic Multidecadal Oscillation) change in signs. On the opposite, the first and third periods are related with warmer polar temperatures that are more intense in the third period but never reach the upper levels of the troposphere. This creates differential changes in baroclinicity. On the one hand, baroclinicity decreases at lower levels and, on the other hand increases at upper levels.

The second part of this thesis is focused on the analysis of the most damaging windstorms of the century. First, Loss and Meteorological indexes (Pinto et al,

2012) are computed for more than twenty countries. Then, a *High-Loss Tracking Method* is developed and the tracking algorithm trajectories are matched with the LI and MI information for each country. A list of storms with their associated damage is obtained. Finally, a composite analysis is made for the most damaging storms of France after separating then according to their relative position to the jet stream. More than seven storms impacting France are Atlantic storms (travelling eastward in the Atlantic storm track) and cross the Jet-stream (35%). Moreover, the jet-crossing of these storms occurs over the English channel and up to 12 hours before reaching France. The re-enforcement associated with the jet crossing happens at the exact moment when the storm is the closest to France.

Résumé

L'étude de la variabilité des cyclones extra-tropicaux (ETC) est non seulement un sujet d'intérêt pour la communauté scientifique mais aussi d'une grande importance en raison de ses impacts socio-économiques. Toutefois, l'étude continué de la variabilité des ETC et de leurs impacts est encore rare, en particulier a l'échelle de temps du Xeme siècle.

Cette thèse vise a étudier la variabilité des trajectoires de tempêtes et de leurs dégâts associés du début du Xxeme siècle a 2010. Pour ce faire, le travail est divisé en deux sections principales, l'une dédiée a la climatologie des ETCs au cours du siècle dernier a partir de données de réanalyse, et la seconde centrée sur le calcul d'indices de pertes et l'évaluation des risques induits par les tempêtes.

On s'intéresse en premier lieu a l'étude de la variabilité des ETCs par l'application d'un algorithme de suivi de cyclone, sur la réanalyse de long terme du Centre Européen (ECMWF) ERA-20C. Le nombre annuel d'ETC modérées a intenses fait ressortir trois périodes historiques distinctes. Deux périodes, l'une au début et la seconde à la fin du Xeme siècle (1900-1935 et 1980-2010) ne présentent aucune tendance tandis qu'au milieu du siècle (1930-1980) une tendance significative à l'augmentation apparait. Cette dernière peut toutefois être interrogée en raison de l'inhomogénéité temporelle des réanalyses de long terme. Pour cette raison, un ensemble de paramètres physiques sont analysés en vue d'interpréter physiquement les trois périodes. Durant la période 1930-1980, un refroidissement général de l'atmosphère est observé, en particulier aux hautes latitudes, qui augmente le gradient méridien de température et en conséquence la baroclinicité et la conversion barocline. Par ailleurs, cette augmentation de la fréquence d'ETC est observée spécifiquement sur le Pacifique (Atlantique) au cours de la première (seconde) moitie de la période en lien avec une inversion de l'indice Oscillation Décennale du Pacifique (Oscillation Multidecennale Atlantique).

La seconde partie de la thèse s'intéresse à l'analyse des tempête scausant les plus forts dégâts du Xeme siècle. Tout d'abord, on calcule un champ d'indices de dégâts de vents forts pour plus de vingt pays. On développe ensuite une *Méthode*

de Suivi de Tempêtes de Forts Dégâts et les résultats de l'algorithme de suivi sont combinés avec les indices de dégâts de vents forts pour chaque pays. On obtient une liste des tempêtes historiques et leurs dégâts associés. Enfin, on effectue une analyse par composite pour les tempêtes les plus sévères en France en lien avec leur position relative au Jet Stream. Les résultats montrent que la majorité des 700 tempêtes les plus sévères en France sont des tempêtes Atlantiques (advectées vers l'Est le long du storm track Atlantique) et 35% d'entre-elles traversent le Jet Stream. Pour celles-ci le croisement du Jet Stream a lieu majoritairement au-dessus de la Manche et jusqu'à 12h avant de parvenir en France. Le renforcement associé au croisement du Jet Stream a lieu lorsque la tempête est a sa distance plus proche de la France.

Resumo

Extratropical cyclones (ETCs) variability is not only a subject that raises interest among the scientific community, but also extremely important in terms of social-economical impacts. Nevertheless, the study of both the extratropical cyclones variability and windstorms impacts is still scarce, particularly at time-scales that cover the twentieth century.

This thesis aims to study, both storms track variability and associated losses from the beginning of the 20th century until 2010. In order to do so, the work was separated in two main parts, one witch focus on ETCs climatology during the last century using reanalysis data and another focused on loss indexes calculations and risk assessment of windstorms.

The first part of this PhD concerns the study of ETCs variability after applying a tracking algorithm on the long-term ECMWF reanalysis ERA-20C. The number of ETCs per year shows three distinct periods for the moderate and deep cyclones. Two periods, one at the beginning and another at end of the century (1900-1935 and 1980-2010) for which no significative trends are observed and a middle-century period between 1935-1980 which presents a significative positive trend. This last trend, however, a deeper analysis on this period should be done due to time-inhomogeneity of long-term reanalysis datasets. For this reason, a set of physical parameters are analysed and a physical interpretation made for each one of the periods. During the middle period, a general cooling of the atmosphere is observed, particularly at high-latitudes, which increases the meridional gradients of temperature and consequently baroclinicity and baroclinic conversion. Besides that, this increase is also observed more specifically in the Pacific (Atlantic) in the first (second) half of this period and linked with a Pacific Decadal Oscillation (Atlantic Multidecadal Oscillation) change in signs. On the opposite, the first and third periods are related with warmer polar temperatures that are more intense in the third period but never reach the upper levels of the troposphere. This creates differential changes in baroclinicity. On the one hand, baroclinicity decreases at lower levels and, on the other hand increases at upper levels.

The second part of this thesis is focused on the analysis of the most damaging windstorms of the century. First, Loss and Meteorological indexes (Pinto et al, 2012) are computed for more than twenty countries. Then, a *High-Loss Tracking Method* is developed and the tracking algorithm trajectories are matched with the LI and MI information for each country. A list of storms with their associated damage is obtained. Finally, a composite analysis is made for the most damaging storms of France after separating then according to their relative position to the jet stream. More than seven storms impacting France are Atlantic storms (travelling eastward in the Atlantic storm track) and cross the Jet-stream (35%). Moreover, the jet-crossing of these storms occurs over the English channel and up to 12 hours before reaching France. The re-enforcement associated with the jet crossing happens at the exact moment when the storm is the closest to France.

Summary

Liste des tableaux

List of figures

0.1. Acknowledgements

I could not start the acknowledgements from someone else than my supervisors. Philippe Arbogast , Gwendal Riviere and Bruno Joly to whom I am very grateful.Thank you for having the patience to explaining me everything in the windstorms world, for the good talks and for the all the time. I would never be able to to half of what I did without you. I must also thanks Marie-Laure Fandeur and Henry Bovy for the support and for helping me understanding windstorms from a re-insurance point of view and, of course, to SCOR for co-financing this thesis. I am also grateful for the time and feedbacks form the member of the jury Franck Roux, Gregor C. Leckebusch, Francis Codron, Len Shaffrey and Pascal Yiou.

There are also so many to whom I am entirely grateful. To my dear Marie Drouard that has proven to be not only a very good friend, but also a very good french teacher, merci Marie. To the recyf Team (Carole, Pierrick, Alan, Anne-Lise, Laurent Dominique, Pascal, Benoit, Marie, Laure, and Matteo) that helped me integrate so easily. Thank you for all the PhDs student that welcomed me warmly at the lunch table every day for 3 years.

Je ne pouvais pas non plus passer sans remercier mon MI pour toute ta patience et le soutien et le positivisme constant. Un gros merci à Zinda et Michel, ma famille française que j'ai connue à Toulouse, que m'ont très bien accueillie et sans laquelle je n'aurais jamais compris la bureaucratie française.

Por fim, eu tenho de agradecer a todos aqueles que a mais de 1500 quilómetros de distancia conseguiram estar sempre presentes. Aos meninos e meninas da fcul (Sílvia Catarina Joana, a Ana a Sofia o Tomas o Pedro o Alex entre tantos outros) por se lembrarem me mim. Às meninas do IPMA (Inês e Marta) pelas mensagens quase-semanais de preocupação e apoio.
Finalmente, tenho de agradecer aos que foram essenciais para que pudesse estar aqui. Nunca teria sido a primeira da família a ter acabado o liceu e chegar a fazer um doutoramento se não fossem os meus pais e todo o que eles fizeram durante

a vida para me ajudarem a la chegar. Serei eternamente grata. Obrigada à minha irmã por estar la sempre para a pipa, aos meus avós por serem uns fofos, aos meus tios e primos que fazem tão parte da minha vida.

Introduction

Extratropical cyclones are a major element of the mid-latitude atmospheric circulation. They are responsible for strong damage as in the case of intense flood episodes or coastal. During the 2013/2014 winter, catastrophic floods affected the United Kingdom and intense coastal erosion was observed along the French coast (figure 0.2).

FIGURE 0.1: Located at 20 kilometres south of the Gironde's estuary, Soulac-sur-Mer ant its iconic near-sea building undergo severe coastal erosion. The 2013 and 2014 storms have significantly increase this erosion. (copyright : CNRS Photo library / EPOC / Cyril FRESILLON)

Besides floods and coastal erosion, intense windsalso cause large damage. In fact, they are associated with the most significant and strongest damage. A better understanding of the strong wind generation in order to better predict this phenomenon is therefore, important for the scientific community and at a social-economical level. A good understanding of those winds can help in the implementation of protection measures that will mitigate its impacts. For the insurance and reinsurance industry, the physical knowledge of strong winds enables the validation of statistical models that depict the variability of extreme events.

To study the variability of mid-latitude cyclones at a daily scale, one appropriate approach is to use the available long-term datasets for two main reasons. On the one hand, time series of observation-based data are scarce and inhomogeneous in time and space. On the other hand, the study of storm variability requires spatial information. With the introduction of the first reanalysis datasets, new subjects among the scientific community were accessible, such as the dynamical climatology of mid-latitude cyclones. At the same time, numerical tools like storm track algorithms have been developed. This is the best approach when studying mid-latitude cyclones since they are coherent structures with a complex life cycle and which travel rapidly, roughly from west to east.This thesis takes advantages of both the available ECMWF reanalysis ERA-20C, that covers the whole century, and the use of a tracking algorithm.

Hewson and Neu (2015) have shown that reanalyses have a too coarse horizontal resolution and small-scale systems linked with strong winds are not well represented. Moreover, winds are stronger over the ocean than over land. Consequently, the use of these datasets must be handled with caution. However, a wind calibration is possible by normalising the wind by its climatology (Pinto et al. (2012)). This approach is applied on ERA-20C reanalysis measuring historical impacts from a list of losses obtained from SCOR.

Another objective of this thesis is to better understand the mid-latitude cyclone's dynamics. A study developed in the framework of the field experiment FASTEX (Joly et al, 1999) has shown that cyclogenesis could be composed of multiple phases and that baroclinic growing is oftern interrupted with phases of latency. Rivière and Joly (2006) have suggested that barotropic processes during the jet crossing play a role equivalent to baroclinic processes. More recent studies on real cases have shown the relevance of this mechanism, although a general characterization was less evident. This thesis statistically evaluates the relevance of the jet crossing effect when a storm affects Europe. Finally, the we want to characterise the mid-latitude storms that stay on the northern side of the jet-stream.

In chapter I a brief history of mid-latitude cyclogenesis is presented. In chapter

II, a brief summary of the ERA-20C data used is exposed and the tracking algorithm method is described in detail. In chapter III the under-revision article entitled "Northern Hemisphere extratropical winter cyclone variability over the 20th Century derived from ERA-20C Reanalysis" is presented. The article describes the variability of the extratropical cyclones throughout the 20th century and the associated baroclinicity, baroclinic conversion and large-scale variability. In chapter IV is described the *High-loss storm tracking* used to compute the 20th-century windstorms catalogue and we present the results for the most severe storms for each European country . In chapter V the composite analysis for the severe windstorms of France is presented for the trajectories separated accordingly to their relative position to France and to the jet stream and the strongest windstorms over France are characterised.

Introduction (Français)

Les tempêtes des latitudes tempérées constituent un élément majeur de la circulation générale atmosphérique. Il s'agit d'un phénomène pouvant être responsable de crues lentes ainsi que de l'érosion irréversible des côtes lorsqu'une répétition d'un grand nombre d'événements sur une durée de quelques semaines affecte une région déterminée de l'Europe. Ainsi lors de l'hiver 2013-2014, avons-nous observé des inondations catastrophiques sur le Royaume-Uni mais aussi une érosion des côtes Atlantiques de la France (voir figure en bas).

FIGURE 0.2: Située à 20 kilomètres au sud de l'estuaire de la Gironde, la commune de Soulac-sur-Mer et son immeuble emblématique subissent une érosion très importante de la plage. Les tempêtes de l'hiver 2014 ont fortement accentué ce phénomène. (copyright : CNRS Photothèque / EPOC / Cyril FRESILLON)

L'impact direct du vent est également redouté. Les structures de vent les plus forts peuvent être dévastatrices. Améliorer la connaissance de ce phénomène dans le but de mieux le prévoir est un enjeu important pour la communauté des sciences de l'atmosphère et du climat. La connaissance de la variabilité du phénomène est de première importance pour les sociétés occidentales. Il s'agit de mieux connaître le phénomène pour concevoir des mesures de protection permettant de réduire l'impact du vent. Pour le monde de l'assurance et de la réassurance la connaissance

physique de l'aléa permet de valider les modèles statistiques simulant la variabilité de l'aléa et la répétition des événements extrêmes.

L'étude de la variabilité des tempêtes de l'échelle journalière à l'échelle séculaire doit être abordée avec des longues séries de données. Les séries temporelles d'observations homogènes sont rares et leur qualité évolue avec le temps. Par ailleurs l'étude des tempêtes requiert une spatialisation de l'information. Aussi, l'apparition des premières réanalyses a-t-elle fait naitre de nouvelles discipline scomme la climatologie dynamique des latitudes tempérées. Cette thèse tire parti de la mise à disposition de la réanalyse ERA20C produite par le CEPMMT et couvrant le 20e siècle. Dans le même temps de nouveaux outils diagnostics comme le suivi des dépressions sont apparus. En effet, la tempête est un objet cohérent qui suit un cycle d'évolution complexe en se déplaçant rapidement et généralement d'ouest en est dont l'analyse tire particulièrement bénéfice de l'approche lagrangienne.

Comme rappelé par Hewson and Neu (2015), les systèmes de réanalyse possèdent des résolutions horizontales et verticales un peu lâches. Les structures de mésoéchelle conduisant au vent les plus fort ne sont pas toujours représentés. Par conséquent l'utilisation directe des réanalyses est sujette à caution. Pourtant, Pinto et al. (2012) montre que l'on peut calibrer le vent d'une réanalyse en normalisant par des éléments du climat du même système d'analyse. Cette approche sera utilisée ici. Nous nous efforcerons de la valider dans le contexte de la réanalyse ERA20C au moyen d'une mesure de l'impact tirée d'un historique des pertes du réassureur SCOR, (co-financeur de la thèse).

L'amélioration de la compréhension de la dynamique des tempêtes par la climatologie est également un objectif que l'on poursuivra. Les travaux autour de l'expérience FASTEX (Joly et al, 1999) ont montré que la cyclogénèse possède de multiples phases de croissance barocline entrecoupées de phases de latence. Rivière and Joly (2006) ont suggéré que les processus baroclines au moment de la croisée du jet pouvaient jouer un rôle équivalent aux processus baroclines. Des travaux sur des cas réels plus récents ont montré la pertinence du mécanisme proposé. En revanche, aucune systématisation n'a pu être mise en évidence. Cette thèse est

l'opportunité pour évaluer statistiquement la pertinence du mécanisme de croisée de jet lorsqu'une tempête affecte l'Europe. Enfin le second point que l'on souhaite aborder est la pertinence du concept de cyclogénèse en air froid, c'est-à-dire lorsque la dépression reste du côte nord du jet et qu'elle ne traverse pas le jet.

Un bref historique de l'évolution des idées sur la cyclogénèse des latitudes tempérées est donné au chapitre 1. Le chapitre 2 présente la réanalyse ainsi que l'outil de suivi des dépressions. Le chapitre 3 porte sur la variabilité des tempêtes sur l'hémisphère et s'appuie sur un article en révision à Climate Dynamics. Le chapitre 4 se focalise sur la détection des événements extrêmes à partir de la réanalyse ERA 20-C. Dans le chapitre 5 nous caractérisons les tempêtes au moyen de l'analyse de la position des composites par rapport au jet basse fréquence.

CHAPTER I

Introduction

1.1. Mid-latitude from General Circulation Dynamics

Differential heating of the earth's surface creates regions of energy surplus on the equator and deficit on the polar regions as seen in figure 1.1.

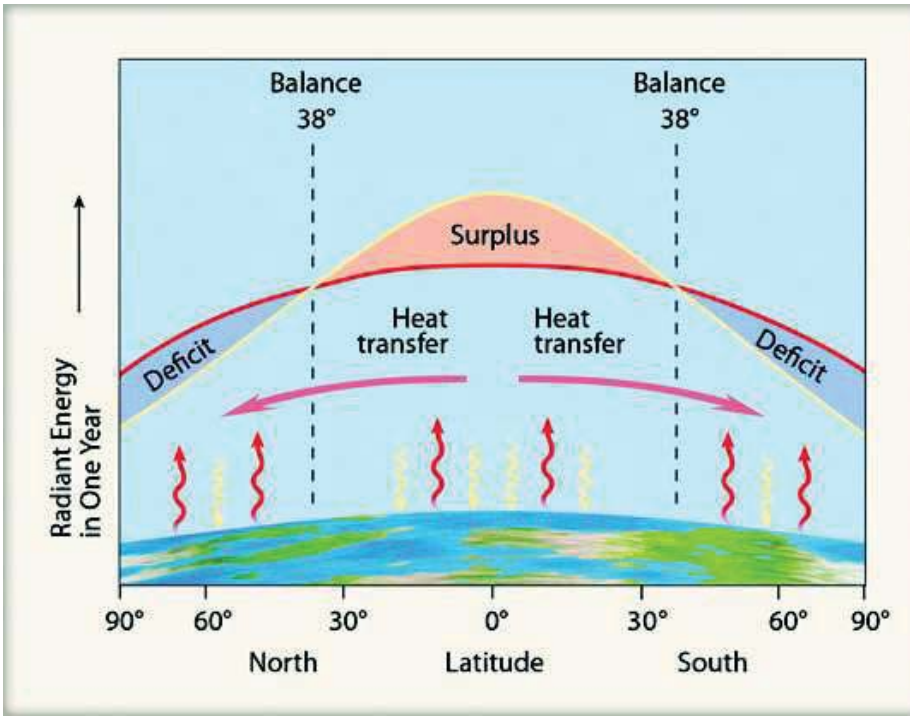

FIGURE 1.1: Representation Scheme of incoming solar radiation (yellow arrows) and infrared radiation emission (red arrows). From Ahrens (2009).

The energy balance is then maintained thanks to a meridional transport of energy from the equator to the poles conducted, on the one hand, by the ocean, and on the other hand by the Atmosphere. The Atmospheric transport is made in both Hemispheres in a symmetric way as suggested by the schematic figure 1.2. Nevertheless, mechanism of heat and moisture poleward transport are complex. At low latitudes, this meridional transport is delivered by the Hadley Cells. On the Northern flank of these cells, one may find a subtropical jet in response to kinetic momentum conservation (figure 1.3). However, the jet is not a simple zonally symmetric strong wind since planetary waves and mid-latitude cyclone activity

leads to more complex jets, with meanders and variations of the wind magnitude along the maximum wind axis.

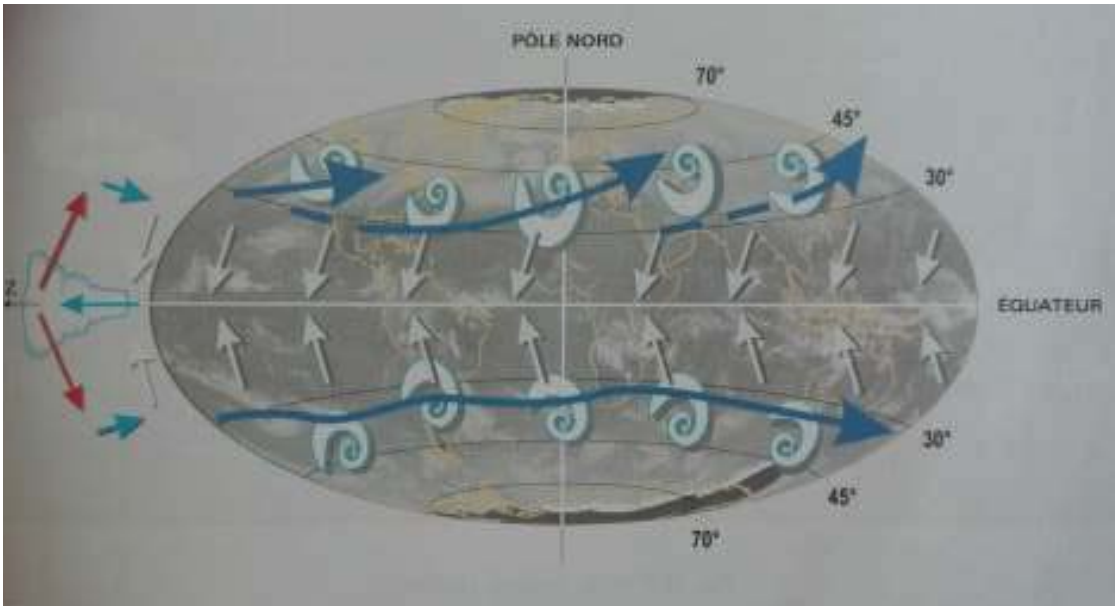

FIGURE 1.2: Image of Malardel (2009) representing a scheme of the meridional circulation on earth's surface.

Associated with this jet,there is an enhancement of the meridional thermal gradient due to thermal wind balance. This area is the baroclinic zone, where mid-latitude cyclones develop.

The first theoretical model explaining baroclinic development is baroclinic instability.

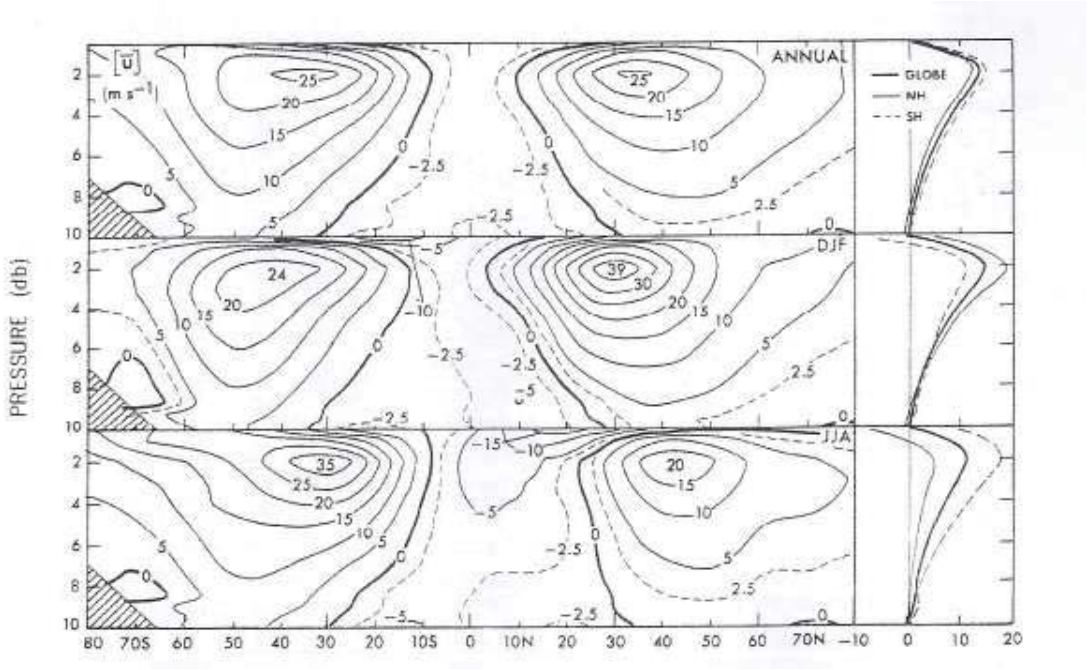

FIGURE 1.3: Zonal-cross section of annual mean zonal wind (top) DJF months (middle), JJA months (bottom) in ms^{-1} and mean vertical profiles (right) from Peixoto and Oort (1992).

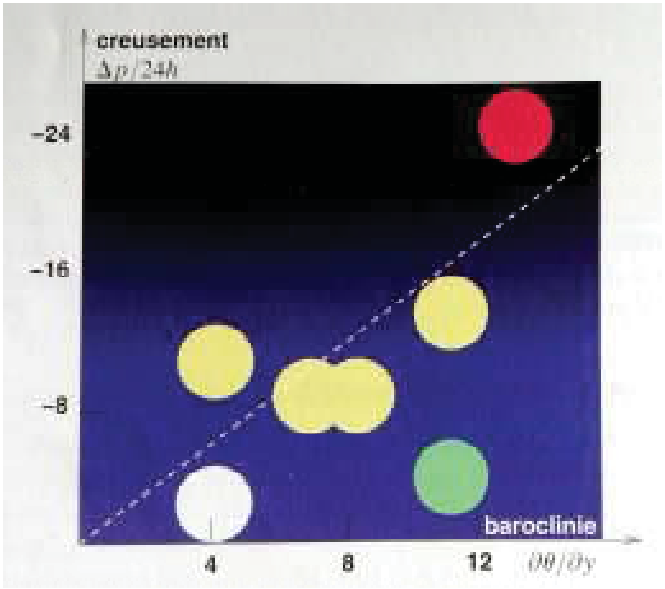

FIGURE 1.4: Relation between the growth rate of a storm and the baroclinic zone intensity for a set of seven mature storms. From Malardel (2009).

1.1.1. Baroclinicity Instability

The first step of the baroclinic instability theory is to linearise the Quasi-geostrophic equations about an Atmosphere with uniform PV (Eady, 1949; Charney, 1947). Its simplicity enables to clarify the full mathematical form of the most unstable mode (figure 1.5).
The development and intensification of extratropical storms within baroclinic environments depends on the baroclinicity of the atmosphere but, it is not the single factor contributing to the growth of a storm. Commonly known by "Eady growth rate", σ, is the potential growth of an extratropical storm and is computed as described in :

$$\sigma = 0.31 f N^{-1} \, dU/dz \tag{1}$$

where N is the static stability, and dU/dz the vertical wind shear.

Other studies have been developed, as the model of Charney (Charney, 1947) and, later, the two layers model of Phillips (1951).
Different storms are presented as a function of growth rate and baroclinic intensity (in color figure 1.4). The results (Ayrault, 1995) showed that, for instance, the red storms (on the top right side of the image) growth rate is proportional to the baroclinic instability but, for the green cases it is not.Therefore, the strength of the baroclinic zone alone cannot explain the storm growth.

1.1.2. Baroclinic interaction

Rather than related to infinitesimal perturbations, a mid-latitude cyclone is more often related to the interaction of pre-existing coherent structures. Figure 1.6 summarises this conceptual model.
The perturbations at the bottom and upper levels are re-enforced. Two interpretations can be given. The first one relies on Rossby wave interaction. Each Rossby wave packet is able to contribute to PV/vorticity advection so that the other structure is re-enforced. The other conceptual model used the stretching term of the vorticity equation. Vertical velocity associated with each structure increases the

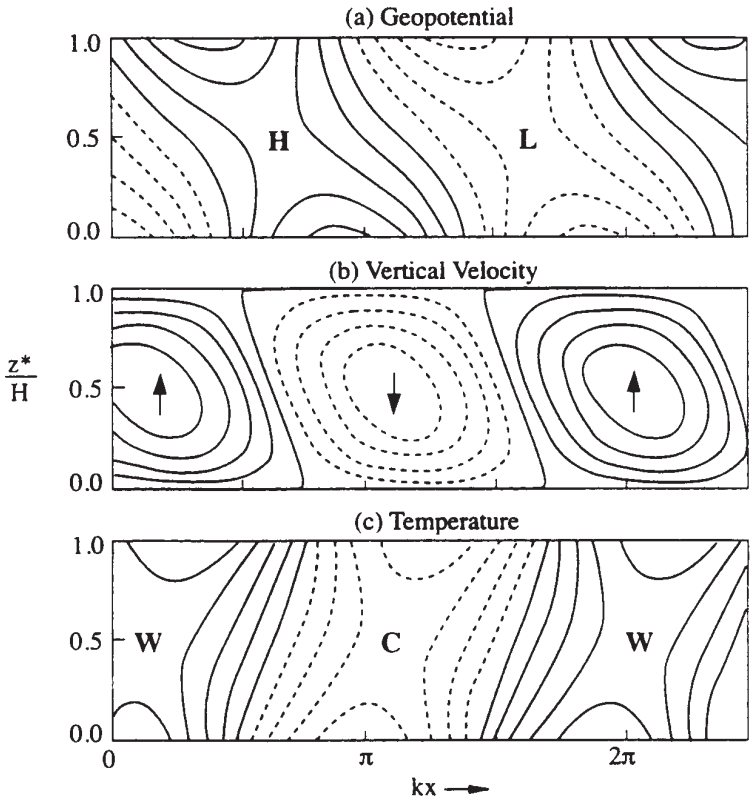

FIGURE 1.5: Properties of the most unstable Eady modes for geopotential heigh (a), vertical velocity(b) and Temperature (C). The H and L represent ridges and trough axes respectivelly adn W and C warmer and cold temperatures respectivelly. From Holton (2004).

vorticity of the feature by stretching. Both conceptual models require the tilt of figure 1.6.

1.1.3. Jet-streak forcing

Strong variations in the intensity of the jet-stream can trigger surface cyclogenesis and storm intensification. These regions of zonal wind maxima, known as jet-streaks (Uccellini, 1990), are associated with ageostrophic winds, that induce convergence (divergence) on the left and right entrance (exit) of the jet core as seen in figure 1.7. The coexistence of a low-level cyclone with aloft divergence creates stronger convergence at the surface and increases the intensity of the storms by

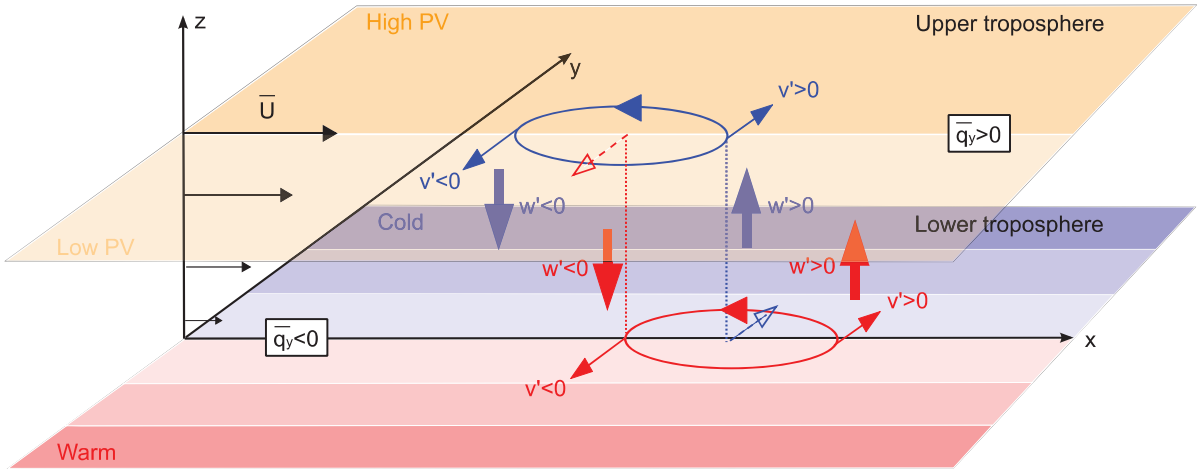

FIGURE 1.6: Schematic representation of baroclinic interaction in the two-layer model of Phillips (1951). The blue and red circles represent the low-warm and cold-upper PV anomalies respectively. From Rivière (2012).

enhanced stretching.

1.1.4. Toward a more realistic model

In the previous section, we have introduced the baroclinic instability models that explain cyclogenesis in PV perspective. However, these models do not dully explain the large variability and complex life-cycles of mid-latitude cyclones.

Baehr et al (1999) have studied the life cycle of several storms observed during the field experiment FASTEX. A set of more than twenty systems were analysed. Most storms were observed with more than one growth phases, or were associated with more than a single upper-level anomaly (figure 1.8). They have proved that a lot of systems cannot be described or characterised only with instability mechanisms nature.

Furthermore, another important indicator from this study is the systematic relation between vorticity maximum growth and the jet stream crossing. In other words, an intense increase in the low-level vorticity maximum was observed for mid-latitude cyclones that crossed the jet-stream from its warm anticyclonic side

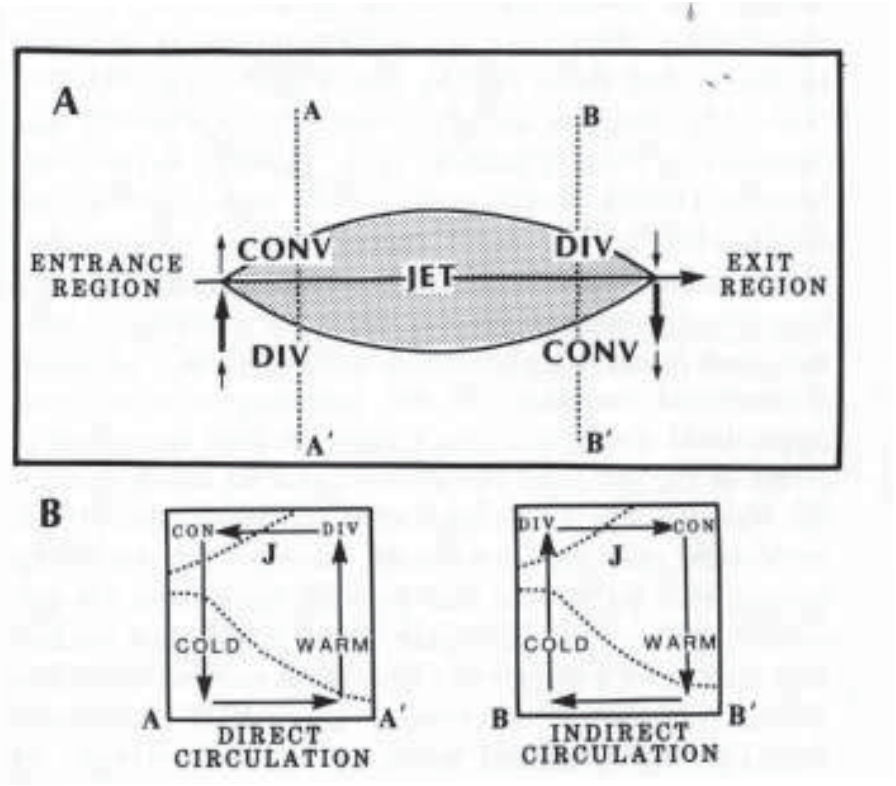

FIGURE 1.7: Schematic representation of the circulation around a jet streak (on the top). At the entrance zone the direct circulation (bottom left panel) creates divergence (convergence) at the right (left) region and at the exit zone an indirect circulation creatse the opposite. From Uccellini (1990).

to the cold or cyclone side of the jet.

1.1.5. Jet crossing

As the previously mentioned studies have shown, a link between a south-north movement of the storms crossing the jet stream and a rapid growth of the storms exists.

Another impact of the large-scale flow on the intensification of storms, is the barotropic deformation of the jet-stream. Rivière and Joly (2006) has shown it has an effect on the development of mid-latitude cyclones.

The authors have shown the existence of this effect for the case of the deadly storm of December 1999, "Lothar". They present a scheme of the movement of a

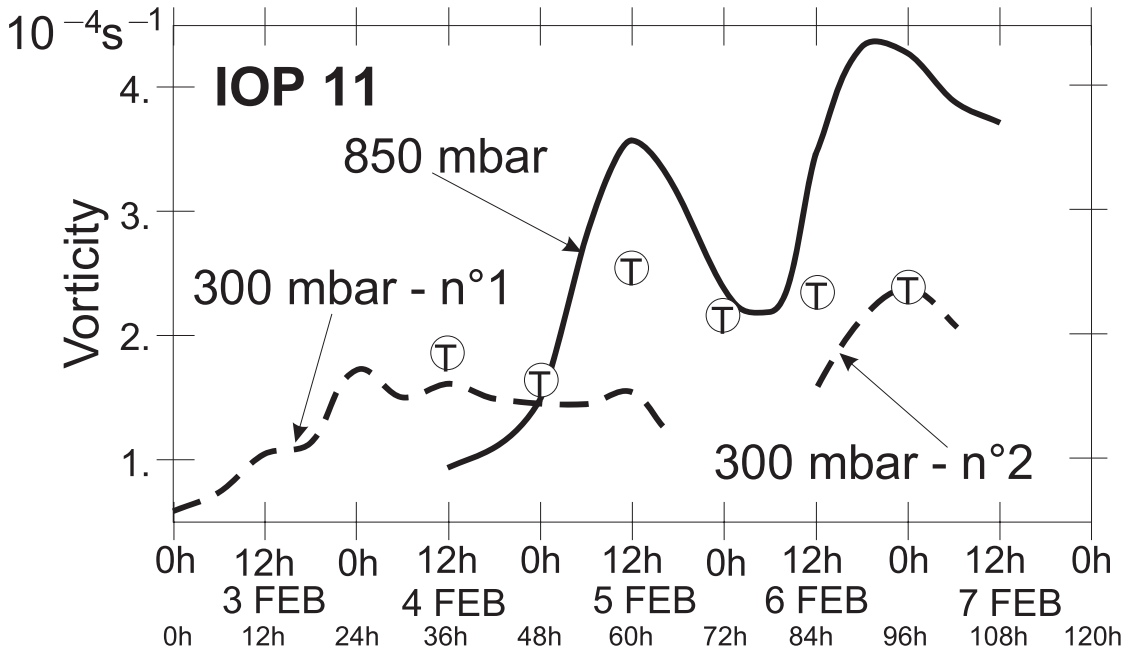

FIGURE 1.8: Vorticity maxima evolution at two levels (850 hPa and 300 hPa) and of the large scale trough (circle T) of a single case . From (Baehr et al, 1999).

storm across the jet axis and the associated deformation (figure 1.9). The region of effective-deformation, i.e., where the low-frequency deformation is higher than the absolute low-level vorticity, is shown to be an area favouring rapid changes in the orientation axis of a mid-latitude cyclone, leading to barotropic growth while the storm crosses the jet.

Gilet et al (2009) have shown that non-linear processes take an important role in the regeneration of a storm after crossing the jet and that the larger the barotropic component is, the fastest the storm regenerates. The same was verified by Oruba et al (2013), who shows northward motion of cyclones when they are more meridionally stretched.

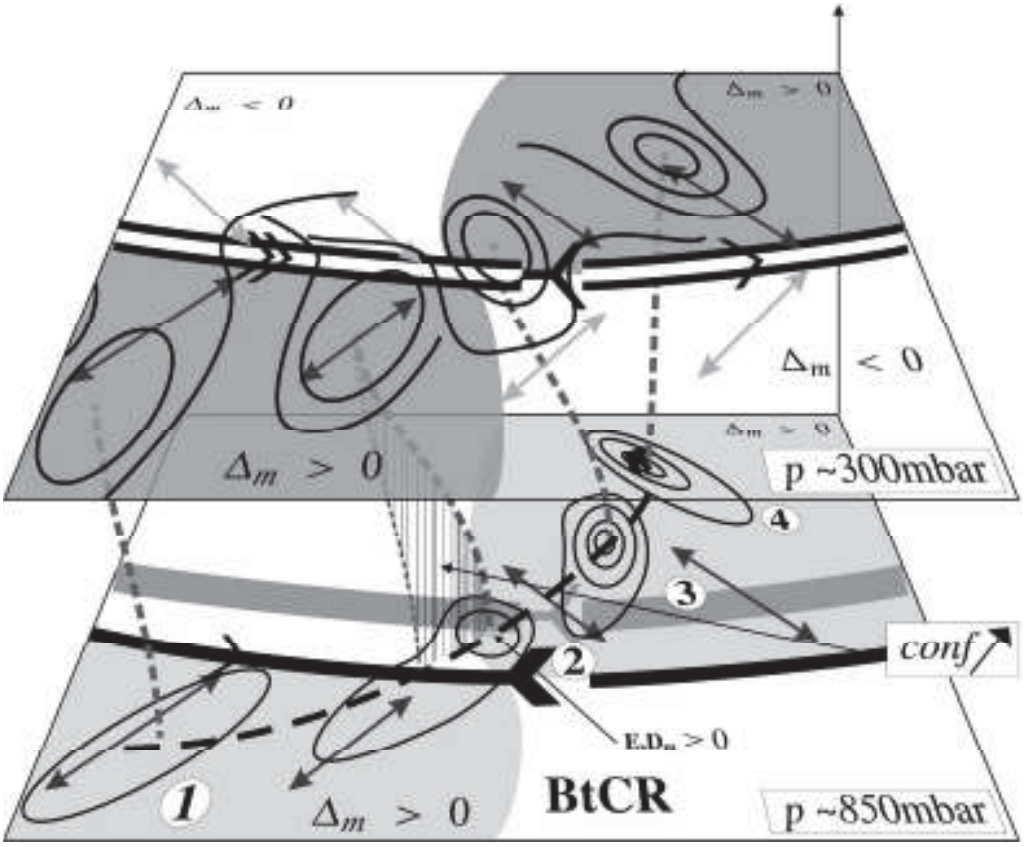

FIGURE 1.9: Shematic summarizing the rapid baroclinic growth of a mid-latitude cyclone in a barotropic critical region. The jet-stream is represented by the two double black lines and its diffluent zone by the inverse " Y". From Rivière and Joly (2006).

1.1.6. Surface winds associated with mid-latitude cyclones

1.1.6.1 *Energy redistribution*

The wind spatial variability has also been proven to change according to where the cyclones are in the southern or northern side of the jet-stream. While in the anticyclonic side of the jet, the most intense winds occur on the southeast side of the cyclones. After crossing the jet, the maximum surface winds are found southwest of the cyclones (Rivière et al, 2015b,a).

1.1.6.2 Sting jets

Some of the most damaging wind features observed within an extratropical cyclone are related to sting jets. This was firstly observed for the case of the "Great storm of 1987" by Browning (2004) and for the storm of 1992 by Gronas (1995) even though this last one used a different nomenclature to describe these phenomena. The sting jets correspond to the Shapiro-Keyser types of storm presented in the right panel of figure 1.10.

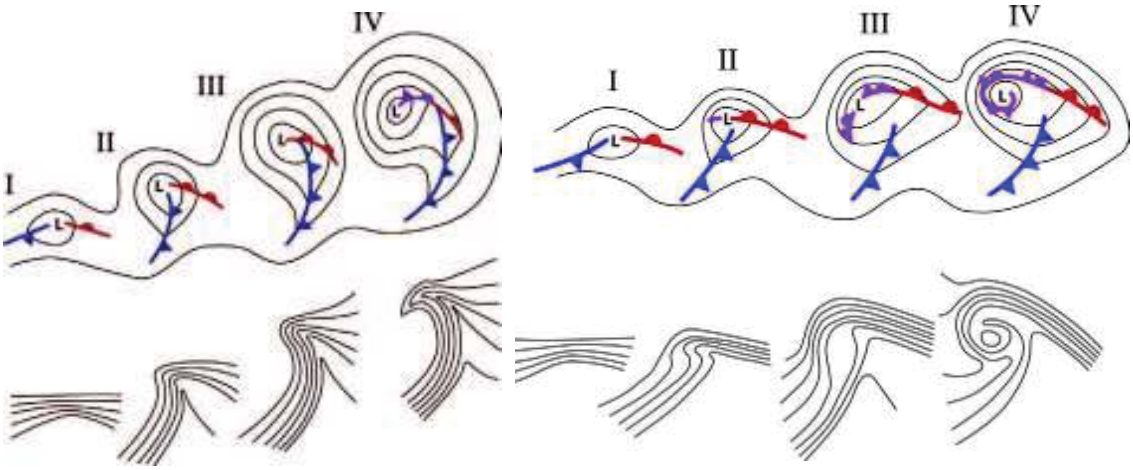

FIGURE 1.10: Conceptual models of Extratropical cyclogenesis for the Norvegian (left) and Shapiro-Keyser (right) standpoints. From Schultz and Vaughan (2011).

This conceptual model by Shapiro and Keyser (1990) describes the life cycle of an extratropical cyclone from its initial phase (I) up to its mature phase (IV). On the contrary of the Norwegian model (Bjerknes and Solberg, 1922), in the Shapiro-Keyser the warm front is the most intense, with a frontal fracture at phase III and IV (figure 1.10). It is at this phase that a bent-back warm front is formed around the storm centre. At the tip of the cloud head, ahead of the fracture zone, diabatic cooling leads to downward motion, accelerating when reaching the lower tropospheric levels. Generate strong surface winds can reach more than 150km/h. These winds are, indeed, among the strongest winds observed in windstorms (Hewson and Neu, 2015) and as Martínez-Alvarado et al (2012) point out, more than one-third of the strongest windstorms of the last decades fulfil sting jets conditions.

1.2. Extratropical cyclones variability

As mentioned before, the variability of the ETCs is one of the most important topics in terms of climate variability at the mid-latitudes. The frequency and intensity of ETCs are absolutely determinant in several social-economical points and have a direct effect on population and industry. Extremes of precipitation and high wind speeds are often associated with ETCs. Therefore, their variability in the present and future climate are of most importance. Nevertheless, their study is quite complex and depends on the data type, resolution and method applied.

1.2.1. Cyclone tracking

The variability of cyclones can be achieved in different ways. One of the easiest is based on high-frequency variables like sea level pressure, geopotential or 300hPa variance on meridional wind (Blackmon et al, 1977; Chang et al, 2002). This Eulerian approach is capable of representing correctly the storm track regions (Hoskins and Hodges, 2002) and is well correlated with storm activity, but has some important limitations that make this approach less reliable. On the one hand, it does not identify individual systems and their life cycle, on the other hand, it cannot distinguish a low from the high-pressure systems. Therefore, while studying winter extratropical cyclones life cycles the best approach is the use of the Lagrangian approach based on cyclone tracking methods that follow the development of a cyclone from its initial stage until dissipation. The variables commonly used are mean sea level pressure, geopotential and low-level vorticity. The first two are very dependent on the background flow, while vorticity can be very noisy (Sinclair, 1997; Hoskins and Hodges, 2002). It should be stressed that this last one is more capable of depicting storms at their earliest stages.
Even when using the same data with the same horizontal and temporal resolutions, the use of different methods can induce different results. A good example of this is the results obtained by Neu et al (2013) presented in figure 1.11. Twenty-two different tracking algorithms using different variables were applied on ERA-Interim datasets.

Nevertheless, the spatial distribution of storms density and storm tracks are pretty consistent. Moreover, while analysing the number of (deep) cyclones in figure

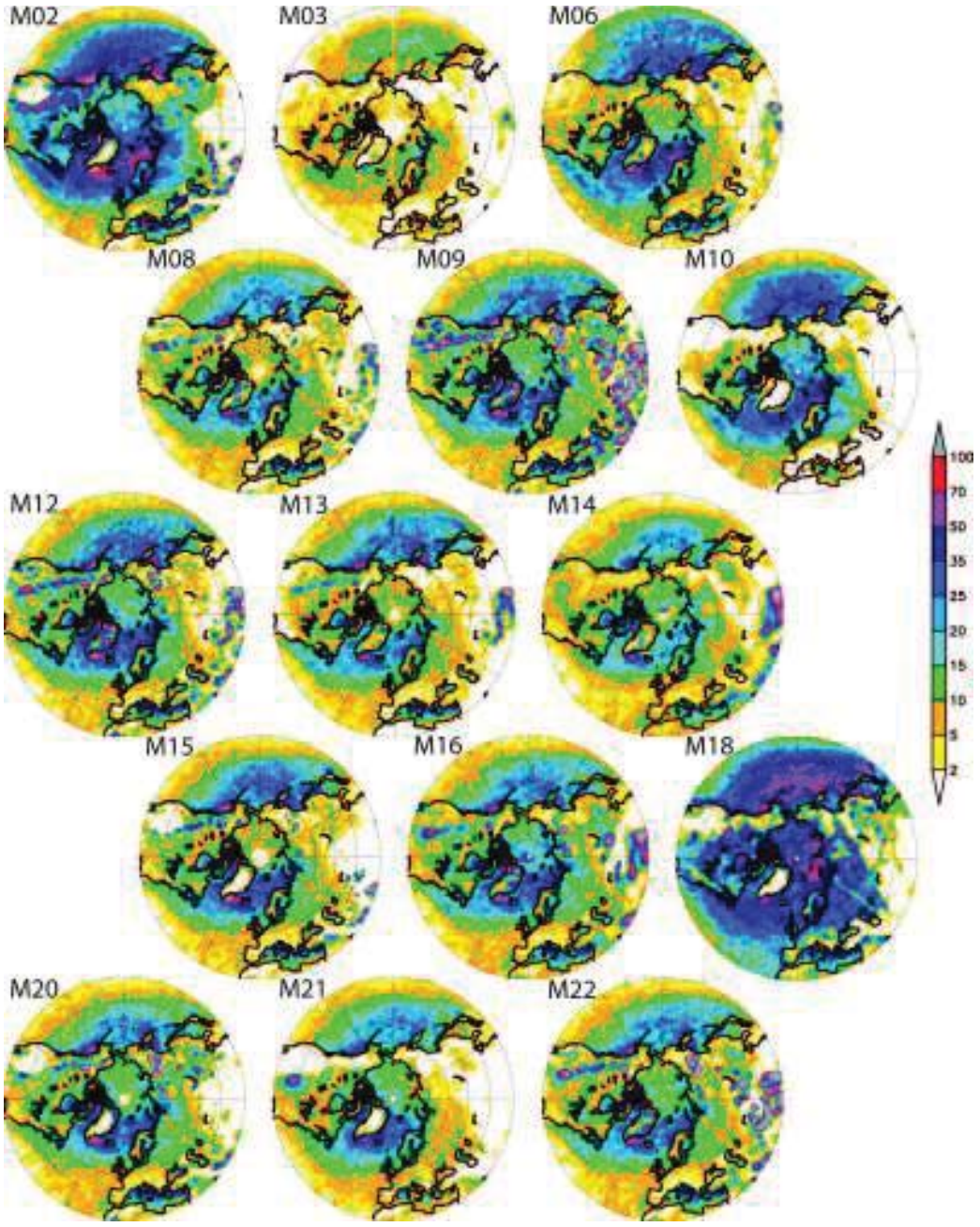

FIGURE 1.11: DJF track density of cyclones for DJF months on twenty two different methods Neu et al (2013) (only cyclones longer than 24 hours are kept).

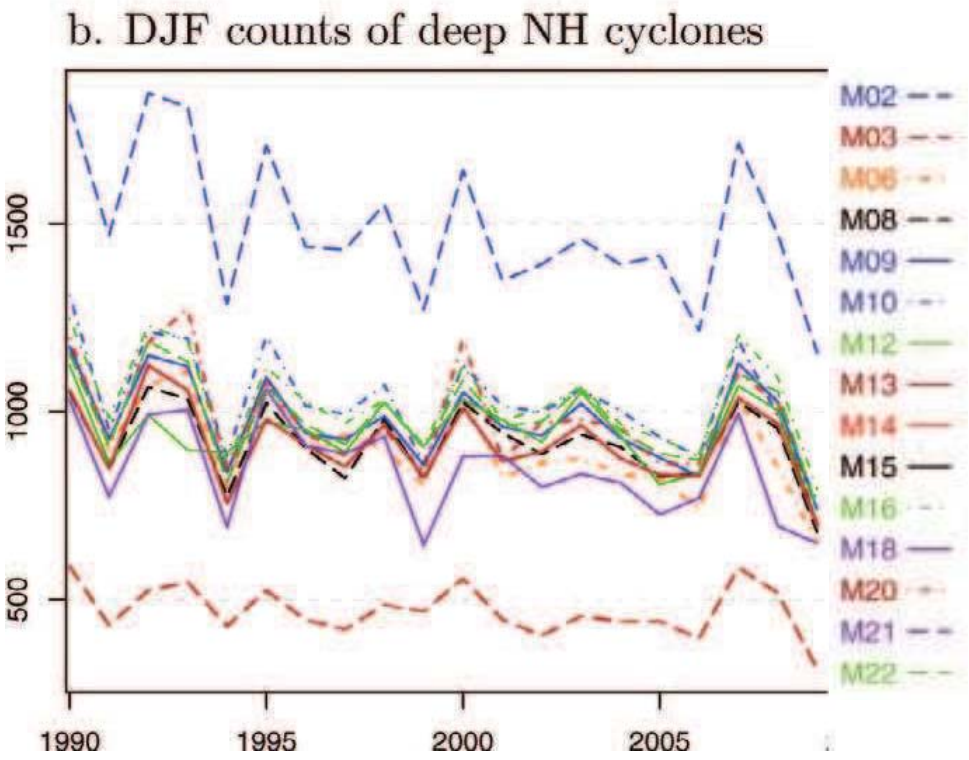

FIGURE 1.12: DJF count on deep cyclones in the NH. From Neu et al (2013).

1.12 from the same study, one can see that even if spatial densities are different, the number of counts does not vary significantly from one method to another and, more importantly, the variability throughout the time of the counts is very similar.

1.2.2. Extratropical cyclones in Present climate

As seen above, different cyclone tracking methods are able to reproduce the same kind of variability in cyclones when applied to the same datasets. One given tracking method applied to different datasets can produce quite different results (Raible et al, 2008; Ulbrich et al, 2009; Tilinina et al, 2013; Neu et al, 2013; Wang et al, 2013; Chang and Yau, 2015; Wang et al, 2016).
Since the main goal of this thesis is to study the twentieth-century variability, only a brief analysis on the two most recent and longest reanalysis is going to be made. These two reanalysis covering the entire twentieth century are NOAA's

20CR (Compo et al, 2011) and ERA-20C from ECMWF (Poli et al, 2013, 2016).

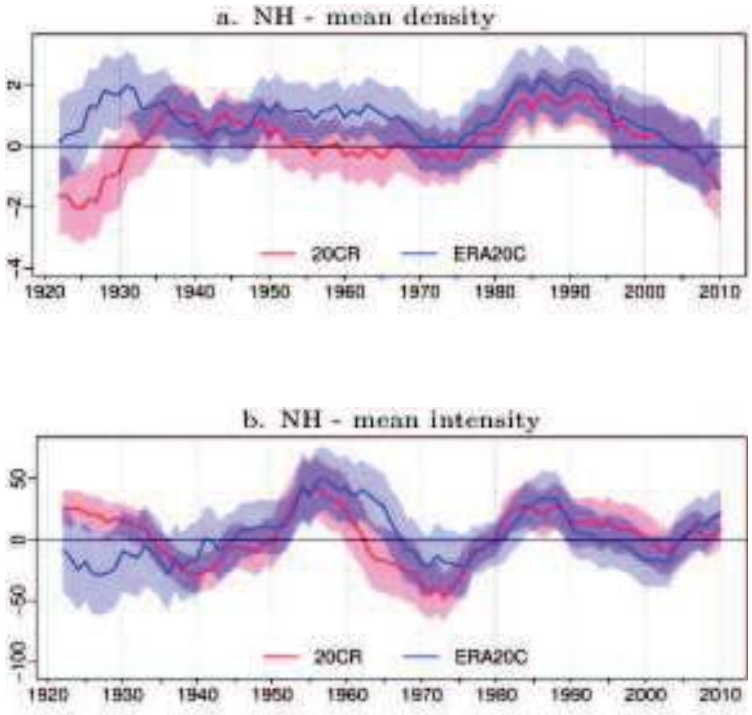

FIGURE 1.13: Mean density (left) and intensity (right) of cyclones in a 23-year moving average time series for ERA-20C (in blue) and 20CR (in red) for the NH in a 1000 km^2. From (Wang et al, 2016).

Wang et al (2016) was one of the first to study long-term trends in ETCs comparing the aforementioned reanalyses datasets using a tracking algorithm. Despite differences in the reanalyses, the results show the same variability most of the time, except for the earliest decades of the century as shown in figure 1.13. Befort et al (2016) also applied a tracking algorithm on the same data sets and concluded that the variability from the reanalyses is in agreement for the recent decades and that only early periods of the twentieth century must be taken with particular care. Chang and Yau (2015) have also studied cyclone activity with these two datasets using upper-level high-frequency wind variability. They have also concluded that the variability in the reanalyses is not fully reliable before the 50's (figure 1.15).

Nevertheless, this last frequency results are less coherent with the previous two, probably because, on the one hand, they have used high-frequency filters rather than a tracking method. For instance the intensity peak on Wang et al (2016) around the 90's and the 50's (note that Wang et al (2016) lines in figures are moving averages) are also observed in the North Hemisphere in Befort et al (2016) but not in Chang and Yau (2015).

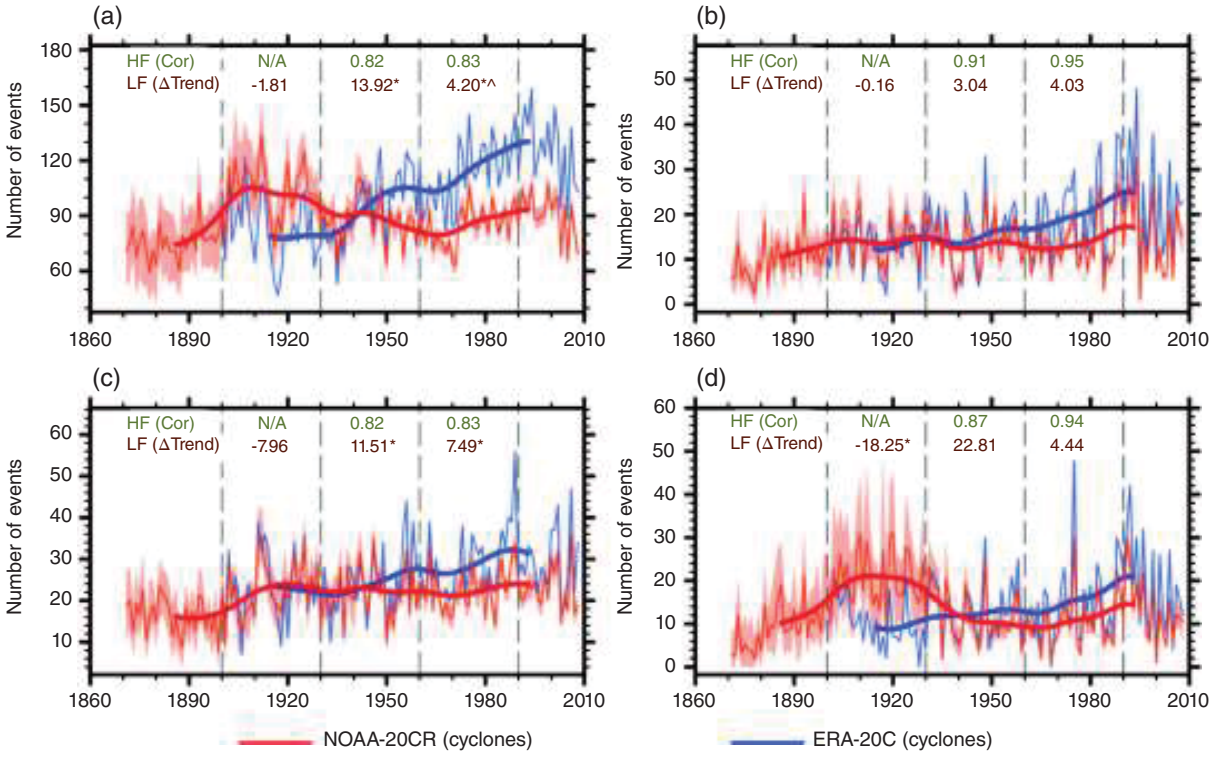

FIGURE 1.14: Number of extreme cyclones per year throughout the century from ERA-20C (in blue) and 20CR (in red) for extra-tropical NH in a , North Europe in b, Nort Atlantic in c and Arctic latitudes in d. From (Befort et al, 2016).

Despite the common concerns about the time-homogeneity of these datasets the results of the two long-term reanalyses show, in general, an increase in mid-latitude cyclones, even just considering the 50's onwards. A clear decrease in cyclones is observed in both reanalyses after the 90's just after a period of increase between

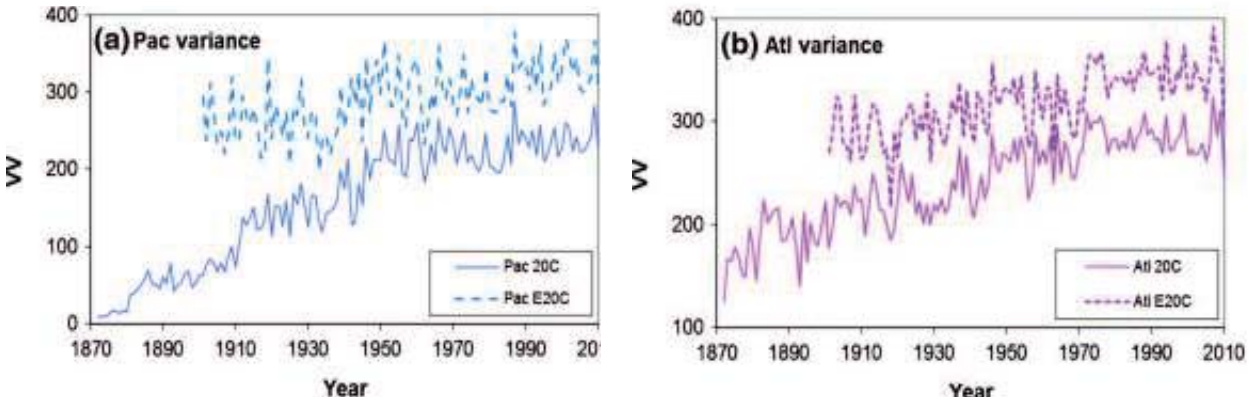

FIGURE 1.15: 300 hPa high-frequency meridional wind variability (a and b). From (Chang and Yau, 2015).

the 70's and the 90's, particularly in the Atlantic. None of the studies dedicated to storms tracks variability have analysed the relationship between storm tracks and baroclinicity.

1.3. Extratropical cyclones and impacts

Despite the variety of studies on Extratropical cyclone dynamics, variability and of wind impacts, few studies exist on the relationship between those research fields.
Damage associated with windstorms are among the highest of natural hazards that provoke most societal and economic damage, reaching in certain cases several billions of euros of loss per windstorm. The study of windstorms linked with impacts has recently raised and most of them motivated and/or funded by (re) industry.

Most of these studies are related with well-known single cases of storms (Wernli et al, 2002; Mathias Dobbertin, 2002; Fink et al, 2009; Liberato et al, 2011). The Why ?, How ? and Where ? questions on the dynamics and/or impacts are analysed in detail and a comprehensive analysis of the storm is drown.

Some other studies (Pinto et al, 2009; Donat et al, 2010; Hanley and Caballero, 2012) analyse large-scale features using a set of intense windstorms known for historical reasons (most of them from the recent decades), sometimes already analyzed as in the studies mentioned before. So far, the common result relates severe windstorms to westerly flows in the Atlantic and to the positive phase of the North Atlantic Oscillation (NAO). During positive NAO, a sea-level pressure dipole between the Azores region and Iceland has stronger meridional gradients in the North Atlantic. Consequently, storms travel northwards and reach northern European countries. Most of the strongest storms of the recent decades occur in the 1989/90 and 1999/2000 winters when a persistent NAO positive index was verified (Donat et al, 2010).

Finally, other studies have used either particular cases or a set of known cases to estimate return periods and analyse impacts in terms of losses computed from severity indexes (Karremann et al, 2014; Pinto et al, 2012; Klawa and Ulbrich, 2003; Della-Marta et al, 2010). Others studied windstorms in future climate change scenarios (Leckebusch et al, 2008; Pinto et al, 2012). An increase in the frequency and intensity of windstorms and associated losses is observed in future climate. A

relation between these changes and the NAO is also observed in future climate.

Hewson and Neu (2015) has recently analysed a set of well-known windstorms from the last decades. They have characterised these storms in terms of locations of the strongest winds (warm, cold sectors or sting-jet) as shown in figure 1.16. They have shown that reanalyses datasets tend to underestimate windstorms and that small-scale systems such as sting jets cannot be depicted in reanalysis data. Thus, the use of reanalysis to access windstorm impact is questionable.
Fortunately, the use of multi-parameters approach in the assessment of damage has also been proved to be a better procedure in order to depict potential damaging windstorms (Deroche et al, 2014), for instance in the case if serial clustering of storms (Mailier et al, 2006; Vitolo et al, 2009; Cusack, 2016).

In most studies, damage is estimate by severity indexes. These indexes are base on the cube of the surface wind, shown to be correlated with the damages of mid-latitude cylones (Businger and Businger, 2001; Klawa and Ulbrich, 2003; MunichRe, 1993). Several indexes exist using the speed of the storms or the size of their footprint (maximum observed gusts around the storms). One of the first indexes introduced is the SSI (equation 2) from Lamb (1991), that used only the cube of maximum wind above a certain threshold, on a damaging area (A_{max}) and period of time (D) to estimate damages. The index is computed as in equation 2.

$$SSI = V_{max}^3 A_{max} D \tag{2}$$

A more complete description on severity storm indexes is presented in chapter IV. The growing interest in the field of windstorm climatology has made available several windstorms catalogues. Mostly document recent events, i.e., from the 80's onwards (Roberts et al, 2014) and none go back into the beginning of the century.

1.3.1. Reinsurance losses and risk management

Despite the huge progress in science, the relation between natural hazards like windstorms and the unpredictability of damage is still to be considered. In most developed countries, existing risks related to natural catastrophes are usually trans-

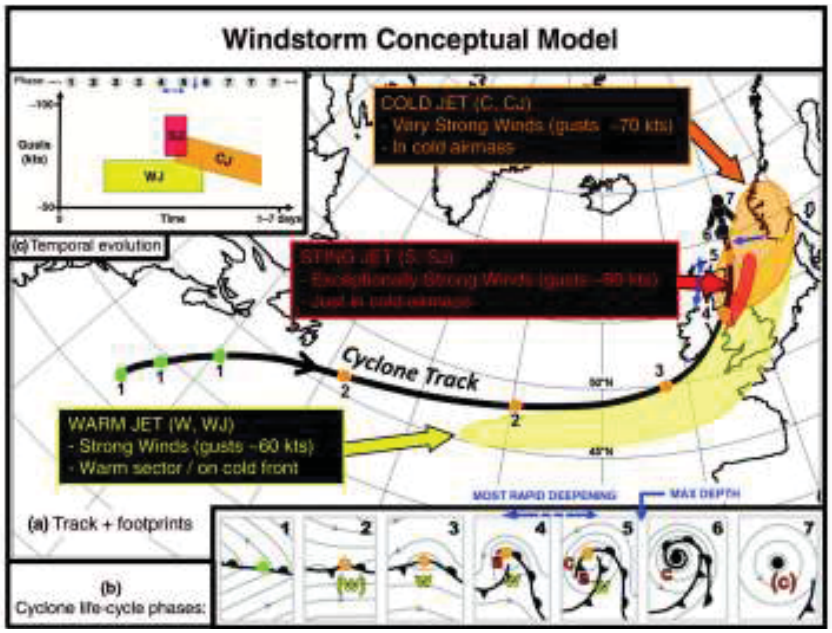

FIGURE 1.16: Conceptual model of an extra-tropical cyclonic windstorm. From Hewson and Neu (2015). In the central panel (a) is a representation of the cyclone with the evolution phase in numbers, linked with panel b, that is the cycle of evolution of Shapiro-Keyser (Shapiro and Keyser, 1990). The areas on yellow, orange and red represent the footprint types for each area of the storm associated with the dominated warm, cold and sting jet respectively. Finally, Panel c shows the time evolution of this wind footprint throughout the lifecycle of the storms.

ferred to the insurance industry and in the most extreme events, to the reinsurance industry.

Therefore, the precision on the estimations of risk, i.e., uncertainty in the economic loss for a particular event is extremely important to manage contracts, portfolios, etc. The economic loss probability in the case of natural catastrophes is made using the Cat Risk models, a tool that uses together science, engineering and statistics to better estimate hazards and vulnerability of a particular geographical area. Different models exist with different configurations and, thus, different outputs.

In figure 1.17 the wind damage for storm Daria in 1990 is presented (McCallum, 1990), according to three different models used by SCOR (Bovy, 2012). The difference between those models is presented in panel b. In some regions, damage can be quite spread as in the central Europe or in the northern region of France.

FIGURE 1.17: Mean damage ratios differences between three different models. From (Bovy, 2012).

Comparative analysis is made between the models, however, this is not a satisfactory validation process. Therefore, there is a need to use independent dataset as a comparative tool in order to benchmark vendor's models. This is the reason why the use of reanalysis datasets is important for SCOR in the context of this thesis. The creation of a catalogue of windstorms with their associated risks using ERA-20C will provide the independent output that re-insurance industry requires.

CHAPTER II

Numerical Tools- cyclone tracking

In this chapter, a brief summary of the reanalysis data and the tracking algorithm used is made. In the first part of the chapter, the homogeneity of the data and its capacity to represent historical storm is verified and compared with observations. In the second and last part of the chapter, the cyclone tracking algorithm is described and first results are presented.

2.1. Data and Methods

Reanalyses are based upon the analysis of historical observations using state-of-the-art data assimilation systems. Only two analysis covering the entire 20^{th} century exist : 20CR from NOAA, released in 2011 (Compo et al, 2011) and the most recent one, ERA-20C, the first long-term reanalysis from the European Centre for Medium-Range Weather Forecasts (ECMWF) released in 2014 (Poli et al, 2013, 2016). The results presented in this thesis are based on this last reanalysis and a cyclone tracking algorithm is applied over the whole century. For that reason, a short presentation of this reanalysis is given in the following paragraphs.

2.1.1. ERA-20C

As previously mentioned, ERA-20C is the ECMWF reanalysis dataset, which starts in 1900 and ends in 2010. The horizontal resolution of the data is about 125 km with available outputs every 3 hours. The reanalysis was computed to be as homogeneous in time as possible. Satellite data, known to create some bias

particularly on cyclone tracking results (Bengtsson, 2004; Bromwich et al, 2007) is not assimilated. Actually, surface marine wind data and surface pressure data are the only assimilated observations used. Nevertheless, the number of surface observations throughout the time is not constant. This can be seen in figures 2.1 and 2.2, extracted from Poli et al (2013).

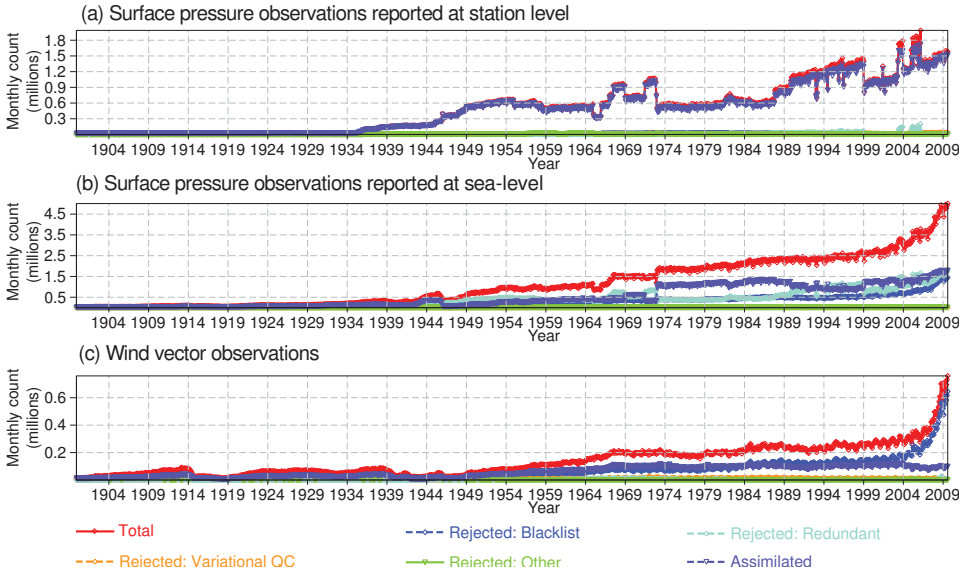

FIGURE 2.1: Figure 2.8 from Poli et al (2013) showing the montly counts of total (red) and assimilated (purple) observations in ERA-20C.

The first figure shows the number of assimilated observations (purple line) per month for surface pressure observations (figures 2.1a and 2.1b and for wind data in figure 2.1c. Surface pressure observations show a clear increase in the number of counts around the 30's (figure 2.1a) with a second higher increase after the 90's. The surface pressure at the sea level and wind observations (figure 2.1b and c) also show a increase with time, though, it is much smoother than the surface pressure data increase.

Figure 2.2 help us to understand the spatial increase in the surface pressure data observations. The first thing that can be inferred from this figure is the increase occurs over the continents in both hemispheres, especially in the Southern Hemisphere. Besides that, Northern Hemisphere seems to be better covered by observations in earlier periods of the century when compared to the Southern Hemisphere. In particular, the mid-latitudes of the Atlantic ocean are "completely"

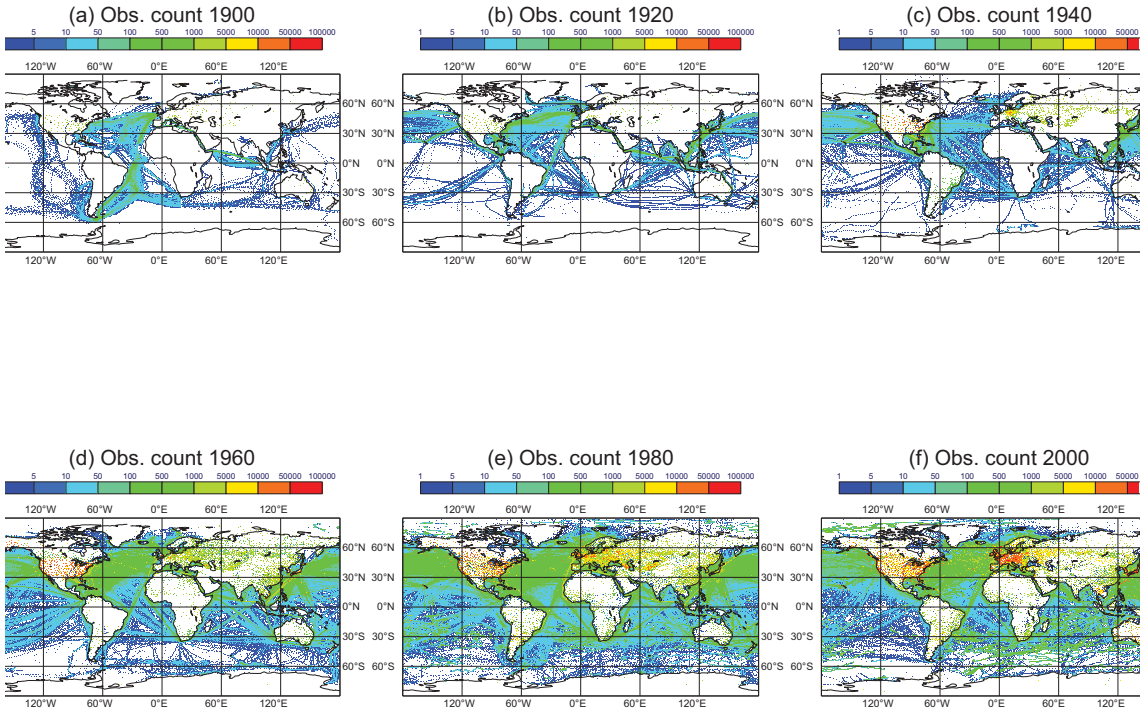

FIGURE 2.2: Figure 3 from Poli et al (2013) showing the spatial counts of assimilated surface pressure observations in ERA-20C for certain years.

covered by observations since the 20's as shown in figure 2.2. For the Pacific region, a good coverage of observations is observed from the 40's onwards.

Besides the time-homogeneity of the reanalysis, also the quantitative representation of the wind is important while studying windstorms. To that end, a comparative analysis is made between the 10-meter reanalysis field and an observation-based wind field (combination of observation data and the forecast model "Arome" kindly provided by Frédéric Sassier and Jean-Michel Soubeyroux) from project Anthémis at Meteo-France (http ://virga-int-p.meteo.fr/anthemis/). In figure 2.3 and figure 2.4 the two wind fields are presented for windstorms "Xynthia" (2010) and "Lothar" (1999) respectively. For Xynthia, the reanalysis wind (right column of figure 2.3) is capable of representing correctly the spatial distribution of the

wind as in the observations (left column of figure 2.3). However, the intensity of the 10-meters wind maximum from the reanalysis is about twice lower than the observed maximum. For the storm Lothar, besides the same difference in intensity (figure 2.4), the wind seems miss-located at 3 a.m. and 6 a.m. The reanalysis strong winds are placed further south than in the observation-based field. This can be due to the nature of the storm (Wernli et al, 2002; Rivière et al, 2010). It is probably too strong and at a scale too small to be well represented with the spatial resolution of the renalysis. This has been shown by Deroche et al (2014) while using an even higher resolution reanalysis ERA-Interim and by Hewson and Neu (2015) studying more than twenty remarkable windstorms of the last decades, particularly for the ones associated with "sting jets" (Browning, 2004).

Variables used

The period of study goes from 1900 until 2010, with annual sequences from the 1st of October to the 31st of March. The spatial and temporal resolution of the data is presented in table 2.1. The extratropical tracking algorithm presented in section 2.2 requires relative vorticity at 850hPa and the zonal and meridional components of the wind at 850 and 700 hPa at every 3 hours with the available horizontal resolution of 1.125°. For chapter III, daily SST is extracted as well as air temperature and the wind components (U and V) at 2 additional levels : 500 and 300 hPa. Finally, 10-meter wind is also interpolated on a 0.25°grid in order to implement damage estimation in IV. It is crossed with population data (Center for International Earth Science Information Network - CIESIN - Columbia University ; Centro Internacional de Agricultura Tropical - CIAT, 2005) that is available at this resolution. This will be further discussed in the next chapters.

Data	Levels	Spatial Resolution	Temporal Resolution
Relative vorticity	850 hPa	1.125°	3h
U and V wind	700,850 hPa	1.125°	3h
U and V wind	850,700,500,300 hPa	1.125°	24h
Air temperature	850,700,500,300 hPa	1.125°	24h
SST		1.125°	24h
U and V wind	10 -meters	0.25°	3 h

TABLE 2.1: Summary of the data used in this thesis, its temporal and spatial resolution.

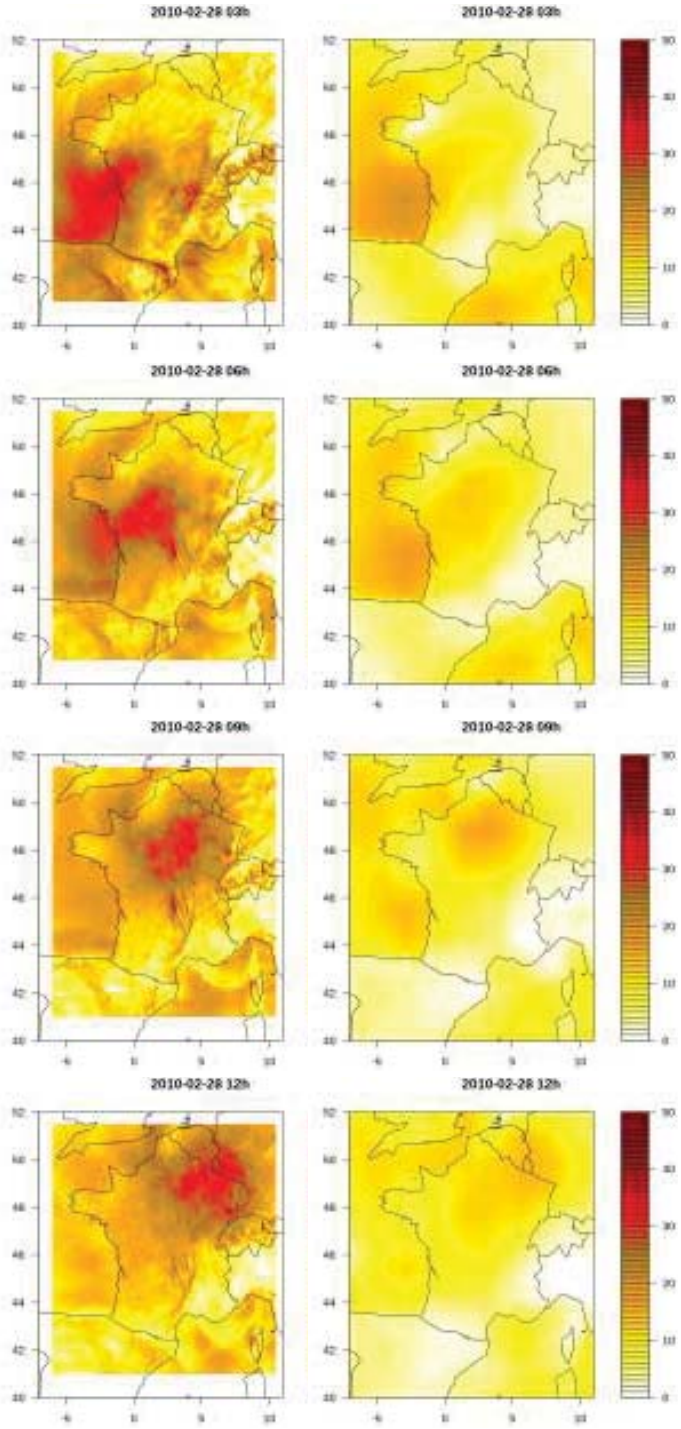

FIGURE 2.3: Observation-based field of wind-gust, computed using both observations and the high-resolution model "Arome" (left) and 10-meters renalysis field (right) for the 28th of February 2010 from 3 a.m. until 12a.m. when storm "Xynhtia" reached France.

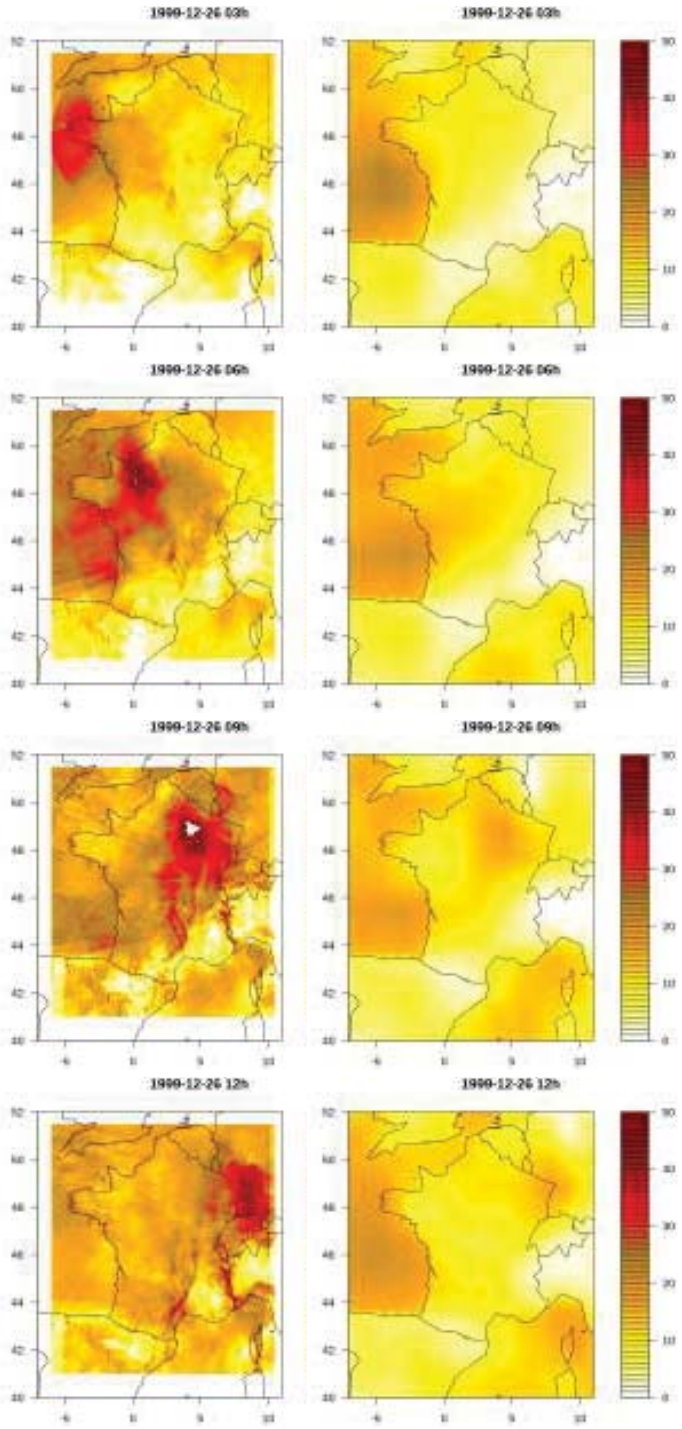

FIGURE 2.4: Same as 2.1 but for the 26th of December 1999, during storm "Lothar".

2.2. Extratropical cyclone tracking

2.2.1. Introduction

Cyclone tracking algorithms enable the identification and reconstruction of the life cycle of cyclone based on a particular variable. Until the 90's the tracking of extratropical cyclones was made in a manual or semi-automatic way. Some of the first fully automatic algorithms were presented by Hodges (1994) and Sinclair (1994). this happen when most of the problems in automatic detection were overcome, e.g., the correspondence between the same features of the tracks in consecutive frames and the definition of centroids when several centres are detected close to each other. Several variables are used to track extratropical cyclones : geopotential height, mean sea level pressure and relative vorticity are the most used. This last one presents some advantages with respect to the two others. On the one hand, it is able to detect extratropical cyclones in their earliest stages of life since it is a high-frequency parameter and, on the other hand, is very noisy and dependent on data resolution (Hoskins and Hodges, 2002). Mean sea level pressure and geopotential heigh are appropriate parameters to represent the large-scale movement of the storms but, they are very dependent on the background field that needs to be filtered before applying the tracking. Neu et al (2013) have studied fifteen cyclone tracking methods with different tracking variables on the same dataset. They have found consistency in the results among the different methods used, particularly for the deep and intense cyclones.

While studying important windstorms, Deroche et al (2014) have shown that the combination of mean sea level pressure, relative vorticity and the ratio of the wind with it 98% percentile is a better approach for detecting windstorms than with one variable only.

In the next section, the relative vorticity based tracking algorithm of Ayrault (1998) is described in detail and some problems encountered and adaptations explained. Then, the quality of the results is estimated by, analysing individual trajectories of well-known cases of storms in the recent decades and in the early century.

2.2.2. The method

Ayrault (1998) has developed a tracking algorithm based on 850 hPa relative vorticity. The method is summarised in the scheme presented in figure 2.5.
The first step of the cyclone tracking method is to apply a spatial filter to the data. As mentioned before, relative vorticity can detect mid-latitude cyclones at their earliest stages of life but is very dependent on the resolution and could be very noisy (Sinclair, 1997; Hodges, 1994). Applying a spatial filter will smooth the data and reduce the noise. The spatial filter used here consists in recomputing the vorticity (V) at a grid point *i,j*, with an approximative distance-weighed mean of vorticity of the four nearest neighbours grid points. This is applied once, as presented in equation 3 and then recomputed twice for a better smooth.

$$V_{(i,j)} = \frac{V_{((i,j))} + 4^{-1}V_{(i,j-1)} + 4^{-1}V_{(i,j+1)} + (4cos(lat_j))^{-1}V_{(i-1,j)} + (4cos(lat_j))^{-1}V_{(i+1,j)}}{1 + 2 * 0.25 + 2 * 0.25/cos(lat_j)} \tag{3}$$

After smoothing the data, the method can be explained in three steps. First, vorticity maximums will be detected within a circle of radius of 225 km at each time steps. Only the major maximum is taken inside this circle. This radius was chosen, by testing different radius and analysing the obtained trajectories of some particular cases.
Secondly, the next step of the algorithm consists in pairing the vorticity maximums between two successive time steps. This is the most sensible aspect of the method since from one time step to another the previously detected maximum can disappear, merge with another maximum, split or a new maximum can appear. Several criteria are used in order to evaluate the quality of pairing two maximums at time steps *t* and *t+1* :

— A resemblance criteria based on the absolute vorticity maximum (AVO) intensity. Here, the AVO should not increase more than 40% from one time

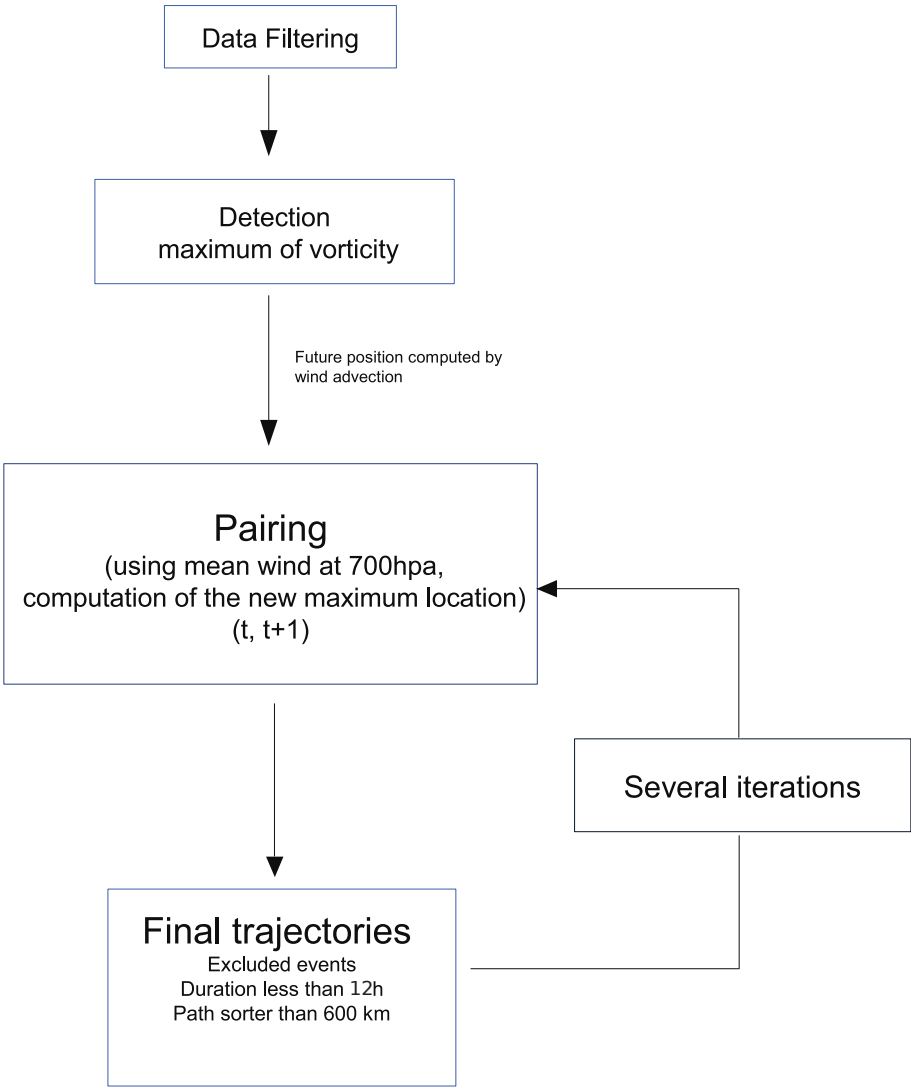

FIGURE 2.5: Diagram of the tracking algorithm steps.

step to the next one.

— A displacement criteria based on a comparison between three positions. Two probable positions of the detected maxima at *t+1*, computed by advection of the detected AVO at time step t using the 700 and 850 hPa winds. And the position of all detected AVO at *t+1*.

Then, the resemblance and displacement criteria are averaged and each detected

maximum from the time step t is paired up with the detected maximum at time step *t+1* that has the highest value.Entire cyclone trajectories are constructed after obtaining paring at each time step of the data.Then,several iterations are applied to the trajectories in order to improve the correspondence of the detected AVOs. If not verified, the algorithm suppresses the correspondence between the detected maximum of t and *t+1* and searches for a new one. Convergence is obtained under a few iterations only. Finally, the trajectories that last for more than 4-time steps (12 hours for ERA-20C dataset) and travelled a total of at least 600 km are kept.

The aforementioned original algorithm was developed and first applied by Ayrault (1998) to 6-hourly data of ERA-15 reanalysis and for the Atlantic region. In this study, we adapted it to detect extratropical cyclones from ERA-20C at every 3-hours over the whole Northern Hemisphere. The original routines are for this reason adapted to a 3-hourly data. Besides this, the continuity around the 180°meridian is insured.

2.2.3. Tracking algorithm's validation

In order to validate the quality of the tracking algorithm, the detected trajectories are analysed for some particular cases.

Four storms are chosen and their trajectories compared with the observed ones : Lothar and Martin in 1999 (Mathias Dobbertin, 2002), Klaus (Liberato et al, 2011) and Xynthia (Liberato et al, 2013) are not detected as one single track but as set of 2 or 3 trajectories. The reason for that was in a small radius used on the vorticity maximum detection. The radius is adjusted to compensate this effect (225 km) until a single trajectory is obtained. The final trajectories are presented in figures 2.6 2.7.

In addition to these more ancient storms are analysed. In figures 2.8 and 2.9, the purple lines presented two trajectories obtained from the algorithm in the first half of the twentieth century. The first storm (figure 2.8), on the 27$^{\text{th}}$ December 1903 corresponds to one storm that caused high damage in Ireland in the early century (available at http ://www.met.ie/climate-ireland/major-events.asp). Its location at 12 a.m. on the 27$^{\text{th}}$ of December is in good agreement with the observed map of

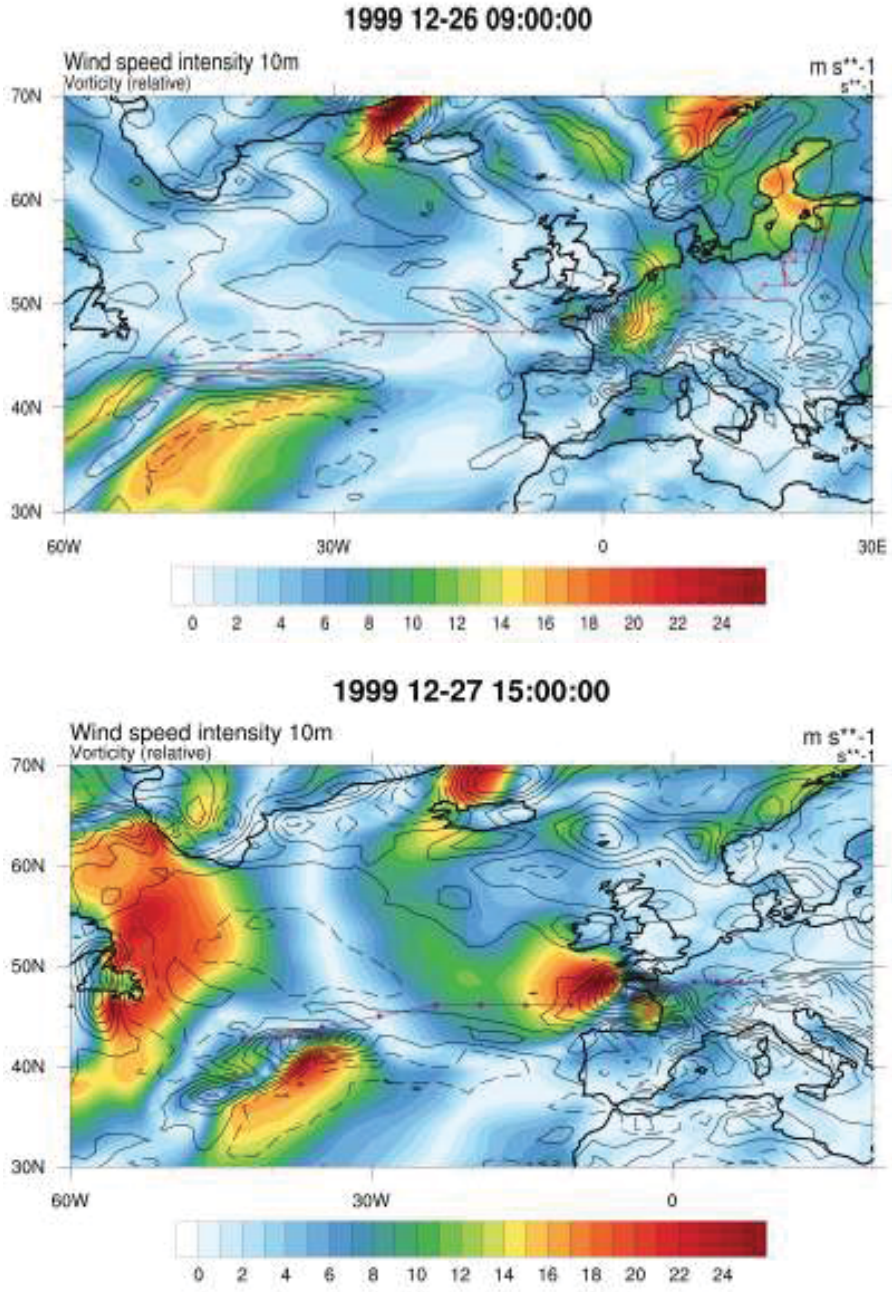

FIGURE 2.6: Trajectory obtained from the tracking algorithm (purple line) with the wind (shaded color contours) and vorticity (black line contours) for the storms :Lothar (top) Martin (bottom).

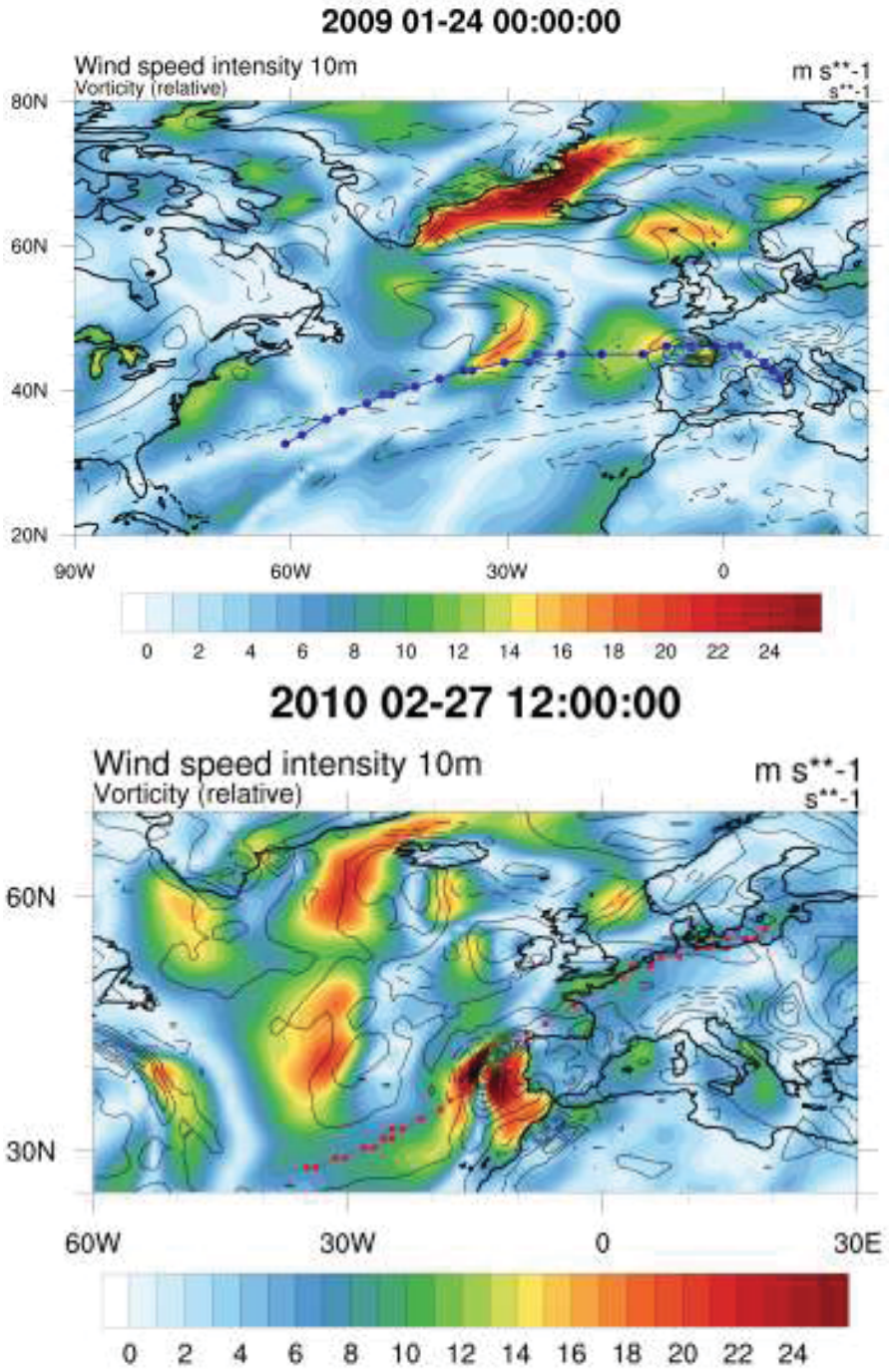

FIGURE 2.7: Same as 2.6 but for Klaus (top) and Xynthia (bottom).

the Irish meteorological service (Met Éireann) for the same hour and day (figure 2.8b). Furthermore, the trajectory detected (purple line of figure 2.8a) corresponds with the analysed trajectory (dot-dash line of figure 2.8b). The second storm (figure 2.9) analysed is the Iberia windstorm on the 15$^{\text{th}}$ of February of 1941. The position of the storm is in agreement with weather charts of the time (figure 2.9b).

Finally, to validate over the whole century, the mean density of storms per grid point is computed with a 300km radius for the whole North Hemisphere (figure 2.10). Two regions of relative maximums appear, one over the North Atlantic and another over the North Pacific, showing a good representation of the storm track regions (Hoskins and Hodges, 2002). Some other local maximums are observed in the Mediterranean or over the Urals mountains. Within storm track regions, the averaged number of tracks per extended winter (October of year y until March of year $y+1$) goes up to forty tracks per year, i.e., approximately a maximum of one to two storms per week, which corresponds well with estimations of storm frequency in these regions (Hoskins and Hodges, 2002; Bengtsson et al, 2006). Besides tracking density, genesis densities (figure 2.11) are in agreement with previous studies (Hoskins and Hodges, 2002), with maximums over the Rocky Mountains, the east coast of the United States, the Gulf stream or the east Japan region.

2.3. Conclusions

The results in this chapter show that the ERA-20C reanalysis is capable of representing correctly the cyclone distribution, even for early century windstorms when few observations are assimilated. The overall spatial and temporal variability of the wind related to the cyclone is accurate despite the fact that it underestimates its intensity, particularly for small-scale systems. This is related to the low horizontal resolution of the dataset.

The tracking algorithm shows a good performance when applied to ERA-20C data. An average of one thousand storms per year is obtained for the whole Northern Hemisphere with a mean density, which corresponds well with the time mean frequency of storms in this region. Most trajectories have one single continuous path. Furthermore, when comparing the detected trajectory of some intense storms of the century to the equivalent observed ones, a good correspondence between the

two paths are obtained.This is also the case for early storms like the Iberia storm in February 1941 and the storm of December 1903. We can then say that both data and algorithm present good results and that further analysis can be done.

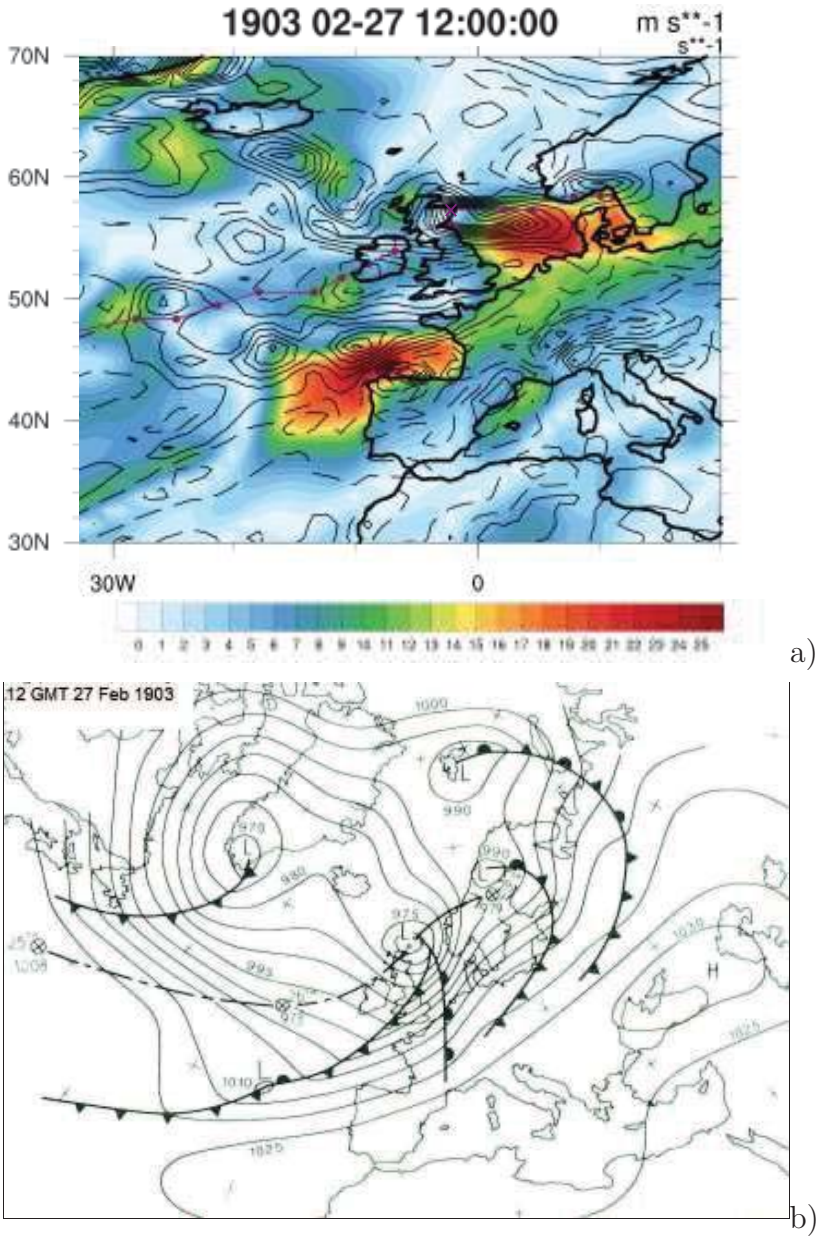

FIGURE 2.8: top- trajectory obtained from the tracking algorithm (purple line) with the wind (shaded color contours) and vorticity (black line contours) fot he storm on the 3rd of December 1903 ; bottom- mean seal level pressure field obtained from the Irish meteorological service MET ÉIREANN at http ://www.met.ie/climate-ireland/major-events.asp.

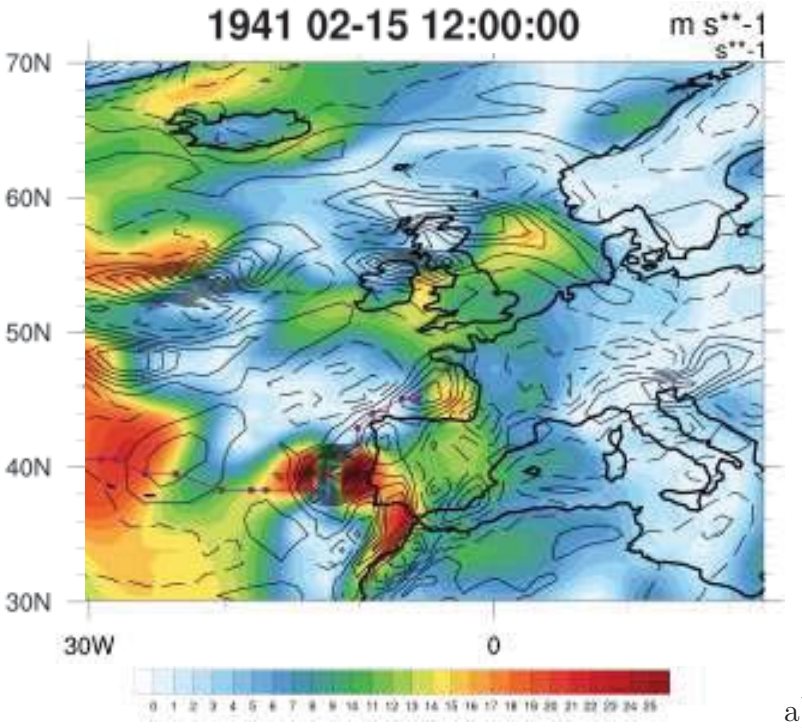

a)

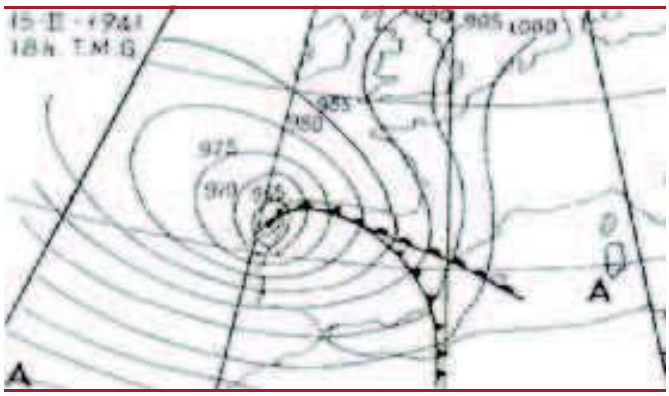

b)

FIGURE 2.9: Trajectory obtained from the tracking algorithm (purple line) with the wind (shaded color contours) and vorticity (black line contours) for he storm on the15th of February 1941 (top). Bottom figure, historical weather chart from (Muir-Wood, 2013).

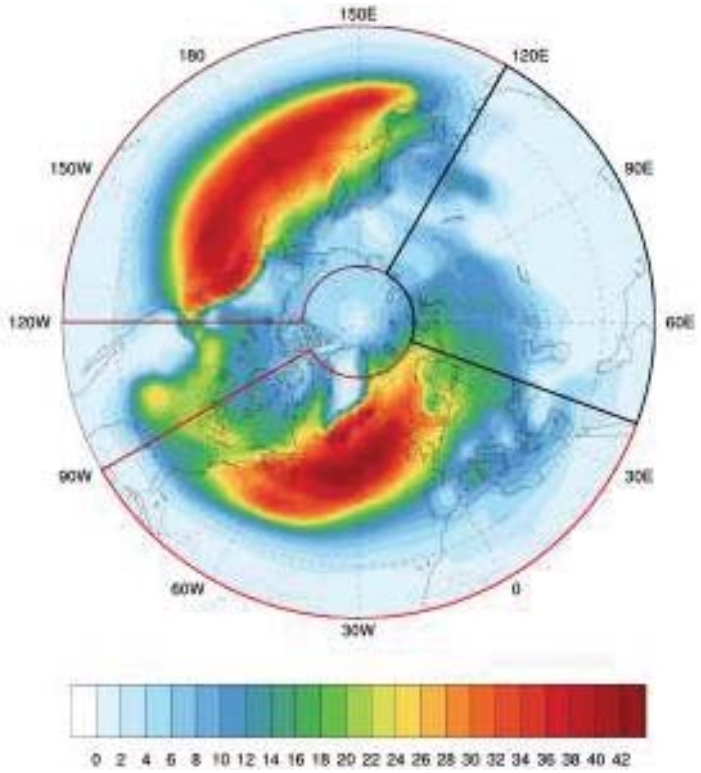

FIGURE 2.10: Mean density per year using a radius 300 km for the Northern Hemisphere (born cyclones/year/300km).

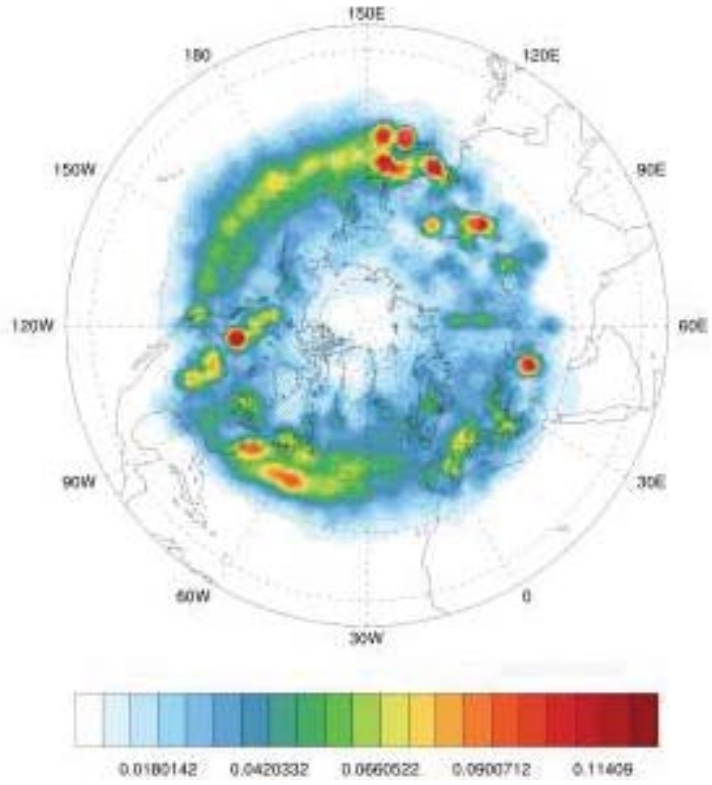

FIGURE 2.11: Mean genesis density per year using a radius 300 km for the northen hemispher (cyclones/year/300km).

CHAPTER III

Northern Hemisphere extratropical winter cyclones variability over the 20th Century derived from ERA-20C Reanalysis

Summary of the Article

As mentioned before an extra tropical algorithm (Ayrault, 1998) was applied for the whole Northern Hemisphere and for the whole century using the ERA-20C reanalysis. In the following article, the inter annual variability of the extratropical cyclones for the twentieth century was studied.
In section 3.1 of the article, the annual mean cyclones per year is analysed and a split into three periods according to the type of trend observed is made. Two periods with no significant trends at the end and at the beginning of the century and one period with significative positive trend in the middle of the century. In Sections 3.2 to 3.3 these trends are compared with eddy kinetic energy and strong wind trends. In section 4, baroclinicity, baroclinic conversion and also vertical profiles of Temperature and zonal wind are analysed. A cold troposphere is found to be related to the middle-century increase in extratropical cyclones while the two periods with non-significant trend is characterised by warming at low levels of the troposphere. Section 5 analyses in more detail the relationship between the ocean variability modes AMO and PDO with the cyclone activity trends observed in the three periods. A relation is found between the PDO and the Northern Pacific meridional thermal gradient that leading to a more intense storm track. Finally, in section 6, a brief analysis on the impact of the time-inhomogeneity of ERA-20C is analysed. It is shown that an increase in the number of observations might lead to a decrease in cyclone activity rather than an increase.

Northern Hemisphere extratropical winter cyclones variability over the 20th Century derived from ERA-20C Reanalysis(article)

Filipa Varino, Philippe Arbogast, Bruno Joly, Gwendal Riviere,Marie-Laure Fandeur, Henry Bovy, Jean-Batiste Granier (2018). Northern Hemisphere extratropical winter cyclones variability

over the 20th Century derived from ERA-20C Reanalysis(Under revision at Climat Dynamics)

https://doi.org/10.1007/s00382-018-4160-0

Northern Hemisphere extratropical winter cyclones variability over the 20th century derived from ERA-20C reanalysis

Filipa Varino[1] · Philippe Arbogast[2] · Bruno Joly[2] · Gwendal Riviere[3] · Marie-Laure Fandeur[4] · Henry Bovy[4] · Jean-Baptiste Granier[4]

Received: 21 March 2017 / Accepted: 15 March 2018

Abstract
The multi-decadal variations of wintertime extra-tropical cyclones during the last century are studied using a vorticity-based tracking algorithm applied to the long-term ERA-20C reanalysis from ECMWF. The variability of moderate-to-deep extra-tropical winter cyclones in ERA-20C show three distinct periods. Two at the beginning and at the end of the century (1900–1935 and 1980–2010) present weak or no significant trends in the Northern Hemisphere as a whole and only some regional trends. The period in between (1935–1980) is marked by a significant increase in Northern Hemisphere moderate-to-deep cyclones frequency. During the latter period, polar regions underwent a significant cooling over the whole troposphere that increased and shifted poleward the mid-latitude meridional temperature gradient and the baroclinicity. This is linked to positive-to-negative shifts of the PDO between 1935 and 1957 and of the AMO between 1957 and 1980 which mainly reinforced the storm-track eddy generation in the North Pacific and North Atlantic regions respectively, as seen from baroclinic conversion from mean to eddy potential energy. As a result, both the North Pacific and North Atlantic extra-tropical storms increase in frequency during the two subperiods (1935–1957 and 1957–1980), together with other storm-track quantities such as the high-frequency eddy kinetic energy. In contrast, the first and third periods are characterized by a warming of the polar temperatures. However, as the stronger warming is confined to the lower troposphere, the baroclinicity do not uniformly increase in the whole troposphere. This may explain why the recent rapid increase in polar temperatures has not affected the behaviour of extratropical cyclones very much. Finally, the large magnitude of the positive trend found in moderate-to-deep cyclone frequency during the second period is still questioned as the period is marked by an important increase in the number of assimilated observations. However, the dynamical link between changes in cyclone frequency, changes in large-scale baroclinicity and ocean decadal variability found in the present study makes us confident on the sign of the detected cyclone trend.

Keywords Storm track · Cyclone tracking · 20th century · ERA-20C · Arctic warming · Climate change

1 Introduction

Mid-latitude cyclones are responsible for the distribution of moisture, temperature and precipitation in the middle latitudes and can produce severe economical and social damages. In the Northern Hemisphere (NH), two particular regions of storms crossing the North Atlantic (ATL) and Pacific (PAC) oceanic basins exist. These regions are known as the storm-track regions (Hoskins and Hodges 2002) and are well depicted by band-pass filters variance of 300 hPa meridional wind-fields (Blackmon et al. 1977; Chang et al. 2002). However, to get an information on the initiation, mature and decay stages of cyclones, cyclone tracking algorithms are more appropriate. These algorithms generally

✉ Filipa Varino
filipa.varino@meteo.fr

[1] CNRM, UMR 3589, Météo-France/CNRS, Toulouse, France

[2] CNRM, UMR 3589, Météo-France, Toulouse, France

[3] LMD/IPSL, Département de Géosciences, ENS, PSL Research University, Ecole Polytechnique, Université Paris Saclay, Sorbonne Universités, UPMC Univ Paris 06, CNRS, Paris, France

[4] SCOR, Paris, France

Published online: 20 March 2018

detect minima in mean sea level pressure (MSLP) or maxima in low-level vorticity and identify them as cyclones' centers. Then, the trajectory of each cyclone is computed by searching the nearest extrema in MSLP or vorticity at successive time steps. However, these methods have some limits. While MSLP can be affected by large scale systems, vorticity is more noisy and more sensitive to data resolution than MSLP. One advantage of the vorticity over MSLP is that it can detect extra tropical storms in its early states (Sinclair 1997; Hoskins and Hodges 2002). Some studies have shown that the choice of the variable together with those of the data resolution and type can change results on cyclones statistics significantly (Neu et al. 2013), especially their intensity (Ulbrich et al. 2009; Bader et al. 2011).

Several authors have compared results from different reanalysis and different tracking methods (Raible et al. 2008; Ulbrich et al. 2009; Tilinina et al. 2013; Neu et al. 2013; Wang et al. 2013, 2016; Chang and Yau 2015). In general, results obtained from reanalysis data are correlated but small changes can be observed due to the use of different methods and/or data resolution. Furthermore several shifts in results were found associated with an increase in assimilated observation and satellite data (Bengtsson 2004; Bromwich et al. 2007; Chang 2007; Wang et al. 2016).

Results in tracked cyclone statistics using reanalysis data in the NH largely differ from one study to another. Gulev et al. (2001) applied a tracking algorithm to NCEP/NCAR MSLP datasets for the JFM months between 1958 and 1999. They found a negative trend in the total number of cyclones in the ATL and PAC and an increase in strong cyclones on the western side of the storm tracks. Using the same NCEP/NCAR reanalysis, Chang and Fu (2002) performed a principal component analysis on the high-pass-filtered 300-hPa meridional wind variance and obtained a decrease in DJF cyclones until the 70s followed by an increase afterwards. Still using the same data and for the same winter months Paciorek et al. (2002) analysed the second half of the 20th century using a tracking algorithm cyclone on MSLP and different indexes as cyclone predictors. They found that there is an increase in intensity of cyclones but that the number of cyclones has not increased. The same increase in intensity was shown in the PAC by Graham and Diaz (2001) for NCEP/NCAR Dec–Mar months and by Wang et al. (2006) in NCEP/NCAR and ERA-40 reanalysis on the NH for the DJF months. This last one also found a shift on the storm tracks, and an increase in deep cyclones over western Europe (from tracked MSLP minimums). Similarly, McCabe et al. (2001) observed a decrease (increase) in mid-(high) latitude cyclone frequency on Nov–Mar months for the same reanalysed MSLP tracked data that goes in agreement with a possible poleward shift of the storm tracks. Trigo (2006) compared Dec–Mar results from ERA-40 and NCEP/NCAR and found an increase in intense cyclones in the ATL and a northward shift of the ATL storm track. In conclusion, despite important discrepancies, most studies seem to agree with an increase in deep cyclones and in a poleward shift of the storm tracks during the second half of the 20th century.

While most studies focused on the recent decades, very few studies exist using long-term reanalysis data covering the whole 20th century, like 20CR from NOAA based on the ensemble Kalman filter approach with fifty six members and ERA-20C from the ECMWF based on the 4DVar approach where the background error covariances are sampled using an ensemble of 4DVar (Compo et al. 2011; Poli et al. 2016). Compared to NCEP/NCAR or ERA40 reanalysis, these long-term reanalysis have the advantage that upper-air datasets coming from satellites were not assimilated, which makes them more homogeneous in terms of the type of assimilated observations. However, their early-century homogeneity is still questioned due to too few observations in some areas. Wang et al. (2013) used 6-hourly MSLP from the 56 members of 20CR between 1871 and 2010 to obtain NH tracked-cyclones information for all seasons. They obtained an increase in intense cyclones and a poleward shift of the storm tracks for the entire century. They also showed that the ATL and European regions are the most statistically homogeneous regions for cyclone statistics since 1871.

Wang et al. (2016) compared eight reanalyses with different resolution and temporal ranges and applied the same tracking algorithm on unfiltered MSLP data for all the seasons. They found important differences in trends due to data resolution. Reanalyses covering recent decades show good agreement, particularly from the beginning of satellite-data assimilation in 1979. For the two long-term reanalysis they found ERA-20C to be more homogeneous than 20CR (specially in the Arctic) and better correlated with other shorter reanalyses. However, both reanalyses show inhomogeneities in the beginning of the century and in the Southern Hemisphere. Regarding cyclones trends, both reanalyses show an increase in deep cyclones over the NH for the 20th century period. However, as shown by several authors, the origin of inconsistencies of observed trends in long-term reanalyses is still on open question. They emphasized that the variation of observations density along the century must be assessed (Krueger et al. 2013; Wang et al. 2016; Chang and Yau 2016). For example, Dell'Aquila et al. (2016) show questionable lower synoptic activity in the early decades of ERA-20C and 20CR.

Finally, Chang and Yau (2016) applied a tracking algorithm to SLP data for the winter months (DJF) using several reanalyses including the two long-term reanalysis and have also computed the 300-hPa meridional wind variance. In general, results for the period 1960–2010 show positive trends in cyclones in ATL and a greater increase in PAC. It confirms previous studies, especially that of Chang and Fu (2003) who showed, following a mean-flow-based proxy,

that storm-track activity was weakest during 1960s and then underwent an upward trend until 1990s.

The present paper aims at investigating temporal trends of moderate-deep winter cyclones using ERA-20C. While Wang et al. (2016) and Chang and Yau (2016) used MSLP tracking algorithms, extratropical cyclones are here detected with a vorticity-based algorithm. Besides, the main originality of the paper relies on the physical interpretation of the detected cyclone trends in terms of barolinicity trends and changes in phase of large-scale modes of climate variability. The results become more robust when a dynamical link between cyclone trends and the large-scale circulation is found. This also helps eliminating some doubts associated with the inhomogeneity of the reanalysis.

There is also a growing literature investigating the evolution of storm tracks and jet stream in a changing climate. A poleward shift of the Atlantic and Pacific storm tracks occurred after the 80s until the end of the 90s (McCabe et al. 2001; Wang et al. 2006) in connection with a tendency toward a positive phase in the North Atlantic Oscillation (NAO) and Arctic Oscillation (AO) indices (McCabe et al. 2001). This has been initially attributed to the anthropogenic forcing (Thompson and Wallace 1998; Corti et al. 1999). However, since the early 2000s, the poleward tendency disappeared and some winters were marked by extreme negative NAO and AO (LHeureux et al. 2010; Cattiaux et al. 2010; Rivière and Drouard 2015). There is thus no general shift of the jet streams or storm tracks in the last decades in the Northern Hemisphere but rather regional shifts (Barton and Ellis 2009). Besides, the variations of the recent decades do not appear unusual (Woollings et al. 2014) and could be due to internal atmospheric variability (Barnes and Screen 2015). Nor is there a strong signal in the future evolution of the Northern Hemisphere storm tracks and jet streams in winter as seen in climate model projections of the Coupled Model Intercomparison Project (CMIP) (Cattiaux and Cassou 2013). Depending on model properties, such as resolution, ocean or sea-ice dynamics, the results can change significantly (Woollings et al. 2012). However, despite a large spread of CMIP5 models, there are some agreements about storm-track changes in the NH: a slight upward and poleward shift in the upper troposphere in both seasons and an overall decrease in the lower troposphere except in some specific regions like an eastward extension of the wintertime storm track over Northern Europe (Chang et al. 2012; Harvey et al. 2013; Zappa et al. 2013).

Mid-latitude cyclone activity strongly depends on baroclinicity, a large-scale atmospheric quantity function of horizontal and vertical temperature gradients (Hoskins and Valdes 1990; Geng and Sugi 2003). The recent strong increase in the Arctic temperature tends to reduce the near-surface meridional temperature gradient and so, the lower-level baroclinicity. The effect is to decrease storm-track activity and displace the jet streams equatorward according to idealized experiments (Butler et al. 2010; Rivière 2011). Consistently, more realistic simulations show that sea-ice reduction favours the occurrence of the negative AO/NAO patterns (Bader et al. 2011; Cohen et al. 2014; Nakamura et al. 2015; Oudar et al. 2016). However, in the upper troposphere, the mid-latitude temperature gradients increase due to a stronger warming in the tropical upper troposphere which counteracts the effect of the decrease in lower-level baroclinicity and acts to shift the storm tracks poleward (Butler et al. 2010; Rivière 2011). These opposing effects of changes in lower- and upper-level baroclinicity participate in keeping the future evolution of the wintertime NH storm tracks uncertain (Shaw et al. 2016). Nevertheless, some consensual results seem to appear with the last multi-model intercomparison studies using cyclone tracking algorithms. We expect an overall decrease in strong winter cyclones and, in the North Atlantic sector, an increase in cyclone frequency near the British Isles (Chang et al. 2012; Zappa et al. 2013). These CMIP5 experiments confirm previous studies relying on single model experiments (Bengtsson et al. 2006; Pinto et al. 2007; McDonald 2010). Even though the present study does not investigate future changes in storm-track activity, the question of the effect of Arctic warming on mid-latitudes will be put in perspective with the earlier periods of the 20th century.

Since the present paper focuses on cyclone variability over more than a century, multi-decadal fluctuations could be detected in connection with well-known modes of ocean (multi-)decadal variability like the Atlantic Multidecadal Oscillation (AMO) and Pacific Decadal Oscilation (PDO). In the Pacific, the PDO is positively correlated with storm tracks until the 80s and its negative (positive) phase is associated with a northward (southward) shift of the Pacific storm track (Lee et al. 2012; Sung et al. 2014). In the Atlantic, the negative AMO phase is related with more zonal and elongated storm tracks (Yamamoto and Palter 2016). A warm AMO has been shown to lead to a negative NAO by a few years (Peings and Magnusdottir 2014; Gastineau and Frankignoul 2015). The AMOC circulation has weakened since the middle of the century and future scenarios predict a constant decrease (Rahmstorf et al. 2015). Its weakening and/or shutdown means less exchange between warm tropical and cool polar waters, an increase in the SST gradients and low-level baroclinicity which leads to an increase in the intensity of the Atlantic storm-tracks, consistent with the Bjerknes compensation mechanism (Shaffrey and Sutton 2006). A more recent study has shown that the dynamical link between the NAO and deep cyclones is modulated by the variability of the AMOC (Gomara et al. 2016).

The present paper is organized as follows. Data and methods are described in Sect. 2. In Sect. 3, moderate to strong extratropical cyclone variability in the NH are first presented and trends for some periods of the 20th century

are identified. A comparison with trends in high-frequency kinetic energy is also made. In Sect. 4, baroclinicity and baroclinic conversion trends that may explain the detected cyclone trends are identified and interpreted in terms of changes in temperature and zonal wind for three different periods. Section 5 makes the link between changes in phase of large-scale modes of atmospheric and oceanic variability and baroclinicity changes. The potential impact of nonhomogeneous assimilated observations is discussed in Sect. 6. Finally, a summary of the results is provided in Sect. 7 and are discussed relative to the existing literature.

2 Data and methodology

2.1 Data

The data used in this study is the ECMWF ERA-20C reanalysis that covers the whole 20th century (Poli et al. 2016). The focus is made on the Northern Hemisphere (0°–90°N; 180°W–180°E) during the cold season (October–March) from 1900 until 2010. Datasets were extracted with a 3-hourly frequency as needed to feed the cyclone tracking algorithm. It concerns the relative vorticity at 850 hPa and the horizontal wind components at 700 and 850 hPa. We extracted the wind and temperature at five vertical levels (850/700/500/300/200 hPa) at a daily frequency as well as the 2-meter temperature, sea surface temperature (SST) and surface pressure. All data was extracted with a spatial resolution of 1.125° × 1.125°.

2.2 Cyclone tracking algorithm

The tracking algorithm used is the one from Ayrault (1998) and Ayrault and Joly (2000) (see also the supplementary material of Michel et al. 2012 for a description of a recent climatology in the North Atlantic). It has been adapted to track 3-hourly relative vorticity maxima at 850 hPa over the entire Northern Hemisphere. A spatial smoothing distance-weighted filter is applied to the relative vorticity at each grid point with respect to its 13 closest neighbours. The tracks are built by pairing successive relative vorticity maxima following several criteria: Two maxima are paired when they present similarity in intensity, and if the displacement between them is coherent with the advection by the background wind as determined by both winds at 700 and 850 hPa. Final trajectories were selected only if the duration of life and travelled distance were superior to 24 h and 600 km respectively. The tracking period runs between the 1st of October to the 31rd of March from 1900 to 2010. Even though the tracking algorithm detects all vorticity maxima, only trajectories whose relative vorticity exceeds 10^{-4} s^{-1}, that is roughly the value of the Coriolis parameter, are kept in the present paper. It means that only moderate to deep cyclones are hereafter considered. The main reason is that such a vorticity-based cyclone tracking algorithm detects small-scale features with relatively weak vorticity values that are not necessarily detected by other tracking algorithms based on geopotential or mean sea level pressure.

2.3 Baroclinicity

In this paper, we compute the baroclinicity and baroclinic conversion as follows:

$$\sigma_{BC} = \frac{1}{\sqrt{S}} \sqrt{\left(\frac{\partial \bar{\theta}}{\partial x}\right)^2 + \left(\frac{\partial \bar{\theta}}{\partial y}\right)^2}, \tag{1}$$

$$BC = -\frac{1}{S}\frac{\partial \bar{\theta}}{\partial y}\overline{\theta' v'} + \frac{1}{S}\frac{\partial \bar{\theta}}{\partial x}\overline{\theta' u'}, \tag{2}$$

where overbar and prime quantities represent the mean flow and eddy fields respectively. The stratification parameter $S = -\frac{p}{R}\left(\frac{p}{p_0}\right)^{-\frac{R}{C_p}}\frac{\partial \theta_R}{\partial p}$ considers a reference potential temperature θ_R which is a priori a function of the pressure only. Variables p and p_0 indicate the pressure and the reference pressure respectively, R and C_p are the gas constant for the air and the specific heat at constant pressure The parameter σ_{BC} corresponds to the maximum baroclinic exponential generation rate, that is the maximum of the ratio between the baroclinic conversion and the eddy total energy (Rivière et al. 2004; Rivière and Joly 2006). In the whole paper, the mean flow and eddy fields correspond to the seasonal mean (October–March) and high-pass-filtered (periods less than 10 days) fields respectively and the reference potential temperature θ_R is taken as the annual mean of θ (i.e $\bar{\theta}$). Finite differences between 200–300, 200–500, 300–700, 500–850 and 700–850 hPa are applied to the potential temperature to compute the stratification parameter at 200, 300, 500, 700 and 850 hPa respectively. Grid points for which the surface pressure is lower than 850 hPa are suppressed from the computation. Note finally that σ_{BC} is just the Eady parameter divided by the constant coefficient 0.31 (Hoskins and Valdes 1990).

2.4 Climate modes of variability

Regarding planetary modes of variability we computed the Atlantic Multidecadal Oscillation (AMO) and Pacific Decadal Oscillation (PDO). The AMO was computed from monthly (October–March) SST anomalies in the North Atlantic (90°W–30°W; 0°N–70°N) that are first detrended and then smoothed with an approximative 120-month running mean (Enfield et al. 2001). The PDO (Mantua et al.

1997) was computed as the first EOF of monthly SST anomalies between 20°N and 90°N in the North Pacific also for the October–March months.

2.5 Trends and statistical significance

Finally, all trends were computed with a robust linear, non-parametric Kendall–Theil trend estimator (Theil 1950), that computes all possible pairwise slopes and takes the median as the summary statistic that describes the trend. We considered a 5% significance level.

3 Extratropical cyclone and storm-track trends

3.1 Cyclone frequency trends

Extratropical cyclones (ETCs) tracks are separated into three categories according to the maximum vorticity intensity. In the whole study, only trajectories with maximum vorticity greater than or equal to the Coriolis parameter ($f_0 = 10^{-4}\mathrm{s}^{-1}$) are considered (hereafter referred to as *All*), which is around 45% of the total number of trajectories. Then, the ones from *All* that never reach its percentile 85 ($2.13 \times 10^{-4}\mathrm{s}^{-1}$) are labelled as *Moderate* and finally the ones that have reached maximum vorticity greater than this value are labelled as *Strong*.

Figure 1a presents the normalized number of cyclones per year in the Northern Hemisphere (here defined as the area 20°–90°N; 180°W 180°E) for *All* (black), *Moderate* (blue)

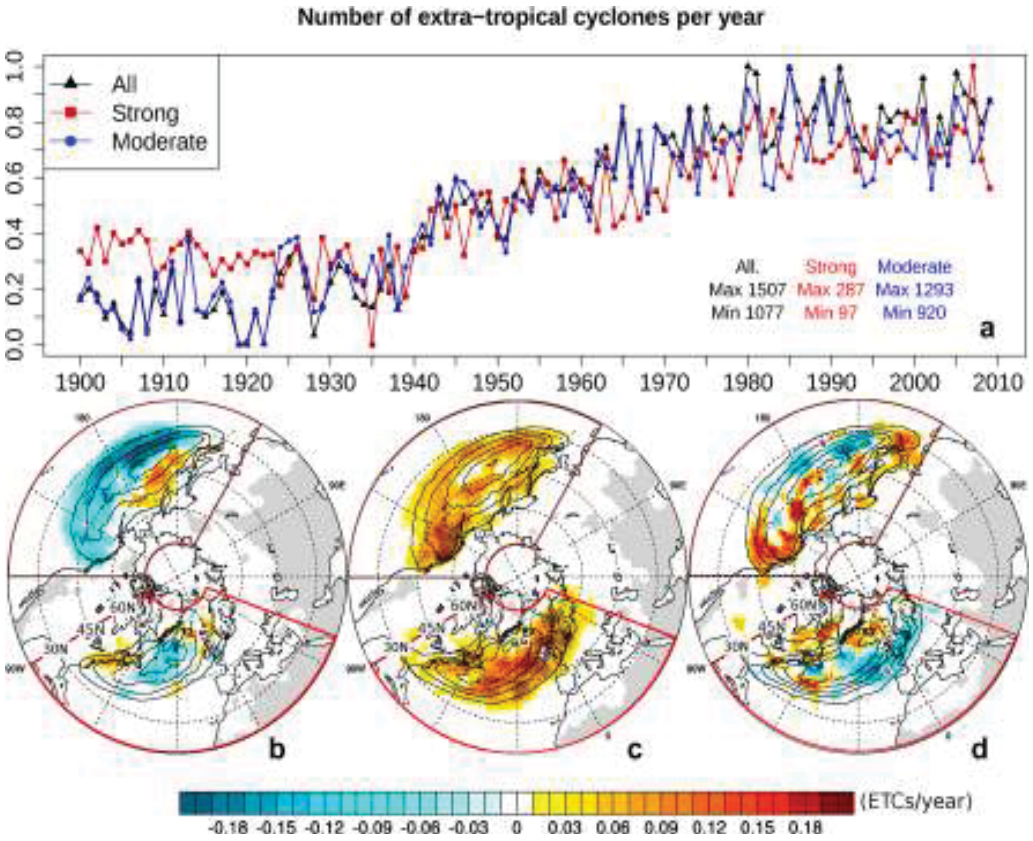

Fig. 1 **a** Time evolution of the number of ETCs with maximum vorticity higher than f_0 for all storms (black line), Strong (red line) and Moderate (blue line). Each number has been first subtracted by the minimum before being divided by the range. Trends in the number of strong ETCs per year are shown for different periods: **b** 1900–1935, **c** 1935-1980 and **d** 1980–2009. The red and brown areas on **b**–**d** represent the Atlantic and Pacific sectors respectively as defined in the study. Contours lines represent the mean number of strong ETCs per year for each period (contour intervals three cyclones per year). Dotted grid points represent significant values with a minimum 95% confidence

and *Strong* (red) ETCs. The normalization is obtained by subtracting the absolute minimum to the number of cyclones per year and then dividing the result by the range over the total period. Three time periods can be distinguished: one period at the middle of the century with a positive trend and two periods at the beginning and at the end of the century that undergo rather small variations in cyclone frequency. The first period goes from 1900 to 1935 and is marked by a very slight decrease in *Strong* cyclones and almost no change in *All* cyclones. The second period from 1935 to 1980 is characterized by an increase in all categories of ETCs and the third period from 1980 to 2010 by almost no change in the number of cyclones. The three periods are hereafter denoted as periods I, II and III. Besides these previously defined three periods, we also consider two different regions: the ATL region (20°–90°N; 90°W–60°E) and the PAC region (20°N–90°N; 120°E -120°W) defined by red and brown polygons in Fig. 1b–d.

We compute ETC density trends (as described in Sect. 2) for these three periods. Trends and related significances are summarised in Table 1. Considering the whole century (Table 1 first column), significant positive trends are observed for all regions and all types of ETCs. The numbers of *All* and *Strong* ETCs increase during the century from 1.5 to 3 times (Fig. 1a). The increased number of ETCs during the century essentially occurs during the second period (1935–1980). PAC and ATL show similar positive trends for this period as for the whole 20th century (Table 1 third column). The *All* ETCs are the ones with higher positive trends while the *Strong* are the ones that show the weakest positive trends. The first period does not present significant trends except for the *All* ETCs in ATL and *Moderate* in PAC (Table 1 second column). The third period does not show any significant trend for any type of ETCs and any region (Table 1 fourth column).

Figure 1b–d present spatial trends in the number of *Strong* ETCs for the three previously defined time periods in the Northern Hemisphere. The first period is characterized by significant negative trends in the southernmost latitudes of the PAC storm track and positive trends on the northwestern part of the storm track. There is a poleward shift of the storm track accompanied by some reduced intensity overall. As suggested by the time series of Fig. 1a, the second period shows significant positive trends in both the Pacific and Atlantic storm-track regions, especially on their eastern sides. The third period shows weak and non-significant trends. We note however some increase in storm frequency in the eastern Pacific and some decrease in the eastern Atlantic.

Table 1 Trends in the number of ETCs per year and regions for the three different periods studied

		1900–2010	1900–1935	1935–1980	1980–2010
ATL	All	1.3**	0.77*	2**	–
	Strong	0.40**	–	0.786**	–
	Moderate	0.90**	–	1.2**	–
PAC	All	1.12**	–	2**	–
	Strong	0.25**	–	0.577**	–
	Moderate	0.86**	0.69*	1.492**	–
NH	All	3.69**	–	5.35**	–
	Strong	0.95**	−0.515**	1.524**	–
	Moderate	2.72**	1.3*	3.75**	–

*p value lower than 0.15, **p value lower than 0.01

3.2 High-frequency eddy kinetic energy trends

Figure 2 displays spatial trends of high-frequency eddy kinetic energy at 300 and 850 hPa. For the first period (Fig. 2a, d), negative trends can be found over the southern and eastern regions of the PAC storm track and positive trends in the northwestern regions at upper levels in particular. In the Atlantic sector, upper and lower levels behave differently with positive and negative trends respectively, except for the east coast of the US which is characterized by an increase at the two different levels, similarly to the number of ETCs (Fig. 1b). For the second period, positive trends are observed over the entire NH at both levels, consistent with the positive trends found in the number of ETCs (Fig. 1a–c). The third period is less characterized by broad areas of significant patterns but rather by small regional changes such as the increase in the northeastern PAC storm-track and decrease in the eastern ATL storm-track. Therefore Figures 1 and 2 show that ERA-20C tracking and high-frequency variance trends are in good agreement regarding the most remarkable features of each period.

Another important feature to notice is that *Strong* ETCs trends are located in the storm-track regions, i.e, over the oceans while *Moderate* trend maximums are also significant over the continents (not shown). This is important because we know that the number of observations assimilated by the reanalysis explodes between the 40s and the 60s over the continents [Fig. 3 from Poli et al. (2016)] while over the oceans the number of assimilated observations is more homogeneous since the beginning of the century (especially over the ATL). Though we are not able to fully address the sensitivity of the storm-track trends to the observation density trends it suggests that *Strong* ETCs trends should be more reliable that *Moderate* ones. Moreover, no decrease in the yearly number of ETCs (Fig. 1) is observed during world war I and II, when the number of observations has dramatically reduced (Fig. 4, Poli et al. 2016). For all the

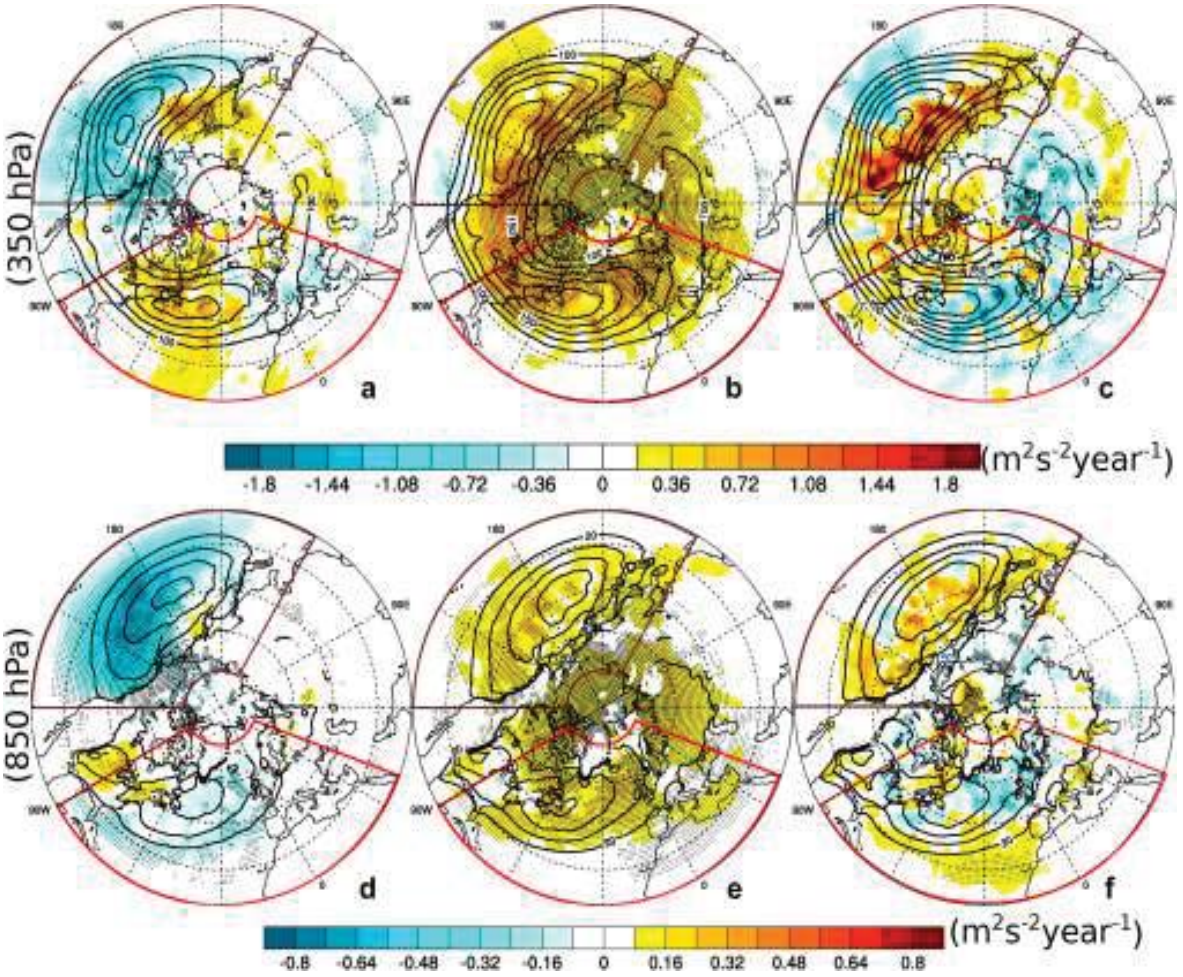

Fig. 2 Spatial trends in high-frequency eddy kinetic energy (shadings; units: $m^2s^{-2}year^{-1}$) at **a–c** 300 hPa and **d–f** 850 hPa for (left column) 1900–1935, (middle column) 1935–1980 and (right column) 1980–2009. The black contours represent the mean field for each subperiod (interval: 25 m^2s^2 for **a–c** and 10 m^2s^2 for **d–f**). Dotted grid points represent significant values with a minimum 95% confidence

aforementioned reasons we decide to focus on the *Strong* ETCs trends only.

3.3 Extreme winds trends

Most of the strong ETCs crossing the Atlantic have a strong impact over Europe. For this reason, extreme winds in the Europe can be used as an indicator of storm intensity. Figure 3 confirms the intensification of extreme ETCs during the 1935–1980 period in the European sector as diagnosed from the 98% percentile of the 10-m wind speed. Before 1935, the yearly 98% percentile is systematically below 11 m s^{-1}. Then, it smoothly increases until the 1980s where it reaches values near 11.4 m s^{-1}. After the 1980s, it slight decreases. It is an important confirmation of the above results using a very different variable.

The rest of the paper is dedicated to exploring the reliability of the previously detected density trends. For that purpose, we compute planetary-scale diagnoses relevant to mid-latitude storm-track dynamics and less sensitive to analysis quality. Section 4 presents the baroclinicity trends as diagnosed for each subperiod, together with the baroclinic conversion, temperature and zonal-mean zonal wind trends.

4 Baroclinicity trends

4.1 Period I: 1900–1935

For the first period, the PAC region shows weak positive and strong negative tendencies of baroclinic conversion

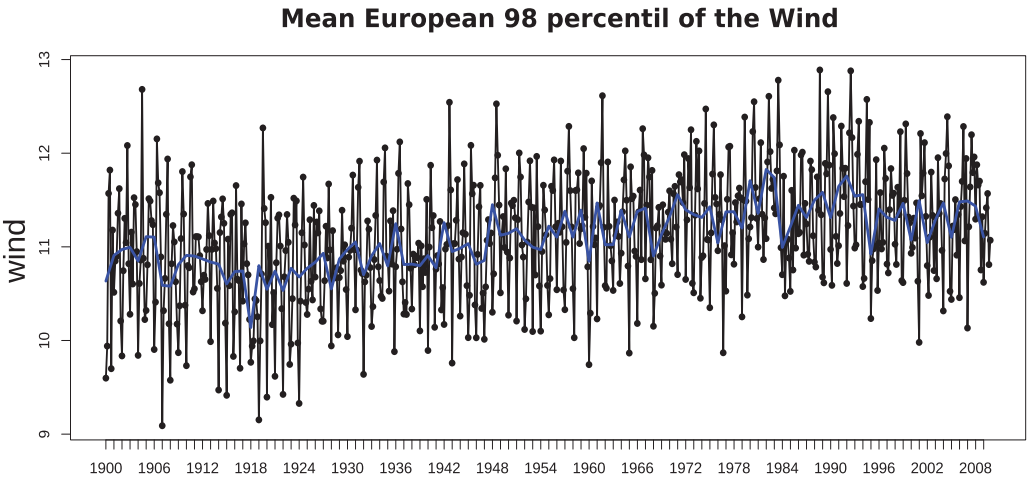

Fig. 3 Monthly (black) and yearly (blue) time series of the mean 98th percentile of 10-m wind speed (units: m s^{-1}) in ERA-20C averaged in the European regions (34°W–30°E, 35°N–75°N)

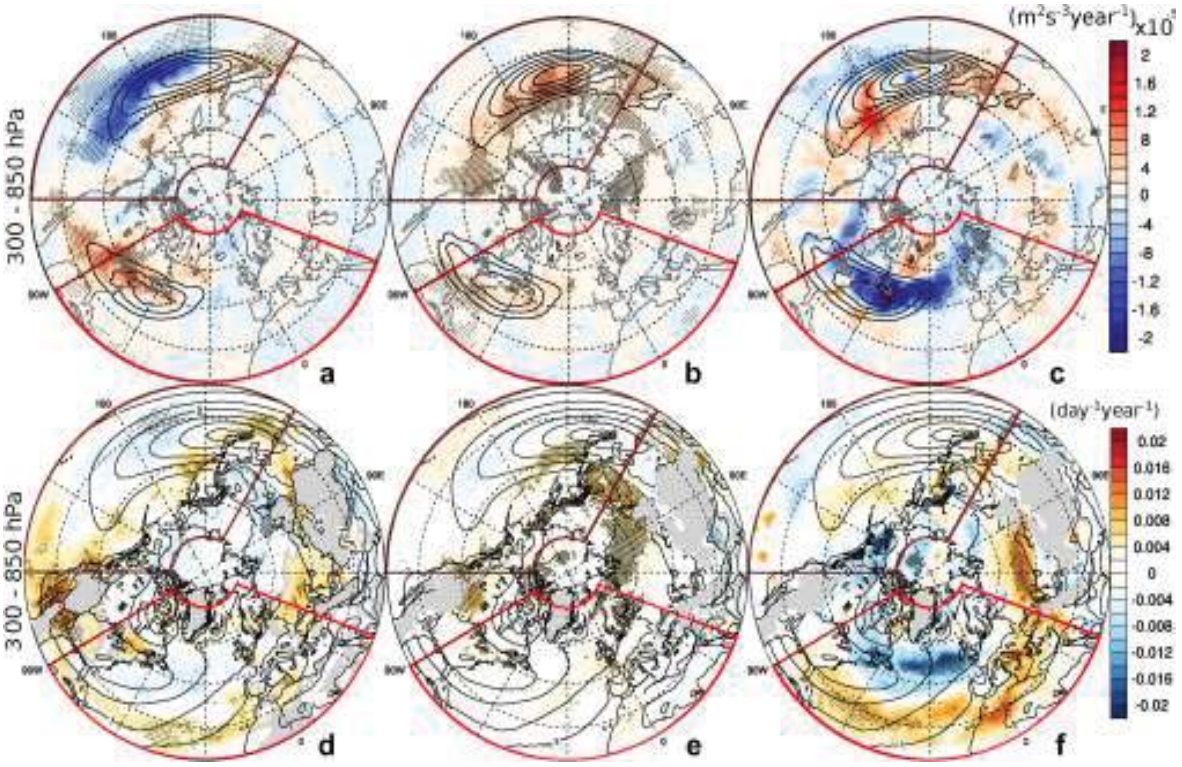

Fig. 4 Same as Fig. 2 but for the vertical average between 300 and 850 hPa of **a**–**c** baroclinic conversion ($m^2s^{-2}year^{-1}$) and **d**–**f** baroclinicity ($day^{-1}year^{-1}$). The black contours represent the mean field for each period (interval: 25 m^2s^{-2} for the baroclinic conversion and 0.5 day^{-1} for the baroclinicity). Dotted grid points represent significant values with a minimum 95% confidence

at northern and southern latitudes respectively (Fig. 4a) leading to an overall decrease and a slight poleward shift of the conversion pattern. These trends are consistent with the storm-track ones. The vertically-averaged baroclinicity also exhibits a poleward shift (Fig. 4d) and the decrease on the equatorward side is more pronounced than that on the

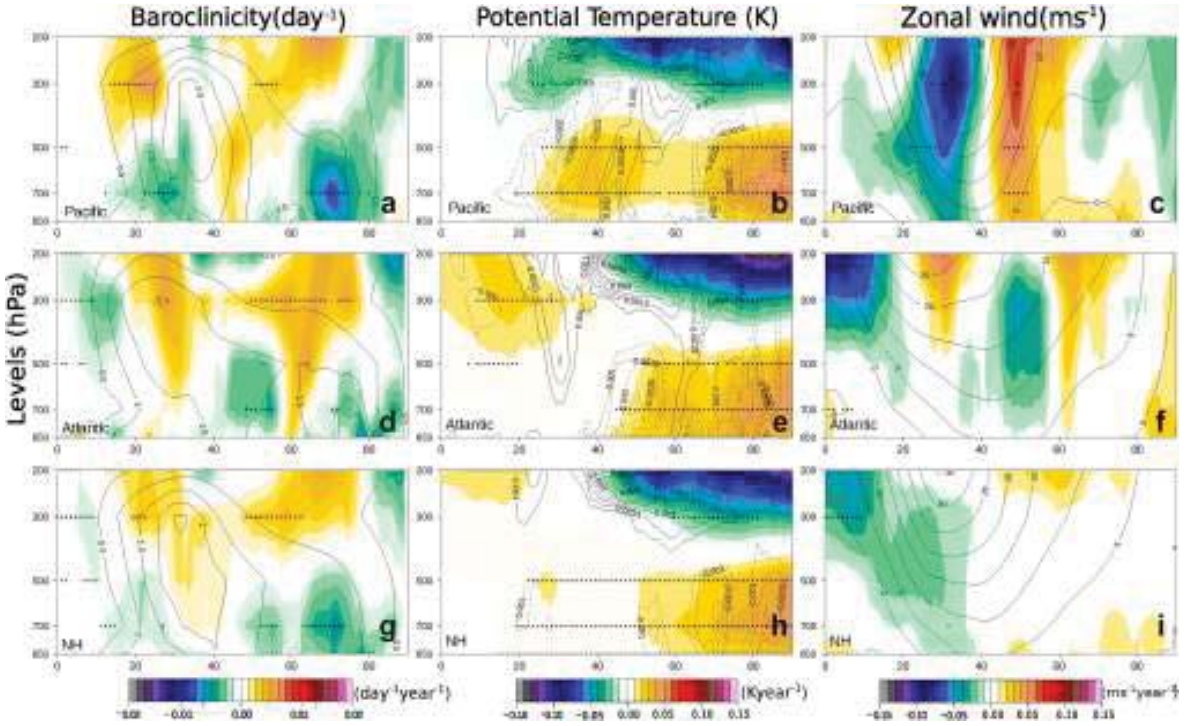

Fig. 5 Vertical profiles for period I (1900–1935) of (first column) the baroclinicity trends (colors, $day^{-1}year^{-1}$) and the mean field (contour); (second column) potential temperature trends (colors, $Kyear^{-1}$) and temperature gradient trends (positive and negative values in solid and dotted contours); (third column) Zonal wind trends (colors, ms^{-1} $year^{-1}$) and mean field (contours; int: 5 ms^{-1}). (top) Pacific, (middle) Atlantic and (bottom) Northern Hemisphere

poleward side in the lower troposphere as seen in Fig. 5a. There is also some decrease in the baroclinic conversion in the polar regions near Alaska which can be explained by a decrease in baroclinicity there (Figs. 4a, d, 5a). However, this should have no impact on the ETCs since it occurs over a region of weak baroclinicity. The baroclinicity trends are well correlated with horizontal temperature gradient trends (Fig. 5b). The poleward shift of the mid-latitude baroclinicity is due to a warming centred near 40°N and the decrease in baroclinicity north of 60°N is due to a stronger warming in the polar cap regions. Finally, westerlies decrease in intensity and are slightly poleward shifted (Fig. 5c) similarly to the Pacific storm-track.

In the ATL region, positive tendencies of the baroclinicity are observed at the entrance of the ATL storm-track (Fig. 4d), an area where the baroclinic conversion tendency is also significantly positive (Fig. 4a). More downstream in the mid-Atlantic, the baroclinicity tendencies are weakly negative and not significative which might be due to the compensation between the negative tendencies at low levels and the positive ones at upper levels (see the vertical cross-section of Fig. 5d). There is some increase in baroclinicity in the subtropical North Atlantic near 30°N (Fig. 4d) which mainly comes from the warming of the upper-level tropical troposphere (Fig. 5d,e). Generally speaking, baroclinicity changes are well captured by horizontal temperature gradient changes. Thus, its decrease in intensity at low levels is explained by the warming of the polar regions below 500 hPa (Fig. 5e). Westerlies generally decrease even though the anomalies are not significative (Fig. 5f).

Northern Hemisphere tendencies (Fig. 5g–i) are much smoother than PAC and ATL ones, since we observe opposite trends for the ATL and PAC regions at many latitudes. The general tendency is a polar warming confined to the lower troposphere that reaches a peak amplitude in the mid-1930s as described in Polyakov and Johnson (2000) and Yamanouchi (2011). The polar warming leads to the decrease in the lower-troposphere baroclinicity. But because the upper-level baroclinicity increases during that period, there is some compensation that may explain why the decrease in storm-track eddy activity is not significant.

4.2 Period II: 1935–1980

For the second period, in the PAC region, baroclinic conversion trends are positive and significant everywhere (Fig. 4b) with a maximum trend reached in the western Pacific where the mean baroclinic conversion is the strongest. This

maximum positive trend is closely related to the area of positive baroclinicity trend northeast of Japan (Fig. 4e). There are also other areas of increased baroclinicity and baroclinic conversion over the continents in Eastern Asia and over the west coast of North America. Zonal averages of the baroclinicity confirms a global increase in baroclinicity in the PAC sector at almost all tropospheric levels between 40°N and 80°N (Fig. 6a). There is just a moderate decrease in baroclinicity on its equatorward flank at low levels near 35°N. The overall baroclinicity increase north of 40°N is due to a cooling at high latitudes (Fig. 6b). The Pacific jet tends to widen with a stronger increase on its poleward flank (Fig. 6c).

In the ATL region, baroclinic conversion trends are also positive and significant in the western Atlantic but amplitudes of the trends are weaker than in the PAC region (Fig. 4b). The vertically-averaged baroclinicity in the ATL sector is weakly positive and not significant and the strongest positive trends are reached over land in the eastern North America and near Scandinavia. Cross-section of Fig. 6d confirms the slight positive trend but the number of significant grid points is smaller than in the PAC sector. Positive significant values north of 60°N at low levels are related with the positive values over the Scandinavian region. The general positive baroclinicity trend can be attributed, as in the PAC sector, to an increase in horizontal temperature gradients due to a cooling at high latitudes over the whole troposphere (Fig. 6e). The ATL jet also intensifies on its poleward flank during that period (Fig. 6f), consistent with the observed cooling.

In the NH, the zonally-averaged tendencies of Fig. 6g–i are quite significant because the PAC and ATL regions undergo more or less the same changes. There is an overall increase in baroclinicity which is more important north of its maximum amplitude (Fig. 6g) due to a general cooling at high latitudes (Fig. 6g, h) as observed by Box et al. (2009) and Kinnard et al. (2008). This is accompanied by an intensification of the westerly jets on their poleward flank (Fig. 6i). The baroclinicity intensification, especially on the northernmost latitudes, explains why there is a global increase in storm-track eddy activity and in the number of moderate and strong ETCs during that period. Further and more detailed analysis for this period is presented on Sect. 5.

4.3 Period III: 1980–2009

Period III shares common features with period I though important differences can be depicted. In the PAC region, both the baroclinic conversion and baroclinicity show positive consistent trends (Fig. 4c, f), accompanied by a northeastward shift (Figs. 4c, f, 7a) similarly to period I. The baroclinicity decrease north of 60°N mainly occurs over

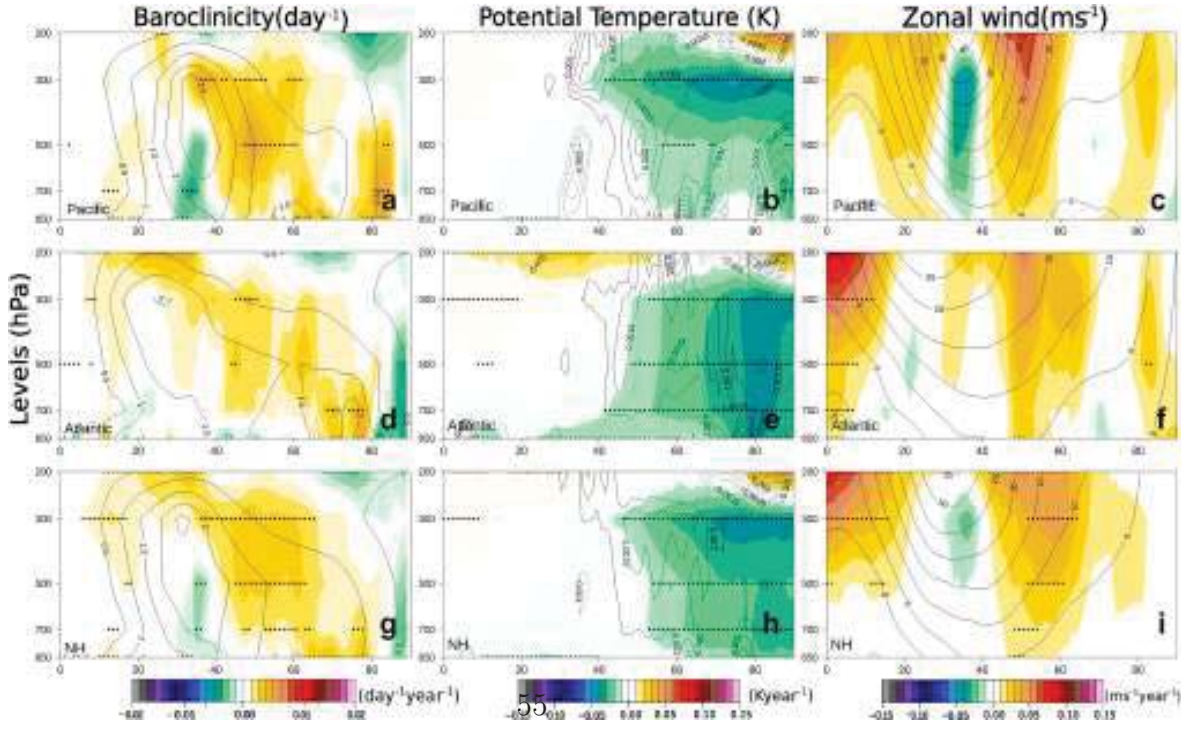

Fig. 6 Same as Fig. 5 but for period II (1935–1980)

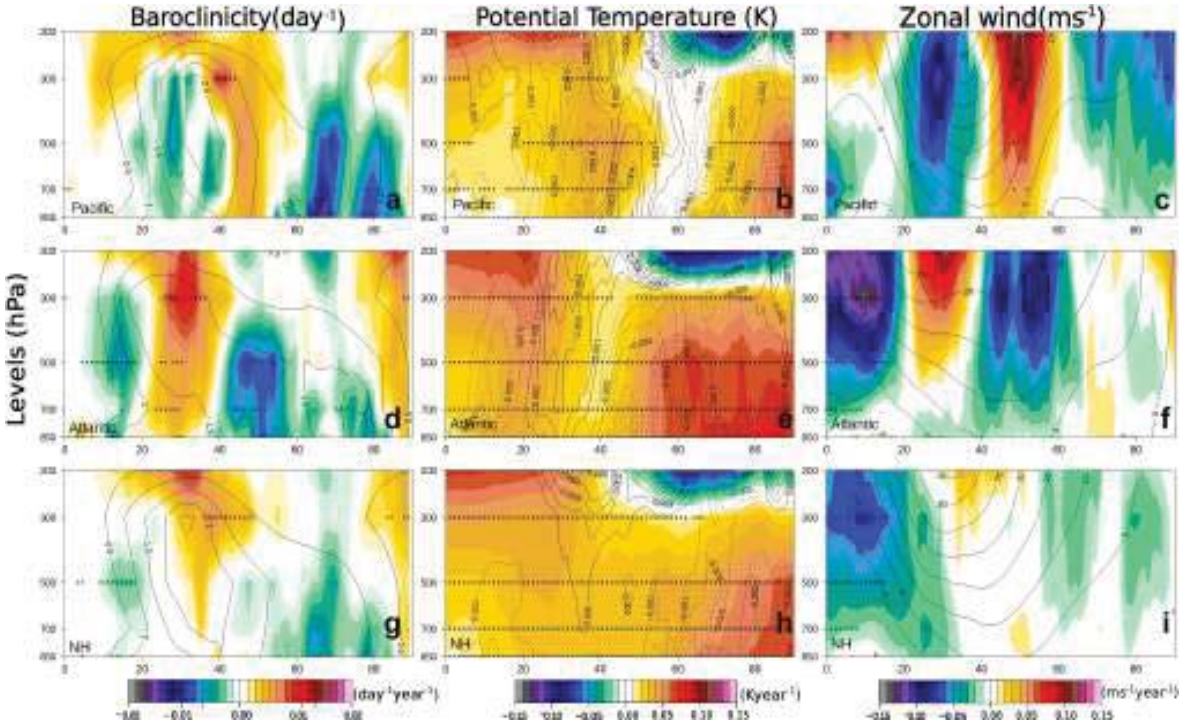

Fig. 7 Same as Fig. 5 but for period III (1980–2010)

Alaska but in a region of weak mean baroclinicity and small-amplitude eddies and this should not affect the storm-track. The poleward-shifted baroclinicity near 40°N is mainly due to a warming there (Fig. 7b) and provides an explanation for the north-eastward shift of the storm-track related parameters (Figs. 1d, 2c, f). There is consistently a clear poleward shift of the westerlies. This is coherent with an increase in intensity of the PAC jet stream at the same location observed by Barton and Ellis (2009).

In the ATL region, nevertheless, significant negative tendencies exist at mid latitudes for both the baroclinic conversion and the baroclinicity (Figs. 4c, f, 7d), while positive trends are observed further north and south of the storm-track latitudes, mostly for the baroclinicity. Temperature profiles show the occurrence of a tropical upper-level warming together with a polar lower-level warming (Fig. 7e) that do impact the baroclinicity and the position and strength of the jet and the storm-track. The tropical upper-level warming induces a baroclinicity increase near 30°N while the high-latitude lower-level warming decreases the baroclinicity in storm-track latitudes. The latter decrease probably explains the diminished storm-track eddy activity in the eastern North Atlantic (Figs. 1d, 2c, f). The eddy-driven jet located between 40°N and 60°N is also decreasing in intensity because of the weakening of the storm track (Fig. 7i).

As in period I, the PAC and ATL tendencies largely compensate each other and the NH tendencies are rather weak (Fig. 7g–i). But the positive temperature trends are more intense, extend more to upper levels and cover more southernmost latitudes than in period I.

4.4 Synthesis

The following section presents a synthesis of the previous results. Figure 8 presents the time evolution of the Northern Hemisphere yearly-mean baroclinicity at different levels together with the vertical average. Linear trends are computed and highlighted (solid straight lines) when significant. For period I, the upper-level baroclinicity has a significant positive trend (red line in Fig. 8), while the low-level baroclinicity (at 850 and 700 hPa) shows significant negative tendencies (green and orange lines of Fig. 8). The vertically-averaged baroclinicity does not present any significant trend. For period II, the yearly-mean baroclinicity increases and has significant positive trends for all levels (except at 850 hPa), including the vertically-averaged baroclinicity (black line in Fig. 8). Finally, during period III, the baroclinicity increases at upper levels and decreases at lower levels, similar to period I.

Figure 9a shows the time evolution of normalized values of yearly (dashed lines) and 11-year running mean (solid

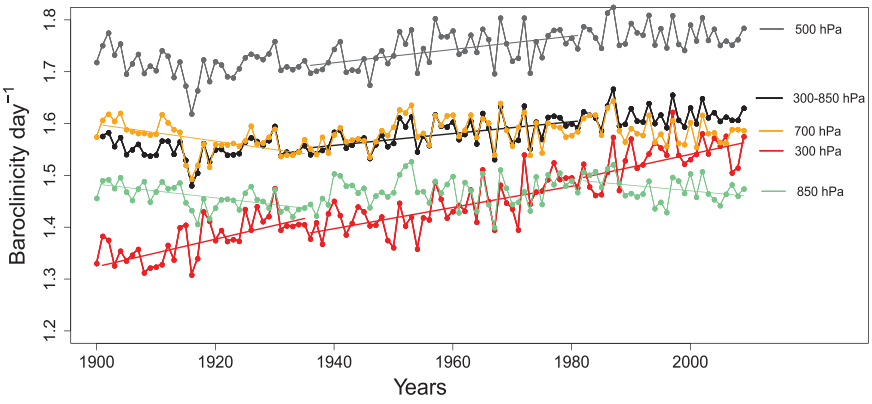

Fig. 8 Time evolution of the Northern Hemisphere baroclinicity (units: day^{-1}) for various vertical levels (color) and the vertical average between 300 and 850 hPa (black)

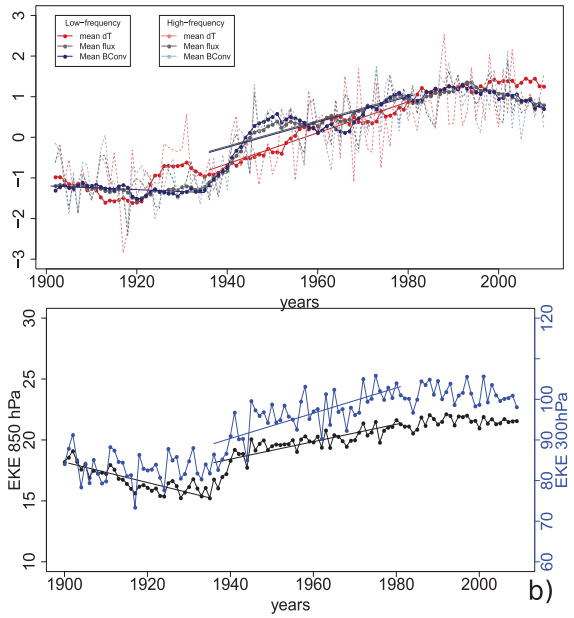

Fig. 9 Top: Northern Hemisphere scaled values of yearly (dashed-blue) and 11-years run-mean (blue) of baroclinicic conversion, yearly (dashed-red) and 11-years run-mean (red) modulus of the horizontal gradient of temperature, yearly (dashed-grey) and 11-years run-mean (grey) modulus of the horizontal mean heat fluxes. Bottom: yearly-mean eddy kinetic energy at 850 hPa (black) and 300 hPa (blue) in the Northern Hemisphere

lines) of the vertical-averaged baroclinic conversion (blue) and its two main components, the magnitude horizontal heat fluxes ($1/\sqrt{S}\sqrt{\overline{\theta' u'}^2 + \overline{\theta' v'}^2}$) in grey and baroclinicity in red (σ_{BC}, Eq. 1).

All parameters show a general positive trend from the 40s up to late 80s However, the baroclinic conversion (black lines of Fig. 9a) is more in phase with the magnitude of the heat fluxes (grey lines of Fig. 9a) than with the baroclinicity (red lines of Fig. 9a). During period II, all the three parameters present significant positive trends together with the eddy kinetic energy at lower and upper levels (Fig. 9b). Period I is marked by significant negative trends for the baroclinic conversion and the lower-level eddy kinetic energy but not for the other parameters of Fig. 9. A particular rapid increase between late 30s and early 40s is visible for all the variables that include quadratic measures of the high-frequency eddies (eddy heat fluxes, eddy kinetic energy and baroclinic conversion) but this is much less visible for the baroclinicity. A deeper analysis show that this rapid increase in eddy-related fields happens in the PAC region and is accompanied by a rapid increase in horizontal temperature gradient though a much less rapid increase in baroclinicity due to the negative trend in the stratification parameter in presence of a strong cooling in the high latitudes near the surface (see supplementary material). To conclude, systematic and significant positive trends are found during period II for all variables measuring the intensity of eddy activity. It is consistently accompanied by a global increase in baroclincity even though some disagreements between the eddy-related parameters and the baroclinicity may appear during specific shorter periods. The purpose of next section is to interpret these changes in baroclinicity and baroclinic conversion especially by looking at the ocean multi-decadal variability.

5 Link with ocean variability

Since significant multi-decadal variability is found in the reanalyses, the role of the ocean variability must be questioned. The AMO index (red line in Fig. 11a) is negative during the beginning of the century and becomes positive at the end of period I, being consistent with SST positive trends during period I (Fig. 10b). Between 1930 and 1950, AMO stays in its warm phase and rapidly shifts to a cold phase between 1960 and 1975, in agreement also with SST negative trends observed in Fig. 10c. After the 90's, SST trends become again strong and positive, showing an

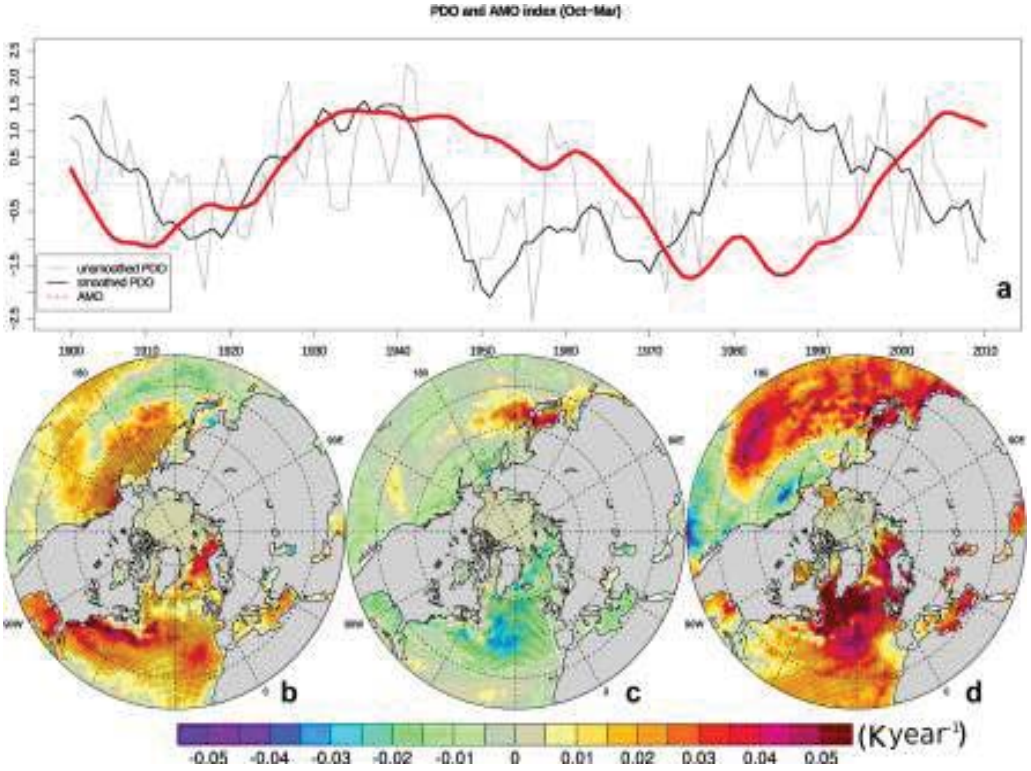

Fig. 10 **a** Twentieth century PDO/AMO indexes (continuous/dotted lines), spacial trends in SST for periods **b** I, **c** II and **d** III. Dotted grid points represent significant values with a minimum 95% confidence

AMO inversion from its extreme negative phase to a positive phase. Changes in the SST trend may have a dramatic impact on the storm-track since it can increase or reduce the low-level atmospheric temperature gradients and then the baroclinicity (Nakamura and Shimpo 2004).

During period I, the PDO index (black and grey line on Fig. 10a) has a minimum negative value in the mid 10s, and two maxima in early 1900 and in the mid 30s. Hence, there is no specific PDO trend during period I. Then, during period II, the PDO abruptly shifts from a strong positive phase in mid 30s to a strong negative phase in early 50s that lasts until the 70s and turns positive again until the late 80s. Hence, the SST trends of period II are well marked by the negative-minus-positive PDO anomalies (Fig. 10c). During period III, it decreases again from the peak in late 80s. Therefore, the two most important changing points of the PDO time series (1930 and 1980) go in agreement with the three periods defined for this article. But because period II is characterized by first an abrupt positive-to-negative PDO transition in the 40s and then an abrupt positive-to-negative AMO transition in the early 1970s, the period is split into two sub-periods: period IIa from 1935 until 1957 and period IIb from 1957 to 1980. Our hypothesis is that for period IIa, it is mainly the PAC region which drives storm-track dynamics while for period IIb, it is mainly the ATL region. The next paragraphs aims at validating this hypothesis.

In the beginning of sub-period IIa, the PDO is positive and rapidly decreases. The cooler (warm) waters in central (north-east) PAC are then replaced by warm (cool) water. This is observed in SST trends shown in Fig. 11a and is more obvious than for the whole period II (Fig. 10c). At the very end of sub-period IIb, PDO changes again to positive phase and the SST pattern drives away from the previous pattern. In the ATL region, the transition from positive to negative AMO phase starts at the end of IIa and mainly occurs during IIb. The negative trends in SST are then more obvious in IIb, especially in a rather large area located south of Iceland near 60°N (Fig. 11b). There are also some positive trends in a narrower area along the east coast of the US in the Gulf Stream region.

Computation of the baroclinic conversion and baroclinicity for the two sub-periods confirms that PAC and ATL play a key role in storm-track dynamics for sub-periods IIa and IIb respectively (Fig. 11c–f). During IIa, when the PDO rapidly shifts toward its negative phase, the baroclinic conversion and baroclinicity increase north and decrease south of their peak amplitudes in PAC, consistent with SST gradient changes. Baroclinicity increase to the north covers a larger

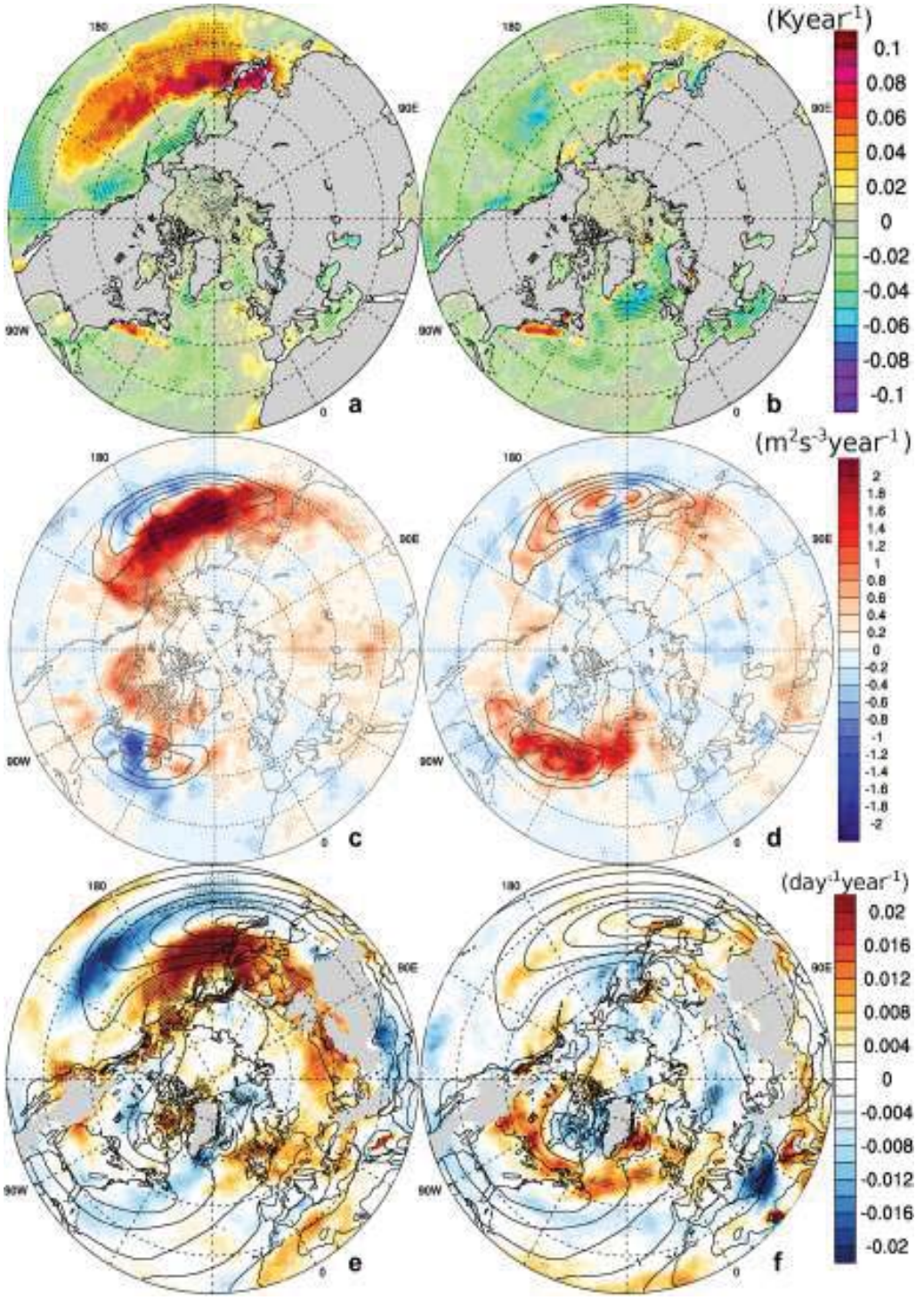

Fig. 11 **a**, **b** Sea surface temperature, **c**, **d** baroclinic conversion and **e**, **f** baroclinicity trends for (left column) period IIa and (right column) period IIb. Contours represent the mean field of the variable for each period in the same units as the trends (contour intervals of 25 m^2s^{-3} and 0.5 day^{-1} for baroclinic conversion and baroclinicity respectively). Dotted grid points represent significant values with a minimum 95% confidence

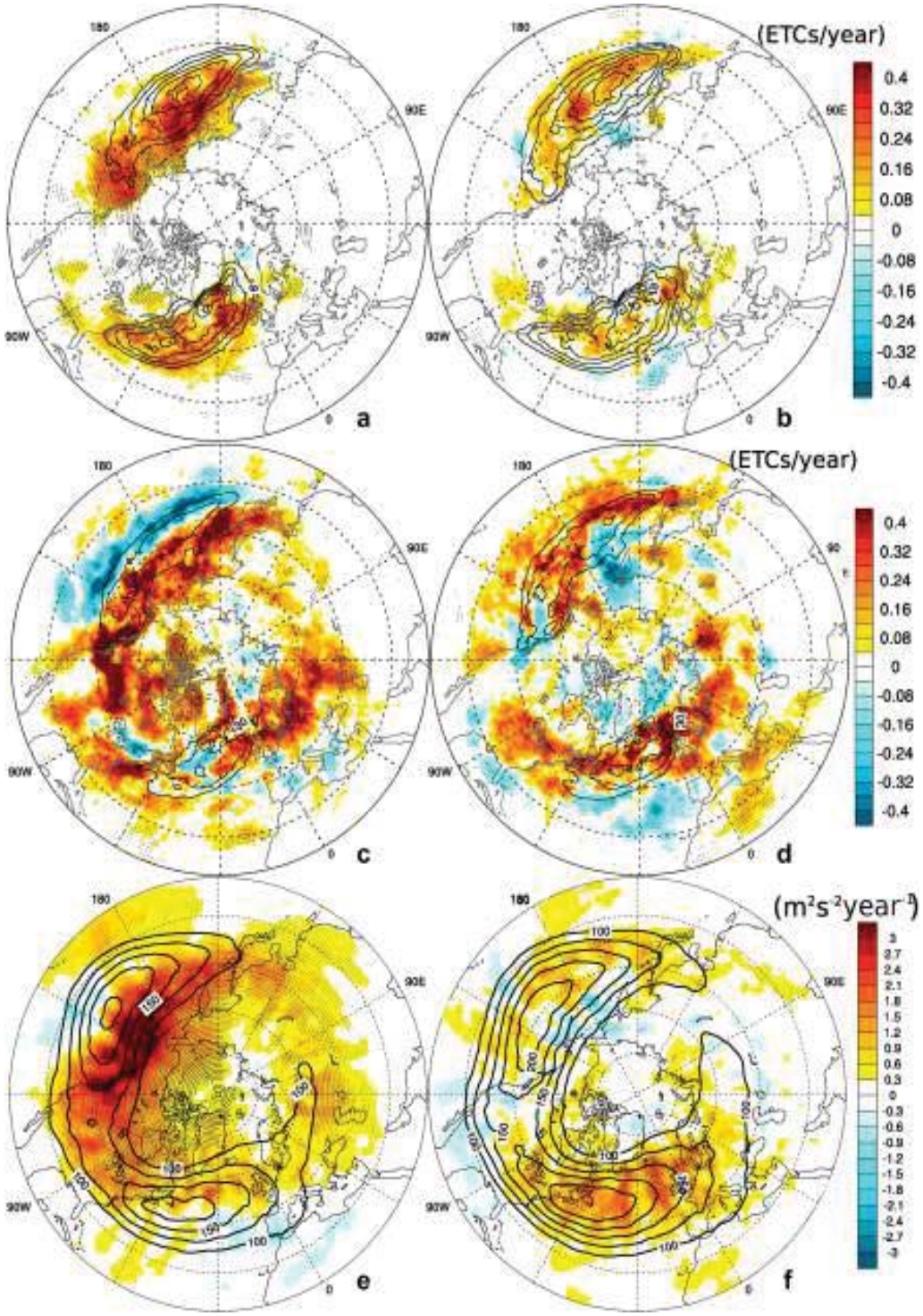

Fig. 12 Same as Fig. 10 but for **a**, **b** *Strong* ETCs **c**, **d** *All* ETCs and **e**, **f** 300 hPa EKE trends

area than the decrease to the south. Baroclinic conversion globally intensifies in PAC (Fig. 11c). This probably explains the strong increase in *Strong* ETC frequencies (Fig. 12a) and 300-hPa EKE (Fig. 12e) in PAC. Interestingly, the *All* ETC frequencies (Fig. 12c) exhibit a poleward-shifted storm-track while the *Strong* ETC frequencies (Fig. 12a) undergo an increase over all PAC regions showing that *Moderate* and *Strong* cyclones do not behave similarly. Generally speaking, these results go in agreement with studies that proved a good correlation between negative PDO and a northward-shifted and intensified PAC storm track (Lee et al. 2012; Sung et al. 2014; Gan and Wu 2013).

During IIa, in ATL, baroclinic conversion tendencies are positive over the Canada but there is no significant change in the baroclinic conversion intensity in the western Atlantic (Fig. 11c). Only some kind of poleward shift can be noticed. Trends in baroclinicity are non significant except over northwestern Europe (Fig. 11e). However, all diagnoses quantifying the intensity of the storm-track eddy activity show a significant positive trend in ATL during IIa (Fig. 12a, c, e). Figure 12e gives us some insights: the upper-level high-frequency eddy kinetic energy shows a large positive trend over North America. Seeding of higher-amplitude upper-level disturbances fromed in the PAC and North American area could trigger more surface cyclones in the ATL sector and might explain the positive trend in ATL storm-track intensity. Another possibility would be that the increased cyclonic activity over the ATL ocean can be attributed to more seeding of surface cyclones having their incipient and main intensification stages over Northern America and the PAC area (Penny et al. 2013) as suggested by the important trend in *All* ETC frequencies (Fig. 12c) in that region. Note in particular that the strong increase in *All* ETC frequencies over North America comes from *Moderate* ETC frequencies as it is not present in *Strong* ETC frequencies (Fig. 12a) in that region but may then trigger *Strong* cyclones further downstream in the Atlantic sector where the mean baroclinicity is the strongest.

During IIb, the opposite is verified: the baroclinic conversion and baroclinicity trends are significantly positive at mid and high latitudes in ATL while no significant tendencies are observed in PAC (Fig. 11d, f). The baroclinicity increase along a band from Newfoundland to the British Isles is consistent with the increase in SST gradient in that sector due to the trend toward negative AMO. This explains the strong positive trend of the baroclinic conversion in the beginning of period IIa together with the global intensification and poleward-shifted of the Atlantic storm track, which is particularly obvious in *All* ETC frequencies (Fig. 12d), going in agreement with studies for the same period (Wang et al. 2006; Trigo 2006). Nevertheless, in the end of period II an increase in ATL baroclinicity is observed from 1970 up to the 1985 (see supplementary material), when the AMO stops decreasing. A deeper analysis shows that there is still an increase in SST gradient in agreement with an increase in the low-level and vertically-averaged baroclinicity during that period (see supplementary material). Hence, there are SST anomalies that may have influenced the ATL storm-track that are not associated with a variation of the AMO index. In PAC, there is no important change in baroclinic conversion and baroclinicity compared to ATL (Fig. 11d, f). Some increase can be however noticed in eastern Asia or more downstream in mid-latitudes and may explain why the PAC storm-track is more intense in its core region. Some decrease in both the baroclinic conversion and baroclinicity appears more poleward, especially near the Kamchatka peninsula, which could explain the reduction in storm-track activity in that particular region as inferred from Fig. 12b, d, f.

6 On the potential impact of the non-homogeneous assimilated observations

Even though a good agreement is found between storm tracks, baroclinicity and large scale modes of variability, the impact of the increasing density of observations assimilated in the reanalysis on the trends observed in Fig. 1 must be assessed. In this perspective, we compare some diagnosis results between ERA20C and member 0 of ERA20CM (Hersbach et al. 2015), which is forced by the same SSTs and does not assimilate atmospheric observations. Figure 13a shows the number of all detected vorticity maxima without any threshold for ERA-20C and without considering the tracking algorithm. Such a number does not present any significant trend for any of the three periods. It therefore suggests there is no heterogeneity in the response to the increase in observation density in the reanalysis. In contrast, when only vorticity maxima greater than $2f_0$ are considered, a general increase is found in ERA-20C during period II as shown in Fig. 13b. This is consistent with the increased number of moderate-to-deep cyclone trajectories shown in Fig. 1a. Therefore, the detected trends for period II are only valid for cyclones having a significant amplitude. Another insight about the effect of assimilation is shown in Fig. 13c, which is the same diagnosis as Fig. 13b, but applied to ERA-20CM. The number of detected vorticity maxima is almost twice higher in ERA-20CM than in ERA-20C during the whole Century and even during period I when observations assimilated in ERA-20C are much fewer. Hence, during period I, the observations have already an important impact on the number of vorticity maxima but it is not clear if they constrain the atmospheric variables in the right way or not. To conclude, unlike the commonly accepted rationale, the addition of a great number of observations into the assimilation

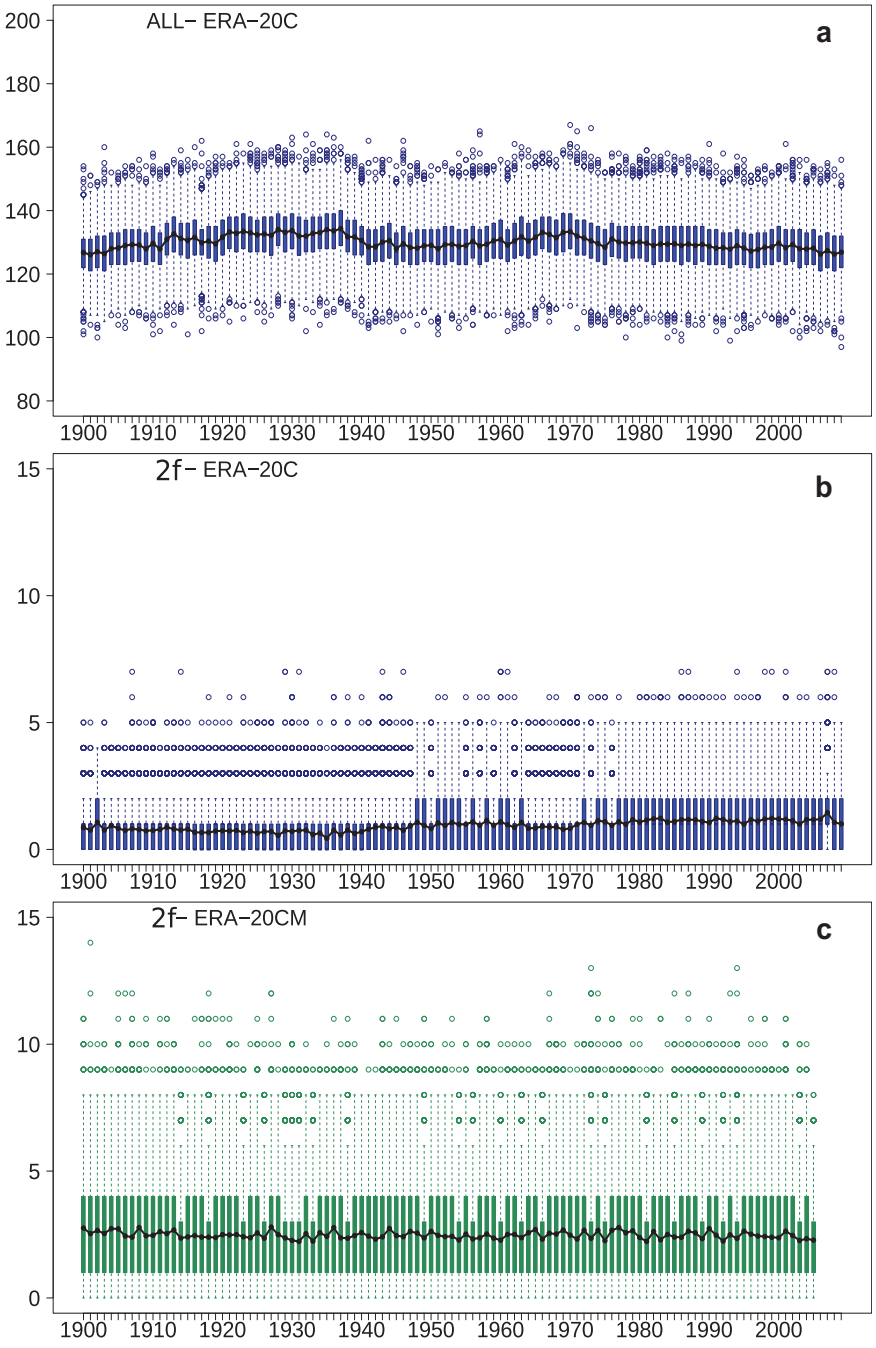

Fig. 13 Time evolution of the pdfs of vorticity maxima in the Northern Hemisphere (20° N–90°N;180°W–180°E) for **a** all maxima in ERA-20C, **b** all maxima greater than $2f_0$ in ERA-20C, **c** same as **b** but in ERA-20CM (member 0). Black line: yearly-mean number of vorticity maxima detected in a radius of 225 km; colors rectangles: inter-quantile distribution of the number of vorticity maxima found every year using 3-hourly data

process does not lead to an increase in the number of vorticity maxima. Thus, the relationship between cyclonic activity and observation density is, for this reason, less trivial than expected.

When comparing ERA-20C with ERA-20CM, it is important to note that there is no trend in ERA-20CM which is not really surprising as the large-scale atmospheric variability significantly differs from ERA-20C (Poli et al. 2016, see e.g., the NAO index in their Fig. 7c). It is not clear how this AMIP simulation accurately represents the response of the baroclinicity to SST AMO/PDO phase variations and further studies would be needed to investigate this particular aspect.

Further insights on the impact of the increased number of observations and the potential biases of ERA-20C can be gained when comparing to other reanalysis datasets during the second half of the 20th century (Wang et al. 2016; Chang

and Yau 2016). These studies emphasized that large inhomogeneities between the reanalysis datasets appear when the number of assimilated observations is small. One example is the Southern Hemisphere during the recent period when non satellite-derived observations were sparse. In this case, results of ERA-20C, (which does not include satellite-derived observations) are questioned. One may think that the NH Pacific in the early period can be thought of as being analogous to the Southern Hemisphere in the recent period in ERA-20C as it also has a limited number of observations. Moreover, the magnitude of the detected trend found in ERA-20C during the second period should be questioned as the previously two studies showed that ERA-20C presents stronger trends than in other reanalysis. It is almost twice higher for deep-cyclones when compared with 20CR in the entire century (Wang et al. 2016) and in general higher than other reanalysis as JRA55 for the period 1959–2010 (Chang and Yau 2016). The reader is referred to the previously cited papers for further information.

7 Conclusion

Mid-latitude wintertime cyclone variability during the Twentieth Century and over the Northern Hemisphere has been analysed by applying a cyclone tracking algorithm to ERA-20C reanalysis datasets. Three main periods have been distinguished and studied separately. We have observed that periods between 1900 and 1935 (period I) and between 1980 and 2010 (period III) were characterized by non-significant trends in ETCs in the NH whereas that between 1935 and 1980 (period II) was characterized by a significant positive trend.

Even though periods I and III are quite different, they bring some similarities: both were marked by an increase in polar temperatures and sea-ice loss, which was more pronounced and covering higher levels and lower latitudes in period III (Harvey et al. 2013; Woollings et al. 2014; Barnes and Polvani 2015; Polyakov and Johnson 2000; Yamanouchi 2011). It led to a reduction in the meridional gradients of temperature and consequently in the mid-latitude baroclinicity (Barnes and Polvani 2015) of the lower troposphere. In contrast, in the upper troposphere, the mid-latitude temperature gradients mainly increased during these two periods due to tropical warming (mainly for period III) and polar cooling near 200–300 hPa. These opposite tendencies of temperature gradients in the lower and upper troposphere are similar to those predicted by future climate scenarios. These tendencies exert opposite influences on storm-track and the net effect is quite uncertain (Butler et al. 2010; Rivière 2011; Shaw et al. 2016) as confirmed in the present study where no global trends were found during periods I and III.

However, more regional changes in the temperature gradients were found. For period I, there was a significant reduction in the North Pacific storm-track eddy activity and westerly jet intensity, especially on the southward flank of their climatological maximum values, which is a consequence of a strong decrease in baroclinicity further south. Over the ATL, no significant changes were noticed. For period III, the North Pacific storm-track shows a northeastward shift, a slight global increase in the various storm-track quantities, which can be attributed to a strong increase in the baroclinicity further north. The latter is probably due to a shift toward the negative phase of the PDO which increased the SST gradient on the northeastern side of the North Pacific basin. This is coherent with an increased intensity of the North Pacific jet stream at the same location (Barton and Ellis 2009). During period III, in the North Atlantic, the baroclinicity conversion significantly decreased in the core region and baroclinicity decreases on the northern flank of its climatological maximum value and increases on its southern flank. It led to an overall decrease in storm-track intensity at middle latitudes. This can be first attributed to the Arctic sea-ice reduction and Arctic warming, which decreases the temperature gradient at low levels. This result is consistent with the studies showing a negative NAO trend response to Arctic warming (Bader et al. 2011; Cohen et al. 2014; Nakamura et al. 2015; Oudar et al. 2016). This can be also attributed to a shift toward the positive phase of the AMO during that period which tends to shift the NAO toward its negative phase and decrease the storm-track intensity (Peings and Magnusdottir 2014; Peings et al. 2016).

Period II, between 1935 and 1980, was characterized by an increased intensity of both the North Pacific and North Atlantic storm tracks as measured by high-pass eddy kinetic energy and ETCs diagnostics. This positive trend can be explained by colder temperatures north of 50°N in connection with more ice cover (Box et al. 2009; Kinnard et al. 2008) that causes the meridional temperature gradient to homogeneously increase over the whole troposphere. Period II was marked by rapid shifts, first toward the negative phase of the PDO between 1935 and 1957 (period IIa), and then toward the negative phase of the AMO between 1957 and 1980 (period IIb). The shift toward the negative phase of the PDO in period IIa is responsible for the warming of the North Pacific ocean between 30°N and 45°N leading to strong increase in SST gradients and baroclinicity north of 45°N. In contrast, the decreased baroclinicity to the south of the Pacific warming is less important and extends over a smaller area. There is thus a poleward shift, together with an overall intensification, of the SST gradient, the baroclinicity and baroclinic conversion which explain the increased frequency of moderate-to-strong ETCs. The intensification of the North Pacific storm-track creates more upstream seeding of the North Atlantic storm-track. This may explain

why the ATL storm-track increases despite the fact that the baroclinicity and baroclinic conversion in the North Atlantic sector have no significant changes. During the second subperiod between 1957 and 1980, it is mainly the Atlantic sector which exhibits the strongest changes in SST gradient, baroclinicity and baroclinic conversion because of the shift toward the negative AMO phase. Similarly to the PDO structure, the transition toward the negative AMO phase creates an increase of all these quantities on the northern flank of their climatological maximum values and a decrease on the southern flank with the former increase being more intense than the latter decrease. For these reasons, the Atlantic storm-track therefore shifted poleward and mainly intensified between 1957 and 1980. Despite an overall intensification of the Pacific storm-track during the same subperiod, it cannot be attributed to well-marked changes of baroclinicity and baroclinic conversion in that region. One possibility is the stronger upstream seeding from the Atlantic storm-track but the signal does not seem to be very strong.

Some general conclusions about the impact of the AMO and PDO on storm-track dynamics can be deduced from the present study. The negative (positive) phases of the AMO and PDO tends to intensify (decrease) and shift poleward (equatorward) the baroclinicity, baroclinic conversion and storm-track quantities of the North Atlantic and North Pacific sectors respectively. This confirms other studies on the topic (Peings and Magnusdottir 2014; Peings et al. 2016; Gan and Wu 2013). This may explain why period III which is marked by a negative PDO trend and a positive AMO trend show opposite tendencies in the Pacific and Atlantic sectors and there is no net change in storm-track dynamics over the whole hemisphere. In contrast, period II is well marked by negative trends in both PDO and AMO indexes that create a net intensification of the Northern Hemisphere storm tracks. To conclude, multi-decadal variabilities during the 20th century of the storm-track and baroclinicity are closely connected and largely depends on decadal oceanic variability patterns as the AMO and PDO. For some periods as periods I and III, the Pacific and Atlantic response is not the same and even tend to oppose to each other which means that hemispheric analysis may not be enough to take general conclusions about the storm-tracks. In contrast, for period II, the tendencies of the two regions tend to add to each other. Of course, this is a quite general picture and the basic knowledge of the PDO and AMO indexes is not enough to understand the structure of the SST anomalies and their impact on the atmosphere as seen for instance in the North Atlantic case at the end of period IIb (supplementary material).

Other general statements can be made about the impact of global warming on storm-track dynamics. First, we found an overall reduction in the Atlantic storm-track activity and a poleward-shift and intensification of the Pacific storm track during period III, consistent with Wang et al. (2017). Our interpretation is mainly based on the transitions toward negative PDO and positive AMO, but the role of these multi-decadal modes of ocean variability should be separated from that of the Arctic amplification to quantitatively assess their impacts in future studies. Another statement can be made about the vertical structure of the trends under global warming. Despite a rapid warming of the polar regions in period III after the 1980s, the decrease in the horizontal temperature gradients and the baroclinicity is rather confined to the lower troposphere and its effect seems to be partly compensated by that of the increased upper-tropospheric temperature gradients. This is to be contrasted with period II between 1935 and 1980 where the moderate cooling in polar regions extends from the surface to the upper troposphere and more homogeneously increases the horizontal temperature gradients in mid-latitudes. As such, the effect of this moderate polar cooling on storm-track appears to be more important. Hence, the effect of polar temperature anomalies on storm-track strongly depends on their spatial patterns and how they extend over the whole troposphere. This should be kept in mind when considering the storm-track response to global warming.

Finally, we have discussed the time inhomogeneity on the amount of observations in ERA-20C. An observation-related trend potentially exists in long-term reanalysis datasets as mentioned by some authors and an overestimation of the period II ETC's positive trends could be a consequence. A comparison between ERA-20C and ERA-20CM was made in order to compare the corresponding trends. Despite to what could be expected from an increased number of assimilated observations, the total number of vorticity maxima detected in ERA-20C does not increase with time. Furthermore, the number of vorticity maxima is in general higher in ERA-20CM than in ERA-20C. The data assimilation system in the presence of dense observations networks can reduce the synoptic activity when the free model does produce too much spurious cyclones. Its real effect is less trivial then expected and could not be fully addressed without further studies. Finally, even though the use of long-term reanalysis must be done with caution, we have shown that conclusive and coherent results can be extracted from this data, regardless the time inhomogeneity of the observations. First, some of these trends are consistent with those found in recent studies: the increase in cyclone counts from ERA-20C reanalyses (Chang and Yau 2016), the generalised cold tropospheric and SST temperatures (Box et al. 2009; Kinnard et al. 2008) and the increased jet strength (Woollings et al. 2014; Barton and Ellis 2009) during period II. Second, we have shown that the ETC trends are consistent with trends in other storm-track diagnostics and, more importantly, can be explained by variations in baroclinicity and large-scale modes of climate variability. The link found between the

synoptic eddy variability and the large-scale baroclinicity is not fully conclusive in itself as both fields might have biases/errors that go together. However, the fact that we also found a link with the rather well-documented 20th century multi-decadal ocean variations gives us more reliability on the sign of the detected trends despite the inhomogeneity of the assimilated observations. Still, one should keep in mind that only a qualitative analysis is made in this study. Even though the positive trend in the middle century is in agreement with several large-scale modes of climate variability, ERA-20C presents trends that are higher than other reanalysis (Chang and Yau 2016), that were not quantitatively explained here. For this reason we cannot exclude a possible overestimation of the trends due inhomogeneity of the assimilated observations, particularly in the middle century.

References

Ayrault F (1998) Environnment, structure et évolution des dépressions météorologiques: réalité climatologique et modèles types. Doctoral Dissertation. Universite Paul Sabatier, Meteo-France, Centre National de Recherches Météorologiques

Ayrault F, Joly A (2000) The genesis of mid-latitude cyclones over the Atlantic Ocean: a new climatological perspective. C R Acad Sci Paris Earth Planet Sci 330:173–178

Bader J, Mesquita MD, Hodges KI, Keenlyside N, Sterhus S, Miles M (2011) A review on Northern Hemisphere sea-ice, storminess and the North Atlantic oscillation: observations and projected changes. Atmos Res 101(4):809–834. https://doi.org/10.1016/j.atmosres.2011.04.007

Barnes EA, Polvani LM (2015) CMIP5 projections of Arctic amplification, of the North American/North Atlantic circulation, and of their relationship. J Clim 28(13):5254–5271. https://doi.org/10.1175/JCLI-D-14-00589.1

Barnes EA, Screen JA (2015) The impact of Arctic warming on the midlatitude jet-stream: can it? Has it? Will it?: impact of Arctic warming on the midlatitude jet-stream. Wiley Interdiscip Rev Clim Change 6(3):277–286. https://doi.org/10.1002/wcc.337

Barton NP, Ellis AW (2009) Variability in wintertime position and strength of the North Pacific jet stream as represented by re-analysis data. Int J Climatol 29:851–862. https://doi.org/10.1002/joc.1750

Bengtsson L (2004) Can climate trends be calculated from reanalysis data? J Geophys Res. https://doi.org/10.1029/2004JD004536

Bengtsson L, Hodges KI, Roeckner E (2006) Storm tracks and climate change. J Clim 19(15):3518–3543. https://doi.org/10.1175/JCLI3815.1

Blackmon ML, Wallace JM, Lau NC, Mullen SL (1977) An observational study of the Northern Hemisphere wintertime circulation. J Atmos Sci 34(7):1040–1053. https://doi.org/10.1175/1520-0469(1977)034<1040:AOSOTN>2.0.CO;2

Box JE, Yang L, Bromwich DH, Bai LS (2009) Greenland ice sheet surface air temperature variability: 1840–2007. J Clim 22(14):4029–4049. https://doi.org/10.1175/2009JCLI2816.1

Bromwich DH, Fogt RL, Hodges KI, Walsh JE (2007) A tropospheric assessment of the ERA-40, NCEP, and JRA-25 global reanalyses in the polar regions. J Geophys Res. https://doi.org/10.1029/2006JD007859

Butler A, Thompson D, Heikes R (2010) The steady-state atmospheric circulation response to climate change-like thermal forcings in a simple general circulation model. J Clim 23:3474–3496. https://doi.org/10.1175/2010JCLI3228.1

Cattiaux J, Cassou C (2013) Opposite CMIP3/CMIP5 trends in the wintertime northern annular mode explained by combined local sea ice and remote tropical influences. Geophys Res Lett 40:3682–3687. https://doi.org/10.1002/grl.50643

Cattiaux J, Vautard R, Cassou C, Yiou P, Masson-Delmotte V, Codron F (2010) Winter 2010 in Europe: a cold extreme in a warming climate. Geophys Res Lett 37:L20704. https://doi.org/10.1029/2010GL044613

Chang EKM (2007) Assessing the increasing trend in Northern Hemisphere winter storm track activity using surface ship observations and a statistical storm track model. J Clim 20(22):5607–5628. https://doi.org/10.1175/2007JCLI1596.1

Chang EKM, Fu Y (2002) Interdecadal variations in Northern Hemisphere winter storm track intensity. J Clim 15(6):642–658. https://doi.org/10.1175/1520-0442(2002)015<0642:IVINHW>2.0.CO;2

Chang EKM, Fu Y (2003) Using mean flow change as a proxy to infer interdecadal storm track variability. J Clim 16:2178–2196

Chang EKM, Yau AMW (2015) Northern Hemisphere winter storm track trends since 1959 derived from multiple reanalysis datasets. Clim Dyn 47(5–6):1435–1454. https://doi.org/10.1007/s00382-015-2911-8

Chang EKM, Yau AMW (2016) Northern Hemisphere winter storm track trends since 1959 derived from multiple reanalysis datasets. Clim Dyn 47(5):1435–1454. https://doi.org/10.1007/s00382-015-2911-8

Chang EKM, Lee S, Swanson KL (2002) Storm track dynamics. J Clim 15(16):2163–2183. https://doi.org/10.1175/1520-0442(2002)015<02163:STD>2.0.CO;2

Chang EKM, Guo Y, Xia X (2012) CMIP5 multimodel ensemble projection of storm track change under global warming. J Geophys Res Atmos 117(D23):D23,118. https://doi.org/10.1029/2012JD018578

Cohen J, Screen JA, Furtado JC, Barlow M, Whittleston D, Coumou D, Francis J, Dethloff K, Entekhabi D, Overland J, Jones J (2014) Recent arctic amplification and extreme mid-latitude weather. Nat Geosci 7:627–637. https://doi.org/10.1038/ngeo2234

Compo GP, Whitaker JS, Sardeshmukh PD, Matsui N, Allan RJ, Yin X, Gleason BE, Vose RS, Rutledge G, Bessemoulin P, Brnnimann S, Brunet M, Crouthamel RI, Grant AN, Groisman PY, Jones PD, Kruk MC, Kruger AC, Marshall GJ, Maugeri M, Mok HY, Nordli Ross TF, Trigo RM, Wang XL, Woodruff SD, Worley SJ (2011) The twentieth century reanalysis project. Q J R Meteorol Soc 137(654):1–28. https://doi.org/10.1002/qj.776

Corti S, Molteni F, Palmer T (1999) Signature of recent climate change in frequencies of natural atmospheric circulation regimes. Nature 398:799–802. https://doi.org/10.1038/19745

Dell'Aquila A, Corti S, Weisheimer A, Hersbach H, Peubey C, Poli P, Berrisford P, Dee D, Simmons A (2016) Benchmarking Northern Hemisphere midlatitude atmospheric synoptic variability in centennial reanalysis and numerical simulations. Geophys Res Lett 43(10):5442–5449. https://doi.org/10.1002/2016GL068829

Enfield DB, Mestas-Nuez AM, Trimble PJ (2001) The Atlantic multidecadal oscillation and its relation to rainfall and river flows in the continental US. Geophys Res Lett 28(10):2077–2080. https://doi.org/10.1029/2000GL012745

Gan B, Wu L (2013) Seasonal and long-term coupling between wintertime storm tracks and sea surface temperature in the North Pacific. J Climate 26(16):6123–6136. https://doi.org/10.1175/JCLI-D-12-00724.1

Gastineau G, Frankignoul C (2015) Influence of the North Atlantic SST variability on the atmospheric circulation during the twentieth century. J Clim 28:1396–1416. https://doi.org/10.1175/JCLI-D-14-00424.1

Geng Q, Sugi M (2003) Possible change of extratropical cyclone activity due to enhanced greenhouse gases and sulfate aerosols—study with a high-resolution AGCM. J Clim 16(13):2262–2274. https://doi.org/10.1175/1520-0442(2003)16<2262:PCOEECA>2.0.CO;2

Gomara I, Rodriguez-Fonseca B, Zurita-Gotor P, Ulbrich S, Pinto JG (2016) Abrupt transitions in the NAO control of explosive North Atlantic cyclone development. Clim Dyn 47:3091–3111. https://doi.org/10.1007/s00382-016-3015-9

Graham NE, Diaz HF (2001) Evidence for intensification of North Pacific winter cyclones since 1948. Bull Am Meteorol Soc 82(9):1869–1893. https://doi.org/10.1175/1520-0477(2001)082<1869:EFIONP>2.3.CO;2

Gulev SK, Zolina O, Grigoriev S (2001) Extratropical cyclone variability in the Northern Hemisphere winter from the NCEP/NCAR reanalysis data. Clim Dyn 17(10):795–809. https://doi.org/10.1007/s003820000145

Harvey BJ, Shaffrey LC, Woollings TJ (2013) Equator-to-pole temperature differences and the extra-tropical storm track responses of the CMIP5 climate models. Clim Dyn 43(5–6):1171–1182. https://doi.org/10.1007/s00382-013-1883-9

Hersbach H, Peubey C, Simmons A, Berrisford P, Poli P, Dee D (2015) ERA-20cm: a twentieth-century atmospheric model ensemble: the ERA-20cm ensemble. Quart J R Meteorol Soc 141(691):2350–2375. https://doi.org/10.1002/qj.2528

Hoskins BJ, Hodges KI (2002) New perspectives on the Northern Hemisphere winter storm tracks. J Atmos Sci 59(6):1041–1061. https://doi.org/10.1175/1520-0469(2002)059<1041:NPOTNH>2.0.CO;2

Hoskins BJ, Valdes PJ (1990) On the existence of storm-tracks. J Atmos Sci 47(15):1854–1864. https://doi.org/10.1175/1520-0469(1990)047<1854:OTEOST>2.0.CO;2

Kinnard C, Zdanowicz CM, Koerner RM, Fisher DA (2008) A changing Arctic seasonal ice zone: observations from 1870–2003 and possible oceanographic consequences. Geophys Res Lett. https://doi.org/10.1029/2007GL032507

Krueger O, Schenk F, Feser F, Weisse R (2013) Inconsistencies between long-term trends in storminess derived from the 20cr reanalysis and observations. J Clim 26(3):868–874. https://doi.org/10.1175/JCLI-D-12-00309.1

Lee SS, Lee JY, Wang B, Ha KJ, Heo KY, Jin FF, Straus DM, Shukla J (2012) Interdecadal changes in the storm track activity over the North Pacific and North Atlantic. Clim Dyn 39(1–2):313–327. https://doi.org/10.1007/s00382-011-1188-9

L'Heureux M, Butler A, Jha B, Kumer A, Wang W (2010) Unusual extremes in the negative phase of the Arctic Oscillation during 2009. Geophys Res Lett 37:L10,704. https://doi.org/10.1029/2010GL043338

Mantua NJ, Hare SR, Zhang Y, Wallace JM, Francis RC (1997) A Pacific interdecadal climate oscillation with impacts on salmon production. Bull Am Meteorol Soc 78(6):1069–1079. https://doi.org/10.1175/1520-0477(1997)078<1069:APICOW>2.0.CO;2

McCabe GJ, Clark MP, Serreze MC (2001) Trends in Northern Hemisphere surface cyclone frequency and intensity. J Clim 14(12):2763–2768. https://doi.org/10.1175/1520-0442(2001)014<2763:TINHSC>2.0.CO;2

McDonald RE (2010) Understanding the impact of climate change on Northern Hemisphere extra-tropical cyclones. Clim Dyn 37(7–8):1399–1425. https://doi.org/10.1007/s00382-010-0916-x

Michel C, Rivière G, Terray L, Joly B (2012) The dynamical link between surface cyclones, upper-tropospheric Rossby wave breaking and the life cycle of the Scandinavian blocking. Geophys Res Lett 39(10):10806. https://doi.org/10.1029/2012GL051682

Nakamura T, Yamazaki K, Iwamoto K, Honda M, Miyoshi Y, Ogawa Y, Ukita J (2015) A negative phase shift of the winter AO/NAO due to the recent Arctic sea-ice reduction in late autumn. negative shift of AO by ARCTIC ice loss. J Geophys Res Atmos 120(8):3209–3227. https://doi.org/10.1002/2014JD022848

Nakamura TSYT H, Shimpo A (2004) Observed associations among storm tracks, jet streams and midlatitude oceanic fronts. vol Earth's climate: the ocean-atmosphere interaction. In: Wang C, Xie SP, Carton JA (eds) Geophys Monogr Ser, pp 329–345. https://doi.org/10.1029/147GM18

Neu U, Akperov MG, Bellenbaum N, Benestad R, Blender R, Caballero R, Cocozza A, Dacre HF, Feng Y, Fraedrich K, Grieger J, Gulev S, Hanley J, Hewson T, Inatsu M, Keay K, Kew SF, Kindem I, Leckebusch GC, Liberato MLR, Lionello P, Mokhov II, Pinto JG, Raible CC, Reale M, Rudeva I, Schuster M, Simmonds I, Sinclair M, Sprenger M, Tilinina ND, Trigo IF, Ulbrich S, Ulbrich U, Wang XL, Wernli H (2013) IMILAST: a community effort to intercompare extratropical cyclone detection and tracking algorithms. Bull Am Meteorol Soc 94(4):529–547. https://doi.org/10.1175/BAMS-D-11-00154.1

Oudar T, Sanhez-Gomez E, Chauvin F, Cattiaux J, Cassou C, Terray L (2016) Respective roles of direct radiative forcing and induced Arctic sea ice loss on the Northern Hemisphere atmospheric circulation. Clim Dyn. https://doi.org/10.1007/s00382-017-3541-0**(in revision)**

Paciorek CJ, Risbey JS, Ventura V, Rosen RD (2002) Multiple indices of Northern Hemisphere cyclone activity, winters 194999. J Clim 15(13):1573–1590. https://doi.org/10.1175/1520-0442(2002)015<1573:MIONHC>2.0.CO;2

Peings Y, Magnusdottir G (2014) Forcing of the wintertime atmospheric circulation by the multidecadal fluctuations of the North Atlantic ocean. Environ Res Lett 9:034018. https://doi.org/10.1088/1748-9326/9/3/034018

Peings Y, Simpkins G, Magnusdottir G (2016) Multidecadal fluctuations of the North Atlantic ocean and feedback on the winter climate in CMIP5 control simulations. J Geophys Res Atmos 121:2571–2592. https://doi.org/10.1002/2015JD024107

Penny SM, Battisti DS, Roe GH (2013) Examining mechanisms of variability within the Pacific storm track: upstream seeding and jet-core strength. J Clim 26(14):5242–5259. https://doi.org/10.1175/JCLI-D-12-00017.1

Pinto J, Ulbrich U, Leckebush GC, Spangehl T, Reyers M, Zacharias S (2007) Changes in storm track and cyclone activity in three SRES ensemble experiments with the ECHAM5/MPI-OM1 GCM. Clim Dyn 29:195–210. https://doi.org/10.1007/s00382-007-0230-4

Poli P, Hersbach H, Dee DP, Berrisford P, Simmons AJ, Vitart F, Laloyaux P, Tan DGH, Peubey C, Thpaut JN, Trmolet Y, Hlm EV, Bonavita M, Isaksen L, Fisher M (2016) ERA-20c: an atmospheric reanalysis of the twentieth century. J Clim 29(11):4083–4097. https://doi.org/10.1175/JCLI-D-15-0556.1

Polyakov IV, Johnson MA (2000) Arctic decadal and interdecadal variability. Geophys Res Lett 27(24):4097–4100. https://doi.org/10.1029/2000GL011909

Rahmstorf S, Box JE, Feulner G, Mann ME, Robinson A, Rutherford S, Schaffernicht EJ (2015) Exceptional twentieth-century slowdown in Atlantic Ocean overturning circulation. Nat Clim Chang 5(5):475–480. https://doi.org/10.1038/nclimate2554

Raible CC, Della-Marta PM, Schwierz C, Wernli H, Blender R (2008) Northern Hemisphere extratropical cyclones: a comparison of detection and tracking methods and different reanalyses. Mon Weather Rev 136(3):880–897. https://doi.org/10.1175/2007MWR2143.1

Rivière G (2011) A dynamical interpretation of the poleward shift of the jet streams in global warming scenarios. J Atmos Sci 68(6):1253–1272. https://doi.org/10.1175/2011JAS3641.1

Rivière G, Drouard M (2015) Dynamics of the northern annular mode at weekly time scales. J Atmos Sci 72:4569–4590. https://doi.org/10.1175/JAS-D-15-0069.1

Rivière G, Joly A (2006) Role of the low-frequency deformation field on the explosive growth of extratropical cyclones at the jet exit.

Part I: barotropic critical region. J Atmos Sci 63(8):1965–1981. https://doi.org/10.1175/JAS3728.1

Rivière G, Hua BL, Klein P (2004) Perturbation growth in terms of baroclinic alignment properties. Q J R Meteorol Soc 130(600):1655–1673. https://doi.org/10.1256/qj.02.223

Shaffrey L, Sutton R (2006) Bjerknes compensation and the decadal variability of the energy transports in a coupled climate model. J Clim 19(7):1167–1181. https://doi.org/10.1175/JCLI3652.1

Shaw T, Baldwin M, Barnes E, Caballero R, Garfinkel C, Hwang YT, Li C, O'Gorman P, Rivière G, Simpson I, Voigt A (2016) Storm track processes and the opposing influences of climate change. Nat Geosci 9:656–664. https://doi.org/10.1038/ngeo2783

Sinclair MR (1997) Objective identification of cyclones and their circulation intensity, and climatology. Weather Forecast 12(3):595–612. https://doi.org/10.1175/1520-0434(1997)012<0595:OIOCAT>2.0.CO;2

Sung MK, An SI, Kim BM, Woo SH (2014) A physical mechanism of the precipitation dipole in the western United States based on PDO-storm track relationship: precipitation dipole in the western US. Geophys Res Lett. https://doi.org/10.1002/2014GL060711

Theil H (1950) A rank-invariant method of linear and polynomial regression analysis. i, ii, iii. Nederl Akad Wetensch. Proc 53 130:386392

Thompson DWJ, Wallace JM (1998) The Arctic Oscillation signature in the wintertime geopotential height and temperature fields. Geophys Res Lett 25:1297–1300. https://doi.org/10.1029/98GL00950

Tilinina N, Gulev SK, Rudeva I, Koltermann P (2013) Comparing cyclone life cycle characteristics and their interannual variability in different reanalyses. J Clim 26(17):6419–6438. https://doi.org/10.1175/JCLI-D-12-00777.1

Trigo IF (2006) Climatology and interannual variability of storm-tracks in the Euro-Atlantic sector: a comparison between ERA-40 and NCEP/NCAR reanalyses. Clim Dyn 26(2–3):127–143. https://doi.org/10.1007/s00382-005-0065-9

Ulbrich U, Leckebusch GC, Pinto JG (2009) Extra-tropical cyclones in the present and future climate: a review. Theor Appl Climatol 96(1–2):117–131. https://doi.org/10.1007/s00704-008-0083-8

Wang J, Kim HM, Chang EKM (2017) Changes in Northern Hemisphere winter storm tracks under the background of Arctic amplification. J Clim 30(10):3705–3724. https://doi.org/10.1175/JCLI-D-16-0650.1

Wang XL, Swail VR, Zwiers FW (2006) Climatology and changes of extratropical cyclone activity: comparison of ERA-40 with NCEP-NCAR reanalysis for 19582001. J Clim 19(13):3145–3166. https://doi.org/10.1175/JCLI3781.1

Wang XL, Feng Y, Compo GP, Swail VR, Zwiers FW, Allan RJ, Sardeshmukh PD (2013) Trends and low frequency variability of extra-tropical cyclone activity in the ensemble of twentieth century reanalysis. Clim Dyn 40(11–12):2775–2800. https://doi.org/10.1007/s00382-012-1450-9

Wang XL, Feng Y, Chan R, Isaac V (2016) Inter-comparison of extra-tropical cyclone activity in nine reanalysis datasets. Atmos Res 181:133–153. https://doi.org/10.1016/j.atmosres.2016.06.010

Woollings T, Gregory JM, Pinto JG, Reyers M, Brayshaw DJ (2012) Response of the North Atlantic storm track to climate change shaped by ocean–atmosphere coupling. Nat Geosci 5(5):313–317. https://doi.org/10.1038/ngeo1438

Woollings T, Czuchnicki C, Franzke C (2014) Twentieth century North Atlantic jet variability. Q J R Meteorol Soc 140(680):783–791. https://doi.org/10.1002/qj.2197

Yamamoto A, Palter JB (2016) The absence of an Atlantic imprint on the multidecadal variability of wintertime European temperature. Nat Commun 7(10):930. https://doi.org/10.1038/ncomms10930

Yamanouchi T (2011) Early 20th century warming in the Arctic: a review. Polar Sci 5(1):53–71. https://doi.org/10.1016/j.polar.2010.002

Zappa G, Shaffrey LC, Hodges KI, Sansom PG, Stephenson DB (2013) A multimodel assessment of future projections of North Atlantic and European extratropical cyclones in the CMIP5 climate models. J Clim 26(16):5846–5862. https://doi.org/10.1175/JCLI-D-12-00573.1

CHAPTER IV

Measuring Windstorms - risk assessment and High-loss tracking method

4.1. Introduction

Windstorms play an important role in the spatial and temporal variability of precipitation, temperature or cloudiness. Furthermore, strong winds associated with some of these storms can lead to several social and economic damage. However, the wind is not the factor of windstorms impacts, but also the displacement speed of the storm, its footprint and the exact position of the storm can be determinant for an accurate estimation of the damage. Furthermore, worsening factors can occur when successive storms follow in a short period of time, as in the case

of the Christmas storms of December 1999 and during the winter of 1990. Very low storm displacement also contribute to increasing storm impact by extending the effect of high winds over a certain area (Mailier et al, 2006; Vitolo et al, 2009; Cusack, 2016).

Several methods are used to compute damage associated with storms. In both scientific community and the (re-)insurance industry, the cubic relationship between damage and wind speed is commonly used. It has been proven that the cube of the wind represents the conversion of the kinetic energy of a storm (Businger and Businger, 2001) and is proportional to economic losses (Klawa and Ulbrich, 2003; MunichRe, 1993). For this reason, most severity indexes used to estimate windstorms damage are based on this relation. Lamb (1991) developed the Severity Storm Index (SSI), previously presented in section 1.3 of this thesis. This index has been adapted and re-adapted into new indexes depending on the study or application. Initially, this threshold was a fixed value according to the insurance industry criteria, usually between 20m/s and 25m/s. Later, it was observed that losses in a particular area were proportional to the local 98^{th} wind percentile since the society (nature, houses, etc) adapts to its local winds (Klawa and Ulbrich, 2003). Thus, most of the recent studies use a local percentile of the wind as the threshold value for severity indexes (Della-Marta et al, 2010; Pinto et al, 2012). Other approaches have also been developed, for instance with the introduction of a population density index per grid point. Some others used a ratio or a difference of the wind to a reference value in the computation of indexes (Klawa and Ulbrich, 2003; Della-Marta et al, 2010; Haylock, 2011; Roberts et al, 2014). These types of indexes have been applied to different studies and datasets. Some used the indexes to study variability of extreme storms events in the present (Haylock, 2011; Cusack, 2016) and future climate (Leckebusch et al, 2007; Pinto et al, 2007; Leckebusch et al, 2008; Pinto et al, 2012), while other used it for estimate risks of storms and study particular storms (Pinto et al, 2007; Roberts et al, 2014).
Nevertheless, most of these studies select a specific set of storms associated with damage and analyse their corresponding footprints. Few or almost no studies have characterised damage first, then select storms linked with that damage. This standpoint is not direct since the chance to obtain a significant set of storms is reduced.

Moreover, damage realistic data is not often available for long periods. However, in this chapter, we propose the estimation of losses in a fully objective way for the whole 20$^{\text{th}}$ Century by the computation of 2D fields of Loss index and Meteorological index (Pinto et al, 2012) based on the wind from reanalysed data. Secondly, the association of damage with specific storms is performed by identifying the storms detected from our tracking method (cf chapter II) that travel near the regions of high impact. The main goal is to characterise the storms trajectories corresponding to higher loss and to build a full catalogue of 20$^{\text{th}}$ century high-losses windstorms for several countries in Europe. On the one hand, these storms can be compared with the highest events from the reinsurance industry and on the other hand, it would permit to study more ancient windstorms. Finally, a study of the most intense storms is presented in chapter V, with a dynamical and life-cycle composite analysis.
Section 4.2 provides a brief description of the calculation of the chosen indexes. In section 4.3 the method that connects the trajectories obtained on chapter II and those indexes is presented. Finally, in section 4.4 some results obtained for twenty-two countries in Europe are presented and the advantages/disadvantages pros and cons discussed.

4.2. Loss index and Meteorological index

4.2.1. Definition

The indexes used in this study are the ones from Pinto et al (2012),the "Meteorological index" (refereed as MI hereafter) presented in equation 4 and the "Loss index" (referred as LI) previously presented in equation 5 :

$$MI(i,j,t) \ = (\ V_{ij}(t)/V_{98_{ij}})^{\ 3}\ I_{(V_{ij}(t),V_{98_{ij}})} \tag{4}$$

$$LI\ (i,j,t) \ = (\ V_{ij}(t)/V_{98_{ij}})^{\ 3}\ I_{(V_{ij}(t),V_{98_{ij}})}\ P_{ij}\ \ L_{ij} \tag{5}$$

where,

$$I_{(V_{ij}(t),V_{98_{ij}})} = \begin{cases} 0 \quad if \qquad V_{ij} < V_{98} \\ 1 \quad if \qquad V_{ij} >= V_{98} \end{cases}$$

These are grid point indexes, based on the ratio of the local wind (V_{ij}) to its percentile 98 ($V_{98_{ij}}$) computed for the entire period of study. The indexes are only positive if V_{ij} exceeds $V_{98_{ij}}$, as indicated by the parameter I. Differences between LI and MI may be found through the Population Density Grid (P_{ij}) and the Land-sea mask (L_{ij}).

4.2.1.1 Wind data

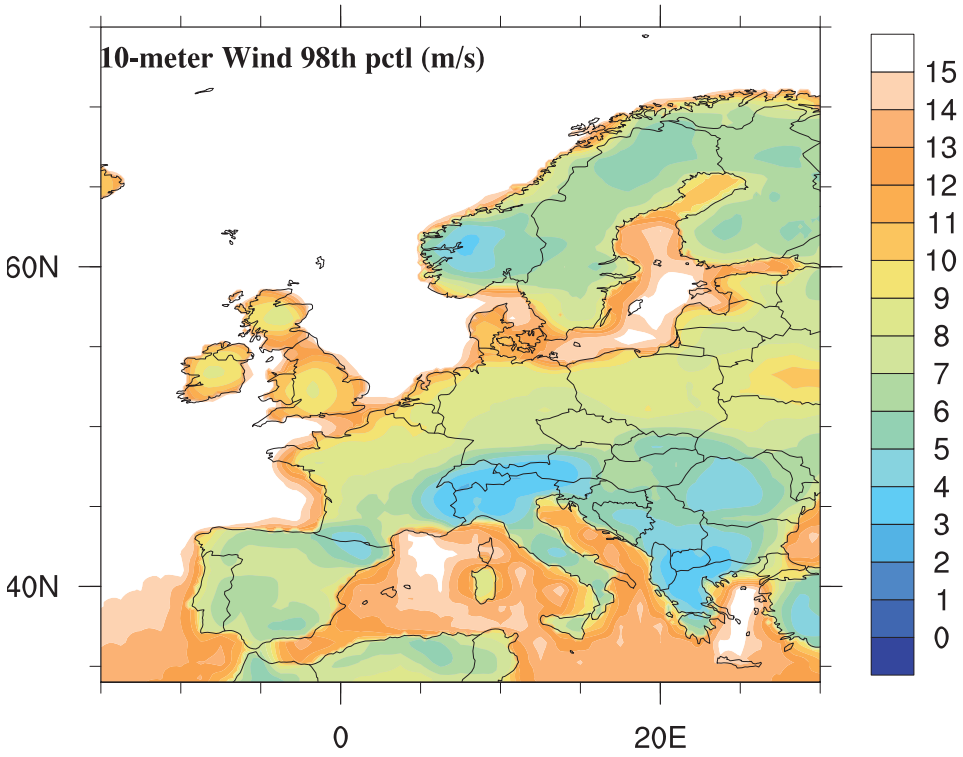

FIGURE 4.1: Wind field of the 98th percentile of 10-meters wind computed from 3-hourly data.

We used the 10-meter wind data from ERA-20C reanalysis (Poli et al, 2016). The LI and MI are computed for a large winter period (from 1st October of year

y to the 31th of March of year $y+1$) since the beginning of the century until 2010 with a temporal resolution of 3-hours. The spatial resolution used is of 0.25°x 0.25°over a large Euro-Atlantic region (100W - 60E , 0 - 90N).

The percentile 98 of the wind (V_{98}) is computed at each grid point using also a 3-hourly resolution data for the winter period of 1900-2010 and is presented on figure 4.1. As expected, it appears that it is stronger over the ocean and it ranges from 4 ms^{-1} over mountain areas like the Alps or the Pyrenees up to 14/15 ms^{-1} over the northwest coast of Europe. The yearly mean time series of the Europe

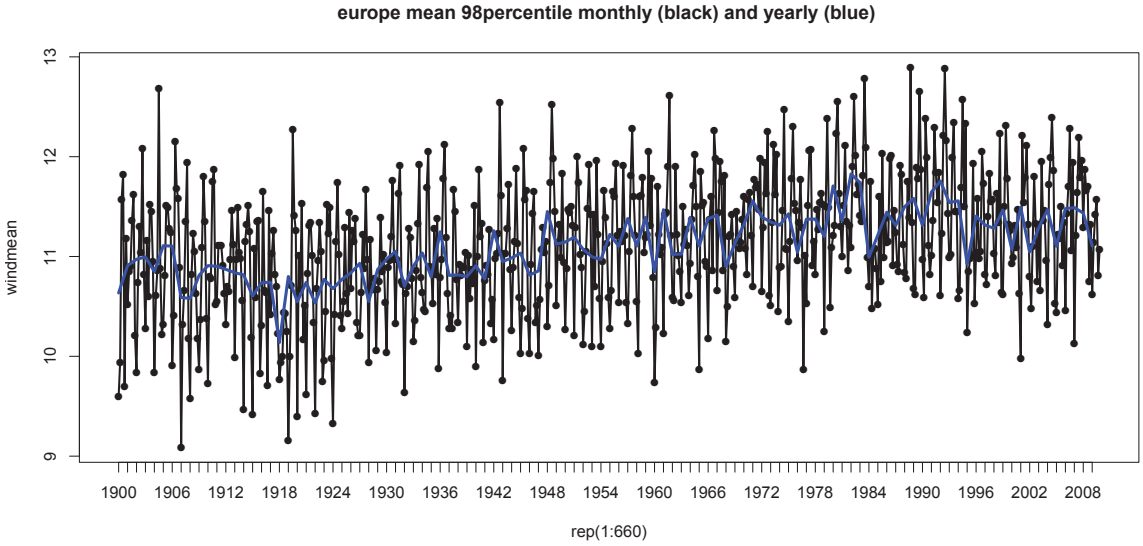

FIGURE 4.2: The temporal evolution of the average V_{98} for the Europe grid points. The black line represents the mean monthly time series and the blue one the yearly time series of this wind.

spatial average V_{98} (figure 4.2) shows an increase during the middle of the century and larger variability in the beginning of the century. This increase in near-surface wind speed is shown to be related to an intensification in the storm-track eddy activity which is the main purpose of chapter III.

4.2.1.2 Population density grid

The population density grid (PD) (figure 4.3) is a product from Center for International Earth Science Information Network - CIESIN - Columbia University ; Centro Internacional de Agricultura Tropical - CIAT (2005) and corresponds to the population of the year 2000 that is kept constant for the entire century.

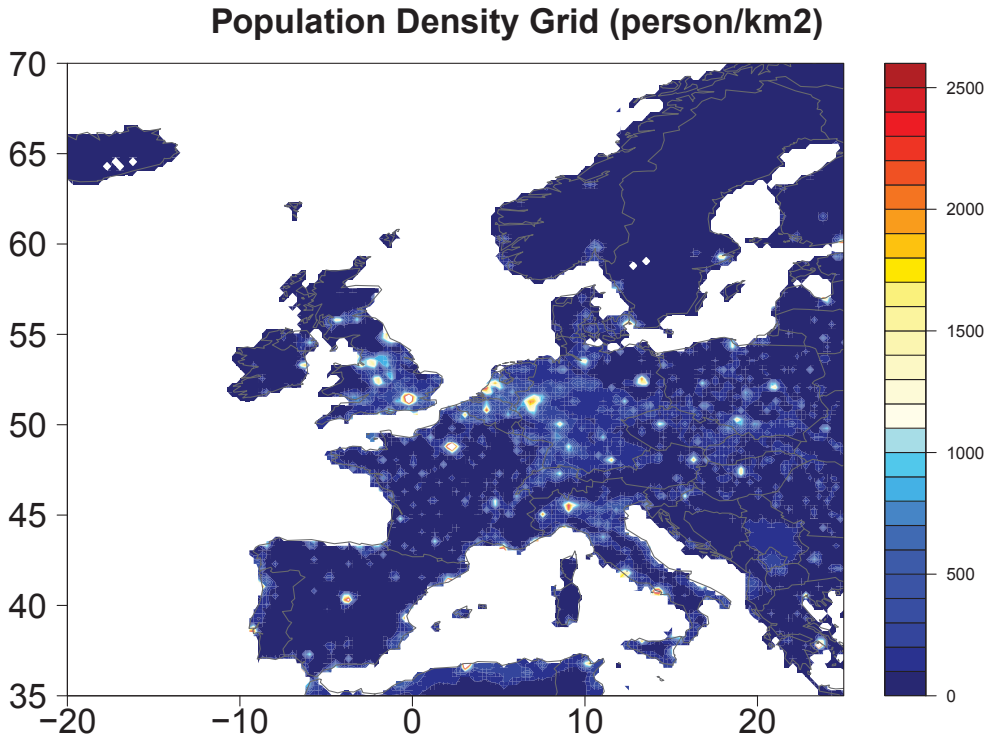

FIGURE 4.3: Population Density Grid.

4.2.2. European Countries' LI

Raw LI and MI values are first computed every 3 hours for the whole domain. Then, sub-domains are created to extract individual database for each of the following countries : France, Belgium, Germany, United Kingdom, Ireland Denmark, Norway, Sweden, Switzerland, Austria, Spain, Portugal, Italy, Finland, Poland, CzechRepublic, Lithuania, Latvia, Estonia, Luxembourg, The Netherlands and for whole domain gathering the ensemble of the previous countries named Emask (coloured areas in figure 4.5 and 4.4).

Finally, we introduce the daily maximum LI which is calculated as for day k

$$DLImax_{country}(k) = max_{t\in k, x\in x_{country}}(LI(x,t)),$$

where x symbolize one gridpoint. Then, we also define $DLIsum_{country}(k)$ as in :

$$DLIsum_{country}(k) = \int_{country} DLI(k,x)dx$$

The same indexes are performed with the MI

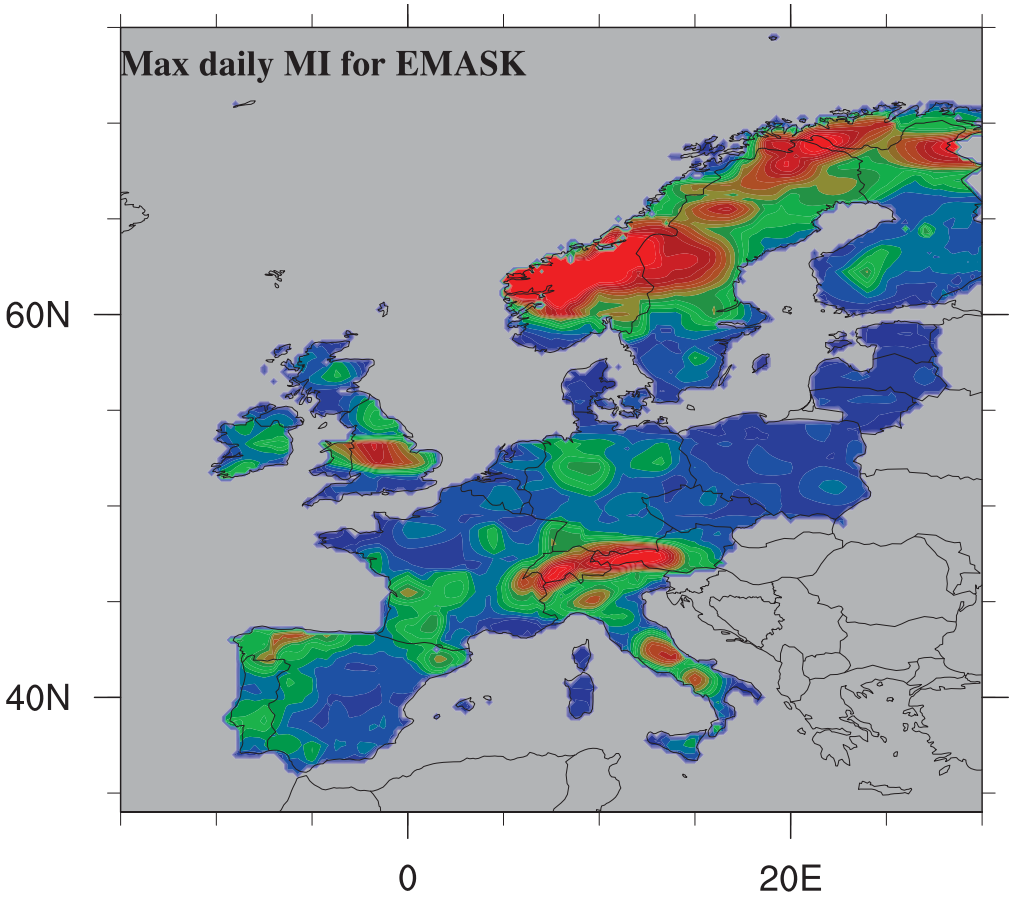

FIGURE 4.4: Twenty-century maximum MI(k,x) over Emask.

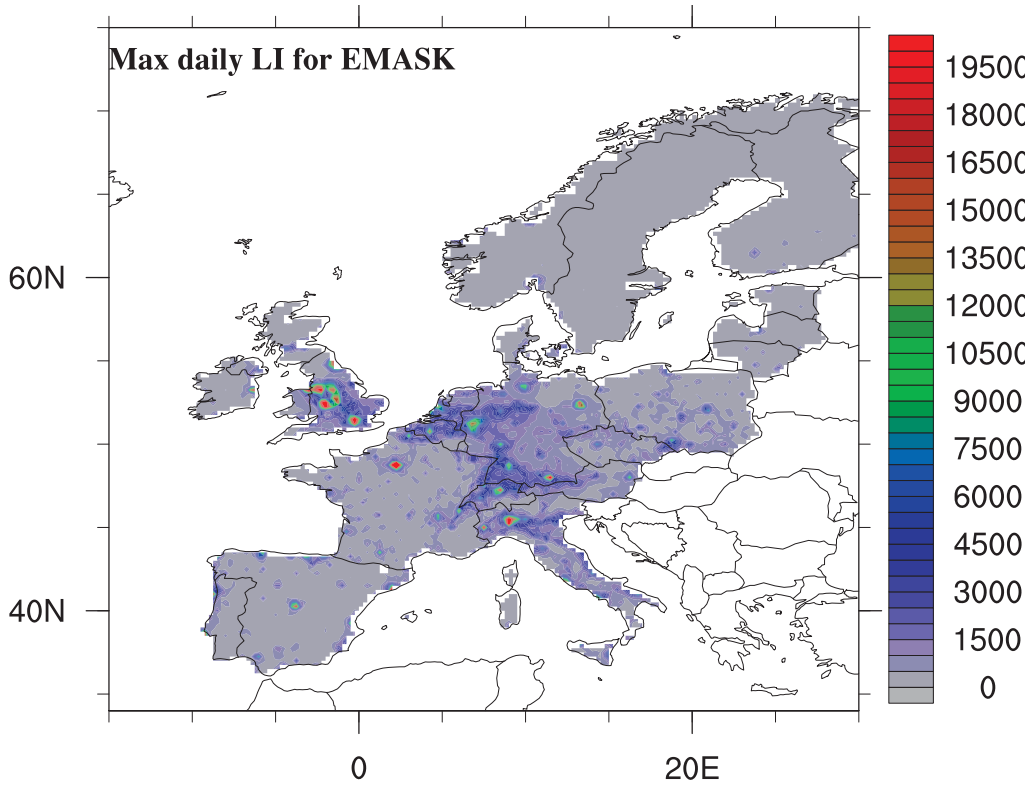

FIGURE 4.5: Same as 4.4 but for the LI.

In Summary, we compiled twenty-two datasets for the twenty-two countries of our study. A first kind of spatialized 3-hourly fields of LI and MI (hereinafter $LI_{country}, MI_{country}$) and a second kind of time series of daily accumulated index ($DLIsum_{country}$, $DMIsum_{country}$) and daily maximum ($DLImax_{country}$, $DMImax_{country}$). This characterisation of wind impact will be helpful to analyse the role of windstorms at a regional scale. To our knowledge, such an attempt to systematically relate any wind impact to specific storm life cycle hasn't been done yet.

4.3. Associating a high-impact weather event to a storm : High-loss Tracking

From section 4.2.2 the list of the days with the highest daily maximum LI values is obtained for each country. However, it does not allow us to directly identify the storm associated with these damage. For this reason, we developed a method that matches previously defined damage fields with the track of a particular extratropical storm detected in chapter II.

4.3.1. Selection of storms

The method of high-loss storm tracking for each country is based on the days when the daily LI maximum ($DLImax_{country}$) is higher than its 75% percentile. The choice of the daily LI instead of the MI is made for two main reasons. First, we expect to obtain the storms that are associated with the highest economical damage, the LI is then more appropriate than the MI. Secondly, the impact of a windstorm over a country occurs at daily scale. Therefore, the day is the most appropriate time unit to sort all the events of the century, while reducing the time of calculation of method but keeping the information at a time-scale short enough so that we do not loose any possible storm. The algorithm is based on 3 main steps and is summarised in figure 4.6a.

1. **Tracks identification**
   First, we introduce the percentile 75 of the $DLImax_{country}$ and we limit to the days k for the ones which $DLimax_{country}(k)$ is higher than this percentile. Only storms with a track passing inside the European domain (15°W - 35°E , 34°N -80°N) are taken into account. One objective of this step is to reduce the time of calculation.

2. **LI and MI of each track**
   Secondly, the distance between the centre of the track and the country is computed at each time steps of the tracks. When this distance is under the R threshold, a circle area of this radius R is defined around the track centre.

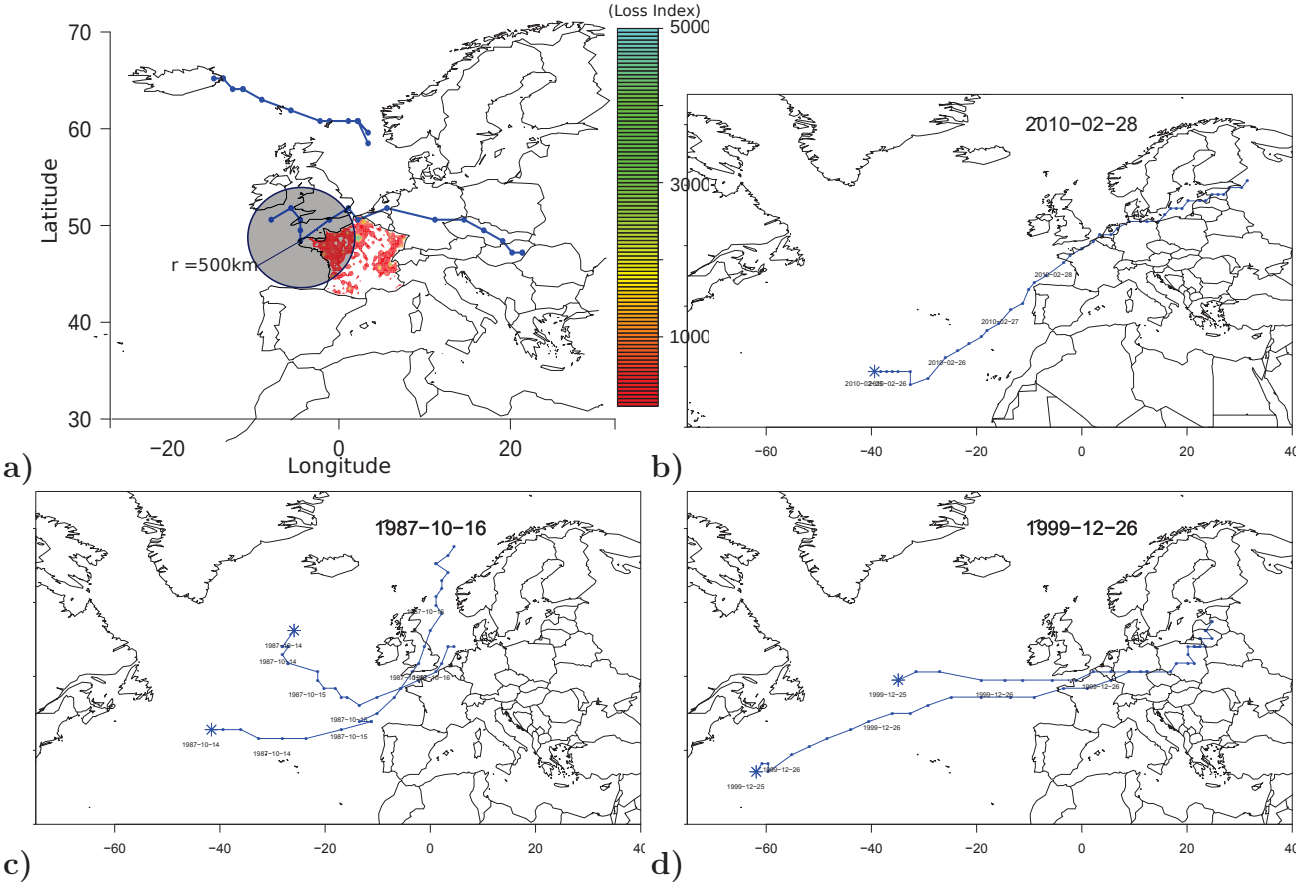

FIGURE 4.6: a)-Trajectories detection method representation. b,c and d)- Examples of tracks found at less than the radius R=500km from France on the 28$^{\text{th}}$ February 2010 (Xynthia), 16$^{\text{th}}$ October 1987 (The great storm) and 26$^{\text{th}}$ December 1999(Lothar).

The MI and the LI can then be extracted in the intersection area between the circle domain and the country area (France area covered by the circle in figure 4.6) for the time steps where the track centre is closer than R. This area will be referred now onwards as *interception area*. Each storm will be then associated with these new LI and MI as in equation 6 and 7 :

$$MI_{track}(x,y,t) = MI((x+x_{track})^2 < R^2,\ (y+y_{track})^2 < R^2,\ dt) \quad (6)$$

$$LI_{track}(x,y,t) = LI((x+x_{track})^2 < R^2,\ (y+y_{track})^2 < R^2,\ dt) \quad (7)$$

where, dt are the time steps the trajectory is at less than the distance R and $x - x_{track}$ an $y - y_{track}$ the *interception area*.

3. **Selected trajectories**
   The selected tracks are the ones that have positive MI_{track} and LI_{track}.

Figure 4.6a shows an example of the method for the case of France. Two tracks are shown, one close to France and another one further north. The northernmost track is at a distance larger than R for the day k and the track will be excluded. The southernmost track is closer than R from France on day k and the LI_{track} is positive in the *interception area*. This track will be taken into account as a storm associated with the damage of day k and its MI_{track} and LI_{track} values will be computed inside the *interception area*.

The value of R used was chosen regarding the mean footprint impact of a windstorm. Depending on the type of wind/front the footprint width and location may strongly vary (Hewson and Neu, 2015). Different values of R were tested. At first glance, R=1000km is a reasonable choice. However, in some cases a great number of tracks were retrieved, some of then clearly not responsible for the strong winds. After a careful examination of some extreme cases, a radius of R=500km was used. This reduces the maximum number of storms selected per day from more than ten to less than three tracks per day.

In addition, a set of other parameters are collected within the *interception area*, resumed in table 4.1 : The *duration of the storm*, number of hours where the storm is less than a distance R from the country ; *Area*, number of grid points whit MI higher than zero in the *interception area* ; *Mean Speed*, mean displacement speed using the first and last time-step when the storm at R km from the country.

Crossing tracks and dates

One important consequence of the adopted method is that, since we are working at a day-scale, the same track is selected on successive days. Therefore, and when this happens, only the day when the track has the highest $LImax_{track}$ (as computed in table 4.1) is considered, removing all the tracks from all other days.

	Description	**Parameter**
Duration	time-steps where R<500km	dt
Area	Number of grid points within a 500km around storm centre with MI>0	$Area_{track}\ (l)\ =$ $\sum_{dt}(x - x_{track})^2 < R^2,\ (y - y_{track})^2 < R^2\ )_{MI>0}$
Mean Speed	Speed of the storm when at less then 500km	$V\ (l)\ =\ \frac{distance(\ k(t_{(x,y)})\ )}{dt}$
LImax	Maximum LI during dt for all grid points	$LImax_{track}(l) = max(\ LI_{track}\ )$
MImax	Maximum MI during dt for all grid points	$MImax_{track}(l) = max(\ MI_{track}\ )$
Lisum	Sum of LImax during dt for all grid points	$LIsum_{track} = \sum_{dt}\ LImax(k,t))$
MIsum	Maximum MI during dt for all grid points	$MIsum_{track} = \sum_{dt}\ LImax(k,t))$
	lat_{track} and lon_{track} are the position of the storm	

TABLE 4.1: Parameter computed for each tracks l at day k in the circle of radius R centred on the storm during the timesteps dt that storm is at less then R km from the country.

We now consider this list of tracks with loss properties associated to $LImax_{track}$ and $MImax_{track}$ values.

4.4. Country by country LI and MI computations

4.4.1. LI and MI per country

The procedures on the calculation of the MI and LI at a daily scale for twenty two countries have been described in section 4.2.2. Here we compare the mean values of these quantities and analyse their variability at a country level. First, only the days with positive values for both indexes $DMImax_{country}$ and $DLImax_{country}$ are selected. Then, variability by country can be analysed from the boxplots figures 4.7 and 4.9 for the MI an LI respectively. Results are quite different between indexes and enable us to confront the population density for the LI and the effect of the geographical variability of the wind and its percentile V_{98}.

From figure 4.7 we can see that Switzerland Austria, Italy and the northeast countries, Norway, Sweden, and Finland show stronger values of DMI and larger extremes. On the contrary, countries like the Netherlands, Belgium or the UK are countries with the lowest variability. Figure 4.8 give us some highlight about the effect of the V_{98} to the DMI distribution. The blue and the red lines on the left panel represent the distribution of the 10-meter daily maximum wind for a specific point in the UK (red) and for a specific point of Norway (blue). Their associated 98% percentile is represented by the vertical lines (14.6ms^{-1} and 6ms^{-1}for UK and Norway respectively). The dashed lines on the right panel represent the $DMImax_{country}$ distribution for the same points and the solid lines the ratio between the wind and its percentile 98. As expected and seen before on figure 4.1, the mean wind is higher in the UK than in Norway, although the $DMImax_{country}$ and $(V/V_{98})^3$ is higher in Norway than the UK. This is related with the positive skewness of the wind distribution amplified by the power 3.

The different values of V_{98} per country are related with the orographic roughness applied on the reanalysis that reduces wind intensity with increasing altitude and is observed on mountainous countries like Italy, Switzerland, Norway or Sweden (figure 4.1)
The mean $DLImax_{country}$ per country, in figure 4.7, show a different result. The highly populated countries as the Netherlands, UK, and Belgium or countries with

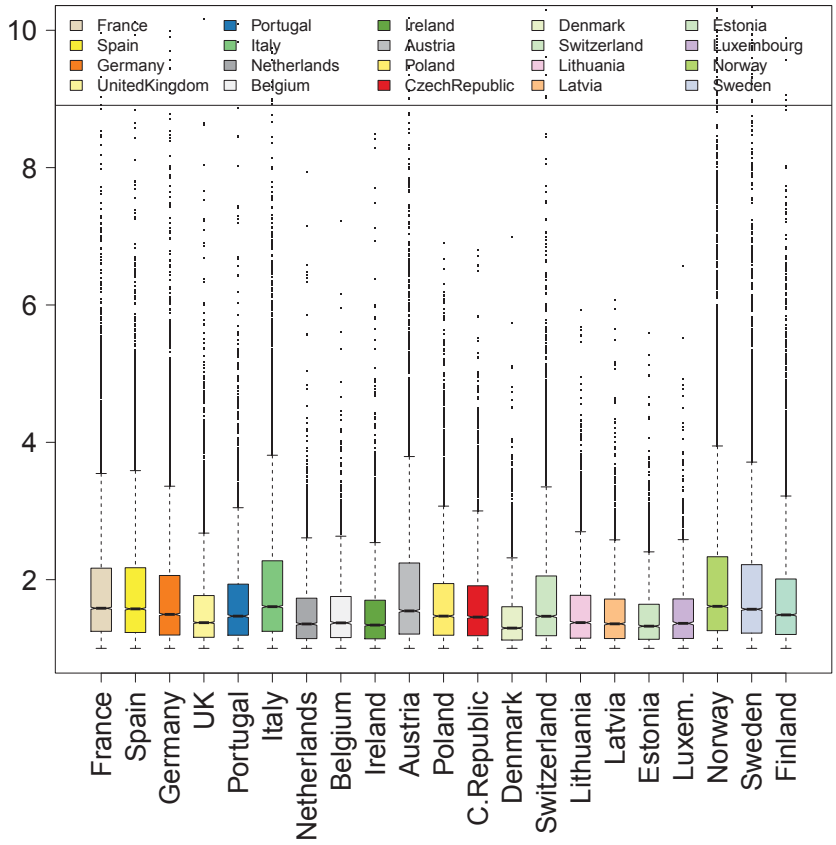

FIGURE 4.7: Boxplot of MI>0 for each country.

big cities as France or Spain (figure 4.3) are the ones that have stronger values of LI. The lowest mean $DLImax_{country}$ are found for low populated regions as the northeastern countries Sweden, Norway or Finland.

4.4.2. Correlations between countries and temporal variability

After looking at the different distributions of wind indexes, a correlation between countries is computed between the daily MI and LI integrated for each country $DLIsum_{country}$ and $DMIsum_{country}$. In figure 4.10a and 4.10b the correlations between all countries are presented. Since the correlations are made between not-lagged time series, stronger positive correlations are found for countries close to each other as France, Germany and Belgium and anti-correlations are found

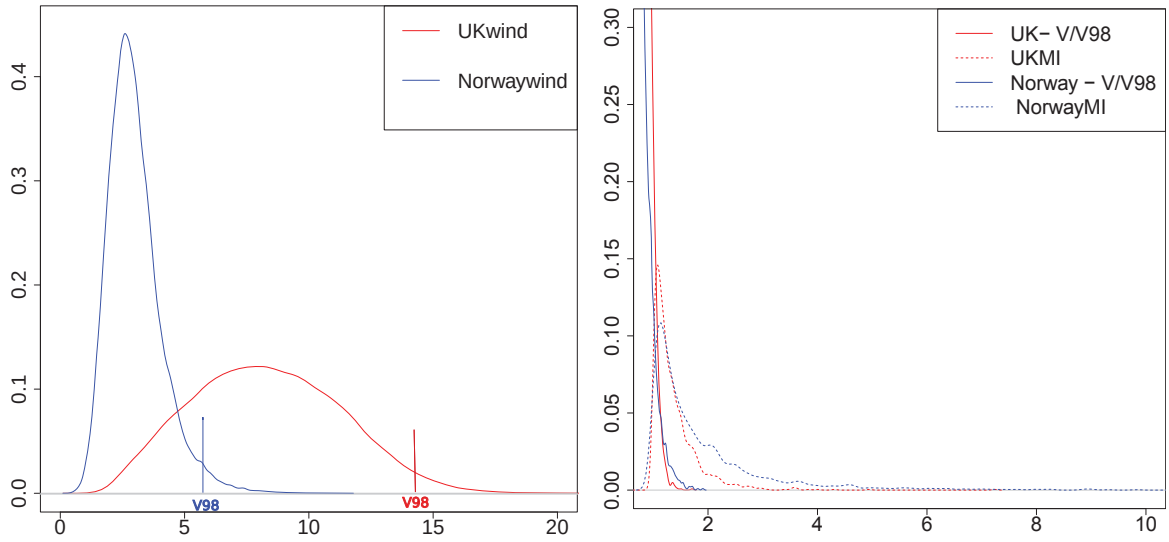

FIGURE 4.8: Probability density function of 10-meter wind (left pannel), MI (dashed lines on rigth panel) and 10-meters wind divised by the percentile 98 (lines rigth panel) for two grid point in the UK (red) and in Norway (blue).

between distant countries as for instance Spain and Norway.

The correlation between each country and European domain "Emask" refers to the size of the country (in the case of the MI) or to the population density (in the case of the LI). The correlations for LI (figure 4.10a) show strong positive correlations between "Emask", Germany, The Netherlands and Luxembourg since they are countries with the highest population density. The "Emask" correlations in term of MI show stronger values for the countries with lower V_{98}. Yet, a good correlation between Germany and France is found (also seen in LI correlations). The fact that both LI and MI show good correlation between "Emask" and France/Germany indicates that these two countries have an important impact in European losses, probably because of their size/population amount compared to all the others countries.

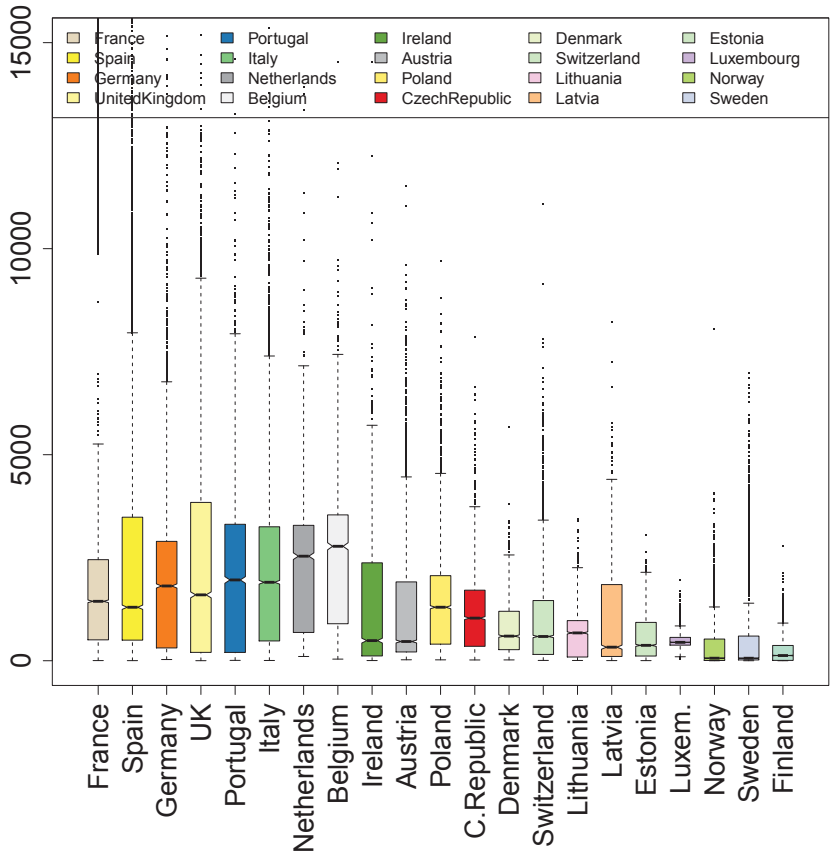

FIGURE 4.9: same as 4.7 but for the LI.

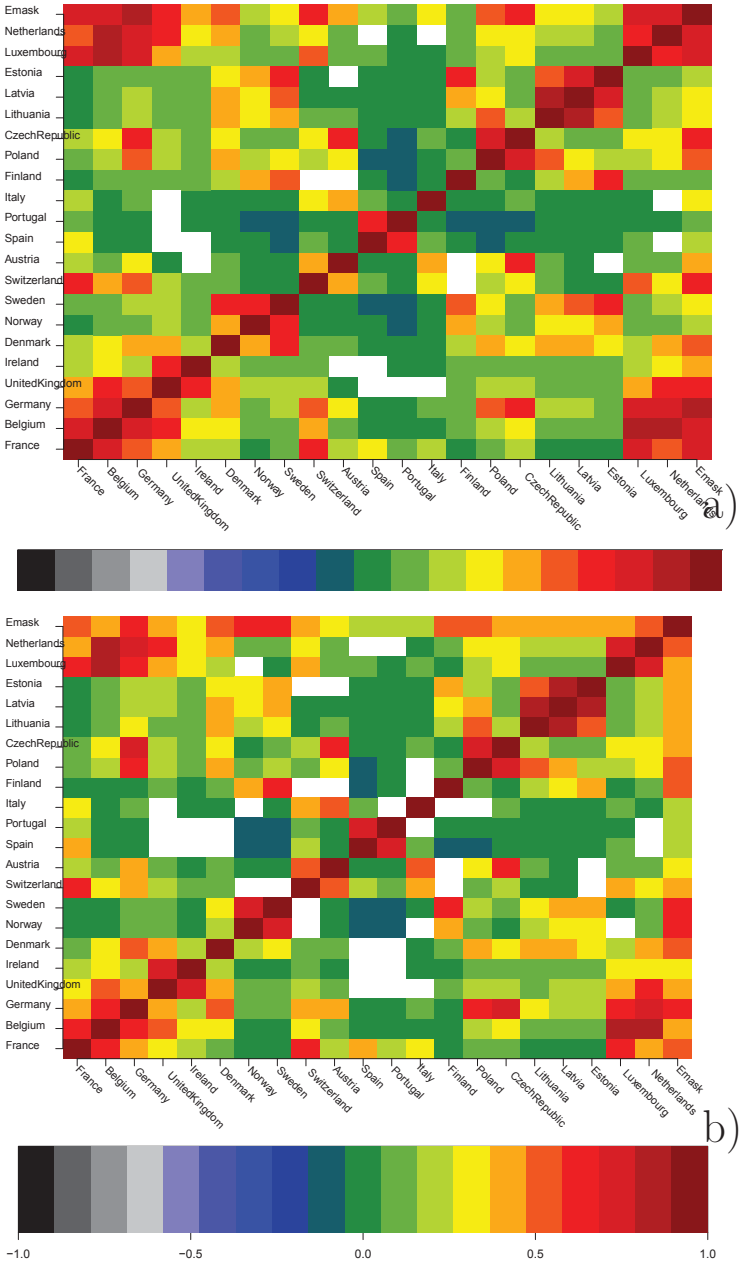

FIGURE 4.10: Correlations of LI (a) an MI (b) between all countries.

4.5. High-loss storm tracking

Table 4.2 shows a summary of what we obtain with the *High-loss storm tracking* for all different domains. The first column shows the number of days in the country with ($DLImax_{country}$) higher than its percentile 75%, the second column shows the total number of trajectories detected by the method and the third and fourth columns are the mean *Area* and *Mean displacement Speed* of these storms as described in table 4.1.

Norway, Sweden and France are the countries with more days with $DLImax_{country}$ above its percentile 75% days and Luxembourg and the Netherlands are the countries with the least corresponding days. The same is observed for the number of trajectories. This can be due to two factors : First, the size of the countries are different and one expects to find more storms for large countries as there is one radius value for the circle defining the intersection area.

Secondly, as mentioned before, the V_{98} (figure 4.1) is not the same for each country. Winds are weaker over land than over the ocean and even weaker over mountain areas. In general, low V_{98} will increase the frequency of days with positive $DMI/LImax_{country}$ and consequently the number of days and tracks that will be associated with it. This can also explain why more days of positive $DMI/LImax_{country}$ and number of tracks are found on for The Netherlands, Denmark, Norway and Sweden.

Mean displacement speed (columns 3 of table 4.2) is dependent on the position of the country in Europe. Northwest and west countries have higher displacement speeds in general, while in southern and east countries it is lower. This may be related with the fact that Northwest countries are concerned by storms taking part of the North Atlantic storm track and travelling eastward into Europe. These storms are usually advected by stronger upper-level winds (Schultz et al, 1998; Rivière et al, 2015b) than storms in the mainland. Moreover, southern countries are mostly affected by more Mediterranean storms (discussed further in this chapter and in the next chapter) over the Genoa's Gulf and Ligurian sea region that do not travel much either have lower displacement speed (Trigo et al, 1999).
Mean *area* (columns 4 of table 4.2) is in average the same for each country with

Country	#days	#traj	Mean Area (grid points)	Mean displacement speed (km/h)
France	2269	1703	3.19	44.32
Belgium	583	266	2.92	60.6
Germany	1634	987	3.18	52.5
UnitedKingdom	1596	1352	3.06	53.9
Ireland	952	570	2.74	52.7
Denmark	708	370	3.44	51
Sweden	2167	1328	3.24	42.2
Austria	1540	248	2.56	40.3
Spain	2090	1037	3.19	39.8
Italy	2363	1234	3.38	29.9
Finland	1762	939	3.35	38.6
Poland	1217	623	3.54	49
Norway	2771	1803	3.24	43.6
Switzerland	1335	10	4.6	57.5
Portugal	925	372	3.34	43.8
CzechRepublic	873	152	3.36	53.1
Lithuania	742	186	3.25	48.9
Latvia	777	171	3.67	44.7
Estonia	716	232 2	3.77	43
Luxembourg	380	44	3.25	62.6
Netherlands	656	240	3.38	58.5
Emask	4722	2046	4.71	46.3

TABLE 4.2: Columns from left to right : number of days where daily LI is higher than its percentile 75% for each country ; Number of trajectories tracked from the *High-loss tracking Method* for the days of column I ; Mean grid points with MI>0 for trajectory ; and mean displacement speed of the trajectories.

the highest values belonging to Switzerland, probably because it has low V_{98} (the same effect as mentioned before for the Norway case).

While looking at individual results per country and particularly to tracks which are associated with highest $LImax_{track}$, a good agreement is found with some historical storms. A summary of this is shown on table 4.3. In this table, the two days of trajectories with highest LI are presented for each country. For Germany and Switzerland, the storms are in good agreement with the data from the reinsurance industry, the storms *Lothar* (1999), *Vivian* (1990) and the *Capella storm* according to the German nomenclature. In the UK, the storms identified are the *Great storm of 1987* (Browning, 2004; Prichard, 2012) and storm *Erwin* in 2005, also in the top storms with historical damage. In Portugal, we are able to track the storm that holds the current wind gust record, in February 1941 (Muir-Wood, 2013; Varino, 2011). For Norway, we find the *New Year's Day Storm* (Gronas, 1995), a storm known as the worse in terms of losses in Norway. For France, the trajectories with the highest $LImax_{track}$ are *Xynthia* (2010) (Vinet et al, 2012; Liberato et al, 2013) and *Herta* (1990). However, we would expect to find storms *Lothar* and *Martin* at first place in terms of $LImax_{track}$ according to the reinsurance data. The reason why these two storms are not in the top ones for France can be related to the physical nature of the storms and the spatial and temporal resolution of wind data and Extra-tropical cyclone tracking information. In other words, the storm *Lothar* was a storm of small size in terms of footprint, with a rapid increase in a short amount of time and with small-scaled intense winds. The 10-meter wind data at a spatial resolution of 25km is unable to represent the real intensity of *Lothar's* strong winds, as mentioned by several authors(Deroche et al, 2014; Hewson and Neu, 2015) and seen in chapter II. The rapid displacement of Lothar (it is one of the ten fastest storms for France) makes even more difficult a correct estimation of the winds since the storm is depicted only a few time steps over France. Nevertheless, these results are quite satisfactory and prove that a good correspondence between losses and storms can be made using only a 2D field of 3-hourly LI and MI and individual tracks.

4.5.1. Density of trajectories for each country

In this subsection, we analyse the spatial distribution of the selected trajectories of table 4.2 by computing the density of those trajectories for each country

Country	Event
France	2010-02-28/1990-02-03
Belgium	1984-11-23/1992-11-11
Germany	1972-11-13/1999-12-26
UnitedKingdom	2005-01-08 /1987-10-16
Ireland	1997-12-24/1999-11-28
Denmark	1999-12-03/ 1956-01-21
Sweden	1906-12-06/ 1913-12-04
Austria	1923-12-25/ 1926-03-13
Spain	2003-10-3/2005-12-021
Italy	1990-02-27/2005-02-23
Finland	2002-02-23/1946-10-11

Country	Event
Poland	1947-12-22/1940-03-05
Norway	1939-11-26/ 1992-01-01
Switzerland	1999-12-26/1990-02-27
Portugal	1941-02-15/1912-02-07
CzechRepublic	1947-12-22/ 1940-11-05
Lithuania	1943-03-02/1931-01-17
Latvia	1993-01-14/ 1978-11-23
Estonia	1983-12-31/1990-02-27
Luxembourg	2010-02-28/2003-01-02
Netherlands	1949-03-01/1929-12-07

TABLE 4.3: Days of storms with the two highest $LImax_{track}$ for each country.

and "Emask" domain (figure 4.11 and 4.12).
The highest densities are found for cases of Norway, Italy and Sweden due to a larger number of storms.
All other countries show maximum density over the centre of the country, as expected. Some countries as UK, Germany or Belgium, Denmark, Ireland, Luxembourg and The Netherlands show a density pattern that covers not only the country but also the western region of the Atlantic ocean, suggesting storms arriving from Atlantic storm track, Central-European countries like Austria, Switzerland, show weaker density maximums with no evident density on the Atlantic. Mediterranean countries like Spain and Italy show maximum density over the Mediterranean, particularity between the Lion's Gulf and Ligurian sea.
France is the only country that shows two density maxima, one over the northern part of the country and another between the Gulf of Lion and the Gulf of Genoa, a pattern that is also visible when we look at the "Emask". The real physical meaning of this two maxima, however, can be questioned. There are, indeed, Mediterranean storms in France that can provoke strong winds and damage over the southern region of the country (Trigo et al, 1999; Lionello et al, 2016), however, this could rather be an effect of searching storms in a radius R. At the same time that we have a storm coming from the Atlantic ocean there could be one simultaneous storm on the Mediterranean side at less than 500km from the coast, both

at a distance lower than 500km from a particular point with positive LI/MI. Therefore, it can be hard to disentangle the which storm is the origin of the observed values of MI/LI.

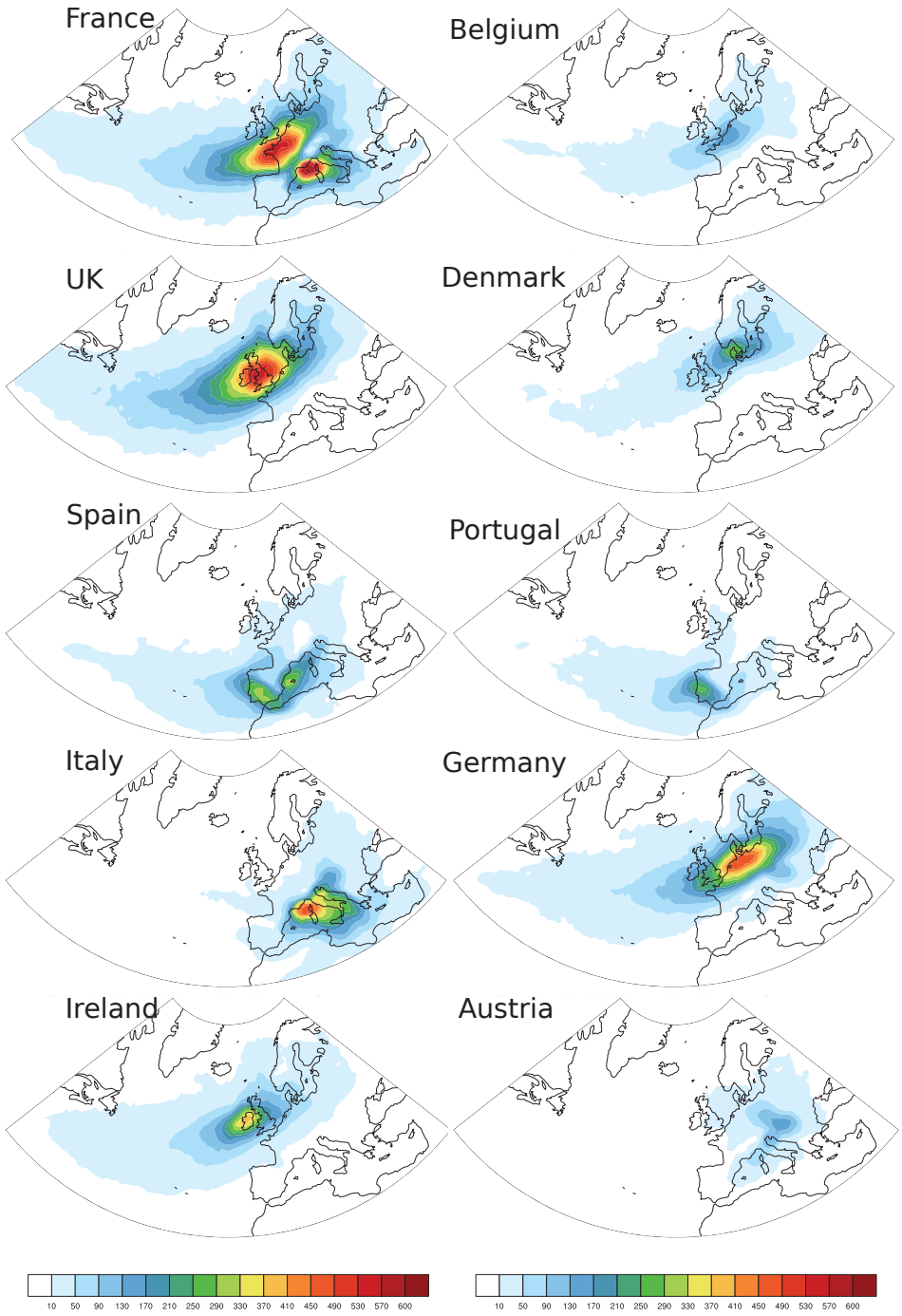

FIGURE 4.11: Density of the detected trajectories for the days with $DLImax_{country}$ above percentile 75% as shown in table 4.2 for the following countries : France, Belgium, UK, Denmark, Spain, Portugal, Italy, Germany, Ireland and Austria.

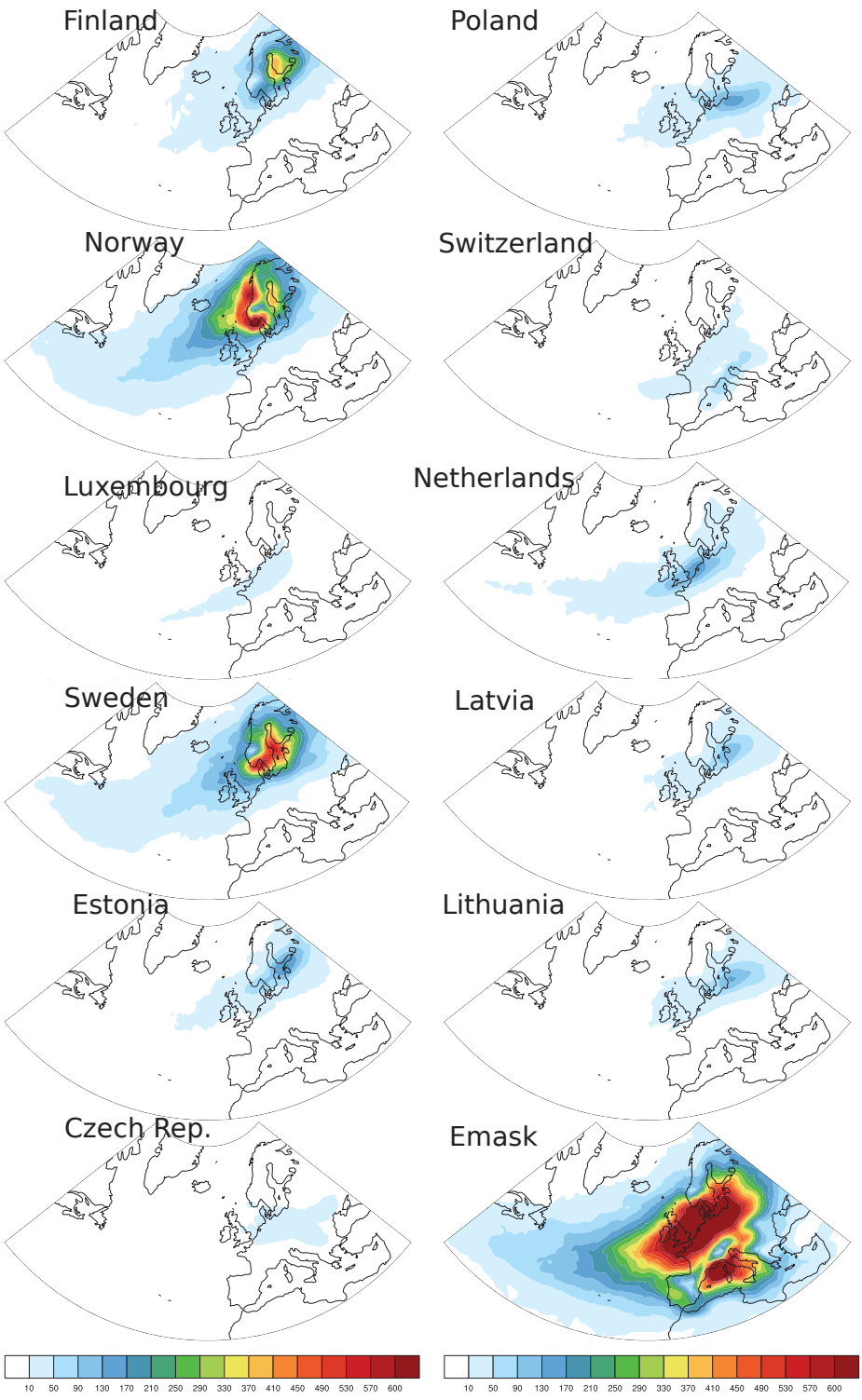

FIGURE 4.12: Same as 4.11 but for Finland, Poland, Norway, Switzerland, Luxembourg, the Netherlands, Sweden, Latvia, Estonia, Lithuania, Czech Republic and Emask.

4.5.2. Case studies

We have observed that, in the case of France, two storm spatial density maxima exist and that in some cases this can be associated with co-existing Altantic and Mediterranean storms. In order to understand the amount, role and importance of this type of storms, a closer look is given to the tracks selected from 3 particular days, 28$^{\text{th}}$ February 2010, 3rd of February 1990 and 15$^{\text{th}}$ of October 1987.

4.5.2.1 28th February 2010 and 3rd February 1990

The first and second days with the highest-LI trajectories for France happen on the 28$^{\text{th}}$ of February 2010 and on the 3rd of February 1990. The trajectories identified by the *High-loss storm tracking* are presented in figure 4.13 and figure 4.14. In these two days, only one trajectory has been selected. In fact, in more than 79% of the days studied for France, there is only one storm selected which shows the discriminant capacity of the algorithm.
The *High-loss storm tracking* is capable of selecting the historically storms "Xynthia" in 2010 and "Herta" in 1990. Some others historical known windstorms are selected at a daily level as Lothar for the 26$^{\text{th}}$ of december 1999, Klaus on the 23rd of January 2009 or Erwin on the 8$^{\text{th}}$ of January 2005. However, we are unable to say if all historical storms are tracked correctly without a complete one-by-one analysis of days and storms. It would require a verification of all selected storms and a comparison with trajectories of historical/catalogued windstorms.

4.5.2.2 15th of October 1987

For the other 21% of the cases, more than one trajectory is selected for one day. The 15$^{\text{th}}$ of October 1987 is a good example of these cases (figure 4.15). A first selected trajectory corresponds to the "Great storm of 1987" that crossed the UK and killed several people (Browning, 2004). A second trajectory is caught at less than 500 km from France on the southernwest side of France. The size and location of this trajectory make us believe that it cannot be the cause of intense winds and that it was simply relatively close to LI positive grid points. However, these LI positive points are related to the first storm and not the small Mediterranean one. In order to verify this, a re-identification of tracks is needed in this cases using the

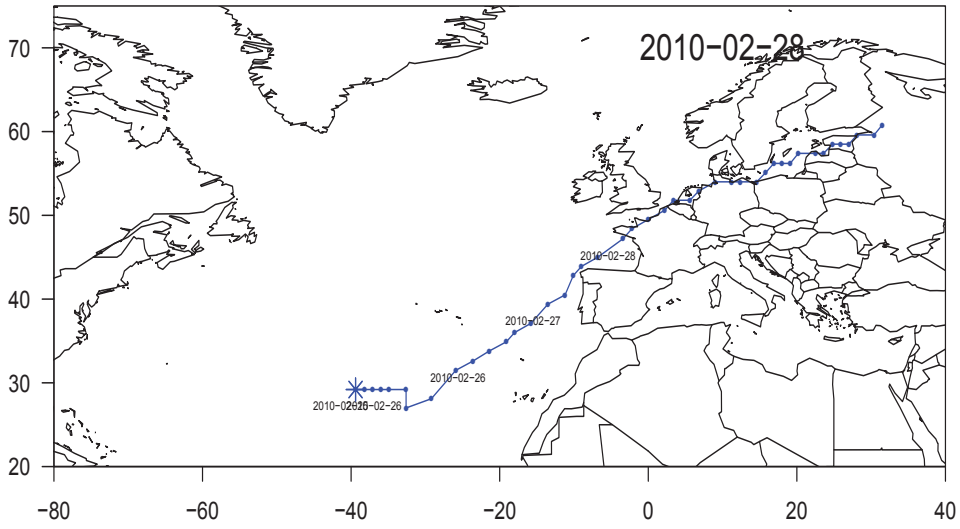

FIGURE 4.13: Trajectories found for the 28th of February 2010.

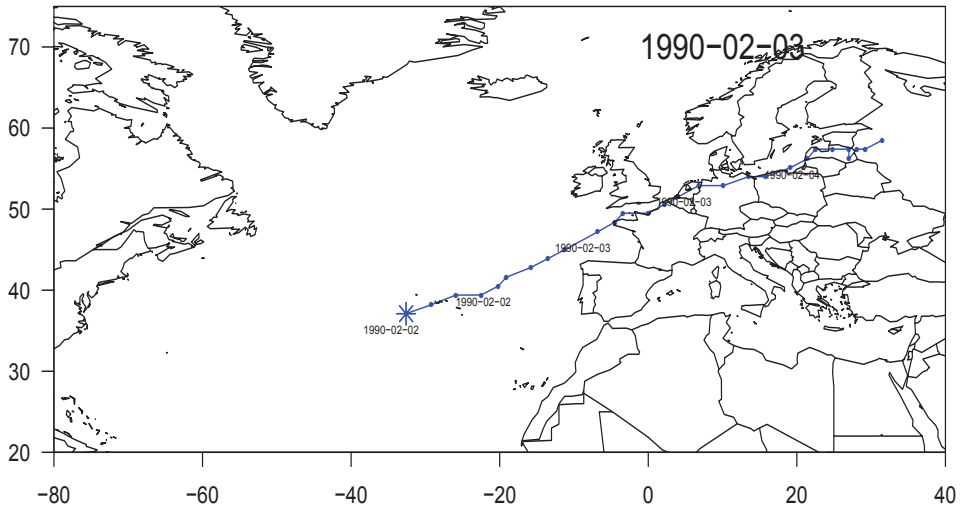

FIGURE 4.14: Trajectories found for the 3rd February 1990.

wind footprint of each trajectory. Figure 4.16a) and 4.16b) show the associated wind footprints in a radius of 500km around storm centre for both storms. The winds from the first storm (figure4.16a)) reach the north/northwestern part of France and are stronger than the ones produced by the second trajectory at the

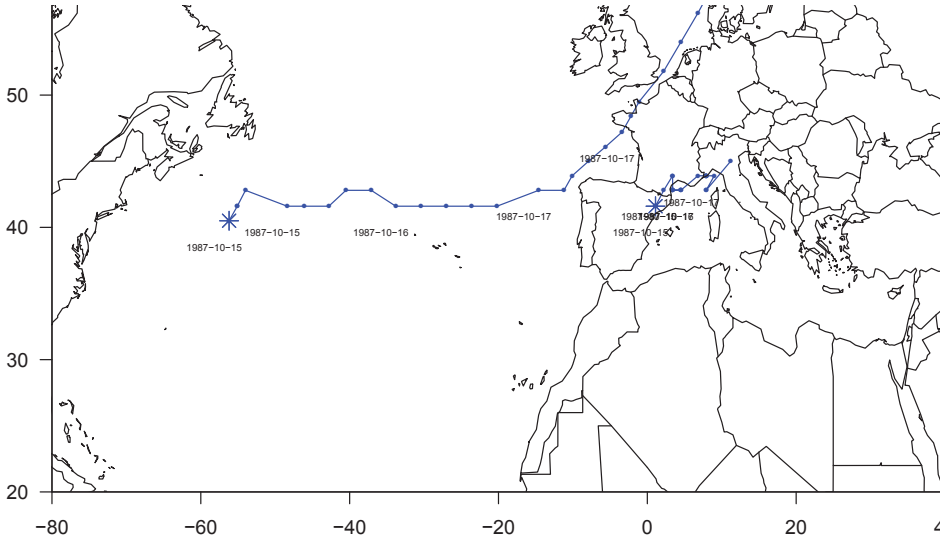

FIGURE 4.15: Trajectories found for the 15$^{\text{th}}$ of October 1987.

southern region (figure 4.16b)).

Furthermore, $LImax_{track}$ for the first storm is in the top highest $LImax_{track}$ in France. The second track $LImax_{track}$ has only rank 1300. We can then assume that this last storm cannot be associated with the daily LI of this day. Some other cases, like the two storms observed in figure 4.6d show however strong values of $LImax_{track}$. This type of cases could be, in a certain way, related with serial clustering.

Despite this last fact, a good approach to reduce such artefact association could be simply to introduce the product of the ranking of the selected trajectories by its individual $LImax_{track}$ and $MImax_{track}$ and working with the ones that have stronger values. The artefact storms, as the one given in the first example, will be then placed as some of the weakest in terms of $LImax_{track}$ and $MImax_{track}$.

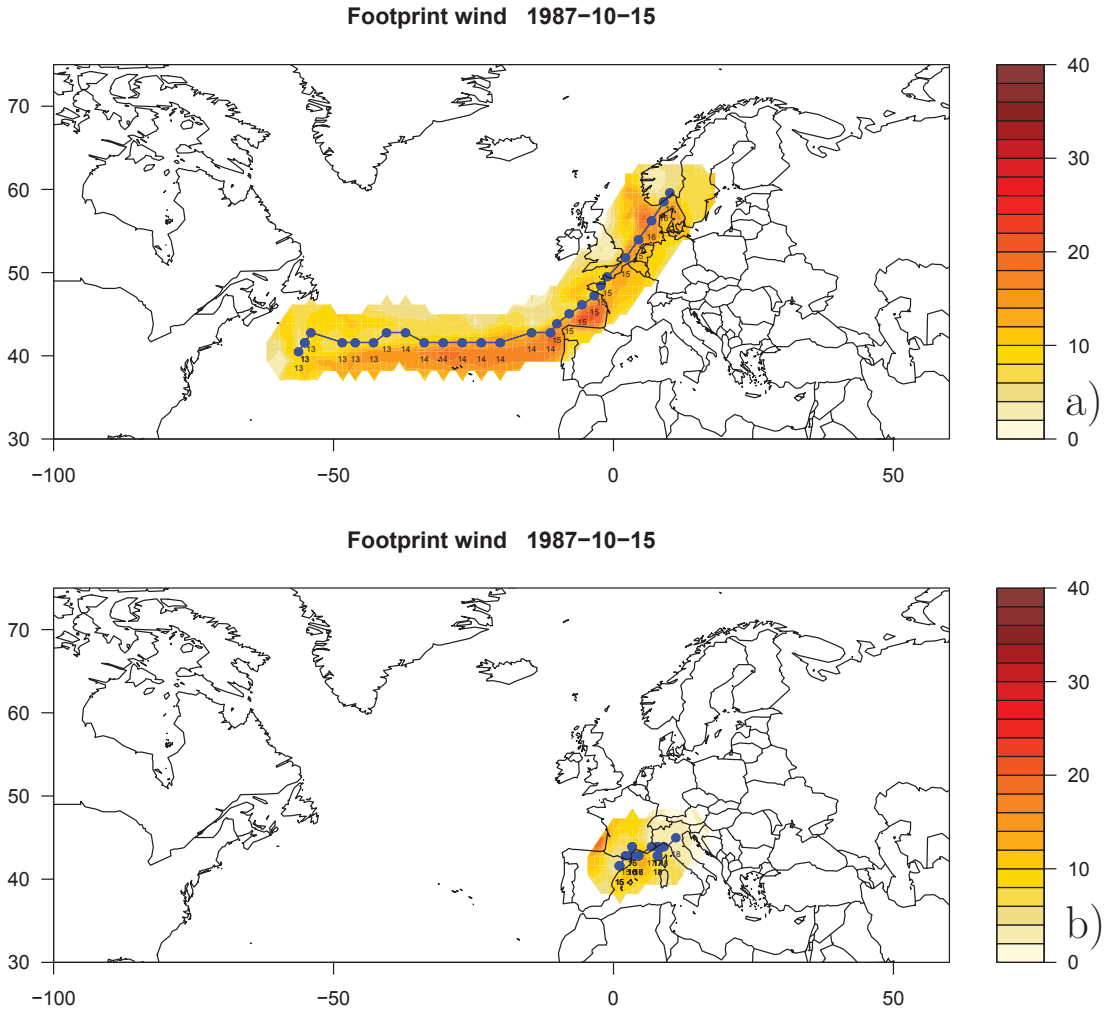

FIGURE 4.16: Wind footprind in a raidus of 500 km around the storm centre fot the two detected storms on the 15th October 1987.

4.6. Summary and Conclusions

In this chapter we have described two indexes used to represent 20^{th} century windstorms damage using a *High-loss tracking* approach.

It was seen that the Loss Index and Meteorological index are different for each country due to different values of population density index and wind percentile. The Meteorological index values per country reflect the variability of the wind above its 98% percentile. The 10-meters wind decreases with increasing altitude, and thus, is weaker for countries with mountains. As a result, higher in average MI are found for countries as Austria, Italy of Norway than the others.

The LI is in general higher for highly populated areas, that is, for countries as The Netherlands, Belgium, UK, France and Germany. These two last countries are better correlated with each other and they show better correlations with "Emask", proving that the average loss in terms of LI in Europe comes mainly from them. In summary, the LI and MI are good representations of losses for this study, however, the limitations of the data in terms of spatial resolution must be taken into account.

Regarding the *High-loss tracking*, the results show that the method is able to correctly select trajectories using only the latitude and longitude points of storms and a 2D LI/MI field, though it can be improved. The 500km radius area is a good approximation for an area of "impact" of a windstorm but is too large (in the case of the Mediterranean storms) and too small in the case of large storms as "Vivian", creating artefact storms or retrieving storms. A new radius, not fixed, but dependent on the 10-meters wind or wind gust gradients around the storm centre could be used. Moreover, the low horizontal resolution underestimates some storms. In order to increase the quality of the wind data, downscale wind or better resolution wind may be used instead on 10-meters wind. This will increase the intensity of underestimated windstorms but will increase the computing cost of the algorithm reducing the possibility of working with more than 100 years and more than twenty countries.

Despite this, the method shows good accuracy while selecting the storms, it

finds only one trajectory per day in more than in 79% of the days of study. On the other 21% of the days more than one storm is detected but no more than three storms are found. Those could be an artefact of the algorithm but, It could also be related with serial clustering, even though no deeper analysis was made on this. All countries present a maximum of density of storms associated with high LI/MI close to the country, except France that has two density maximums, one over the northwestern part of France and another over the Mediterranean. While evaluating the individual storms tracked we can see that, most of the times, when more than one storm is selected, one is located on the Atlantic side and another over the Mediterranean. The different effect of this two types of storms for France is going to be analysed in more details in the next chapter.

Predicting the reinsurance loss using the LI or the MI alone shows a poor skill. Then, an ongoing point of work between Météo-France and SCOR shows that loss predictor is improved when four parameters are used. Using a non-linear version of SVM, 60% among SCOR's extreme events can be predicted.

CHAPTER V

Characterization of high-damaging windstorms in France

In the previous chapter, it was shown how the selection of the trajectories with higher LI and MI was made for a set of European countries. In this chapter, we analyse the windstorms hitting France on a dynamical viewpoint.

As seen at the end of chapter IV, France high-damaging storms have two maxima density, one on the Atlantic side and another on the Mediterranean side. Since the cyclogenesis processes associated with these two types of storms are quite different, storms are first separated according to their relative position to France. The separation is made for three types of storms, the Atlantic the Mediterranean and the ones that cross France.
Secondly, as suggested by some previous studies (Uccellini, 1990; Rivière and Joly, 2006; Oruba et al, 2012), barotropic and baroclinic processes during jet crossing can interact and lead to a re-enforcement of the storm at this moment, resulting

in strong winds and sometimes to the sting jets. The second part of this chapter is focuses on the relevance of this crossing on storms' impacts. A classification of cyclones according to their relative position to the jet stream is made and particular attention is given to the two most frequent types, the storms that stay on the northern side of the jet and the ones that cross the jet from is warm to its cold side. A composite analysis is performed for these two types of storms but also for the three types of storms associated with the two peaks of density mention above.

In section 5.1.1 and 5.1.2 the methods used for splitting trajectories according to France and jet stream are presented respectively. The results of the splitting and some statistics in terms of Loss and Meteorological index exposed. In section 5.2, the composite analysis method is presented. In section 5.2.2 the results concerning the three composites for the types of storms separated according to their relative position to France are analysed. Finally, in section 5.2.3 the composites for the storms that stay on the north side of the jet and the ones that cross it from the south to the north are evaluated.

5.1. Analysis of the diversity of trajectories hitting France

5.1.1. Relative position to France

It was seen in the previous chapter that storms associated with high LI and MI in France have two density maxima areas, one in the northwestern side of the country and another one in the Mediterranean sea over the Lion's and Genoa's Gulf (figure 4.11). In order to perform a composite analysis, the trajectories associated with these two maxima need to be previously separated. The separation of the two maxima is a two step process. First, a broken line is defined separating approximately the southern and the northern region of France (see the black line of figure 5.1). Secondly, the trajectory paths approaching France at a distance lower than 500 km are selected. Then, the difference between the latitude of the storm and latitude of that line is computed (referred to as ΔLAT hereafter) and trajectories separated into three types : the ones with $\Delta LAT > 0$ are considered

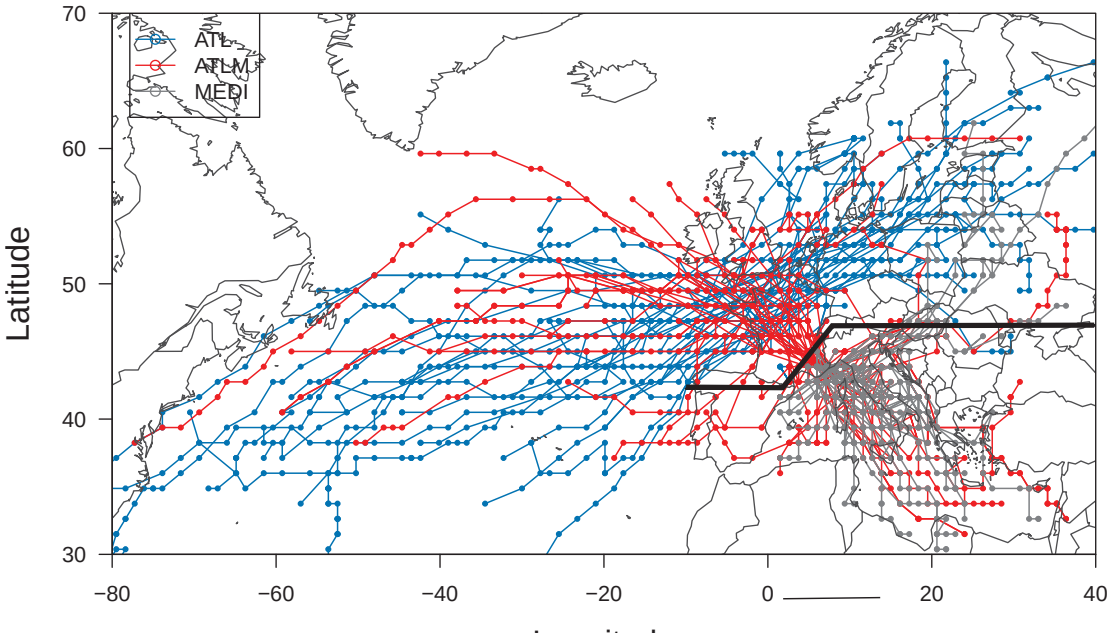

FIGURE 5.1: Trajectories for France with the highest MI separated into three categories : the ones always on the northern side of the separation line (the black straight legs), Atlantic (ATL, blue tracks) ; the ones that cross that line, Atlantic-Mediterranean (ATLM with red tracks) and the ones always south of this line, Mediterranean (MEDI, grey tracks).

as "Atlantic" cyclones and are called ATL hereinafter. The trajectories fulfilling $\Delta LAT < 0$ are considered as Mediterranean cyclones and are labelled MEDI. The trajectories that have ΔLAT that changes in sign, are associated with a cross of the line and classified as "Atlantic-Mediterranean" and labelled ATLM.

5.1.1.1 *ATL ATLM and MEDI impacts*

Figure 5.1 shows the results of the aforementioned separation of storms with the *ATL* storms, in blue, the ATLM in red and finally the MEDI in grey. The ATL trajectories are the ones that have a wider longitude extension, starting on the western side of the Atlantic basin, crossing it and ending on the eastern side of Europe. The MEDI trajectories, on the contrary, are constricted to the Medi-

terranean area between the southern side of France and Greece, with only some trajectories progressing further North. The ATLM trajectories, as the ATL ones, also cross the Atlantic within northwesterlies whereas the ATL ones are rather associated to westerlies. Nevertheless, ATLM cyclones converge between the Lion's and Genoa's Gulf as they enter the Mediterranean. The ATL, ATLM and MEDI storms correspond to 61%, 17% and 22% of the total number of trajectories affecting France.

Type of trajectories

After splitting the trajectories, we analyse some parameters of the three types of trajectories, particularly the Loss and Meteorological indexes.

Figure 5.2 shows in the z axis and in colours, the $MImax_{track}$ (left column) and $LImax_{track}$ (right column) of the trajectories as a function of the displacement speed (x axis) and Area (y axis) for the ATL (figures 5.2a and 5.2b) ATLM (figures 5.2c and 5.2d) and MEDI storms (figures 5.2e and 5.2f). Events with the highest values are labelled using the corresponding date.

First of all, in some cases, an increase in $MImax_{track}$ is observed for storms with a large area. On the contrary, no apparent relationship between the speed and the $MImax_{track}$ can be found.

One can remark that the typical area and displacement speed are very different for each type of trajectories. The MEDI trajectories (figures 5.2e and 5.2f) are mainly concentrated on the bottom left side of the graph, which means they have low displacement speed and low area values, going in agreement with the typical size and displacement speed we find in the literature (Trigo et al, 1999). ATL and ATLM trajectories (figures 5.2a to 5.2d), on the contrary, show a large variability in terms of displacement speed. This is related to the fact that these storms are born on the western side of the Atlantic basin and travel eastward following the upper-level winds on the Atlantic ocean (Schultz et al, 1998). Also, Figures 5.2c and 5.2d suggest that cyclones crossing France (ATLM) have larger areas whereas ATL ones (figures 5.2a to 5.2b) are rather marine cyclones affecting

marginally the continent or affecting France over a short period of time and, thus, with smaller areas. Moreover, ATL cyclones have rather low MIMAX which is consistent with the fact that those storms marginally affect France. Nevertheless, the strong LIMAX reached by some ATL cyclones suggests that in those cases the most populated area (Paris, as far as France is concerned) are affected. High MIMAX found for ATLM cyclones are consistent with their size : more points with positive MI are obtained for this type of storms (Note that the Area is computed from the MI which is 0 over the ocean). However, no strong LIMAX are found in this type of storms. It can be inferred from this very first analysis that ATLM storms are large-scale mature storms travelling within north-westerly upper-level flows.

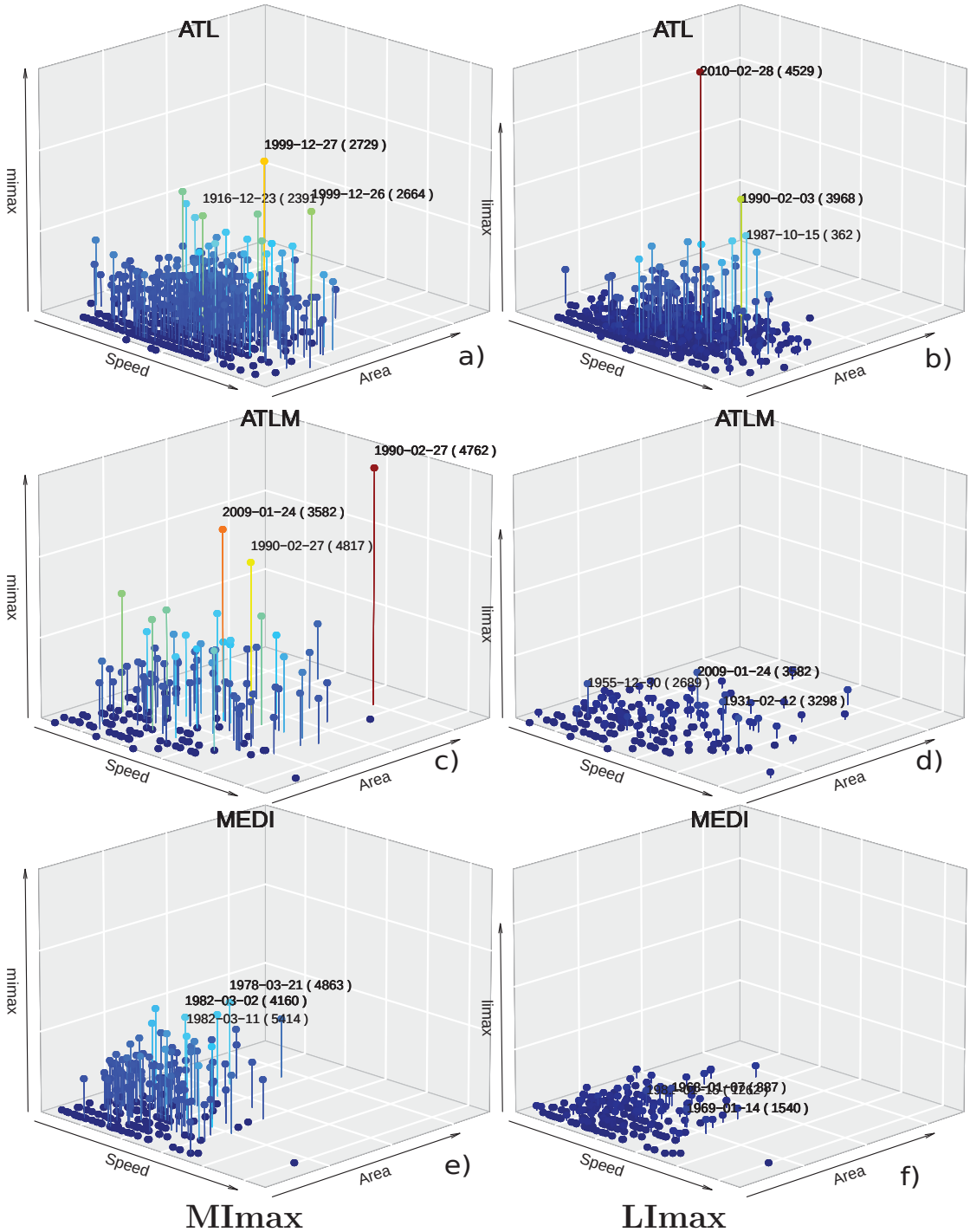

FIGURE 5.2: Mimax (left columnn) and LImax (right columns) in the Z axis and colours as a function of the displacement speed of the trajectory and Area of each trajectory of the ATL type(a and b) ; ATLM ; (c and d) MEDI(e and f).

MI and LI

$MImax_{track}$ are generally weaker for the MEDI trajectories (figure 5.2e) and higher for the ATL and ATLM (figure 5.2a and c). This demonstrates that the tail of the wind probability density function associated with MEDI cases is narrower than for the ATL/ATLM ones. This together with the fact that MEDI storms are the slowest of the three types, go in agreement to what was previously mentioned in chapter IV. In the case of two storms found at the same time by the *High loss tracking method*, one ATL/ATLM and another one belonging to the MEDI class, it is more likely that the damage is related to the ATL or ATLM storms than with the MEDI.

The top storms with high $MImax_{track}$ for the ATLM type are Klaus (Liberato et al, 2011; Rivière et al, 2015b) and two cyclones on the 27th of February 1990, both secondary vorticity maximums of the storm "Vivian" (Mathias Dobbertin, 2002) as shown in figure5.3. For the ATL type, the extreme cases found are Martin, Lothar (Wernli et al, 2002; Rivière et al, 2010) and a storm in 1916 (NYT, 1916).

Regarding the distribution of the maximum $LImax_{track}$ (right column of figure 5.2) for the three types of trajectories, the ATL trajectories are associated with high $LImax_{track}$, while the other types, ATLM and MEDI, have weaker $LImax_{track}$. In fact, the trajectory density of the ATL storms (figure 5.1) may explain this. These trajectories are at further north latitudes than the other two types of storms. These areas are the most populated ones in Europe, even for France, where the city of Paris is located. The probability of reaching highly populated areas is higher for these storms and may explain the highest $LImax_{track}$. The ATLM storms enter France further south and west, having a lower probability of reaching big cities like Paris France.

The top three $LImax_{track}$ storms observed for ATL are Xynthia in 2010 (Liberato et al, 2013; Vinet et al, 2012), Herta in 1990 and the Great storm of 1987 (Browning, 2004; Prichard, 2012).

Surprisingly, the storm with maximum $MImax_{track}$, "Lothar" (figure 5.2a) does not display a strong $LImax_{track}$. This demonstrates the importance of the population density index and the trajectory of the storm. As mentioned in chapter II, Lothar's winds from the reanalysis do not pass over the highly populated region of France (figure 2.4 of chapter II) due to the coarse time and spatial resolution of the data. Over Paris, the wind caused by Lothar is lower than the wind caused by Xynthia and consequently, this last one has higher $LImax_{track}$.

For the ATLM storms, the maximum $LImax_{track}$ is obtained for the storm Klaus (Rivière et al, 2015b; Liberato et al, 2011), yet, less intense than ATL's $LImax_{track}$. No evident relation between the displacement speed/area and the storm $LImax_{track}$ is found.

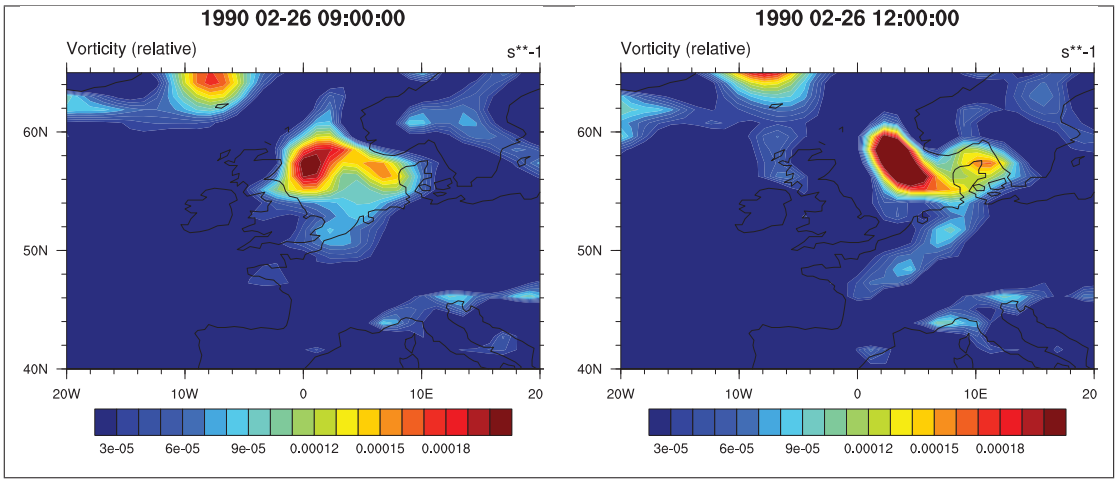

FIGURE 5.3: Relative vorticity field for the 26th of February 1990 during the passage of Strom Vivian between the UK and the Scandinavia (maximum in red). Two vorticity maximum develops southwest of the storm and cross France (on over France another over Germany). These two trajectories are the ones associated with the highest MI/LI for ATLM storms.

5.1.2. Relative position to the Jet Stream

It has been shown that to detect some of the major European events, wind-related predictors within the frame of the cyclone are relevant. Nevertheless, for some cyclones, this is not sufficient and a deeper analysis should be made. In this

sense, we will attempt to characterise the dynamical processes associated with the detected cyclones.
We focus in this chapter on the dynamical processes and, more specifically, on baroclinic interaction and relative position of the cyclone with respect to the jet axis. To do so, after separating the storms according to their trajectory type, a second classification is made according to their relative position to the jet stream. The method used is presented below.

Jet identification

The position of the storm will be calculated with respect to a low-frequency (LF hereafter) upper-level wind axis. This LF wind is defined as a seven-day run mean of the 300hPa wind module. The method consists in using the difference between the latitude of the storm (φ_s) and the latitude of the jet-stream maximum at the same longitude of the trajectory (φ_j) as shown in figure5.4a. There is one major drawback of this approach : in the case of two close jet axes, the algorithm could detect a maximum that is not related to the jet stream. φ_j is then computed in a more complex way : the maximum of the jet at the time step *t+1* is searched at the neighbour latitudes of the maximum in time step t represented by the red rectangle of figure 5.4b. The maximum of the jet for the time step t is then,

$$UV_{axis}(t) = max_{\varphi_j(t-1)-2\delta\varphi \leq \varphi \leq \varphi_j(t-1)+2\delta\varphi}(UV(\theta, \varphi, t))$$

where $\delta\varphi$ stands for the data resolution chosen, 1.125°.
This eliminates the possibility of large variations on the jet latitude.

Relative position of a vorticity maximum with respect to the Jet-Storm

The relative position of the storms to the jet stream is obtained computing the

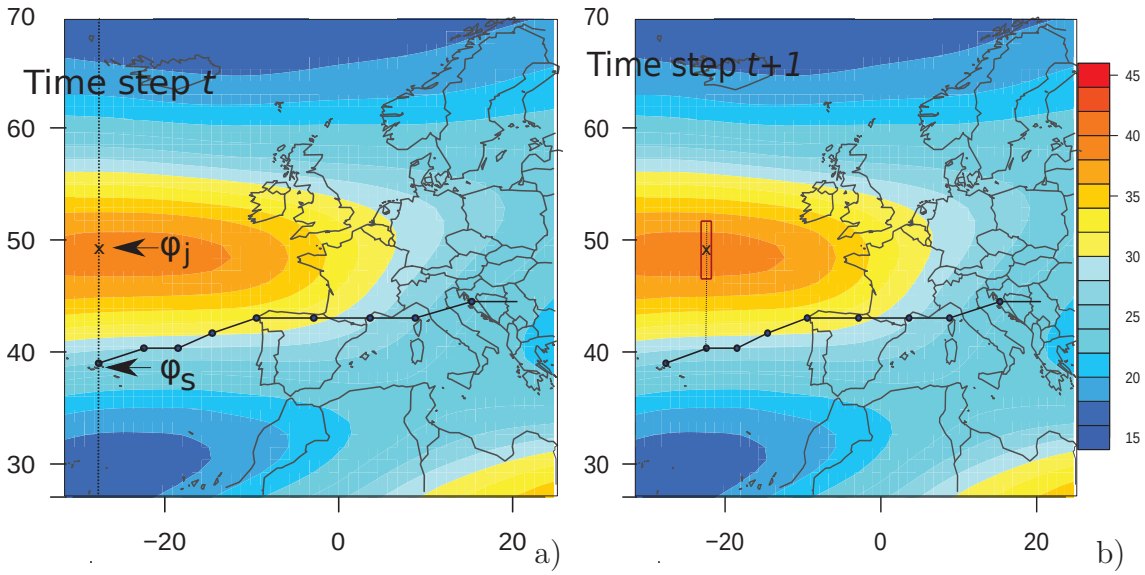

FIGURE 5.4: Schematic representation of the method used to identify the jet maximum latitude at the longitude of the storm at the first time step (a) and for the following time steps (b). The maximum latitude of the jet (φ_j) in time step *t+1* is searched at the storm longitude (φ_s) but at a latitude close to the latitude obtained in the previous time step.

difference between the jet stream and the trajectory as in :

$$\Delta\varphi(t) = \varphi_j(t) - \varphi_s(t) \tag{8}$$

We also need the time variation of the sign of that difference at each time step :

$$S(t) = \delta sign(\ \Delta\varphi(t)\ )/\delta t \tag{9}$$

Then, according to these two quantities a selection of storms in relation to the jet position is achieved. The criteria are explained below.

1. If $S(t)$ is always zero, it means that the difference between the max of the jet and the storm is always either positive or negative, and so, that there is no crossing. In this case :

   — If $\Delta\varphi(t)$ is mostly negative, the storm is classified as *Always north* if

the trajectory never stayed more than two degrees south of the jet,
— If $\Delta\varphi(t)$ is mostly positive, and the trajectory never stayed more than two degrees north of the jet, it is classified as *Always south*.

2. If $S(t) \neq 0$ then the storm crosses the jet **once** and $Tcross{=}t$:
   — If $S(Tcross) > 0$ then the storm progresses from the north side to the south side ($JET\ NS$)
   — If $S(Tcross) < 0$ the storm moves from from the south side to the north side ($JET\ SN$).

Finally, all trajectories must have a minimum duration of 24h and jet stream maximum latitude should not be greater than 20°, otherwise, the storms are excluded.
The previous method of selection enables the classification of more than 75% of the ATL trajectories. Nevertheless, the remaining 25% have more sinusoidal paths in latitude and the classification is not always clear. For those cases, a re-selection is made using some changes in the previous criteria.

Reclassification of ambiguous cases

Previously, after the first step classification, two main classes were obtained, the *JET SN* or *Always North*. This point will be discussed further in this chapter. Since there are the two main types, we decide to restrain the implementation of this second step selection only to these two types, the remaining storms are classified as *others*.

First, many ambiguous cases are found when the storm evolves slightly around the jet axis, passing several times on each side of it. This problem is handled by virtually enlarging the latitude the jet axis to $4\delta\varphi$ before computing its relative position to the storm. Consequently, two $\Delta\varphi$ are obtained, one between the cyclone and the southward side of the artificial jet, $\varphi_1(t) = \varphi_j(t) - 2\delta\varphi - \varphi_s(t)$, and another with the upper limit northward, $\varphi_2(t) = \varphi_j(t) + 2\delta\varphi - \varphi_s(t))$. Then S is replaced by S' :

$$S'(t) = \frac{\delta(\ sign(\ \Delta\varphi_1(t))sign(\Delta\varphi_2(t))\ )}{\delta t} \tag{10}$$

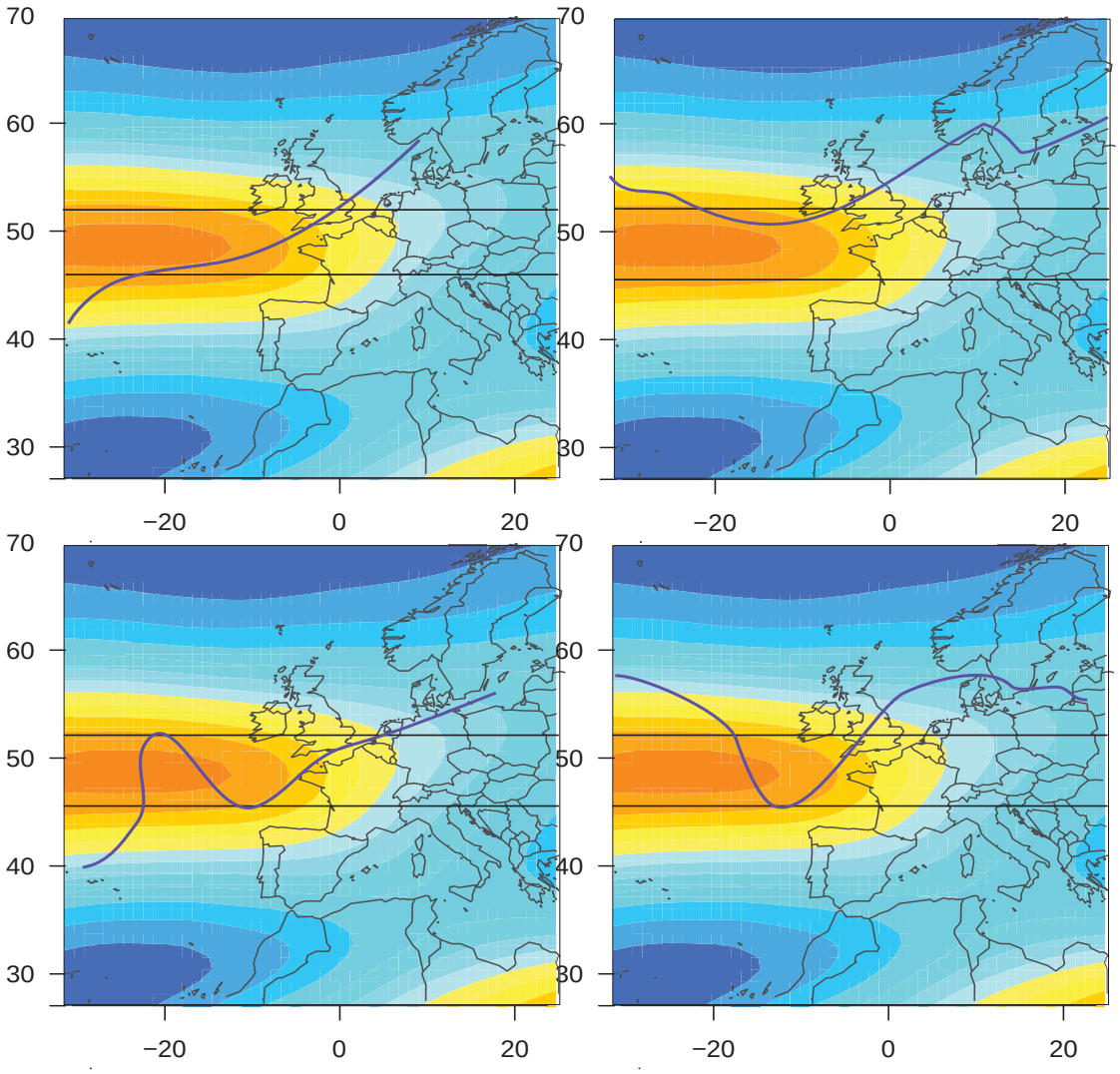

FIGURE 5.5: Schematic representation of simple *JET SN* (left) and *Alwasy North* (right) trajectories in relation to the low frequency jet for a simple case (top) and for an ambiguous case (bottom). The wider jet maximum is represented by the two black lines.

The trajectory will have a clear path with respect to the jet if $\Delta\varphi_1(t)$ and

$\Delta\varphi_2(t)$ have the same sign, and so, if their product is always positive. The separation between *Always North* and *JET SN* considers the sign evolution of $\Delta\varphi_1(t)$ and $\Delta\varphi_2(t)$. All the other storms that have $S'(t)$ below zero will have trajectories considered in this work as too sinuous. Then, if a trajectory stays more time steps north of the jet and if it never goes more than two grid points southward of the jet axis, it is classified as *Always North*. On the opposite, it is classified as *JET SN* if the trajectory stays beyond two grid points north and south of the jet, which then means it crosses clearly the jet.

A short representation of this is made in figure 5.5. The top figures represent a simple trajectory that clearly is *JET SN* (left) or *Always North* (right). The bottom figures are the ambiguous cases of *JET SN* and *Always North*. If the winder jet maximum is considered (represented by two black horizontal lines) the storm of the left crosses only once the jet and is *JET SN* and the storms on the right is *Always North* since it stays always north of the wider jet maximum.

5.1.2.1 "Jet types" impacts

The method presented before was applied for the ATL storms only. Table 5.1 shows a summary of the main characteristics of ATL sub-classes of storms with respect to the jet position and the way the cyclones eventually cross the jet. The storms are separated into several types : *JET SN* and *JET NS* for the storms crossing the jet from south to north or from north to south respectively, *Always North* for the storms that stayed always on the north side of the jet and *Always south* for the ones that stayed south and finally *others* for those that don't fit in those types.

From the 702 ATL storms used as input 84 are excluded either because they are too short (less than 24 hours) or the jet latitude variation is larger than 20°. The remaining ATL storms (table 5.1) are dominated by two types. Firstly, the *JET SN* and secondly the *Always North* that represent 35% and 33.2% of the total ATL storms respectively. The *Always south*, *JET SN* and *others* represent a minority of 13.8% 7.4% and 10% of the storms. With respect to the mean speed, the *JET SN* are the ones with highest displacement speed and Area, which means highest footprints over land. The highest values of $MImax_{track}$ and $LImax_{track}$ are also observed for the *JET SN* types. The *Always South* also show higher values

of $LImax_{track}$.

ATL	%	Speed	Area	$LImax_{track}$	$MImax_{track}$
JET SN	**35.2**	59	4.0	**3199**	2.2
Always north	33.2	48	3.4	2330	1.9
Always south	13.8	49	3.3	3114	1.9
JET NS	7.4	51	3.6	1554	1.9
others	10	59	3.7	2823	2.2

TABLE 5.1: Mean features of the 702 ATL storms when classified according to the jet stream. From the first to the fifth columns : percentage of storms found for each type and each jet type ; mean displacement speed ; mean Area ; mean $LImax_{track}$ and mean $MImax_{track}$.

Storm	Date	Speed (m/s)	$LImax_{traj}$	$MImax_{traj}$	Type	
Lothar	1999-12-26	83	2950	7.6	JET SN	ATL
unnamed	1916-12-23	55	5464	7.2	Alw. north	ATL
unnamed	2003-01-02	63	26770	6.9	others	ATL
unnamed	1984-11-16	26	6954	6.8	others	ATL
unnamed	1992-12-04	81	2696	6.8	JET SN	ATL
Channel Islands Storm	1964-10-09	61	3637	5.7	JET SN	ATL
Boxing Day storm	1998-12-20	32	3625	5.4	others	ATL
unnamed	1980-11-30	16	4509	5	JET NS	ATL
Xynthia	2010-02-28	48	77177	5.1	JET SN	ATL
Herta	1990-02-03	74	43300	5.1	Alw. south	ATL
The Great Storm	1987-10-15	64	27489	4.9	JET SN	ATL
Verena	1993-01-13	93	18598	3.1	JET SN	ATL
Vivianbis1	1990-02-27	72	4817	14.7	Alw. south	ATLM
Klaus	2009-01-24	40	12819	11.37	JET SN	ATLM
Vivianbis	1990-02-27	48	5854	9.3	Alw. south	ATLM

TABLE 5.2: Jet-crossing classification of some of the first storms with the highest $MImax_{track}$ for the ATL type.

With respect to some particular cases, table 5.2 presents a list of historical storms with the highest $MImax_{track}$ found for the ATL and ATLM types. Among

them, *JET SN* cyclones are expected to be well represented according to the results of tables 5.1.
The storms "Lothar" (Wernli et al, 2002; Rivière et al, 2010), "The Great Storm" (Browning, 2004), "Klaus" (Liberato et al, 2011) or "Xynthia" (Rivière et al, 2012) are found to be crossing the jet as mentioned in several studies. In addition, some older storms with high $MImax_{track}$ are classified *JET SN* as the storm of 1964 and the early 1993 storms "Verena" and two unnamed and unknown storms in December 1992 and November 1980. None of them has been studied by the scientific community. There are few storms either *Always North* or *Always South* among the ones with high $MImax_{track}$.
Finally, three major storms are classified as *others*, i.e., their trajectory in relation to the jet is not clear enough to be placed in one of the other categories.

From a more general point of view, a simple projection of trajectories helps us to better understand some of the classifications obtained above.
Figures 5.6 shows the trajectories (left column) and the density (right column) of the main types of trajectories mentioned above for the ATL storms.

The density of the ATL trajectories from figure 5.6 (right column) show that *JET SN* and *Always North* dominate storm's classes as mentioned before, since the corresponding density maps are more intense (figures 5.6b and 5.6d). Moreover, most of these trajectories emerge over the eastern coast of North American continent and are characterised by long trajectories. They are longer and more north for the *JET SN* than for the *Always North* (figures 5.6a and 5.6c). The *Always South* and *JET NS*, in contrast, have short trajectories with genesis in the middle of the Atlantic ocean and do not extend far eastwards (figures 5.6e and 5.6g). The main difference between these two types lies in the latitude of the genesis of storms. *JET NS* (figures 5.6g) start at much higher latitudes than the *Always south* (figures 5.6e) which, on the contrary, have genesis at more subtropical latitudes over the west coast of Iberia and Morocco.

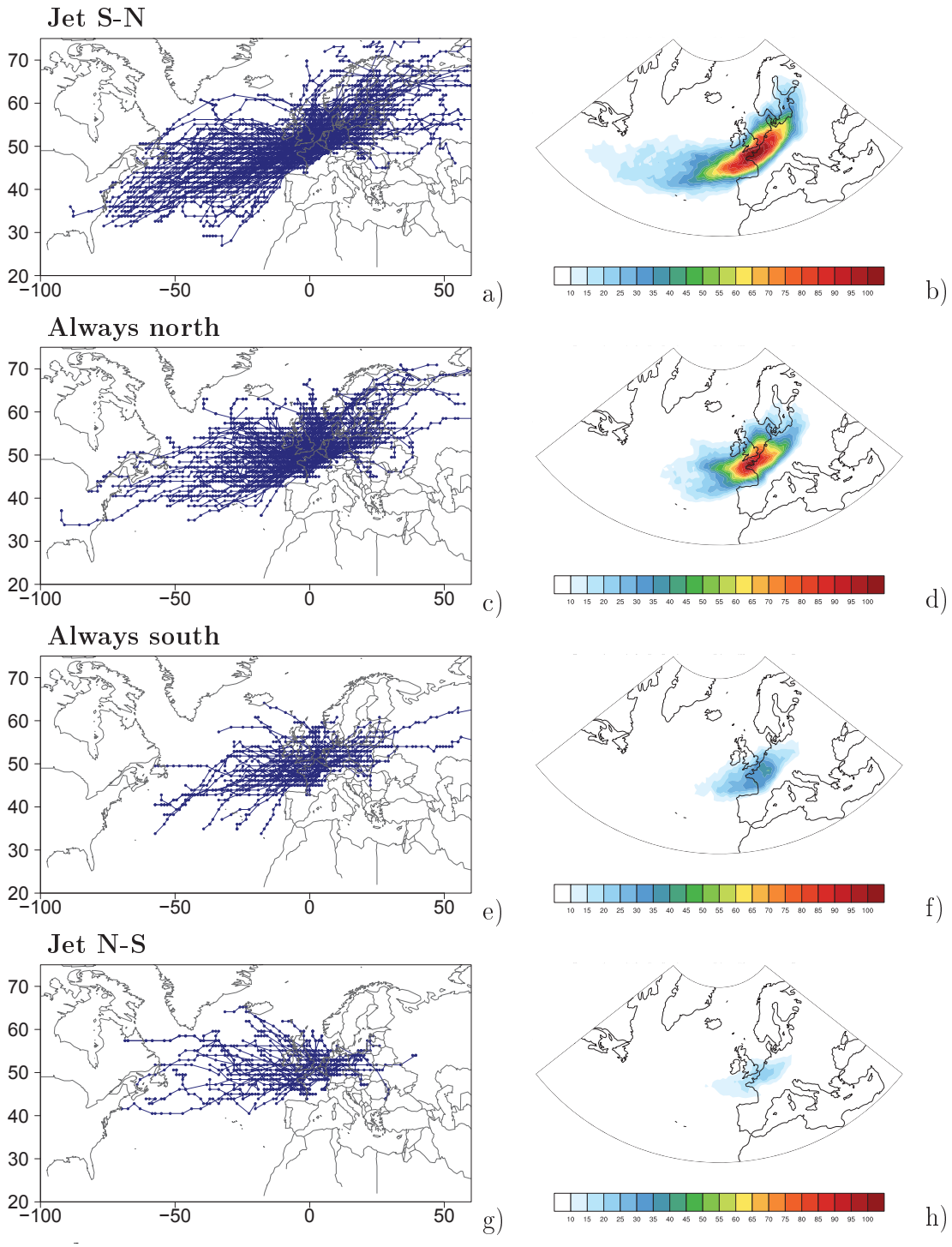

FIGURE 5.6: Trajectories (left) and Densities (right) of trajectories types for the ATL storms.

5.2. Composite Analysis

5.2.1. Method

To achieve the analysis of some dynamical processes within the environment of the storm, we handle a composite analysis. It is based on averaging several atmospheric parameters within an area around the storm centre at specific common time steps and follow them from a Lagrangian point of view.

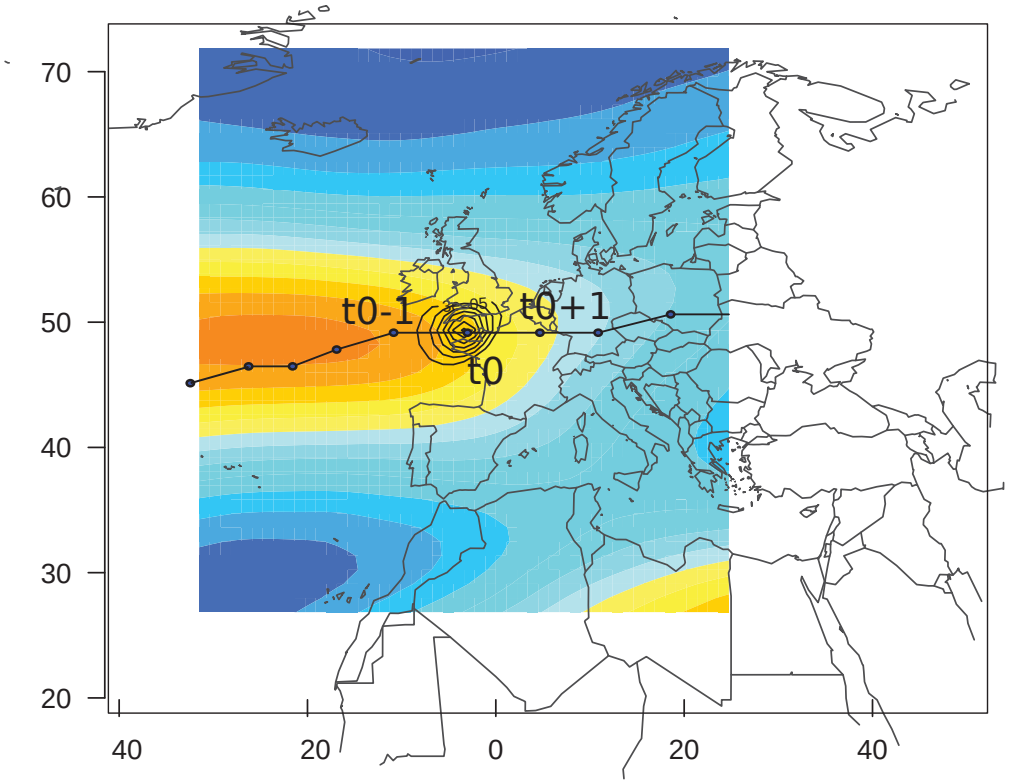

FIGURE 5.7: Scheme representing a wind composite field (color) obtained at a the moment *t0* (storm is the the closest possible to France). This is made at every 3 hours for the previous (and following) four days of the moment when the storm is close to France (*t0*).

Before averaging the fields, they are synchronized referring to a time mark *t0*, which in our case is chosen to focus on storms associated with losses in France. *t0* of this composite analysis is the moment when storms reach France mainland for the first time (figure 5.7). In the case of not touching the France mainland, *t0*

is considered as the moment when the storm is the closest possible from France. The moment of maximum vorticity could also have been chosen for a better perspective on storm life cycle analysis. However, our choice highlights the large-scale atmospheric characteristics of high-damaging storms.

For each storm trajectory assembling the composite, all time steps are retained when available in an eight days time windows (60 δt) centred on *t0*. At each timestep, the atmospheric variable of the composite is first extracted within a box of 45°in latitude and 55°in longitude, and then, averaged for all storms as shown by the coloured area of figure 5.7. Then, this mean composite field is positioned at the average location of the storm centre. Numerous variables are composited with this method : relative vorticity at 850 hPa ; wind intensity at 300, 850 hPa and at 10-meter ; HFmeridional wind at 300 hPa ; air temperature at 300, 500, 700 and 850 hPa and Geopotential height at 300, 500, 700 and 850 hPa.

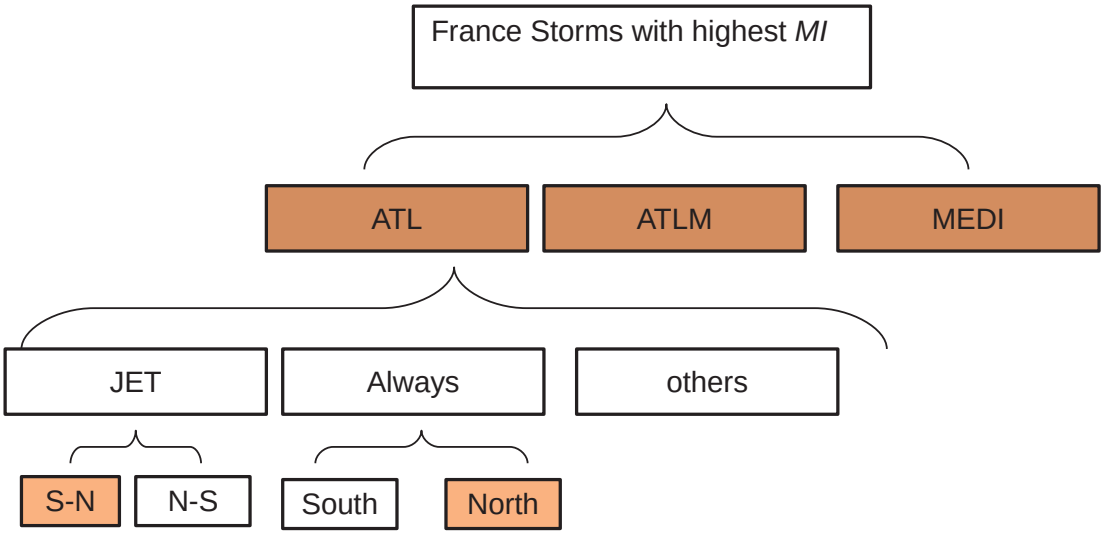

FIGURE 5.8: Representative diagram showing all the selections of storms made since chapter IV until now. Orange boxes represent the storms types to which a composite analysis is applied.

. Before advancing on the composite results, a summary of the storm's classifications made so far should be done. First, a catalogue of high-damaging ($MImax_{track}$) storms for France has been computed for the whole twentieth cen-

tury. The storms impacting France have two density maxima, one on the northern side of France and another over the Gulf of Lyon/Genoa. For this reason, storms have been separated into three categories, ATL, ATLM and MEDI, on which the composite analysis will be first carried out (figure 5.8). Then, two storm types be calculated their relative position to the jet-stream are studied *JET SN* and *Always North* only for the ATL type. It was chosen to study only these two types because of a large amount of trajectories obtained for this type in comparison to the others and they are also the ones for which the classification is less ambiguous.

5.2.2. ATL ATLM and MEDI composites

The first results to be presented are the composites of the trajectories of type ATL, ATLM and MEDI. The number of trajectories used at each time step is presented in figure 5.9. As seen before ATL is the type to which more trajectories are associated, not only in total but also per time step, with a good amount of storms obtained even in the first and last time steps (blue line of figure 5.9). The ATLM and MEDI storms have fewer storms more particularly in the first time steps (red and grey lines of figure 5.9). Close to *t0*, they increase rapidly, which could be related to many emerging storms. This is congruent with the observed short trajectories with genesis close to the European continent of figures 5.6.

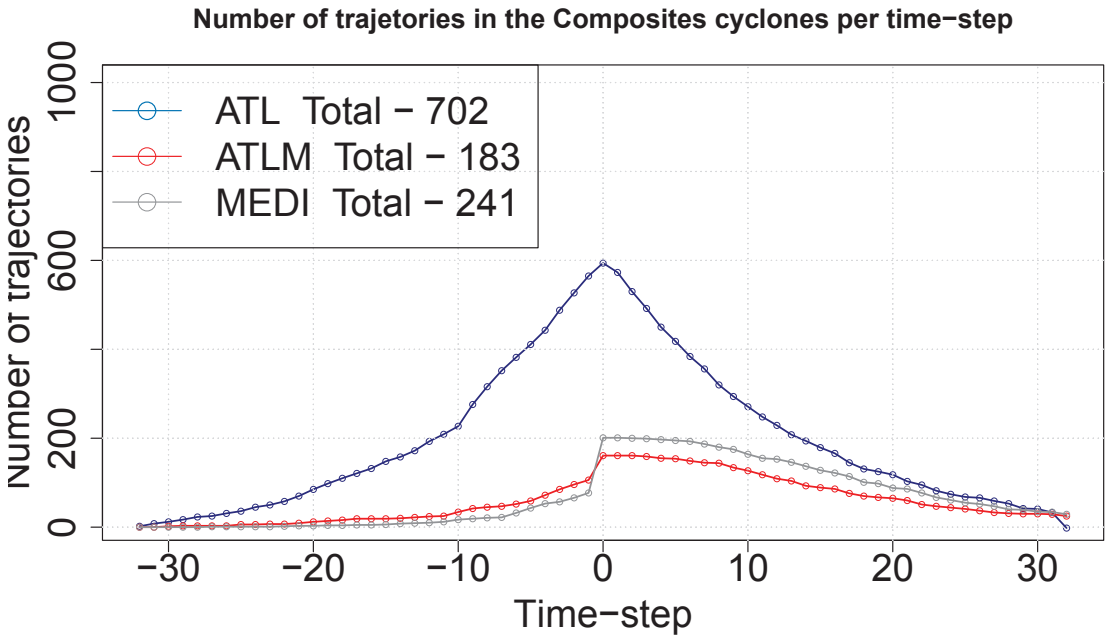

FIGURE 5.9: Number of trajectories used at each time step of the composites for the 3 types of trajectories, ATL, ATLM and MEDI.

Some composite fields are presented in figures 5.10, 5.11 and 5.12 for the ATL (left column) ATLM (middle column) and MEDI (right column). In figure 5.10 we present horizontally the composites according to time steps *t-15* (upper line), *t-13* (middle lines) and *t-8* (lower line), only for the ATL storm classes (MEDI and

ATLM classes have few storms and noisy fields at these time steps). For the time steps *t-3* and *t0* and *t+3* in figure 5.11 and finally for *t+5* and *t+10* and *t+15* in figure 5.12. Several differences between the three types are observed throughout the time steps.

First, the upper-level LF jet (UV300) (green lines of figures 5.10, 5.11 and 5.12) is more strong and more zonal with time in ATL while ATLM and MEDI present an anticyclonic curvature. Besides that, ALT cyclones, tend to cross the jet from the southern side towards the northern side while ATLM and MEDI cyclones stay beneath the left-jet exit.

Secondly, the HF meridional wind at 300 hPa (V300 hereafter), representing the signature of an upper-level trough or Potential Vorticity anomaly (colours of figures 5.10, 5.11 and 5.12) is noteworthy during the growing phase and constructive baroclinic interaction. It is found in the 3 cases since the surface cyclone is beneath upper-level southerly winds.

Then, ATLM and MEDI share common features (middle and right columns of figures 5.10, 5.11 and 5.12) . For instance, the jet structure (magnitude, location and curvature) are comparable in both cases. Nevertheless, MEDI look like explosive cyclones with genesis close to *t0*, while ATLM are preexisting cyclones forming over the Atlantic ocean and France with no further intensification over the Mediterranean. Moreover, the upper-level precursor is more developed for MEDI cyclone developments. The fact that the southerly wind branch is stronger than the northerly one can be due to the presence of an ridge downstream. It would make sense to look at diabatic processes to understand the differences between both classes.
The last difference is the horizontal tilt which shows clearly a tendency of anticyclonic wave breaking. Interaction with the subtropical jet could be envisaged though we do not provide any demonstration in this dissertation.

Finally, the 10-meter wind module composites are presented here in figures 5.13 and 5.14 for fewer time steps. As for the previously verified, the wind is very

different among the three types.
The ATL storms are the ones with the strongest winds that increases alongside with relative vorticity(RV) and V300 until *t-3* (figure 5.14a). The ATLM and MEDI show weaker winds around the RV maximum. However, they show an important feature. From time step *t-10* until time step *t0* a 10-meter wind maximum is located on the northwest side of France (figure 5.14f and and 5.15c). This could have two interpretations.
On the one hand ,this suggests that some MEDI storms exist at the same time that a large Atlantic cyclone exists. This goes in agreement with results obtained from figure 5.2 and with the idea that the detected MEDI storms are not necessarily associated with damage. However, we cannot discard the fact that some of the MEDI storms are able to create strong winds and provoke serious damage.
On the other hand, the ATLM and MEDI UV300 are very similar, which suggests a relation between them. For instance, the ATLM storms could provide the conditions for the development of some MEDI storms. This remains an open question that requires further analysis to be answered.

In summary, the previous results show that ATL storms are not only more numerous, but also more intense and dynamic. They are associated with a stronger and more zonal jet stream and with stronger 10-meter winds. This proves that a separation of storms according to their relative position to the jet stream is, indeed, more appropriated for this type of storms.

ATLM

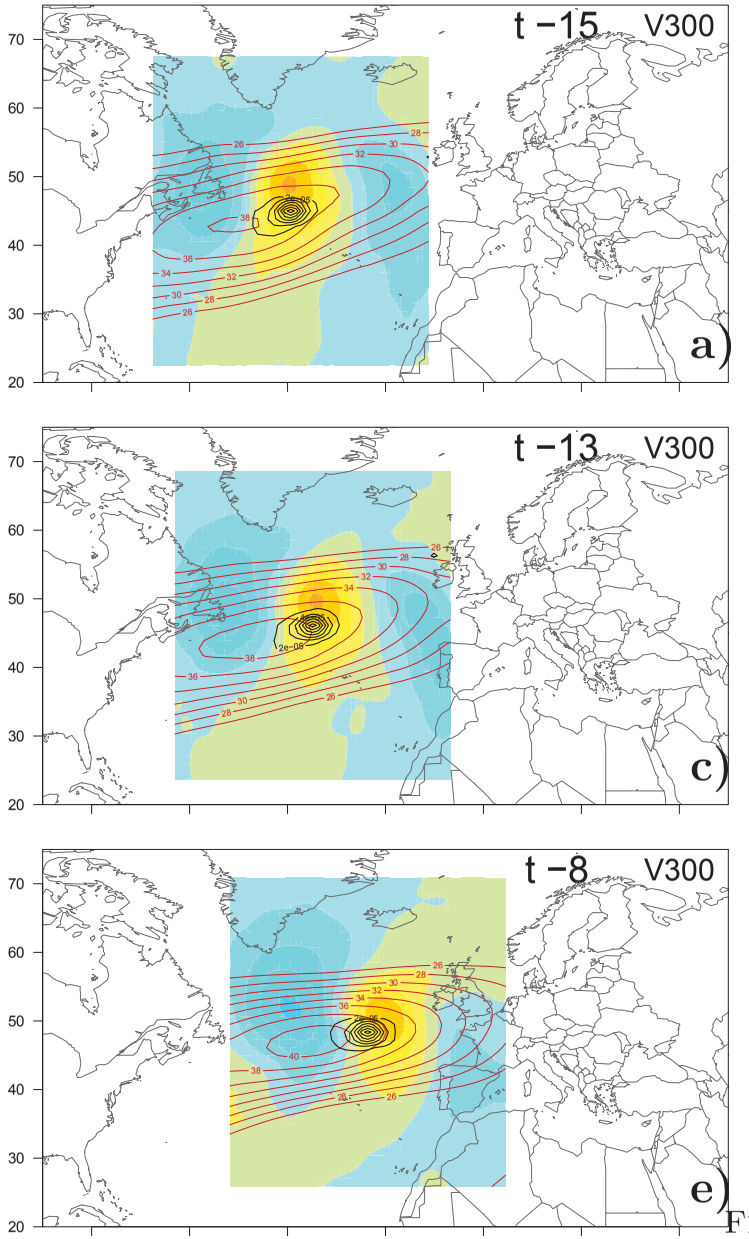

FIGURE 5.10: Composites fields at time steps *t-15, t-13* and *t-8* of relative vorticity maximum (black contours), HF meridional wind at

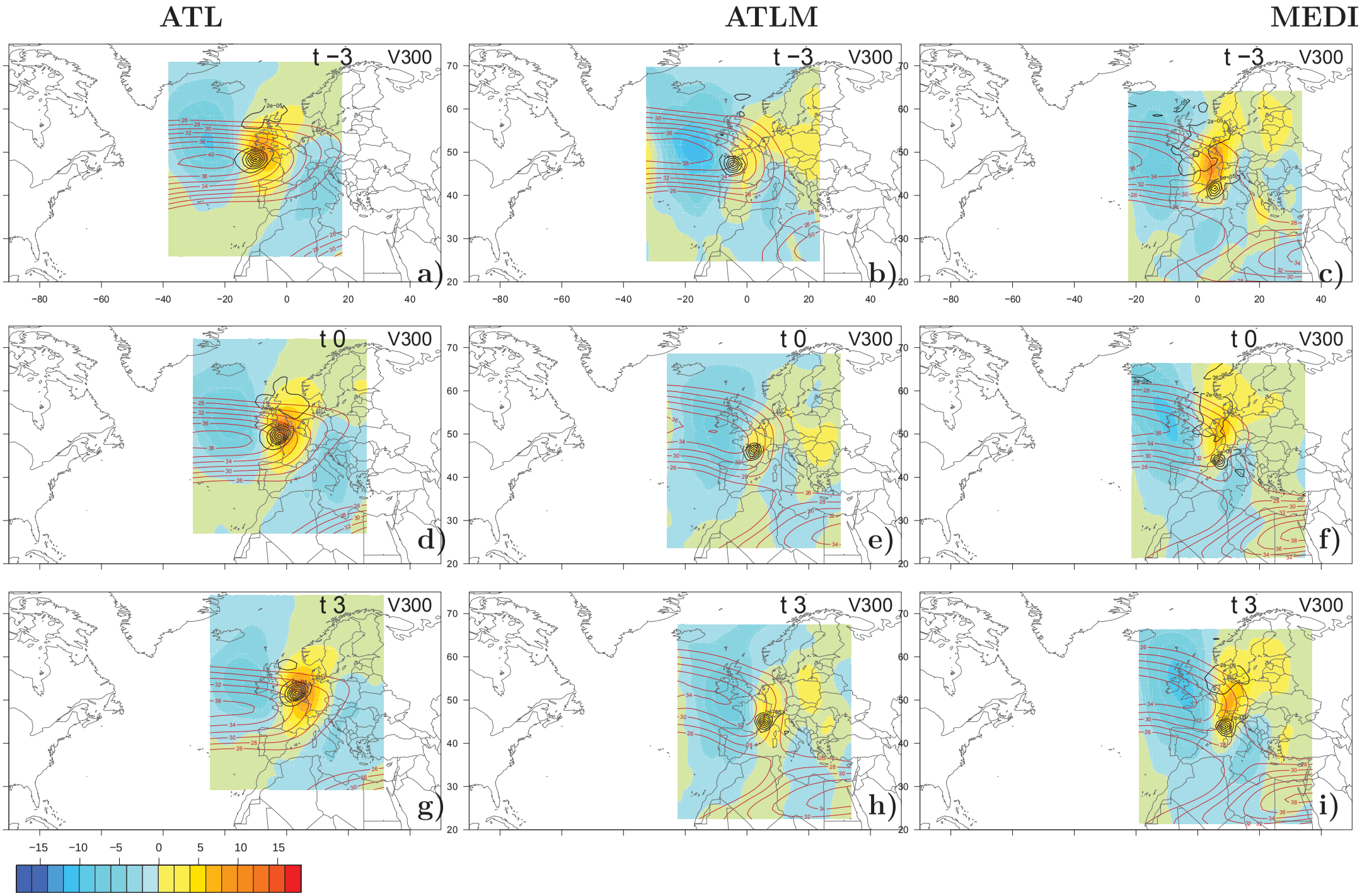

FIGURE 5.11: Same as 5.10 but for the time steps *t-3*, *t0*, *t+3*.

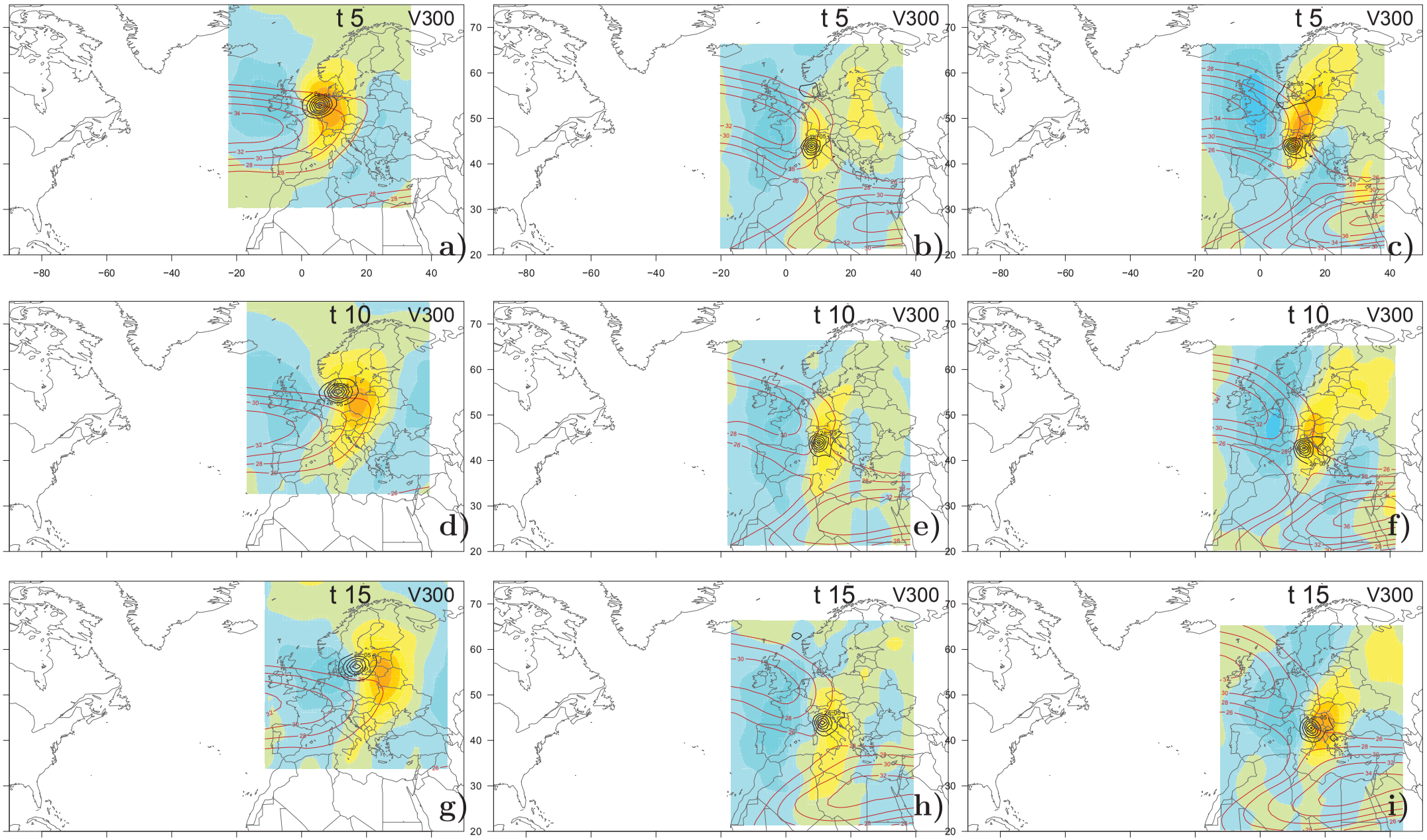

FIGURE 5.12: Same as 5.10 but for the time steps *t+5*, *t +10*, *t+15*.

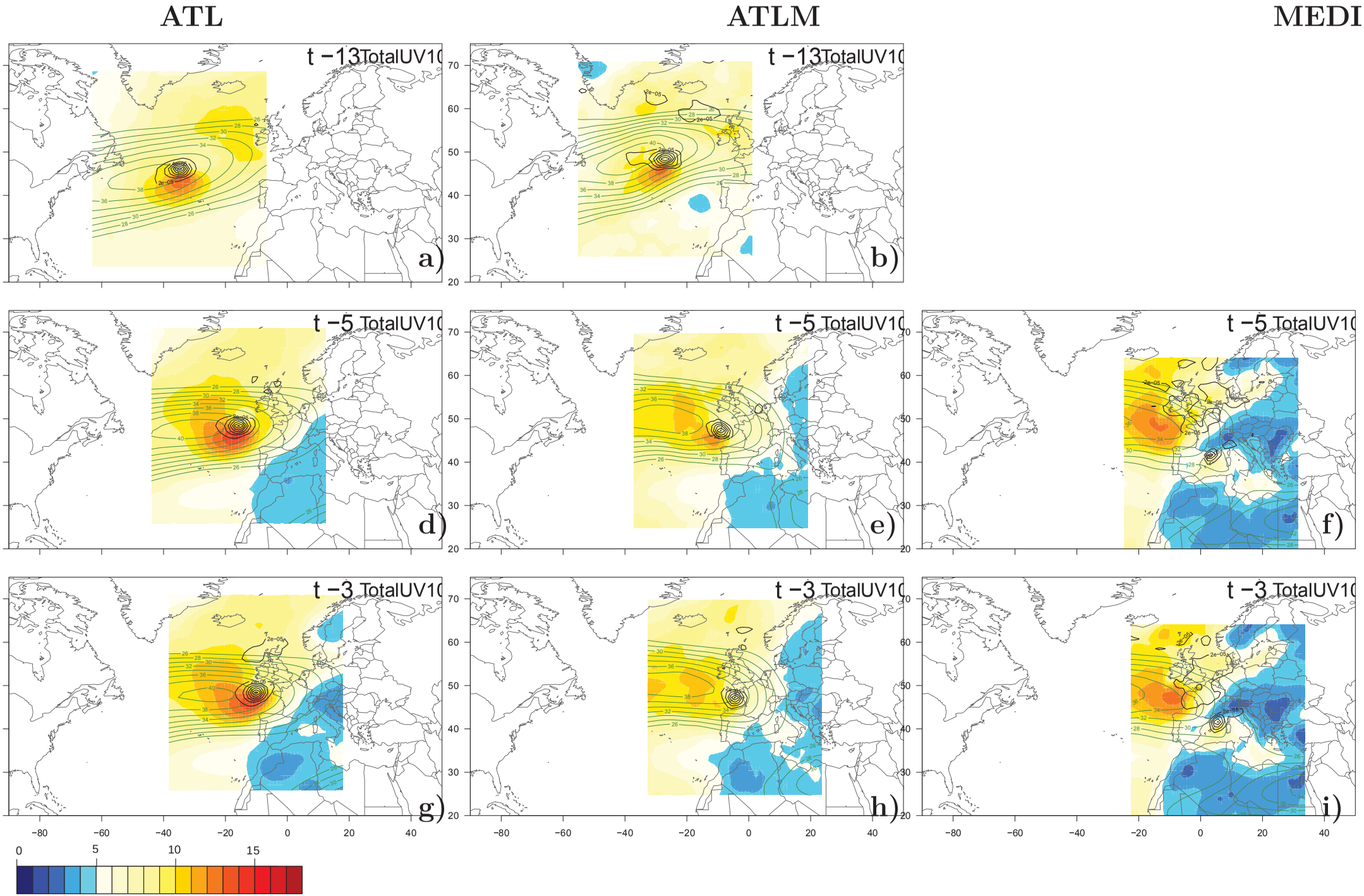

FIGURE 5.13: Composites fields at time steps *t-13 t-5* and *t-3* of relative vorticity (black contours), 10-meter wind (shaded colours) and LF 300 hPa upper-level winds in green contours.

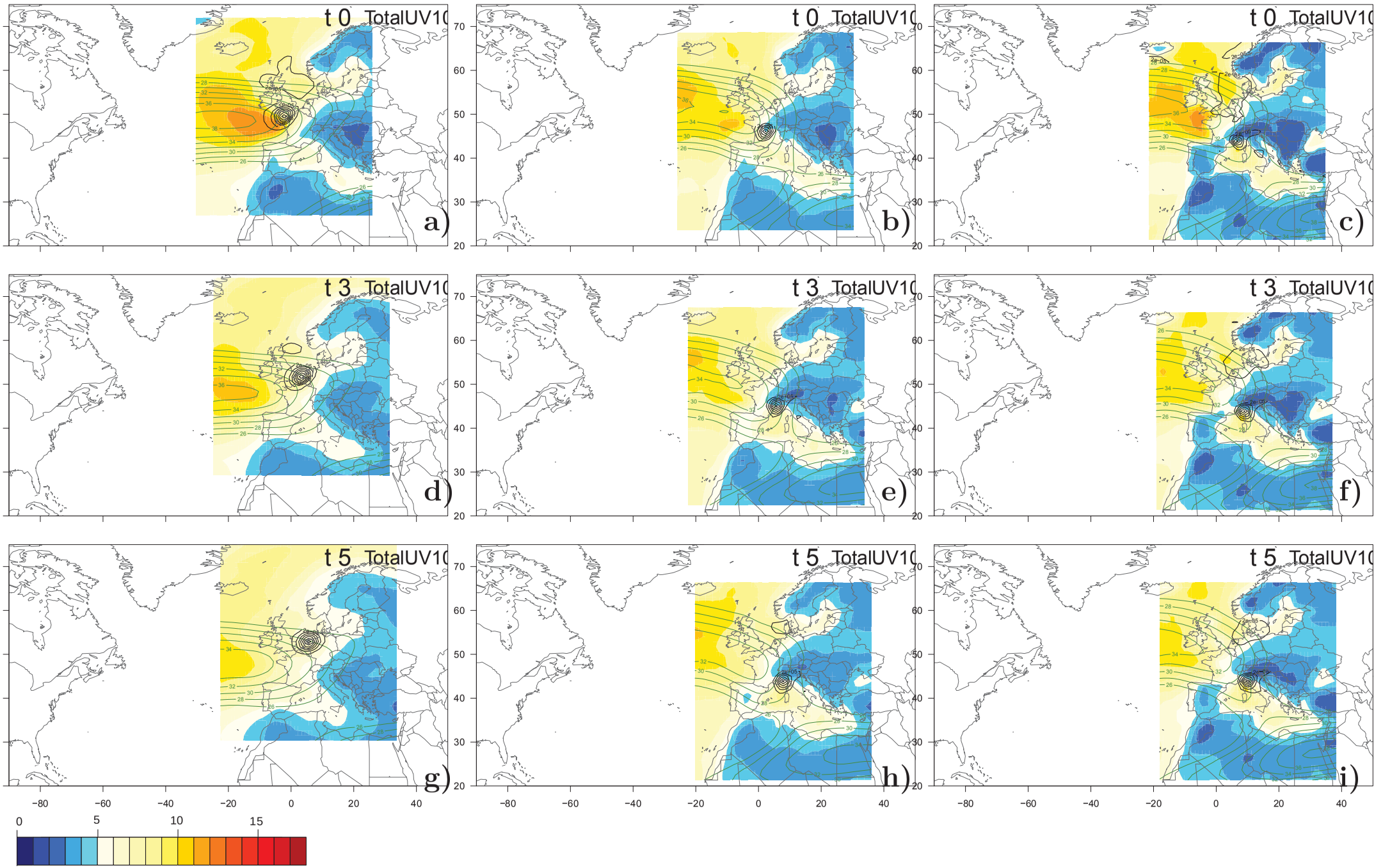

FIGURE 5.14: Same as figure 5.13 but for *t0*, *t+3* and *t+5*.

5.2.3. *JET SN* and *Always North* composites

We have shown that the ATL storms are the ones more frequent and with stronger 10-meter and upper-level winds. These storms were separated into several categories according to their position in relation to the jet stream.
The number of storms per time step for the five categories of storms is presented in figure 5.15. As, expected the *JET SN* and *Always North* are the ones with more trajectories per time step, with a minimum that doesn't go below ten storms per time step. All the other types show less than a half of the storms. For this reason, only these two last types are going to be more deeply studied.

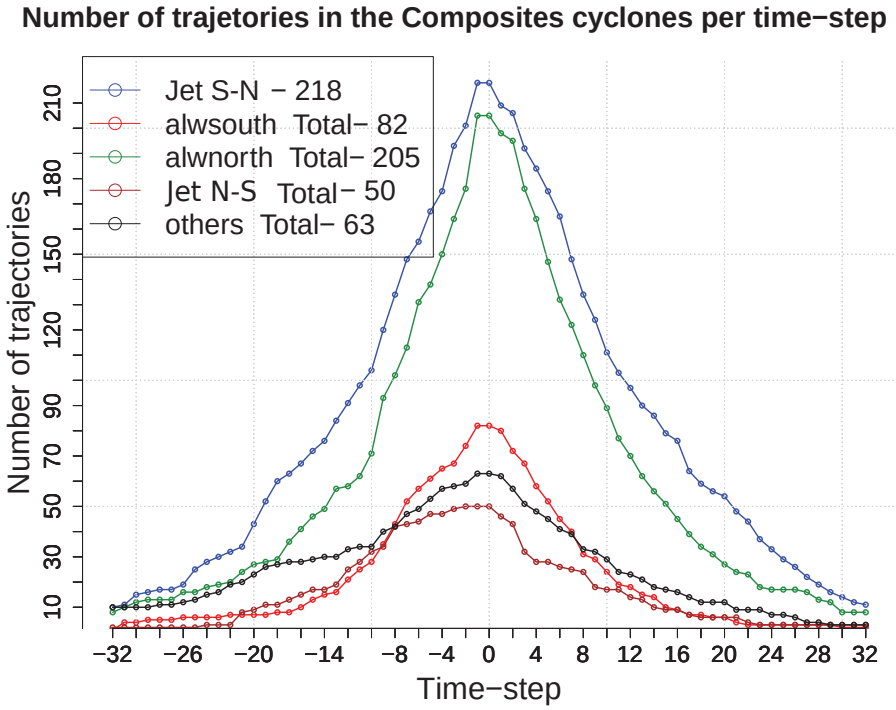

FIGURE 5.15: Number of trajectories used at each time step of the composites for the 5 types of trajectories separated according to their relative position to the jet stream .

We analyse here the same variable composites as in the previous section,V300, UV300 and RV maximum, with the insertion of the position of the maximum UV300 at the longitude of the storm at each time step (red star-dashed line) on

figures 5.16, 5.17 and 5.18.
The first clear difference between between *JET SN* and *Always North* is the position and intensity of the jet-stream (green lines figures 5.16 and 5.17 and 5.18). The *JET SN* storms (left panels) have a more intense and North jet-stream that the *Always North* (right panels) throughout all the time steps (Gronas, 1995; Nielsen and Sass, 2003; Rivière et al, 2010). It is attested by the latitude of the mean UV300 maximum (red-dashed line) much more north for the *Jet SN*, particularly in the first time steps around 50 N, and 35 N for the *Always North* at *t-18* (figure 5.16a and b). While approaching *t0* the jet becomes more tilted to the southern latitudes for the *Always North* and for the *Jet SN* it becomes more zonal.
With respect to the HFV300 (colours in figures 5.16 and 5.17 and 5.18), the *JET SN* show stronger values throughout all time step, while the *Always North* doesn't change much, suggesting a weaker intensification for these last ones. The location of it is also different in the two storm types. The *JET SN* V300 is located northward until *t0* and progresses east after that, while the *Always North* are mostly located east.

The maximum RV for the *JET SN* crosses the jet axis between *t-3* and *t-1* (figure 5.17c and 5.17e). At the moment of crossing the storm translates to the left-exit side of the jet stream while in the previous time steps was located south of the jet core. The *Always North*, on the opposite travel mostly on the left exit side of the jet.
Some authors have shown that RV maximums tend to stretch southwest-northeast (Northwest-southeast) while in the anticyclonic (cyclonic) side of the jet (Gilet et al, 2009). Here, no stretch on the *JET SN* RV maximum can be identified, probably due to the fact that the storms are not centralized at the moment of crossing and consequently are not at the same maturity stage.

The temporal evolution of the *JET SN* and *Always North* relative vorticity per time step is observed in figure 5.19. The black line represents the mean and the coloured rectangles the boxplot of all storms per time step. Only the time steps where more than fifteen storms exist are taken into account.

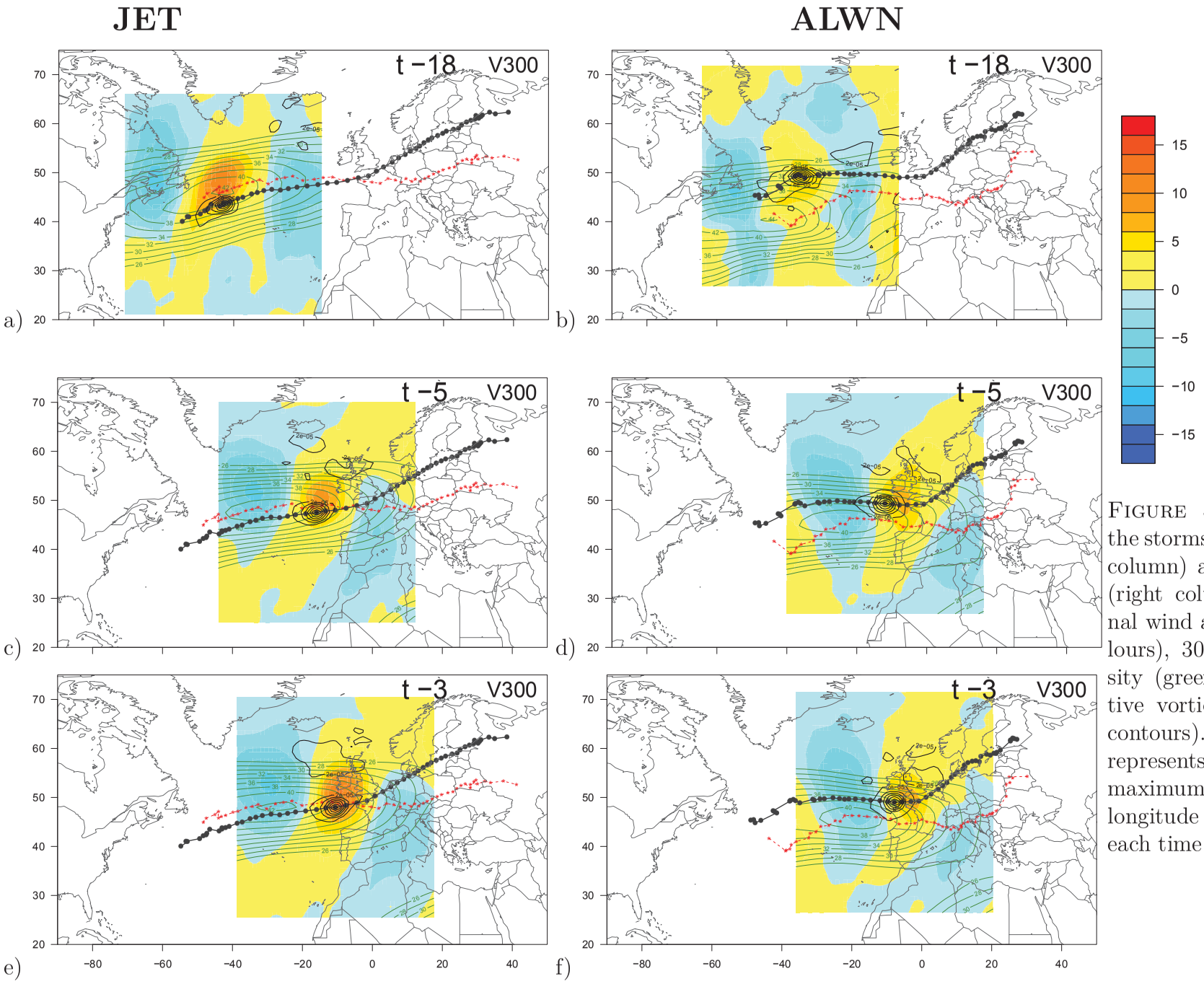

FIGURE 5.16: Composites for the storms that cross the jet (left column) and stay always north (right column) of HF meridional wind at 300hPa (shaded colours), 300hPa LF wind intensity (green contours) and relative vorticity maximum (black contours). The red-dashed line represents the location of the maximum UV300 at the same longitude of the trajectory at each time step.

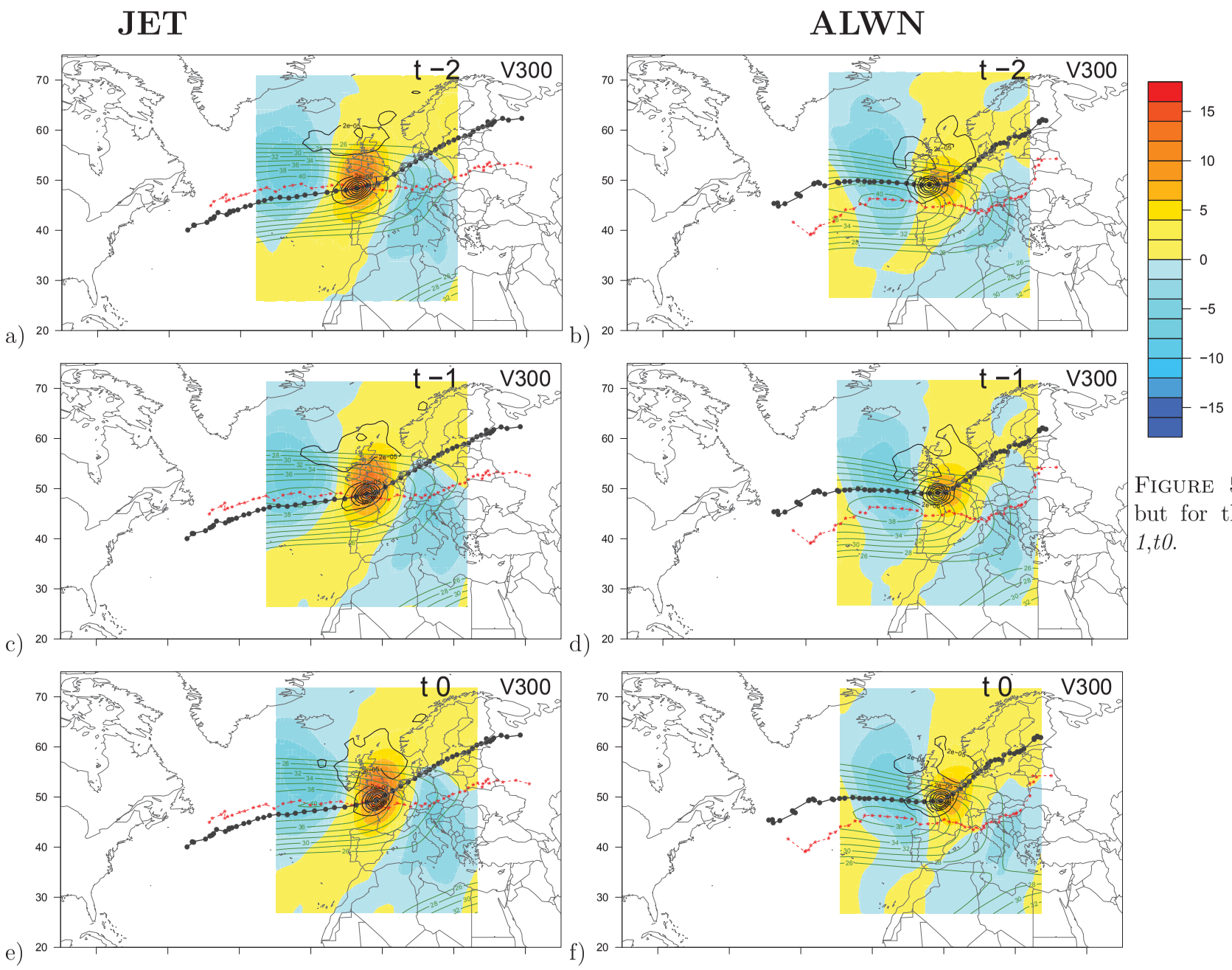

FIGURE 5.17: Same as 5.16 but for the time steps *t-2*,*t-1*,*t0*.

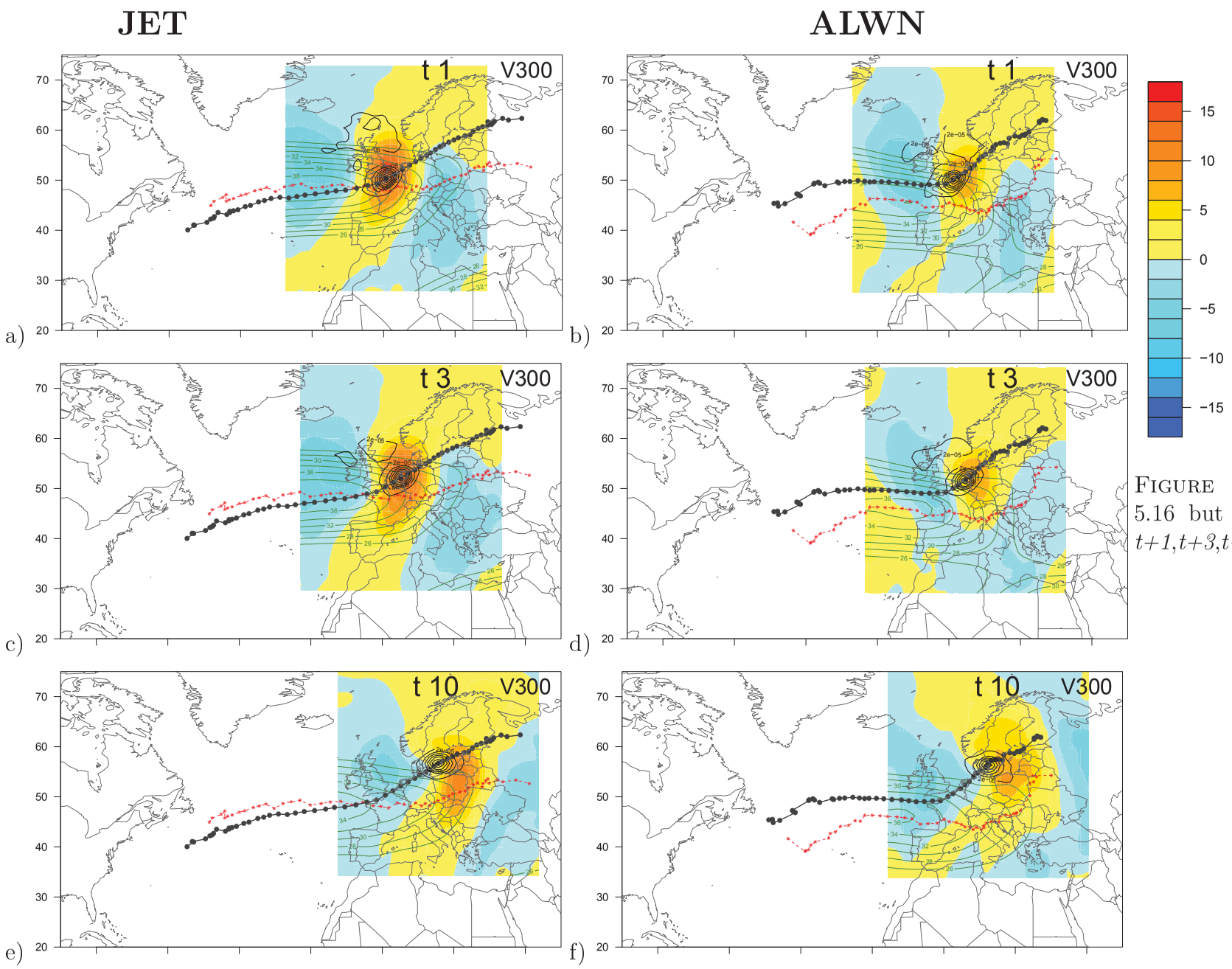

FIGURE 5.18: Same as 5.16 but for the time steps *t+1,t+3,t+10*.

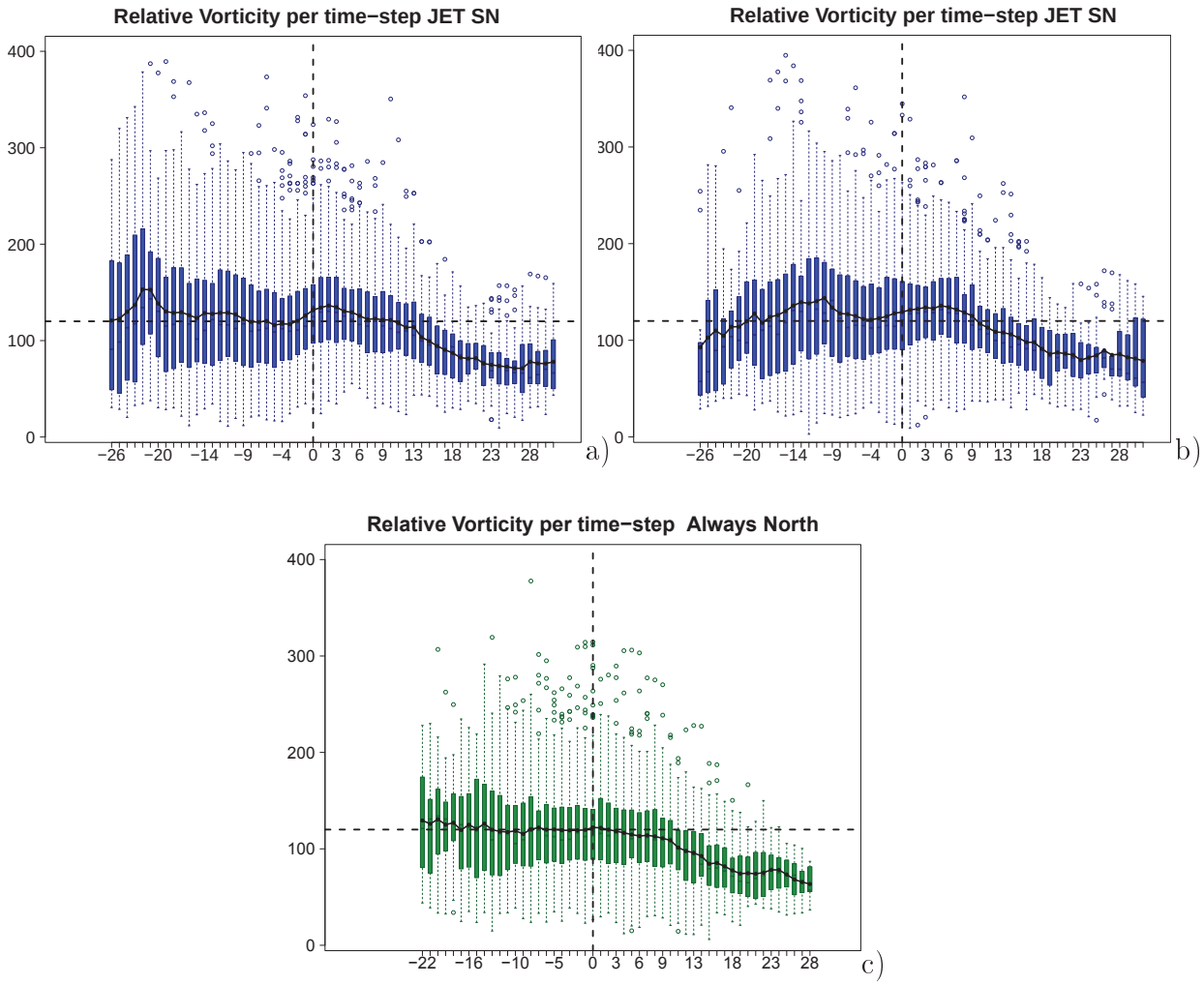

FIGURE 5.19: Boxplot (blue) and mean (black) relative vorticity per time step for the *JET SN* centred at *t0* (a) and centred at *newt0* (b). boxplot (green) and mean (black) relatve vorticity for the *Always North* (c).

For the *JET SN* two RV growth phases are observed, one in the first time steps and another around *t0* (figure 5.19a). The two peaks may be related to previous stud's conclusions (Baehr et al, 1999; Rivière et al, 2010). The first peak is observed around *t-18* s at westernmost longitudes in a phase driven by baroclinic growth. A second peak, just before *t0*, is related with the jet-crossing moment (Baehr et al, 1999; Rivière et al, 2010).Nevertheless, defining *t0* as the moment

when the storms are at the closest distance to France means that they are at different maturity stage and thus, figure 5.19a may mix different individual vorticity tendency.
Therefore, a new time distribution of the RV is computed with instant *t0* corresponding to the moment of jet crossing, defined as *newt0*.
The results (figure 5.19b) show the same two maxima observed in figure 5.19a, one of them after the *newt0*, confirming the re-intensification of extratropical storms after crossing the jet-stream (Gronas, 1995; Rivière and Joly, 2006; Rivière et al, 2010, 2015b). Furthermore, for the first time steps, the value of RV in 5.19a is much lower than the ones from figure 5.19b, validating that storms are well tracked in their initial stage. This means that the high mean RV at first time steps in figure 5.19 is indeed a consequence of *t0* definition.
Finally, the similarity between the position of the second peak between figure 5.19a and figure 5.19b permits us to conclude that storms associated with damage for *Jet SN* ATL storm category undergo a process of re-intensification before striking France. This happens independently of the mature state of the storms and may explain the high-damage over France.

For the *Always North* the mean RV (black line figure 5.19c) is fairly constant before decreasing after time step *t+9* when the storms are over the European continent. Even though, the extreme values (outliers) verified from *t-5* to *t+5* show that the more intense storms achieve their maximum phase while reaching France. The reason why we do not observe any vorticity increasing phase in the first time steps may be related to time shift between storm's life cycle of the composite which enhance variability of RV at these time steps.

In figure 5.20, we compare the time evolution vorticity maximum of the corresponding composite for both storms categories. One can see that *Jet S-N* storms increase around *t0* (blue line) is stronger than the *Always north* (green line).

The time evolution of other composite parameters is also analysed. In the case of 10-meter wind speed (figures 5.21), a maximum is sampled within a radius of 350 km from the storm centre at each time step. The boxplot distribution shows a severe decrease at the moment *t0*. This is related to the fact that, as we already

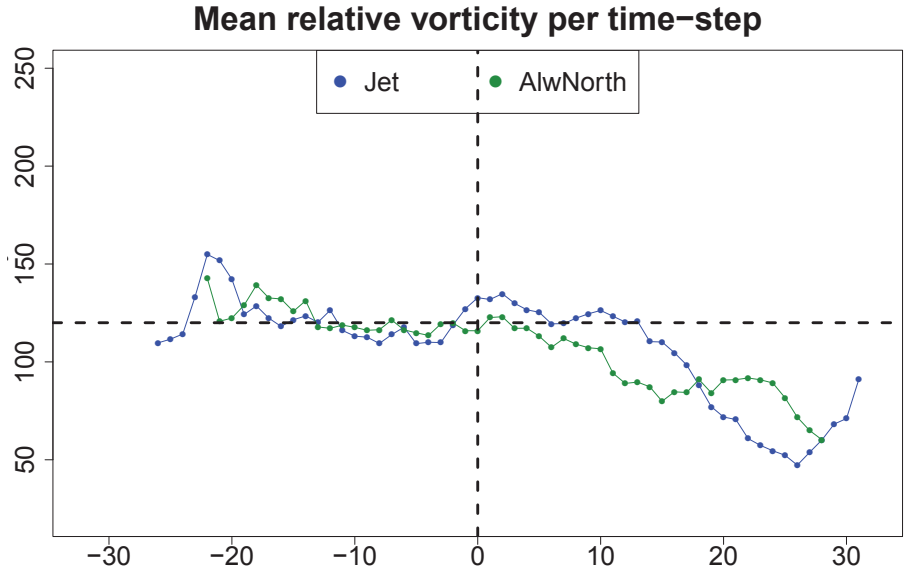

FIGURE 5.20: Mean relative vorticity per time step for the *JET SN* (blue) and *Always North* in green. *t0* is the moment the storm is close to France

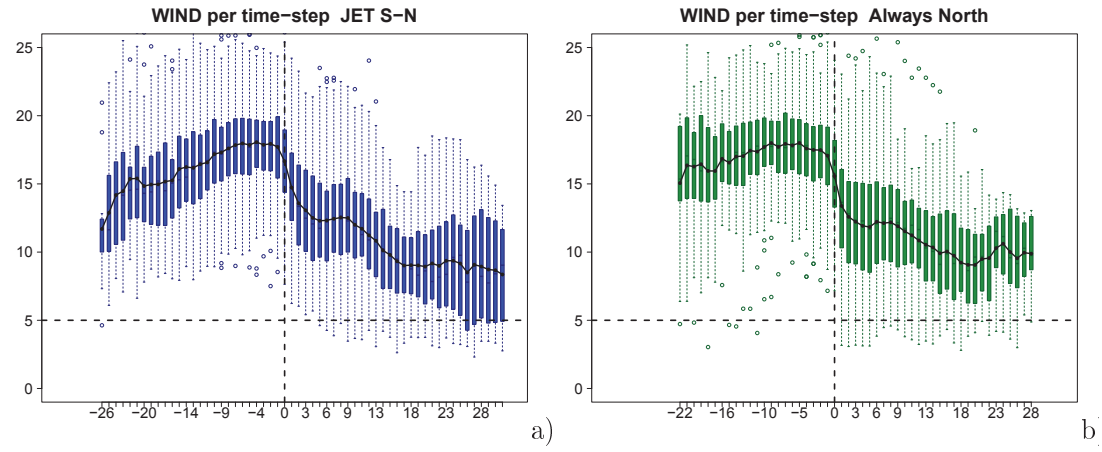

FIGURE 5.21: Boxplot (colours) and mean (black line) 10-meter wind speed per time step for the *JET SN* (blue, at left) and *Always North* (green, at right). *t0* is the moment the storm is close to France

analysed, storms enter mainland around *t0*. As seen before on chapter III, 10-meter wind speed is higher over the ocean than over the continents due to friction. Though, box-plots for both storm categories look similar, quantitative differences

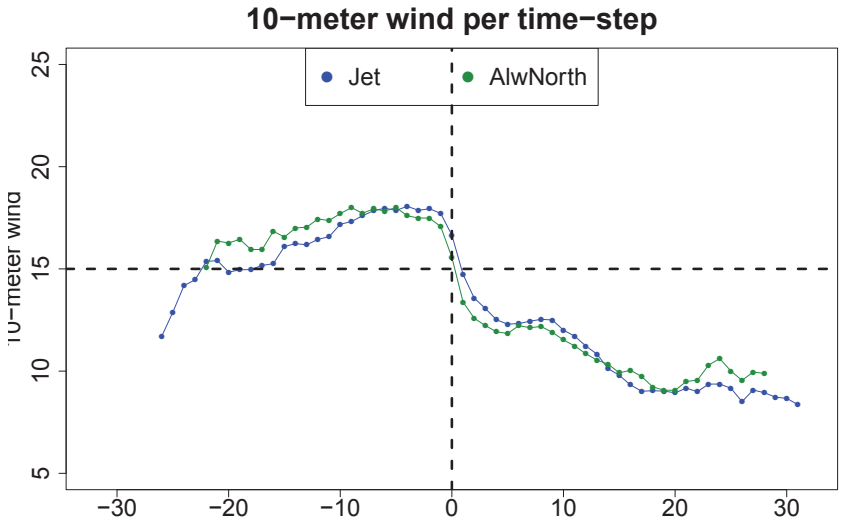

FIGURE 5.22: Mean 10-meter wind per time step for the *JET SN* (blue) and *Always North* in green. *t0* is the moment the storm is close to France

appear when focusing on 10-meter average speed 5.22. Between *t-8* and *t15*, *Jet S-N* winds are stronger (even if lightly) than the *Always North*.

MI and LI

The clear effect of the land-sea contrast shows that the quantitative evolution of the wind is not fully representative of the storm impact. One should use the severity indexes MI and LI to measure the intensity of the storm. To do that, the maximum value of the MI and the LI in a radius of 350 km from the storm centre. We remind the reader that LI can take non-null values over mainland only, while MI is computed globally. The results are presented in figures 5.23.
Both the MI and the LI increase significantly around *t0*. The MI (figures 5.23a and 5.23b) reaches the maximum value at *t0* and is, throughout all time steps, higher *Always North* than for the *JET SN*.
This is confirmed by figure5.24a where we can see that the *JET SN* trajectories (blue line) have stronger values of MI than the *Always North* (green line), not only at the moment they reach France, but also in the previous and following moments. The LI time evolution should be analysed keeping in mind that LI is based

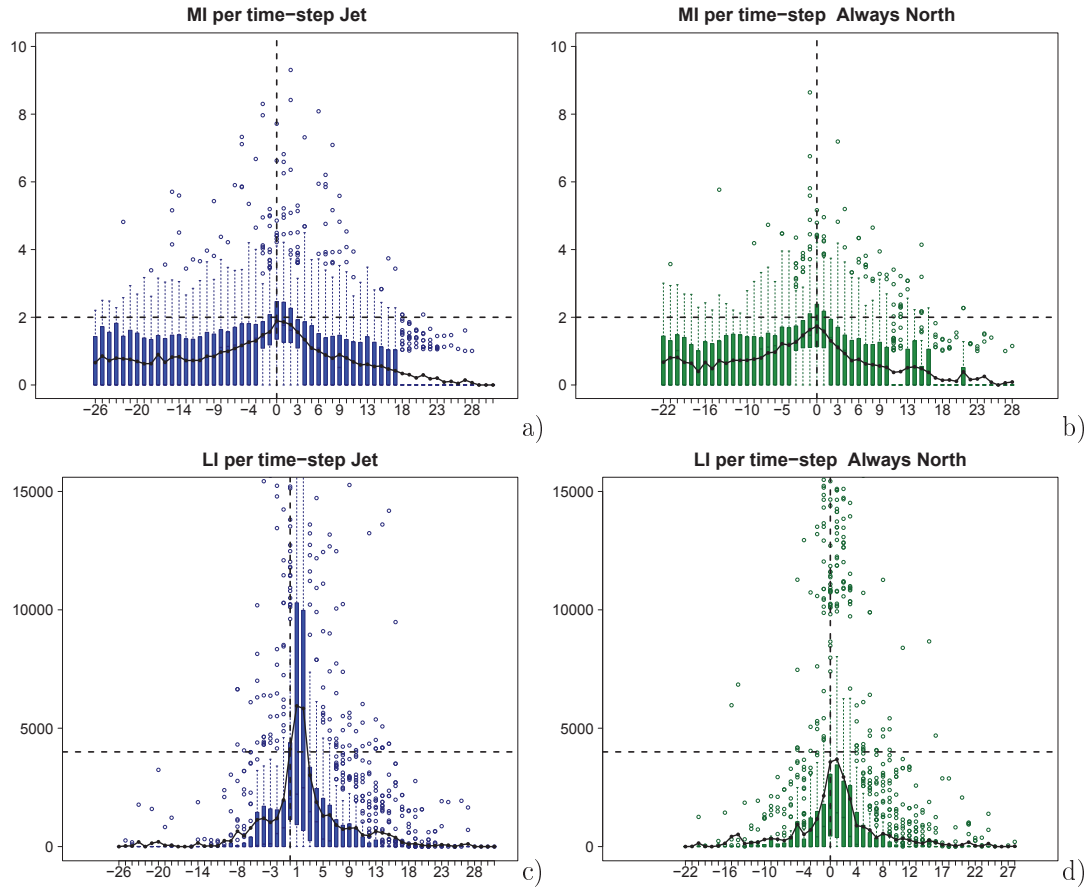

FIGURE 5.23: Mean (black lines) and boxplot (colours) of MI (a and b) and LI (c and d) per time step for the *JET SN* (blue, panel a and c) and *Always North* (green, panels b and d). *t0* is the moment the storm is close to France

on the population density index, not only from France, but also from the other countries where the storm passes. As seen from figures 5.16 to 5.18, both types of trajectories travel from the west and reach the first populated region between the 45°N and 55°N, i.e., between France and UK/Ireland. A first maximum is observed around *t-8* for both types which may be related to some storms reaching Ireland at this early moment before striking France. High values of LI are observed with a clear maximum value around *t0*. Their, major damage occurs when the storms reach countries and big cities as Paris and London and the *LI* increases even more. After *t0* the LI decreases rapidly, around *t9* for the *Jet S-N* and *t4* for *Always*

North as the storm decays in intensity.

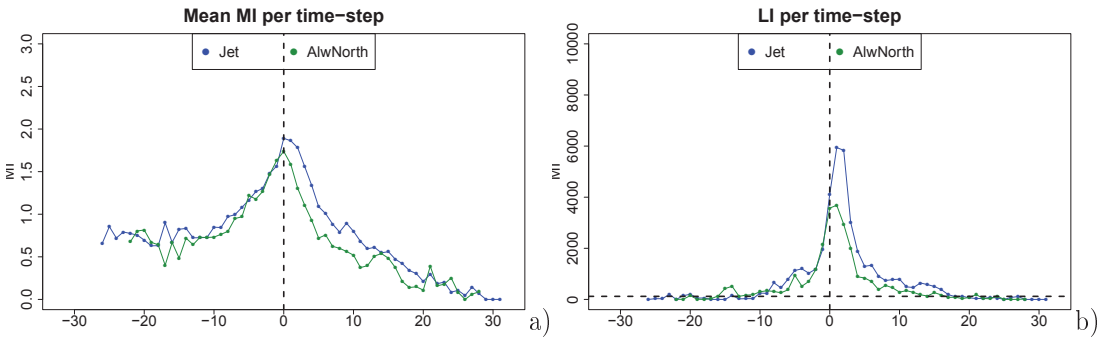

FIGURE 5.24: Mean MI (left) and LI (right) per time step for the *JET SN* (blue) and *Always North* (green). *t0* is the moment the storm is close to France

Finally, the crossing coordinates of the *JET SN* storms are retrieved and a Kernel density estimator applied to the sample. The resulting density, in figure 5.26, shows a density maximum located over the English Channel, meaning that the crossing happens mostly in this area. If we keep in mind that the average crossing occurs at the instants *t-3* to *t0* this means the storm re-enforcement after crossing the jet close to France is the main reason for the strong LI and MI.

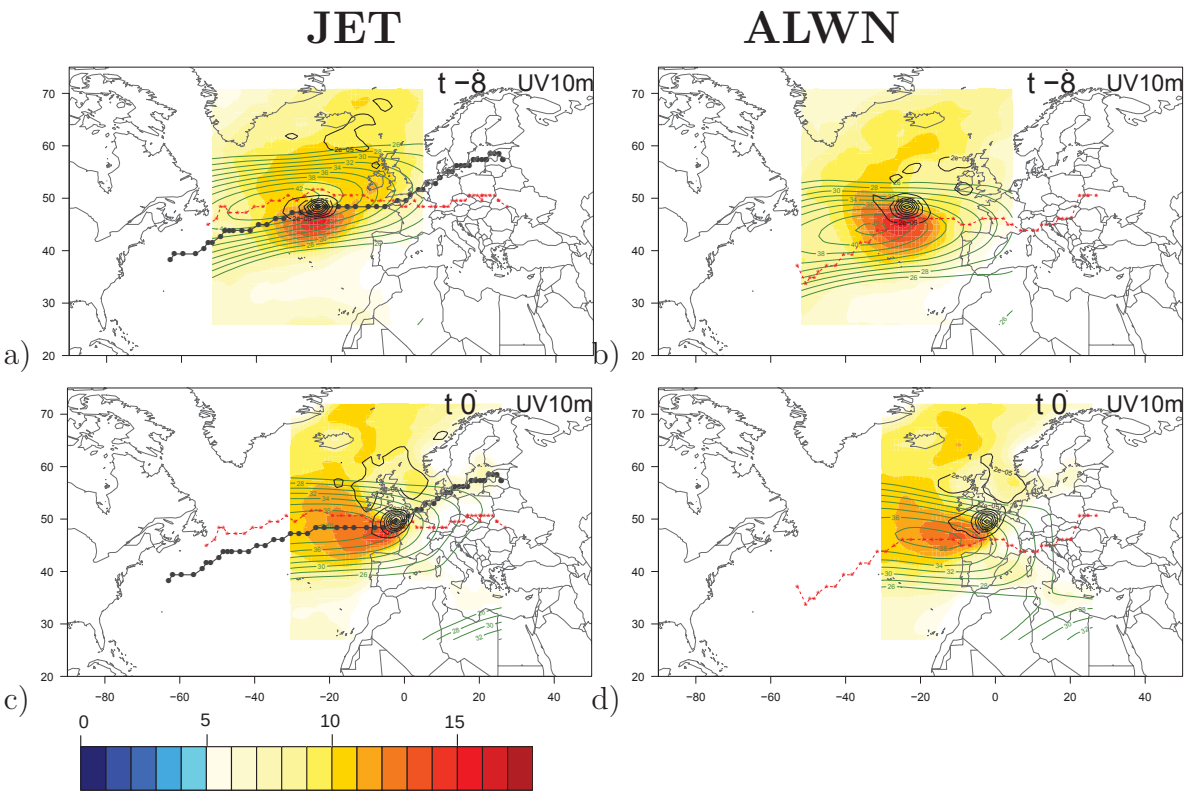

FIGURE 5.25: Composites for the storms that cross the jet (left column) and centralised North (right column) of 10-meter wind speed (shaded colours), LF wind speed at 300hPa (green contours) and relative vorticity maximum (black contours). The red-dashed line represents the location of the maximum UV300 at the same longitude of the trajectory at each time step.

5.3. Conclusions

In this chapter, an analysis of high-damage storms in France was done using more than one thousand storms that are selected according to their relative position to France and the Jet-axis.

Firstly, it was seen that the ATL storms are the ones more numerous, travelling from the western side of the Atlantic ocean. They are linked with strong and zonal jet-stream and with the strongest 10-meter winds among the three types. In general, the ATL MI and LI are higher, however, the ATLM storms are the ones associated with the extremes in $MImax_{track}$. This is linked to the fact that while ATL mainly affects northwestern regions of France, ATLM storms cross mainland

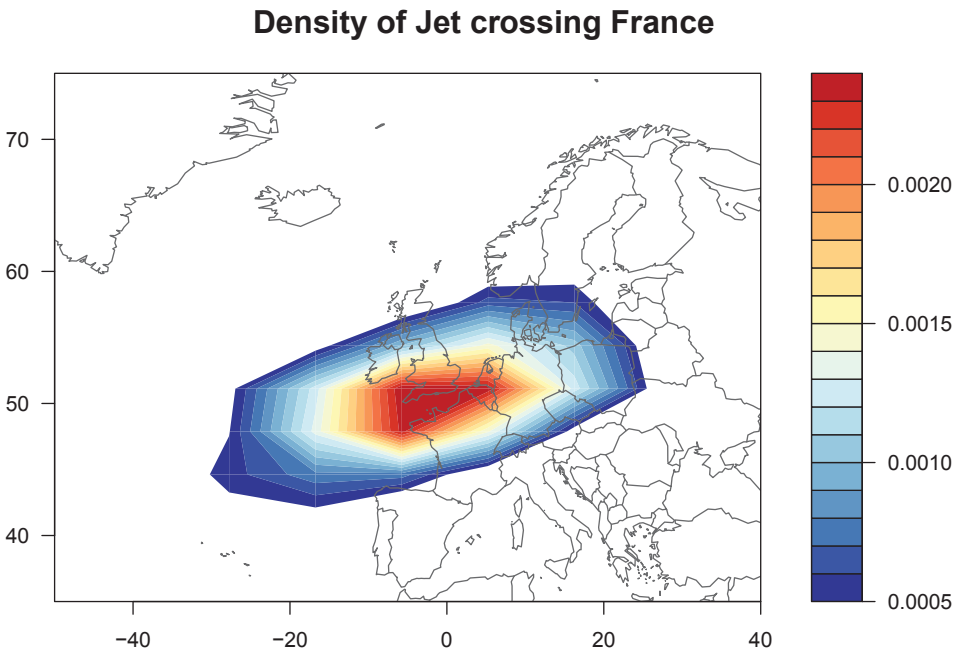

FIGURE 5.26: Density of trajectories crossing the jet for the Case of France.

regions of France which means touch more areas of France and areas with lower wind quantiles. On the contrary, the ATLM are associated with concave trajectories and a more concave northwest - southeast oriented jet-stream that becomes more zonal when the storms approach Europe. A sub-tropical jet stream is observed for these storms. The same type of jets are observed for the MEDI storms that have small area (*Area*) and displacement speed. Their wind footprint from the composite analyses shows a maximum over the Atlantic which makes unclear the actual origin of the impact of these types of storms, which should be studied separately.

Secondly, considering the role of large-scale flow, it has been shown that ATL storms are mainly from the *Jet S-N type* and *Always South* types. While no distinction can be made between both types concerning the averaged $MImax_{track}$, *Jet S-N* storms are the ones that produce the highest mean $LImax_{track}$ values.

When focusing on ATL storms only, the two most frequent types, *Always North* and *Jet S-N* are both characterised by a peak in MI and LI for the instant *t0*

and by stronger 10-meter winds. For high-damage *Jet S-N* storms, RV maximum basically travels eastward close to the jet axis until the moment of crossing. The associated upper-level winds are very strong and the jet very zonal. Moreover, these upper-level winds are located north of vorticity maximum before crossing, suggesting that this anomaly may help to advect the storm northward. There is a clear growing stage of these storms after the moment of crossing which occurs up to nine hours before hitting France. Simultaneously, a 10-meter wind and RV increase is observed. Apart from that, one of the most important factors that relates those types of storms with high damage in France is the region where most storms cross the jet, i.e., the English Channel. This proximity between the area of jet crossing and France is identified as one main cause of highest damage of storms hitting this country.

CHAPTER VI

Conclusions and perspectives

6.1. Conclusions

In this study, we have analysed twentieth-century storms using the ERA-20C reanalysis. On the one hand, a characterization of their variability throughout the century was made, linking this variability with the trends in baroclinicity, baroclinic conversion and ocean variability to the AMO and PDO. On the other hand, a climatology of these storms' damage was established. To that end, we used severity indices to estimate damages. Finally, a dynamical description of the storms was provided in relation to their relative position with respect to the Jet Stream.

6.1.1. Storm track variability in the 20th Century

Fro the first part of this thesis, we applied a tracking algorithm from Ayrault (1998) and studied the 20th-century variability of mid-latitude cyclones. The number of Extratropical cyclones per year obtained from ERA-20C reanalysis shows three different periods. The first (1900-1935) and last (1980-2010) periods show no significant trends whereas the mid-century period (1935-1980) shows a positive trend.
We addressed the robustness of this result to the time inhomogeneity of the reanalysis. An analysis using the number of detected maximums per year was made for ERA-20CM free run. It was observed that cyclone activity in ERA-20CM is syste-

matically higher than in ERA-20C, showing that the assimilation of observations reduces the synoptic eddy activity. On the contrary to what was so far mentioned in the literature, we showed that an increase in the number of assimilated observations doesn't lead to an increase in the cyclone activity.
To interpret the trends in extratropical cyclonic activity, we have studied the evolution of the cyclones density observed with a series of large-scale parameters. The first and the last periods show an increase in temperatures at lower (higher) tropospheric levels for northern (southern) latitudes. Baroclinicity consequently increases (decreases) in the upper (lower) levels of the atmosphere and generate opposite responses on storms-track. This provides a physical rationale for the absence of any significant trend in those periods. For the second period, which shown a significant positive trend of cyclonic activity, we identify a decrease in temperature over the whole Northern Hemisphere and an increase in baroclinicity and baroclinic conversion. This period is characterised by strong variations in the PDO and AMO indices in the first and second half of the period, respectively. The swing from positive to negative PDO in the late 30's increases the SST gradients in the North Pacific ocean and an increase in baroclinicity is verified leading to a stronger positive trend of ETCs in the Pacific than in the Atlantic. A similar trend is observed later in the Atlantic, but related to a shift in the AMO from positive to negative in the 50's.
The direct response of cyclonic activity to baroclinicity, however, is not trivial. It is likely that a "seeding" effect explains some correlations between the Pacific and the Atlantic storm tracks.

6.1.2. Windstorms and damage

The second part of this thesis gave emphasis to the impact of windstorms in Europe. Damages were assumed to be linked to the ratio between the wind and its 98^{th} percentile. Moreover, a series of indices (MI and LI, maximum and integrated over the storm trajectory) were used to analyse the capacity of the reanalysis to detect high-damaging storms. A comparison between losses from SCOR reinsurance company and the predictors obtained from the reanalysis was made. It showed that a multi-parameters approach is better to estimate damages than simply using

the wind.

The density of high-loss storms depends on the country studied. Northern-European countries such as the UK, Belgium or The Netherlands have highest damages when they are affected by Atlantic storms coming from the western Atlantic region. Central Europe countries have fewer storms and those need to cross the whole country to create damages. Mediterranean countries like Spain or Italy have their maximum high-loss storms density in the vicinity of the Mediterranean Sea.
France is the only country that has two high-loss storms density maxima, one over the Atlantic and the other one over the Mediterranean. A third type of storms was observed, the ones that enter France through the Gulf of Biscay and travel southeastward to the Mediterranean sea.

6.1.3. Dynamical analysis of windstorms

Windstorms intensity depends on several factors as baroclinicity or its crossing of the Jet Stream. A composite analysis was made enabling to characterize the low-frequency environment of the storms when crossing the jet stream.
It was observed that storms crossing the jet-stream over the English Channel up to 12h before reaching France are the most frequent ones and are associated with the strongest damages. The storms remaining on the northern side of the jet stream are relatively scarcer. They travel most of the time beneath the left exit of the jet-stream, a region that is favourable for low-level intensification of the storm.

6.2. Perspectives

The perspectives for the first part of the PhD consist in a better understanding of the assimilated observations in early periods of the twentieth century in the reanalysis.
Besides the member zero ERA-20CM and ERA-20C outputs analysed here, the ensemble of this first one and other variability parameters as the temperature evolution and SST or baroclinicity can be analysed for the same periods. Another

possible approach is the application of the tracking algorithm to the 20CR reanalysis from NOAA in order to compute the same diagnostics made in chapter III. Trends in cyclones, baroclinicity, temperature or SST could be used to verify if the relation between 20CR cyclones and large-scale variability is also observed in this data and if it goes in agreement with ERA-20C.
With respect to the second part of this thesis, the perspectives are numerous.
First of all, the link between losses and storms can be improved, for instance, using a dynamical footprint-dependent radius for each trajectory.
Secondly, a wind calibration could be computed using observations and/or dynamical downscaling to simulate measoscale strong wins features. However, this method would limit the study to fewer storms and cannot be applied to all countries and all 110 years of study.
Also, the temporal variability of the high-loss storms wasn't studied in this thesis. The frequency of severe storms throughout the 20^{th} century could be a valuable tool to both the reinsurance industry and the scientific community. Then, linked with this temporal variability is the serial clustering of storms. The density of cyclones could be used to compute under-and-over dispersion of storms. (Mailier et al, 2006) throughout the century. Moreover, a method to select this "serial clustered" storms in the 110 years of data could be developed which would enable a composite analysis.

Finally, the work presented in chapter V on storms dynamics could be enriched. i) The composite analysis was made only for France and for the Atlantic storms. It could be performed also to the Mediterranean storms of France and all other countries studied, including Europe. ii) We could develop more advanced dynamical diagnostics such as energy exchanges between the environment and the storms or the role of diabatic processes.

CHAPTER VII

Conclusions et perspectives (Français)

7.1. Conclusions et perspectives

Nous avons étudiéles tempêtes du XXe siècle au moyen de la réanalyse centennale ERA 20-C disponible depuis fin 2014. Nous avons étudié la variabilité multi décennale des tempêtes en lien avec des paramètres caractérisant la baroclinie de grande échelle. Nous avons également abordé la climatologie des tempêtes du point de vue de l'impact en travaillant à partir d'indices de pertes. Enfin dans une dernière partie nous avons analysé les tempêtes affectant la France d'un point de vue dynamique en nous concentrant sur leur position par rapport à l'axe de jet.

7.1.1. Variabilité des tempêtes au cours du XXe siècle

La détection des tempêtes à partir du suivi des maximums de tourbillon au moyen de la méthode de Ayrault (1998) sur l'hémisphère nord conduit à séparer 3 périodes bien distinctes. La première (1900-1935) ainsi que la 3e (1980-2010) ne présentent pas de tendances significatives concernant l'activité dépressionnaire aux latitudes tempérées. La seconde période (1935-1980) présente, elle, une tendance positive significative.

Néanmoins, les réanalyses sont souvent critiquées pour leur manque d'homo-

généité dans le temps en raison des évolutions que les systèmes d'observations ont connu au fil du temps. Par conséquent, nous avons appliqué une méthode de détection des maximums de tourbillon à une simulation de 100 ans forcée seulement par les mêmes SST que la réanalyse. Il apparait que le modèle libre présente une activité dépressionnaire plus importante que le système d'assimilation de données utilisé pour la réanalyse. Cela nous conduit à penser que l'apport des observations n'est pas simplement d'augmenter le nombre de systèmes dépressionnaires mais aussi de filtrer des systèmes parasites conséquences des erreurs de modélisation. Finalement nous en arrivons à remettre en question la relation entre tendance positive de densité d'observations avec tendance positive de l'activité dépressionnaire puisque l'argumentaire précédent justifie le contraire.

Pour autant, afin d'évaluer la robustesse de nos résultats nous avons confronté l'évolution des rails des dépressions avec quelques paramètres de plus grande échelle car probablement plus robustes.

Nous avons donc croisé ces résultats avec des diagnostics de baroclinie (mesurée par le taux de croissance du mode le plus instable dans le modèle de Eady).

En première et troisième période, on observe une hausse de la température en basses couches et une diminution dans la stratosphère conduisant à diminuer les gradients méridiens de température dans la basse troposphère et à les augmenter dans la stratosphère. Cela conduit à une diminution de la baroclinie en basses couches et à une hausse dans la stratosphère. Ces réponses contrastées sont perçues comme cohérentes avec les tendances moyennes de dépressions non significatives.

La seconde période présente un comportement bien différent : une diminution de la température aux latitudes élevées conduit à une hausse de la baroclinie dans toute la troposphère. Par ailleurs, cette seconde période présente une variabilité interne que l'on a pu relier aux principaux modes de variabilité océaniques que sont l'AMO et la PDO. Par exemple, la bascule d'une PDO en phase positive vers la phase négative à la fin des années 30 conduit à une augmentation des gradients de SST sur le Pacifique nord et conduisant à une augmentation de la baroclinie. La même réponse est observée sur l'Atlantique lors du passage d'une AMO positive vers une AMO négative pendant les années 50.

La réponse (au premier ordre) de l'activité dépressionnaire à la baroclinie ne semble pas être toujours triviale. En réalité, le mécanisme connu sous le vocable de

« seeding » permet probablement d'expliquer les corrélations entre les tendances sur le rails Atlantique et Pacifique. Quelques diagnostics ont permis d'envisager ce dernier mécanisme sans pour autant apporter une réponse définitive.

7.1.2. Tempêtes et impacts

Nous nous sommes également intéressés à l'étude de l'impact des tempêtes sur l'Europe dans une seconde partie. On fait l'hypothèse que l'impact d'une tempête est lié localment à l'écart entre le vent subi et la climatologie du vent. L'impact construit à partir d'une normalisation du vent de la réanalyse par un quantile de la réanalyse permet également une calibration du produit ainsi construit. Par exemple, l'impact sur les continents est aussi fort que sur mer alors que le vent y est bien moins fort.

La question de la capacité d'un système de réanalyse dont nous rappelons que sa résolution horizontale permet de représenter les principaux éléments d'une cyclogénèse mais pas toujours les structures de vents forts est posée. Dans le but de quantifier la capacité de la réanalyse à détecter les tempêtes, nous avons tenté de relier quelques prédicteurs tirés des trajectoires de dépressions (LI ou MI les plus forts le long de la trajectoire, valeurs intégrées le long des mêmes trajectoires...) à l'impact mesuré par la perte subie par le réassureur SCOR par une analyse de sensibilité. On a constaté qu'une approche multi-paramètre présente un intérêt et qu'un modèle statistique non-linéaire s'appuyant sur la technique SVM permet de prévoir 60 % des cas les plus intenses. La tempête Lothar (26/12/1999) fait partie des cas prévisibles avec cette approche.

Les pays de l'Europe du Nord comme la Belgique ou les Pays-Bas sont affectés par des systèmes dépressionnaires océaniques se formant souvent à l'ouest du bassin. Les systèmes affectant l'Europe centrale sont plus rares et généralement traversent la région qu'ils impactent. Les pays possédant une côte méditerranéenne ont un maximum de densité de dépressions sur la méditerranée occidentale. La France est le seul pays d'Europe dont les tempêtes qui l'affectent possèdent deux maximums de densité, le premier sur l'Atlantique et le second en Méditerranée. Une dernière catégorie de dépression se formant sur l'Atlantique, traverse la France puis pénètre en Méditerranée. Ces systèmes semblent affecter l'Ile-de-France de

manière systématique puisqu'ils possèdent de très forts LI tandis que les MI sont dans la norme.

7.1.3. Analyse dynamique des tempêtes

L'amplitude que peut atteindre une tempête dépend de plusieurs facteurs comme la baroclinie, la présence de précurseurs, structures préexistantes et d'événements brusque comme la traversée du jet. Nous avons donc caractérisé l'environnement basse fréquence, la présence d'une structure d'altitude éventuellement en interaction barocline avec la surface et l'occurrence d'une traversée du jet basse-fréquence. Nous avons montré que les tempêtes qui traversent le jet dans les 12 h précédant le début de l'impact sur la France sont les plus fréquentes des tempêtes lorsque l'on ne considère que les plus intenses. Moins étudiées, les tempêtes circulant du côté nord du jet depuis leur stade de naissance jusqu'à leur stade de décroissance, aussi appelées dépressions « en air-froid » sont moins fréquentes mais leur nombre est toutefois significatif. Il est à noter que l'interaction barocline opère d'une manière différente et que le maximum de tourbillon reste longtemps sous la région de sortie gauche du jet basse fréquence, région privilégiée de forçage des ascendances par la théorie quasi-géostrophique.

7.2. Perspectives

L'application de la méthode de suivi des maximums de tourbillon devrait être appliquée à d'autres réanalyses (notamment 20CR de la NOAA) et à des simulations en mode climat. Un des objectifs est de se confronter aux autres méthodes publiées. Il s'agirait également de prolonger l'analyse de l'impact de la variation de la densité des observations assimilées au cours du temps. Il pourrait être intéressant d'appliquer notre approche consistant à comparer les rails des dépressions à des indications de baroclinie de grande échelle à ces différents systèmes.

L'analyse des pertes en lien avec les trajectoires de dépressions pourrait être affinée. Il serait par exemple utile d'introduire un rayon d'influence des dépressions dans le calcul des empreintes (« footprints ») adaptatif et non statique comme dans cette thèse.

Une sérieuse calibration du vent doit être entreprise. Pour cela on peut s'ap-

puyer sur les analyses climatologiques disponibles. De manière générale le recours à la descente d'échelle dynamique au moyen de modèles résolvant la convection et à des résolutions proches du km devrait être envisagé.

L'analyse de l'évolution temporelle de la variabilité des pertes économiques est également un prolongement naturel de ce travail. De même, la capacité prédictive de l'impact à partir de la réanalyse de grande échelle doit encourager les études portant sur la prévision de l'impact dans les simulations du changement climatique.

L'analyse des tempêtes répétées (« serial clustering ») est également un point que nous n'avons pas abordé dans cette thèse. L'ensemble des points précédents est de nature à faire progresser la connaissance du phénomène tempête mais représente une information d'une richesse incomparable pour le monde de l'assurance et de la réassurance pour qui la connaissance de l'aléa est primordiale.

Enfin, citons quelques axes de recherche relatifs à la compréhension dynamique du phénomène tempête : i) L'analyse des composites, limitée à la France ici, devra être étendue aux autres pays européens. Une analyse spécifique des évènements méditerranéens devra être menée afin d'identifier les points communs mais aussi les différences avec les dépressions Atlantiques. ii) L'analyse dynamique devra faire appel à des outils plus avancés que ceux employés au cours de cette thèse. On pense notamment aux diagnostics permettant d'approcher la nature des échanges énergétiques (barocline, barotrope, diabatiques).

Références

Ahrens CD (2009) Meteorology today : an introduction to weather, climate and the environment, 9th edn. Brooks/Cole, Belmont, CA, oCLC : 254623478

Ayrault F (1995) Climatologia des cyclogégèses sur l'atlantiqye nord :premiers résultats. Note de centre GMME

Ayrault F (1998) Environnment, structure et évolution des dépressions météorologiques : réalité climatologique et modèles types (PhD thesis). Universite Paul Sabatier, Meteo-France, Centre National de Recherches Météorologiques

Baehr C, Pouponneau B, Ayrault F, Joly A (1999) Dynamical characterization of the fastex cyclogenesis cases. Quarterly Journal of the Royal Meteorological Society 125(561) :3469–3494, DOI 10.1002/qj.49712556117

Befort DJ, Wild S, Kruschke T, Ulbrich U, Leckebusch GC (2016) Different long-term trends of extra-tropical cyclones and windstorms in era-20c and noaa-20cr reanalyses. Atmospheric Science Letters 17(11) :586–595, DOI 10.1002/asl.694, URL http ://dx.doi.org/10.1002/asl.694

Bengtsson L (2004) Can climate trends be calculated from reanalysis data ? Journal of Geophysical Research 109(D11), DOI 10.1029/2004JD004536

Bengtsson L, Hodges KI, Roeckner E (2006) Storm Tracks and Climate Change. Journal of Climate 19(15) :3518–3543, DOI 10.1175/JCLI3815.1

Bjerknes J, Solberg H (1922) Life cycle of cyclones and the polar front theory of atmospheric circulation. Geofys Publikasjoner

Blackmon ML, Wallace JM, Lau NC, Mullen SL (1977) An Observational Study of the Northern Hemisphere Wintertime Circulation. Journal of the Atmospheric Sciences 34(7) :1040–1053, DOI 10.1175/1520-0469(1977)034<1040 :AOSOTN>2.0.CO ;2

Bovy H (2012) Navigation model change. Focus, SCOR GLOBAL P&C pp 15–20

Bromwich DH, Fogt RL, Hodges KI, Walsh JE (2007) A tropospheric assessment of the ERA-40, NCEP, and JRA-25 global reanalyses in the polar regions. Journal of Geophysical Research 112(D10), DOI 10.1029/2006JD007859

Browning KA (2004) The sting at the end of the tail : Damaging winds associated with extratropical cyclones. Quarterly Journal of the Royal Meteorological Society 130(597) :375–399, DOI 10.1256/qj.02.143, URL http ://doi.wiley.com/10.1256/qj.02.143

Businger S, Businger JA (2001) Viscous Dissipation of Turbulence Kinetic Energy in Storms*. Journal of the Atmospheric Sciences 58(24) :3793–3796, DOI 10.1175/1520-0469(2001)058<3793 :VDOTKE>2.0.CO ;2

Center for International Earth Science Information Network - CIESIN - Columbia University ; Centro Internacional de Agricultura Tropical - CIAT (2005) Gridded Population of the World, Version 3 (GPWv3) : Population Density Grid. Palisades, NY : NASA Socioeconomic Data and Applications Center (SEDAC) URL https ://doi.org/10.7927/H4XK8CG2

Chang EKM, Yau AMW (2015) Northern Hemisphere winter storm track trends since 1959 derived from multiple reanalysis datasets. Climate Dynamics 47(5-6) :1435–1454, DOI 10.1007/s00382-015-2911-8

Chang EKM, Lee S, Swanson KL (2002) Storm Track Dynamics. Journal of Climate 15(16) :2163–2183, DOI 10.1175/1520-0442(2002)015<02163 :STD>2.0.CO ;2

Charney JG (1947) The dynamics of long waves in a baroclinic westerly current. Journal of Meteorology 4(5) :136–162, DOI 10.1175/1520-0469(1947)004<0136 :TDOLWI>2.0.CO ;2

Compo GP, Whitaker JS, Sardeshmukh PD, Matsui N, Allan RJ, Yin X, Gleason BE, Vose RS, Rutledge G, Bessemoulin P, Bronnimann S, Brunet M, Crouthamel RI, Grant AN, Groisman PY, Jones PD, Kruk MC, Kruger AC, Marshall GJ, Maugeri M, Mok HY, Nordli, Ross TF, Trigo RM, Wang XL, Woodruff SD, Worley SJ (2011) The Twentieth Century Reanalysis Project. Quarterly Journal of the Royal Meteorological Society 137(654) :1–28, DOI 10.1002/qj.776

Cusack S (2016) The observed clustering of damaging extratropical cyclones in Europe. Natural Hazards and Earth System Sciences 16(4) :901–913, DOI 10.5194/nhess-16-901-2016, URL http ://www.nat-hazards-earth-syst-sci.net/16/901/2016/

Della-Marta PM, Liniger MA, Appenzeller C, Bresch DN, Köllner-Heck P, Muccione V (2010) Improved Estimates of the European Winter Windstorm Climate and the Risk of Reinsurance Loss Using Climate Model Data. Journal of Applied Meteorology and Climatology 49(10) :2092–2120, DOI 10.1175/2010JAMC2133.1, URL http ://journals.ametsoc.org/doi/abs/10.1175/2010JAMC2133.1

Deroche MS, Choux M, Codron F, Yiou P (2014) Three variables are better than one : detection of european winter windstorms causing important damages 14(4) :981–993, DOI 10.5194/nhess-14-981-2014

Donat MG, Leckebusch GC, Pinto JG, Ulbrich U (2010) Examination of wind storms over central europe with respect to circulation weather types and nao phases. International Journal of Climatology 30(9) :1289–1300, DOI 10.1002/joc.1982, URL http ://dx.doi.org/10.1002/joc.1982

Eady ET (1949) Long waves and cyclone waves. Tellus 1(3) :33–52, DOI 10.1111/j.2153-3490.1949.tb01265.x, URL http ://dx.doi.org/10.1111/j.2153-3490.1949.tb01265.x

Fink AH, Brücher T, Ermert V, Krüger A, Pinto JG (2009) The European storm Kyrill in January 2007 : synoptic evolution, meteorological impacts and some considerations with respect to climate change. Natural Hazards and Earth System Sciences 9(2) :405–423, DOI 10.5194/nhess-9-405-2009, URL http ://www.nat-hazards-earth-syst-sci.net/9/405/2009/

Gilet JB, Plu M, Rivière G (2009) Nonlinear Baroclinic Dynamics of Surface Cyclones Crossing a Zonal Jet. Journal of the Atmospheric Sciences 66(10) :3021–3041, DOI 10.1175/2009JAS3086.1, URL http ://journals.ametsoc.org/doi/abs/10.1175/2009JAS3086.1

Gronas S (1995) The seclusion intensification of the New Year's day storm 1992. Tellus A 47(5) :733–746, DOI 10.1034/j.1600-0870.1995.00116.x, URL http ://tellusa.net/index.php/tellusa/article/view/11571

Hanley J, Caballero R (2012) The role of large-scale atmospheric flow and rossby wave breaking in the evolution of extreme windstorms over europe. Geophysical Research Letters 39(21) :n/a–n/a, DOI 10.1029/2012GL053408, URL http ://dx.doi.org/10.1029/2012GL053408, l21708

Haylock MR (2011) European extra-tropical storm damage risk from a multi-model ensemble of dynamically-downscaled global climate models. Natural Hazards and Earth System Science 11(10) :2847–2857, DOI 10.5194/nhess-11-2847-2011

Hewson TD, Neu U (2015) Cyclones, windstorms and the IMILAST project. Tellus A 67(0), DOI 10.3402/tellusa.v67.27128, URL http ://www.tellusa.net/index.php/tellusa/article/view/27128

Hodges KI (1994) A General Method for Tracking Analysis and Its Application to Meteorological Data. Monthly Weather Review 122(11) :2573–2586, DOI 10.1175/1520-0493(1994)122<2573 :AGMFTA>2.0.CO ;2

Holton JR (2004) An introduction to dynamic meteorology, 4th edn. International Geophysics Series, Elsevier Academic Press,, Burlington, MA, URL http ://books.google.com/books ?id=fhW5oDv3EPsC

Hoskins BJ, Hodges KI (2002) New Perspectives on the Northern Hemisphere Winter Storm Tracks. Journal of the Atmospheric Sciences 59(6) :1041–1061, DOI 10.1175/1520-0469(2002)059<1041 :NPOTNH>2.0.CO ;2

Joly A, Browning KA, Bessemoulin P, Cammas JP, Caniaux G, Chalon JP, Clough SA, Dirks R, Emanuel KA, Eymard L, Gall R, Hewson TD, Hildebrand PH, Jorgensen D, Lalaurette F, Langland RH, Lemaître Y, Mascart P, Moore JA, Persson PO, Roux F, Shapiro MA, Snyder C, Toth Z, Wakimoto RM (1999) Overview of the field phase of the fronts and atlantic storm-track experiment (fastex) project. Quarterly Journal of the Royal Meteorological Society 125(561) :3131–3163, DOI 10.1002/qj.49712556103, URL http ://dx.doi.org/10.1002/qj.49712556103

Karremann MK, Pinto JG, Reyers M, Klawa M (2014) Return periods of losses associated with european windstorm series in a changing climate. Environmental Research Letters 9(12) :124,016, URL http ://stacks.iop.org/1748-9326/9/i=12/a=124016

Klawa M, Ulbrich U (2003) A model for the estimation of storm losses and the identification of severe winter storms in Germany. Natural Hazards and Earth System Sciences 3(6) :725–732, DOI 10.5194/nhess-3-725-2003

Lamb H (1991) Historic Storms of the North Sea, British Isles and Northwestern Europe. Cambridge University Press, Cambridge

Leckebusch GC, Ulbrich U, Fröhlich L, Pinto JG (2007) Property loss potentials for European midlatitude storms in a changing climate : LOSS POTENTIALS UNDER CLIMATE CHANGE. Geophysical Research Letters 34(5), DOI 10.1029/2006GL027663, URL http ://doi.wiley.com/10.1029/2006GL027663

Leckebusch GC, Weimer A, Pinto JG, Reyers M, Speth P (2008) Extreme wind storms over europe in present and future climate : a cluster analysis approach. Meteorologische Zeitschrift 17(1) :67–82, DOI 10.1127/0941-2948/2008/0266

Liberato MLR, Pinto JG, Trigo IF, Trigo RM (2011) Klaus – an exceptional winter storm over northern iberia and southern france. Weather 66(12) :330–334, DOI 10.1002/wea.755, URL http ://dx.doi.org/10.1002/wea.755

Liberato MLR, Pinto JG, Trigo RM, Ludwig P, Ordóñez P, Yuen D, Trigo IF (2013) Explosive development of winter storm Xynthia over the subtropical North Atlantic Ocean. Nat Hazards Earth Syst Sci 13(9) :2239–2251, DOI 10.5194/nhess-13-2239-2013, URL http ://www.nat-hazards-earth-syst-sci.net/13/2239/2013/

Lionello P, Trigo IF, Gil V, Liberato MLR, Nissen KM, Pinto JG, Raible CC, Reale M, Tanzarella A, Trigo RM, Ulbrich S, Ulbrich U (2016) Objective climatology of cyclones in the mediterranean region : a consensus view among methods with different system identification and tracking criteria. Tellus A : Dynamic Meteorology and Oceanography 68(1) :29,391, DOI 10.3402/tellusa.v68.29391

Mailier PJ, Stephenson DB, Ferro CAT, Hodges KI (2006) Serial Clustering of Extratropical Cyclones. Monthly Weather Review 134(8) :2224–2240, DOI 10.1175/MWR3160.1, URL http ://journals.ametsoc.org/doi/abs/10.1175/MWR3160.1

Malardel S (2009) Fondamentaux de météorologie : à l'école du temps. Cépaduès-éd., URL https ://books.google.fr/books ?id=EvDjPgAACAAJ

Martínez-Alvarado O, Gray SL, Catto JL, Clark PA (2012) Sting jets in intense winter north-atlantic windstorms. Environmental Research Letters 7(2) :024,014, URL http ://stacks.iop.org/1748-9326/7/i=2/a=024014

Mathias Dobbertin (2002) Influence of stand structure and site factors on wind damage comparing the storms Vivian and Lothar. ResearchGate

McCallum E (1990) The burns' day storm, 25 january 1990. Weather 45(5) :166–173, DOI 10.1002/j.1477-8696.1990.tb05607.x, URL http ://dx.doi.org/10.1002/j.1477-8696.1990.tb05607.x

Muir-Wood R (2013) "the 1941 february 15th windstorm in the iberian peninsula".

MunichRe (1993) Winterstürme in europa. Publication of the Munich Re,Ordering Number 2041-E-d, Tech rep

Neu U, Akperov MG, Bellenbaum N, Benestad R, Blender R, Caballero R, Cocozza A, Dacre HF, Feng Y, Fraedrich K, Grieger J, Gulev S, Hanley J, Hewson T, Inatsu M, Keay K, Kew SF, Kindem I, Leckebusch GC, Liberato MLR, Lionello P, Mokhov II, Pinto JG, Raible CC, Reale M, Rudeva I, Schuster M, Simmonds I, Sinclair M, Sprenger M, Tilinina ND, Trigo IF, Ulbrich S, Ulbrich U, Wang XL, Wernli H (2013) IMILAST : A Community Effort to Intercompare Extratropical Cyclone Detection and Tracking Algorithms. Bulletin of the American Meteorological Society 94(4) :529–547, DOI 10.1175/BAMS-D-11-00154.1

Nielsen NW, Sass BH (2003) A numerical, high-resolution study of the life cycle of the severe storm over denmark on 3 december 1999. Tellus A 55(4) :338–351, DOI 10.1034/j.1600-0870.2003.00022.x

NYT (1916) Library and of and congress, new-york tribune, december 24, 1916. New York NY, 1866,Newspaper URL https ://www.loc.gov/item/sn83030214/1916-12-24/ed-1/(Accessed June 01, 2017.)

Oruba L, Lapeyre G, Rivière G (2012) On the northward motion of midlatitude cyclones in a barotropic meandering jet. Journal of the Atmospheric Sciences 69(6) :1793–1810, DOI 10.1175/JAS-D-11-0267.1

Oruba L, Lapeyre G, Rivière G (2013) On the poleward motion of midlatitude cyclones in a baroclinic meandering jet. Journal of the Atmospheric Sciences 70(8) :2629–2649, DOI 10.1175/JAS-D-12-0341.1

Peixoto J, Oort A (1992) The Physics of Climate. Springer-Verlag GmbH, URL http ://books.google.es/books ?id=3tjKa0YzFRMC

Phillips NA (1951) A simple three-dimensional model for the study of large-scale extratropical flow patterns. Journal of Meteorology 8(6) :381–394, DOI 10.1175/1520-0469(1951)008<0381 :ASTDMF>2.0.CO ;2

Pinto J, Ulbrich U, Leckebush GC, Spangehl T, Reyers M, Zacharias S (2007) Changes in storm track and cyclone activity in three SRES ensemble experiments with the ECHAM5/MPI-OM1 GCM. Clim Dyn 29 :195–210

Pinto J, Mk K, K B, Pm DM, M K (2012) Loss potentials associated with European windstorms under future climate conditions. Climate Research 54(1) :1–20, DOI 10.3354/cr01111, URL http ://www.int-res.com/abstracts/cr/v54/n1/p1-20/

Pinto JG, Zacharias S, Fink AH, Leckebusch GC, Ulbrich U (2009) Factors contributing to the development of extreme north atlantic cyclones and their relationship with the nao. Climate Dynamics 32(5) :711–737, URL http ://centaur.reading.ac.uk/32782/

Poli P, Hersbach H, Tan D, Dee D, Thepaut JJ, Simmons A, Peubey C, Laloyaux P, Komori T, Berrisford P, Dragani R, Trémolet Y, Hólm E, Bonavita M, Isaksen L, Fisher M (2013) The data assimilation system and initial performance

evaluation of the ECMWF pilot reanalysis of the 20th-century assimilating surface observations only (ERA-20C). Reading, Berkshire, U.K. : European Centre for Medium Range Weather Forecasts, 2013.

Poli P, Hersbach H, Dee DP, Berrisford P, Simmons AJ, Vitart F, Laloyaux P, Tan DGH, Peubey C, Thépaut JN, Trémolet Y, Hólm EV, Bonavita M, Isaksen L, Fisher M (2016) ERA-20c : An Atmospheric Reanalysis of the Twentieth Century. Journal of Climate 29(11) :4083–4097, DOI 10.1175/JCLI-D-15-0556.1

Prichard B (2012) The Great Storm of 16 October 1987 : The Great Storm of 16 October 1987. Weather 67(10) :255–260, DOI 10.1002/wea.1983, URL http ://doi.wiley.com/10.1002/wea.1983

Raible CC, Della-Marta PM, Schwierz C, Wernli H, Blender R (2008) Northern Hemisphere Extratropical Cyclones : A Comparison of Detection and Tracking Methods and Different Reanalyses. Monthly Weather Review 136(3) :880–897, DOI 10.1175/2007MWR2143.1

Rivière G (2012) Dynamique des dépressions des latitudes tempérées et leur rôle dans la circulation générale de l'atmosphère. Habilitation à diriger des recherches en sciences de l'univers, de l'environnement et de l'espace, UNIVERSITE Toulouse III - Paul Sabatier, 159 pages

Rivière G, Joly A (2006) Role of the Low-Frequency Deformation Field on the Explosive Growth of Extratropical Cyclones at the Jet Exit. Part I : Barotropic Critical Region. Journal of the Atmospheric Sciences 63(8) :1965–1981, DOI 10.1175/JAS3728.1

Rivière G, Arbogast P, Maynard K, Joly A (2010) The essential ingredients leading to the explosive growth stage of the european wind storm *Lothar* of christmas 1999 pp n/a–n/a, DOI 10.1002/qj.585, URL http ://doi.wiley.com/10.1002/qj.585

Rivière G, Arbogast P, Lapeyre G, Maynard K (2012) A potential vorticity perspective on the motion of a mid-latitude winter storm. Geophysical Research Letters 39(12) :n/a–n/a, DOI 10.1029/2012GL052440, l12808

Rivière G, Arbogast P, Joly A (2015a) Eddy kinetic energy redistribution within idealized extratropical cyclones using a two-layer quasi-geostrophic model : Eddy kinetic energy redistribution within idealized extratropical cyclones using a two-layer quasi-geostrophic model. Quarterly Journal of the Royal Meteorological Society 141(686) :207–223, DOI 10.1002/qj.2350

Rivière G, Arbogast P, Joly A (2015b) Eddy kinetic energy redistribution within windstorms klaus and friedhelm. Quarterly Journal of the Royal Meteorological Society 141(688) :925–938, DOI 10.1002/qj.2412, URL http ://dx.doi.org/10.1002/qj.2412

Roberts JF, Champion AJ, Dawkins LC, Hodges KI, Shaffrey LC, Stephenson DB, Stringer MA, Thornton HE, Youngman BD (2014) The XWS open access catalogue of extreme European windstorms from 1979 to 2012 DOI 10.5194/nhess-14-2487-2014, URL https ://ore.exeter.ac.uk/repository/handle/10871/21082

Schultz DM, Vaughan G (2011) Occluded Fronts and the Occlusion Process : A Fresh Look at Conventional Wisdom. Bulletin of the American Meteorological Society 92(4) :443–466, DOI 10.1175/2010BAMS3057.1, URL http ://journals.ametsoc.org/doi/abs/10.1175/2010BAMS3057.1

Schultz DM, Keyser D, Bosart LF (1998) The effect of large-scale flow on low-level frontal structure and evolution in midlatitude cyclones. Monthly Weather Review 126(7) :1767–1791

Shapiro, Keyser (1990) Fronts, jet streams and the tropopause. extratropical cyclones, the erik palmen memorial volume c. w. newton and e. o. holopainen, eds. American Meteorological Society p 167–191

Sinclair MR (1994) An objective cyclone climatology for the southern hemisphere. Monthly Weather Review 122(10) :2239–2256

Sinclair MR (1997) Objective Identification of Cyclones and Their Circulation Intensity, and Climatology. Weather and Forecasting 12(3) :595–612, DOI 10.1175/1520-0434(1997)012<0595 :OIOCAT>2.0.CO ;2

Tilinina N, Gulev SK, Rudeva I, Koltermann P (2013) Comparing Cyclone Life Cycle Characteristics and Their Interannual Variability in Different Reanalyses. Journal of Climate 26(17) :6419–6438, DOI 10.1175/JCLI-D-12-00777.1

Trigo IF, Davies TD, Bigg GR (1999) Objective climatology of cyclones in the mediterranean region. Journal of Climate 12(6) :1685–1696

Uccellini LW (1990) Processes contributing to the rapid development of extratropical cyclones. Extratropical Cyclones : The Erik Palmén Memorial Volume pp 81–105

Ulbrich U, Leckebusch GC, Pinto JG (2009) Extra-tropical cyclones in the present and future climate : a review. Theoretical and Applied Climatology 96(1-2) :117–131, DOI 10.1007/s00704-008-0083-8

Varino F (2011) Reassessing the impacts and atmospheric circulation of large storms over Portugal (MSc thesis). University of Lisbon

Vinet F, Lumbroso D, Defossez S, Boissier L (2012) A comparative analysis of the loss of life during two recent floods in France : the sea surge caused by the storm Xynthia and the flash flood in Var. Natural Hazards 61(3) :1179–1201, DOI 10.1007/s11069-011-9975-5, URL https ://link.springer.com/article/10.1007/s11069-011-9975-5

Vitolo R, Stephenson DB, Cook IM, Mitchell-Wallace K (2009) Serial clustering of intense european storms. Meteorologische Zeitschrift 18(4) :411–424, DOI 10.1127/0941-2948/2009/0393

Wang XL, Feng Y, Compo GP, Swail VR, Zwiers FW, Allan RJ, Sardeshmukh PD (2013) Trends and low frequency variability of extra-tropical cyclone activity in the ensemble of twentieth century reanalysis. Climate Dynamics 40(11-12) :2775–2800, DOI 10.1007/s00382-012-1450-9

Wang XL, Feng Y, Chan R, Isaac V (2016) Inter-comparison of extra-tropical cyclone activity in nine reanalysis datasets. Atmospheric Research 181 :133–153, DOI 10.1016/j.atmosres.2016.06.010

Wernli H, Dirren S, Liniger MA, Zillig M (2002) Dynamical aspects of the life cycle of the winter storm 'Lothar' (24–26 December 1999). Quarterly Journal of the Royal Meteorological Society 128(580) :405–429, DOI 10.1256/003590002321042036